University of Nottingham
UK | CHINA | MALAYSIA

Combining extracellular matrix hydrogels and electrical stimulation to influence macrophage polarisation

Charlie D. Whitehead, BMed.Sci

School of Pharmacy

Thesis submitted to the University of Nottingham for the degree of Doctor of Philosophy

May 2023

“It’s a process, not an ideology”

- Hank Green

Abstract

The research and development that is invested in the complex process that is wound healing is vast. The volume of wound care research is accelerating in response to skyrocketing costs of complex wound care; ageing populations with increased comorbidities being the significant element. These variables lead to a greater quantity of complex and chronic wounds, which are more costly to treat. One major factor in limiting normal wound repair is persistent inflammation. Macrophages and fibroblasts are crucial regulators of inflammation, amongst other aspects of the wound healing process. In a chronic wound macrophage function has been shown to be impaired, leading to prolonged inflammation; while impacts on fibroblast function have been shown to delay wound closure. Drivers behind these deviations from normal healing are likely due to changes in local stimuli. To address this issue and enhance the treatment of chronic wounds, it becomes imperative to explore innovative strategies aimed at modulating cell function.

An expanding field branching into wound care is that of bioelectronic medicine: the fusion of biology and electronics. Electrical stimuli have already been shown to influence migration, phagocytotic activity, and the hastening of wound closure. Electrical stimuli-based therapies are already being used clinically to accelerate wound healing. However, there is a limited understanding about how electrical signals specifically modulate macrophage phenotype, and therefore function. Despite the advancements made in the biological understanding of wound healing and therapies used to treat it, the use of traditional two-dimensional cell culture is still commonly utilised as the first step in the research process. The use of these methods leads to cell morphologies and behaviour that are alien compared to the in vivo equivalent. The application of biomaterials has been utilised to develop a more representative microenvironment. Such models enable cultured cells to better replicate the behaviour that is seen in vivo compared to conventional tissue

culture plastic, with biomaterials often offering both structural and biochemical components to augment the in vivo mimetic models. Animal-derived extracellular matrices have been used in for these purposes.

In this thesis, it is hypothesised that combining extracellular matrix biomaterials with exogenous electrical stimuli will drive macrophage polarisation towards a pro-healing phenotype. To address this hypothesis, extracellular matrix hydrogels combined with electrical stimuli propagating carbon nanotubes were interrogated for their mechanical and electrical properties. After which, said biomaterials were used in the multi-dimensional culturing of THP-1 derived macrophages and BJ fibroblasts whilst stimulated exogenously with both direct current and electric field effects; with cellular readouts revolving around biocompatibility and cytokine secretion.

The incorporation of carbon nanotubes into an extracellular matrix hydrogel generated a novel biomaterial, with softer mechanical and enhanced electrical properties compared to the carbon nanotube free control. The biomaterials generated all proved to be biocompatible, yet the incorporation of carbon nanotubes hindered the acquisition of both qualitative and quantitative data. Regardless, it was shown that the culture of macrophages on the extracellular matrix hydrogels promoted the pro-healing phenotype, as did the stimulation with electric fields.

The data posed in this thesis demonstrate the importance of increasing how representative the microenvironment is when it comes to obtaining cellular readouts. Whilst it produces more complex experimental designs with their own challenges, it will allow for a greater confidence in results translated into further in vivo study and beyond.

Impact statement

This impact statement explores the profound influence of COVID and financial circumstances on both my laboratory time and the writing process throughout the course of my thesis.

The COVID-19 pandemic impacted the project directly for approximately six months between March and September 2020. Effects of the pandemic were exacerbated by the fact almost three months' worth of laboratory time was lost just prior to the first lockdown. This was a result of the transition from the old Centre of Biomolecular Sciences to the new BioDiscovery Institute from November 2019 to January 2020. Upon return to the laboratory in the BioDiscovery Institute, progress was further hindered by COVID regulations. Social distancing meant that laboratory space was limited, with some virtually inaccessible for long periods due to the large demand. An effect of this was training opportunities were heavily limited and delays on new techniques were abundant. Procurement of reagents and assay kits was also impacted, not only due to the pandemic but as an aftermath of Brexit. Deliveries which usually took a matter of days ended up taking several weeks, if not months. Factors which led to this include supplier and delivery staff contracting COVID-19 and items getting delayed at customs as a result of new import legislation. Laboratory consumables were also heavily affected by the issues stated above, as well as being impacted due to the demand of said consumables in government laboratories across the country, given the increased test and trace capabilities. There were many occasions where experiments would be planned out, laboratory space booked, and all reagents having had arrived; yet a lack of simple consumables such as pipette tips of any size. Various permutations of this scenario occurred for at least another year; not in such a way where it was as detrimental to work as the initial period in March to September 2020, but still limiting the output of time spent collecting data to produce this thesis.

As a result of missing out on laboratory time due to COVID, I spent more time in the laboratory than expected which infringed on the time I'd allocated for writing. This meant that my writing time was now fully unfunded. Given that the cost-of-living crisis was in full swing and with my personal circumstances leaving me no choice, I had to take up employment during my writing time to pay for the essentials. This encroached into my writing time; meaning I often wrote late into the night after a full day of other commitments.

Acknowledgments

Firstly, I would like to thank Frankie Rawson for accepting me onto this project way back in 2018. He believed in me before anyone else and for that I am forever grateful. This belief continued throughout my time at the University of Nottingham, enabling me to build enough belief in myself to get through the trials and tribulations produced by a PhD during a global pandemic. Secondly, I would like to thank Lisa White for providing her academic expertise and support throughout. Thirdly, I would like to thank Amir Ghaemmaghami for sharing his laboratory and consumables for my cell-based work, as well as his swift feedback.

A PhD cannot be completed without the support of colleagues. I would like to acknowledge Josh Jones for the many hours spent discussing our projects, academia, and current affairs, as well as the many hours spent "team building" in Verdansk – you really helped me pull through. There are many others who I interacted with throughout my project who made me feel included and more knowledgeable through their insights. To Paola Sanjuan-Alberte for her kindness in welcoming me to the world of academia and electrochemistry. To Matt Vassey for his introduction to cell culture, guidance in experimental planning, and general enthusiasm for science. To Dom Mosses for his discussions regarding the state of all things academia, willingness to listen to me vent, and his ability to help me work through crackpot ideas. To George Loxley for his cheery conversation over many long ELISA days, as well as his calm advice upon many failures in the lab. To Steve Gibney, Andie Shaw, Jacqui Hicks, and all in the Rawson Group who made me feel a part of the team. To Simon Kellaway, Rabea Loczinski, Elisa Tarsitano, I-Ning Lee, Ami Nash, and all in the White group who sat through my bumbling presentations on multiple occasions and provided meaningful comments to help me improve. To Mitchell Day, Arsalan Latif, Lisa Kämmerling, and all in

the Immunology and Immuno-Bioengineering Group who introduced me to the wonderful world of macrophages and cytokines, thanks for sticking with my stupid questions.

I would also like to thank Teresa Marshall, Ann Williams and Karen Lawler for keeping the laboratories in which I worked running smoothly whilst providing training and a shoulder to moan on regularly. Research would not be possible without you. Research would also not be possible without the collective effort of teams around the world sharing their findings, therefore I would also like to show my appreciation for Alexandra Elbakyan in making that work available to all, not just those who have the means to peek over the paywall.

Lastly, I would like to thank my wife, Mia. You have been my rock throughout this process and have essentially held me together at multiple points. I cannot articulate how much this means to me, and how grateful I am that you push me to continue forward when life is difficult. I dedicate this thesis, the culmination of the last five years of my life, to you.

Contents

Abstract i
Impact statement iii
Acknowledgments v
List of figures x
List of tables xii
Abbreviations xiii
Chapter 1 | Introduction 1
1.1 Cellular response during the wound healing process 2
1.2 In vitro wound healing models 7
1.3 Bioelectronic medicine 11
1.3.1 Electrical stimuli 14
1.3.2 Application of electrical stimuli 18
1.3.3 Electrical stimuli in the context of wound healing 27
1.4 Extracellular matrix biomaterials 42
1.4.1 The extracellular matrix 42
1.4.2 Decellularisation 49
1.4.3 Biomaterial form 52
1.5 Hypothesis and aims 54
Chapter 2 | Materials and Methods 56
2.1 Materials 56
2.2 Equipment and software 57
2.3 Chapter 3 methods 58
2.3.1 DNA analysis 58
2.3.2 Electrical characterisation 59
2.3.3 GAG analysis 60
2.3.4 Material generation 61
2.3.5 Mechanical characterisation 66
2.3.6 Visual characterisation 67
2.4 Chapter 4 methods 68
2.4.1 Biocompatibility analysis 69
2.4.2 BJ fibroblast culture 70
2.4.3 Electrical stimulation 71
2.4.4 ELISA 72
2.4.5 Immunocytochemistry 74

2.4.6 THP-1 monocyte culture 74
2.5 Chapter 5 methods 76
2.5.1 Bioprinting 76
2.5.2 Room temperature rheology 77
Chapter 3 | CNT-ECM incorporated hydrogels 78
3.1 Introduction 78
3.2 Experimental design 84
3.2.1 Post-decellularisation biochemical quantification 84
3.2.2 FEG SEM preparation 86
3.2.3 Hydrogel mechanical quantification 87
3.2.4 Hydrogel electrical quantification 90
3.3 Results and discussion 93
3.3.1 SIS-ECM generation and decellularisation success criteria 93
3.3.2 SIS-ECM hydrogel generation and macrophotography 97
3.3.3 Carbon allotrope incorporated SIS-ECM hydrogels microstructure 98
3.3.4 MWCNT incorporation confirmation via Raman spectroscopy 101
3.3.5 Mechanical properties of carbon allotrope incorporated ECM hydrogels 104
3.3.6 Electrical properties of carbon allotrope incorporated ECM hydrogels 122
3.4 Conclusions 127
Chapter 4 | Cellular response to ECM coupled with DC stimulation 129
4.1 Introduction 129
4.2 Experimental design 130
4.2.1 Macrophages and fibroblasts 130
4.2.2 Cellular readouts 134
4.2.3 Culture dimensions 136
4.2.4 Electrical stimuli 137
4.3 Results and discussion 139
4.3.1 Hydrogel biocompatibility 139
4.3.2 Impact of growth substrate on macrophage polarisation 146
4.3.3 Electrical stimulation cytocompatibility 157
4.3.4 Combinatory impact of growth substrate and electrical stimulation 164
4.3.5 Impact of growth substrate on cytokine release 172
4.4 Conclusions 174
Chapter 5 | Discussion, future work, and conclusions 176
5.1 Discussion 177

5.1.1 SIS decellularisation methods are robust, yet the criteria governing “success” require attention 177
5.1.2 CNT incorporation influences hydrogel characterisation 178
5.1.3 CNT-ECM hydrogels are biocompatible while electrical stimuli are biocompatible at strengths noted in vivo 179
5.1.4 ECM hydrogels promote M2 polarity, electrical stimuli influence both phenotypes 179
5.2 Limitations within the results 180
5.3 Future work 184
5.3.1 Primary cells and co-culture 184
5.3.2 PCR 185
5.3.3 Adding further complexity to the wound healing model 185
5.3.4 Bioinks and 3D bioprinting 186
5.4 Conclusions 191
References 193

List of figures

Figure 1.1: Cellular influence in wound healing. 3
Figure 1.2: A combinatory approach to in vitro models. 11
Figure 1.3: Ion and electron movement induces a current, allowing conductivity across membranes of cells and organelles. 14
Figure 1.4: Waveforms of alternating and direct current. 19
Figure 1.5: Pulse currents. 21
Figure 1.6: Hexagonal configuration within the CNT lattice. 25
Figure 1.7: Transepithelial potential mechanism. 29
Figure 1.8: A representation of reepithelialisation. 37
Figure 2.1: Gel-electrode set up during EIS interrogation. 60
Figure 2.2: Preparation and generation of decellularised small intestinal submucosal ECM. 63
Figure 2.3: Electron micrographs of the two MWCNT forms utilised in this thesis. 65
Figure 2.4: Rheometer configuration during experimentation. 67
Figure 2.5: Electrical stimulation set-up schematic. 72
Figure 3.1: Impedance, the result of reactance (X) and resistance (R). 92
Figure 3.2: Decellularisation success criteria using dsDNA as an indicator. 94
Figure 3.3: GAG retention in decellularised SIS-ECM. 96
Figure 3.4: Hydrogel formation and macrophotography of the carbon allotrope incorporated hydrogels. 98
Figure 3.5: Representative microstructures of SIS-ECM hydrogels via FEG-SEM at different magnifications. 100
Figure 3.6: Raman spectra and mapping of carbon allotrope incorporated hydrogels. 103
Figure 3.7: Typical gelation profiles of hydrogels containing 0.2% w/v allotropes of carbon. 106
Figure 3.8: Loss tangent transformations of the gelation profiles of hydrogels containing 0.2% allotropes of carbon. 108
Figure 3.9: Typical gelation profiles of hydrogels containing 0.02% w/v allotropes of carbon. 111
Figure 3.10: Tanδ transformations of the gelation profiles of hydrogels containing 0.02% allotropes of carbon. 113
Figure 3.11: G' values at 1% strain of varying ECM and carbon allotrope concentrations. 115
Figure 3.12: Typical amplitude sweeps of hydrogels containing 0.2% w/v allotropes of carbon. 117
Figure 3.13: Typical amplitude sweeps of hydrogels containing 0.02% w/v allotropes of carbon. 118
Figure 3.14: Impedance and corresponding admittance spectra of SIS-ECM hydrogels containing 0.2% allotropes of carbon. 123
Figure 3.15: Impedance and corresponding admittance spectra of SIS-ECM hydrogels containing 0.02% allotropes of carbon. 124
Figure 4.1: Metabolism of THP-1 derived M0-like macrophages (ATCC® TIB-202™) after 24 h post-differentiation growth on TCP vs. SIS-ECM hydrogels of varying concentrations. 140
Figure 4.2: Metabolism of THP-1 derived M0-like macrophages (ATCC® TIB-202™) after 24 h post-differentiation growth on three substrates. 142

Figure 4.3: Fluorescent microscopy and quantitative analysis of hydrogel cytotoxicity on BJ fibroblasts (ATCC® CRL-2522™)..... 144
Figure 4.4: Brightfield microscopy of M0 THP-1 derived macrophages (ATCC® TIB-202™) grown for 3 days in 2.5D culture on three substrates. on TCP, ECM hydrogels, and 0.2% w/v CNT-ECM hydrogels. 147
Figure 4.5: Fluorescent microscopy of THP-1 derived macrophages (ATCC® TIB-202™) grown on three substrates 3 days post-PMA differentiation. 149
Figure 4.6: Cytokine profiles of THP-1 derived macrophages (ATCC® TIB-202™) grown on three substrates 3 days, post-PMA differentiation. 152
Figure 4.7: Fluorescent microscopy of THP-1 derived macrophages (ATCC® TIB-202™) grown on three substrates 6 days post-PMA differentiation. 153
Figure 4.8: Cytokine profiles of THP-1 derived macrophages (ATCC® TIB-202™) grown on three substrates 6 days, post-PMA differentiation. 156
Figure 4.9: Analysis of cell lysis and metabolism of THP-1 derived M0-like macrophages (ATCC® TIB-202™) after 24 h post-differentiation growth on TCP when exposed to electrical stimulation. 159
Figure 4.10: Analysis of cell lysis products of THP-1 derived M0-like macrophages (ATCC® TIB-202™) after 24 h post-differentiation growth on TCP when exposed to 2.4 V DC electrical stimulation for two exposure durations. 161
Figure 4.11: Metabolism of THP-1 derived M0-like macrophages (ATCC® TIB-202™) grown on three substrates, 6 days post-stimulation. 163
Figure 4.12: Cytokine profiles for M1 markers of THP-1 derived M0-like macrophages (ATCC® TIB-202™) grown on three substrates, 6 days post-stimulation. 166
Figure 4.13: Cytokine profiles for M2 markers of THP-1 derived M0-like macrophages (ATCC® TIB-202™) grown on three substrates, 6 days post-stimulation. 168
Figure 4.14: Cytokine profiles for pro-immunomodulatory markers of BJ fibroblasts (ATCC® CRL-2522™) grown on three substrates, 4 days post-stimulation. 170
Figure 4.15: Cytokine profiles for pro-inflammatory markers of BJ fibroblasts (ATCC® CRL-2522™) grown on three substrates, 4 days post-stimulation. 172
Figure 4.16: Cytokine profiles of spiked cell culture media incubated on four different substrates..... 174
Figure 5.1: The number of publications featuring the phrase “wound healing” between 1950-present. 176
Figure 5.2: Quantification of decellularisation metrics across three separate small intestines. 182
Figure 5.3: A schematic presenting an improved experimental model. 186
Figure 5.4: Macrophotography of printed CNT-ECM pre-gels in a gelatine bath and the resultant hydrogels created. 188
Figure 5.5: Gelation profiles of 8 mg.mL^{-1} ECM only and 0.2% w/v CNT-ECM hydrogels produced at 21 °C. 190

List of tables

Table 1.1: Macrophage phenotypes noted in wound healing scenarios: functions and markers. 5
Table 1.2: Additives used in biomaterials to primarily enhance conductivity. 23
Table 1.3: A summary of the components within in vivo extracellular matrix. 47
Table 2.1: Materials used, and the supplier associated. 56
Table 2.2: Equipment and software used, and the supplier associated. 57
Table 2.3: Formulation table concerning the production of SIS-ECM hydrogels of varying ECM concentrations. 64
Table 2.4: Formulation table concerning the production of carbon allotrope incorporated SIS-ECM hydrogels of varying concentrations. 66
Table 3.1: Tabulated ECM and carbon allotrope concentration dependant linearity limit and yield point data from Figures 3.12 and 13. 120
Table 4.1: Relationship between stimuli strength applied across the well and the resultant field strength. 138

Abbreviations

AC	Alternating current
ADP	Adenosine diphosphate
ATCC	American Type Culture Collection
ATP	Adenosine triphosphate
bFGF	Basic fibroblast growth factor
bp	Base pairs
BSA	Bovine serum albumin
CCL18	Chemokine ligand 18
CPD	Critical point drying
CNT	Carbon nanotube
DAPI	4',6-Diamidino-2-phenylindole
DC	Direct current
dH_2O	Deionised water
DMMB	1,9-Dimethyl-methylene blue
DNA	Deoxyribonucleic acid
ECM	Extracellular matrix/matrices
EDTA	Ethylenediaminetetraacetic acid
EIS	Electrochemical impedance spectroscopy
ELISA	Enzyme-linked immunosorbent assay
FEG SEM	Field emission gun scanning electron microscope
FRESH	Freeform reversible embedding of suspended hydrogels
GAG	Glycosaminoglycan
GM-CSF	Granulocyte macrophage colony-stimulating factor
HA	Hyaluronic acid
HCl	Hydrochloric acid
HGF	Hepatocyte growth factor
HRP	Horseradish peroxidase
IFN-γ	Interferon-gamma
IL-10	Interleukin-10
IL-1β	Interleukin-1 beta
IL-4	Interleukin-4
IL-6	Interleukin-6
LPS	Lipopolysaccharide
LVE	Linear viscoelastic
M0	Naïve macrophage
M1	Inflammatory macrophage
M2	Immunomodulatory macrophage
MBV	Matrix-bound vesicle
MCP-1	Monocyte chemoattractant protein-1
M-CSF	Macrophage colony-stimulating factor
MMP	Matrix metalloprotease
MW15	Multi-walled carbon nanotube with a 15 nm outer diameter
MW30	Multi-walled carbon nanotube with a 30 nm outer diameter
MWCNT	Multi-walled carbon nanotube
Na^+/K^+ ATPase	Sodium-potassium pump
NC	Mixed nanocarbon
PAA	Peroxyacetic acid

PBS	Phosphate buffered solution
PI(3)Kγ	Phosphophatidylinositol-3-kinase gamma
PMA	Phorbol 12-myristate 13-acetate
RFU	Relative fluorescent units
ROS	Reactive oxygen species
RPMI	Roswell Park Memorial Institute
SDS	Sodium dodecyl sulphate
SIS	Small intestinal submucosa
SWCNT	Single-walled carbon nanotube
TE buffer	Tris-EDTA buffer
TGF-β1	Transforming growth factor beta 1
THP-1	Human leukaemia monocytic cell line
TNF-α	Tumour necrosis factor alpha
VEGF	Vascular endothelial growth factor

Chapter 1 | Introduction

A wound is defined as disruption to the integrity of tissue through physical, thermal, or chemical means. This disruption means the skin barrier is compromised, with the tissues below exposed to the outside world. Wounds can be acute; healing via a regular process over a period of four to six weeks on average (Wallace et al., 2023). The regular wound healing process involves four overlapping phases: haemostasis, inflammation, proliferation, and tissue remodelling (Guo and DiPietro, 2010). It is crucial that these phases occur in the correct order and for appropriate timeframes, otherwise an acute wound can become chronic. Wounds can be considered chronic if healing isn't progressing after four weeks (Frykberg and Banks, 2015), or completed within six weeks (Scotton et al., 2014). Complex wounds often become chronic rather than acute. Complex wounds often possess, at a minimum, one of the following: large loss of biological material (i.e. layers of skin), frequent infections within the area, tissue necrosis or damage to local circulatory architecture, or the patient also suffers from an otherwise unrelated disease which can impair wound healing: such as diabetes, vascular diseases, and immunosuppression (Ferreira et al., 2006; Park et al., 2010). Treatment plans for complex wounds are inherently more challenging, often requiring concurrent treatments leading to increased costs (Frykberg and Banks, 2015). Research today is focused on developing novel therapies to treat various types of wounds by better understanding the mechanisms involved in the wound healing process. This continued discovery is vital, as the cost of wound care is on the rise. A study into the wound care spending by the NHS in the fiscal year of 2017-18 showed that the cost of general wound management reached £8.3 billion, with 3.8 million patients requiring care (Guest et al., 2020). The authors of this study estimate that patient numbers will rise by 11% per annum, meaning budgets are required to stretch even further due to increased ageing (Storey et al., 2018) and comorbidities (Nussbaum et al., 2018). It is not only

comorbidities that are on the rise, but treatment costs have been increasing for decades. For example, the treatment for diabetic foot ulcers increased almost 3-fold in 20 years (Harrington et al., 2000), rising by over £200M per annum (Dowsett et al., 2014). As discussed, complex wounds are inherently harder and thus more expensive to treat due to the associated steps required (Olsson et al., 2018). While a healthy patient may require only a clean dressing, a patient with comorbidities may require a clean dressing along with antibiotics, multiple GP/specialist visits and even surgery to apply a skin graft or to amputate irreparable tissues (InformedHealth, 2006). With comorbidity impacted wound healing and the increase of the elderly within the population, spending is set to skyrocket in the future.

1.1 Cellular response during the wound healing process

The major cell types involved throughout the wound healing process are platelets, neutrophils, macrophages, and fibroblasts (Yussof et al., 2012) (Figure 1.1). Platelets initiate healing through haemostasis. The aggregation and activation of platelets, aided by vasoconstriction, slows and eventually prevents further haemorrhaging (Periayah et al., 2017).

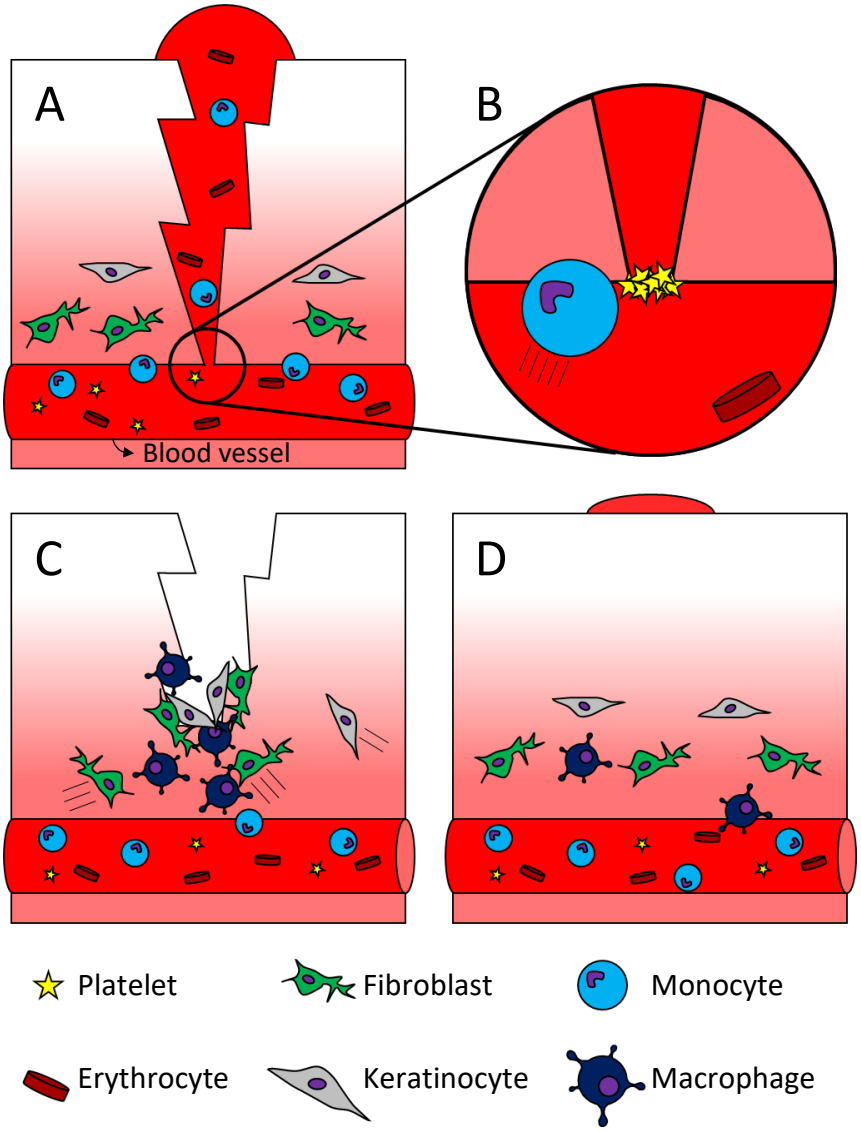

Figure 1.1: Cellular influence in wound healing. Wound generation inflicts damage upon the architecture of the epidermis, dermis, and vasculature (A). Platelet activation causes aggregation at the site which the vasculature is impacted, creating a plug (B). Various cell types migrate to the site to restore and repair; macrophages engulf foreign bodies and cellular debris, fibroblasts remodel damaged and deposit new ECM, and keratinocytes re-epithelialise the damaged region (C). Macrophages engulf redundant cells which have undergone apoptosis, while fibroblasts and keratinocytes return to their pre-wound generation states, maintaining the dermis (D). The pink-white gradient represents the cellular dermis, in pink, and acellular epidermis, in white. Adapted with permission from Gushiken et al. (2021).

Growth factors and cytokines released by platelets, and the wound site cell population, lead to the recruitment of other immune cells; initiating the inflammatory stage (Wallace et al., 2023). Circulating neutrophils first migrate toward the site via chemotaxis, acting through phagocytosis and degranulation. The release of proteases allows for the

degradation of extracellular matrix (ECM) proteins while cytokines, such as TNF-α, are vital for further cell recruitment (Baum and Arpey, 2005; Komi et al., 2019). Monocytes are recruited to the wound site and activated by local chemical stimuli, with one of the pathways leading to monocyte-macrophage differentiation (Krzyszczky et al., 2018). Naïve macrophages (M0) can then polarise further on a spectrum from inflammatory (M1) to anti-inflammatory and immunomodulatory (M2). These two sides of the macrophage polarity spectrum are key for the wound healing process to proceed in a normal, healthy manner (Martin and Leibovich, 2005). However, this spectrum is fluid. Macrophages can exhibit both M1 and M2 behaviours and thus populations are described as heterogeneous, acting as M1- or M2-like (Ogle et al., 2016). M2-like cells can be further categorised depending on functionality and associated markers (Krzyszczky et al., 2018). Similar to the M1/M2 spectrum, macrophages can transfer between these various subsets (Ogle et al., 2016). A summary of macrophage phenotypes is presented in Table 1.1.

Table 1.1: Macrophage phenotypes noted in wound healing scenarios: functions and markers. This is not a comprehensive list of markers as the literature quite often reports them overlapping, making defining macrophages difficult given the inherent complexity. Other distinctions of macrophage have been identified but have little association to wound healing and therefore have not been included in this table, see Krzyszczky et al., 2018 for these other phenotypes.

Phenotype		Function	Markers		References
			Surface	Secreted	
M1		Classically activated immune cells which participate in pro-inflammatory responses and host defence mechanisms. Can persist in chronic wounds.	CD86, calprotectin	TNF-α, IL-6, IL-12, IL-1β	Ogle et al., 2016; Zhao et al., 2016; Hesketh et al., 2017; Krzyszczky et al., 2018
M2		Alternatively activated, involved in the promotion of tissue repair, reduces inflammation, and regulates the immune response by releasing anti-inflammatory cytokines. There are a variety of subsets, see below, that have more specific functionality.	-	-	Ogle et al., 2016; Krzyszczky et al., 2018
M2 subsets	M2a	Associated with wound repair, through inflammation resolution and promoting healing through cytokine signalling and phagocytosis.	Mannose receptor (CD206), CD163	IL-10, CCL18, CCL22, TGF-β, IL-1α	Spiller et al., 2014; Ogle et al., 2016; Yao et al., 2019
	M2b	Regulatory macrophages, expressing both inflammatory and anti-inflammatory markers to manage the immune response and resulting inflammatory reaction.	CD86, CD258	IL-10, CCL1, TNF-α, IL-6	Wang et al., 2018
	M2c	Inactivated macrophages which primarily engage in phagocytosis of apoptotic cells and ECM debris, whilst being involved in the matrix formation via matrix metalloproteinase (MMP) production.	MerTK, Arg-1	IL-10, CCL16, CCL18, TGF-β, CXCL13	Zizzo et al., 2012; Krzyszczky et al., 2018; Yao et al., 2019
	M2d	Proangiogenic with influences in tumour progression.	IL-10R, IL-12R	VEGF, IL-10, iNOS	Ferrante and Leibovich, 2012; Yao et al., 2019

During the inflammation stage M1-like macrophages engulf bacteria and dead cells to allow for efficient tissue repair, while releasing enzymes such as MMPs to degrade damaged ECM components which clears the space for new ECM. Pro-inflammatory macrophages continue the production of inflammatory cytokines to further recruit and differentiate incoming immune cells.

Fibroblast recruitment signals the initiation of the proliferative stage, due to cytokine release from both platelets and macrophages. The fibroblast's main role is MMP secretion and ECM precursor production, with the former's activity waning as damaged ECM is removed via phagocytic cells (Mirastschijski et al., 2010). Macrophages remain a major force in the proliferative stage, transitioning from an M1- to M2-like state. In this form, anti-inflammatory effects are promoted through cytokine release from subsets M2b/c (Krzyszczky et al., 2018), leading to the recruitment of further fibroblasts as well as endothelial cells and keratinocytes. Said cytokines also promote the proliferation of these cell types. Endothelial cells and M2d macrophages drive angiogenesis which further aids migration while supplementing glucose, oxygen, et cetera to the site (DiPietro, 2016). Keratinocytes migrate from the wound edge and begin re-epithelialisation (Landén et al., 2016); this phase beings towards the tail end of the inflammatory response. Tissue remodelling is the stage in which deposited ECM is processed into its final form and any cells which are no longer of use undergo apoptosis. Cytokines released from M2a-like macrophages cause fibroblast transdifferentiation into myofibroblasts. This is a specialist cell type responsible for promoting the contraction of ECM fibres, leading to wound closure due to the upregulation of α-smooth muscle actin. Whilst cytokines, mainly TGF-β1, influence myofibroblast transdifferentiation, ECM proteins do too. Prior to wound closure, collagen I overtakes collagen III in terms of the predominant ECM protein present. This shift is facilitated by myofibroblast contractility, so the relative reduction of collagen III is a cue for that transdifferentiation of fibroblast-myofibroblast to occur (Volk et al., 2011). Once

wound closure is achieved, myofibroblasts undergo apoptosis. This is thought to be a combination of self-inflicted burial in the ECM they secrete, leading to a suspension in the cell cycle (Koyama et al., 1996) and a reduction in adhesion (Carragher et al., 1999). Macrophages clean up during this phase, whether that be dead cells or obsolete vasculature debris once a mature acellular and avascular epidermis is achieved.

One way chronic wounds form is as a result of the inflammatory stage lingering, leading to further tissue damage and blocking the pro-immunomodulatory proliferation and remodelling phases from completion. It has been suggested that a potential culprit for this in some cases is due to macrophages remaining in the M1-like state (Zhao et al., 2016; Hesketh et al., 2017), which causes further disruption through further ECM degradation, hindering the processes which lead to wound closure.

1.2 In vitro wound healing models

Due to the complexity of the wound healing process, it is currently not feasible to replicate it as a whole. Therefore, in vitro wound healing models instead aim to replicate small parts to build a picture of how it and potential treatments work (Masson-Meyers et al., 2020). Traditionally, models were designed to investigate one aspect of wound healing, such as migration and proliferation. The scratch assay, for example, utilises simple two-dimensional (2D) cultures to investigate cell migration and proliferation, as markers of wound closure, across an area which has had cells removed (Liang et al., 2007). While this is a simple and cheap experiment to utilise, there are glaring differences between this and in vivo healing which raises doubts as to how applicable any results are for clinical applications. Stamping has been used to eliminate some of these limitations. Stamping refers to the application of pressure on an area of a cell monolayer (Lee et al., 2010). It is an improvement on the

scratch assay in that the cellular debris and underlying ECM remain in place, meaning it is more like the in vivo environment. However, it is still underpinned by 2D culture and therefore isn't necessarily translatable from bench to bedside.

Research performed in 2D culture is known to be challenging to translate in vivo as the in vivo environment is not 2D, it is three-dimensional (3D). Hence the push to move away from 2D platforms for cell culture to become the norm. 2D culture has advantages: it is easy to set up and perform experiments in a simplistic and easy-to-control way. However, the downsides are that it is far from representative of the in vivo environment. Cells grown on a 2D monolayer are often noted as more spread out in their morphology compared to their in vivo counterparts (Edmondson et al., 2014). This distorted morphology is matched to a distorted phenotype, with cell behaviour not matching the respective in vivo setting due to the inadequate mimicking of the environment (Duval et al., 2017). Sun et al. (2006) reported that culturing in a more representative 3D environment elicits an increased resistance to hydrogen peroxide and silver nitrate, even at concentrations which render cells cultured in conventional 2D conditions unviable, therefore it can be postulated that the cellular response to treatments could differ that much too. This is likely influenced by diffusion rates through 3D environments compared to the 2D monolayer (Temple et al., 2022). Hsieh et al. (2015) also discuss reduced drug sensitivity in 3D cultures as well as other changes in proliferation and metabolic activity, suggesting that different culture models promote fundamental differences in cell behaviour. This is undesirable as many treatments could fail in vitro testing in 2D but pass in the more representative 3D environments, or vice versa, meaning wasted time, money, and opportunities in the drug discovery process. Caliari et al. (2016), among others, state that factors such as substrate stiffness and degradability have an impact on cell phenotype, meaning the conventional tissue culture plastic is far from ideal. A method that partly combats the flaws of 2D culture is to culture in two-and-a-half-dimensions (2.5D). In 2D culture, the substrate used is flat,

usually tissue culture treated plastic or glass. In 2.5D culture, the substrate used allows for variation of the cell-substrate environment leading to a more representative microenvironment compared to conventional 2D culture. Nonetheless, the most representative culture method is 3D cell culture. Here, cells are surrounded by cell-cell or cell-substrate interactions all around them, which are missing in 2D culture environments (Sun et al., 2006). These cultures can mimic the in vivo environment and thus the cell morphology may be more similar to the in vivo scenario (Ravi et al., 2014). Often the materials used are much softer than the tissue culture plastic (TCP) of 2D culture too, allowing for a better in vivo cell-substrate representation.

Hydrogels are a common 2.5/3D culture substrate. They possess a high-water content, due to the hydrophilic nature of the polymeric network, which means they can provide nutrient and gas exchange throughout the structure, mimicking in vivo environments. Hydrogels can be formed from many materials. Synthetic materials have been used, such as polyethylene glycol (Chia et al., 2012) and polyacrylamide (Liu et al., 2010), as they have the ability to undergo functionalisation: vitronectin has been used to enhance cell attachment on pentaerythritol triacrylate biomaterials (Vaithilingam et al., 2021) and fibronectin has been used to functionalise polyethylene glycol to investigate markers of tumour migration (Singh et al., 2014), for example. This can allow for the customisation of various factors such as stiffness and cellular interactions, via crosslinking bioactive molecules respectively (Kudva et al., 2018; Ahmed et al., 2022). Natural materials provide alternative advantages. Utilising materials such as collagen (Lin et al., 2019) and glycosaminoglycans (GAGs) (Burdick et al., 2011) may provide innate bioactivity, with cells able to modulate the hydrogels through enzymatic degradation and further ECM secretion. Hydrogels of this type have been used to investigate certain parts of the wound healing process, including macrophage and fibroblast behaviour (Zhang et al., 2019; Sapudom et al., 2021; Yang et al., 2021).

An increasing number of wound healing models are defined as human skin equivalents. These models combine cellular aspects of wound healing, such as fibroblasts, and acellular aspects, such as components of the ECM. Human skin equivalents have been used as a model for in vitro analysis for a range of utilities in recent decades, becoming more complex over time. From the study of specific pathways such as fibrosis in developing an environment for the analysis of anti-fibrotic therapies (Matei et al., 2019), to aiming to reduce the reliance on animal models for the most in vivo-like through more representative data before phase I clinical trials (Xie et al., 2010). Human skin equivalents often incorporate the air liquid interface (Roger et al., 2019), as this mimics an important part of the skin and other epithelia in terms of maintaining a physical barrier to opportunistic and invading pathogens and chemicals; fast closure of wounds on epithelial tissues are key for efficient and successful repair.

While the progression from conventional 2D culture to 3D, and human skin equivalents, culture models increase the representativity of the in vitro studies, it still pales in comparison to the complexity of the in vivo environment. Tissues and organ systems in vivo have a range of stimuli which impact their behaviour. Biochemical cues are a well-studied stimuli, whether that be growth factors, toxins, or micromolecules. Another well-studied stimuli are mechanical stimuli; this includes varying topographies, stiffnesses, environmental dimensions, and even combines biochemical stimuli in the form of different surface chemistries. More recently, electrical stimuli have been studied as a factor in mammalian models, given that said cues are responsible for orchestrating a wide range of systems in vivo. However, most research only investigates cellular responses to one of these forms of stimulation. Yet all three are vital factors in all aspects of in vivo processes and therefore should be studied simultaneously, when possible, to achieve the most representative model in which data can be obtained (Figure 1.2).

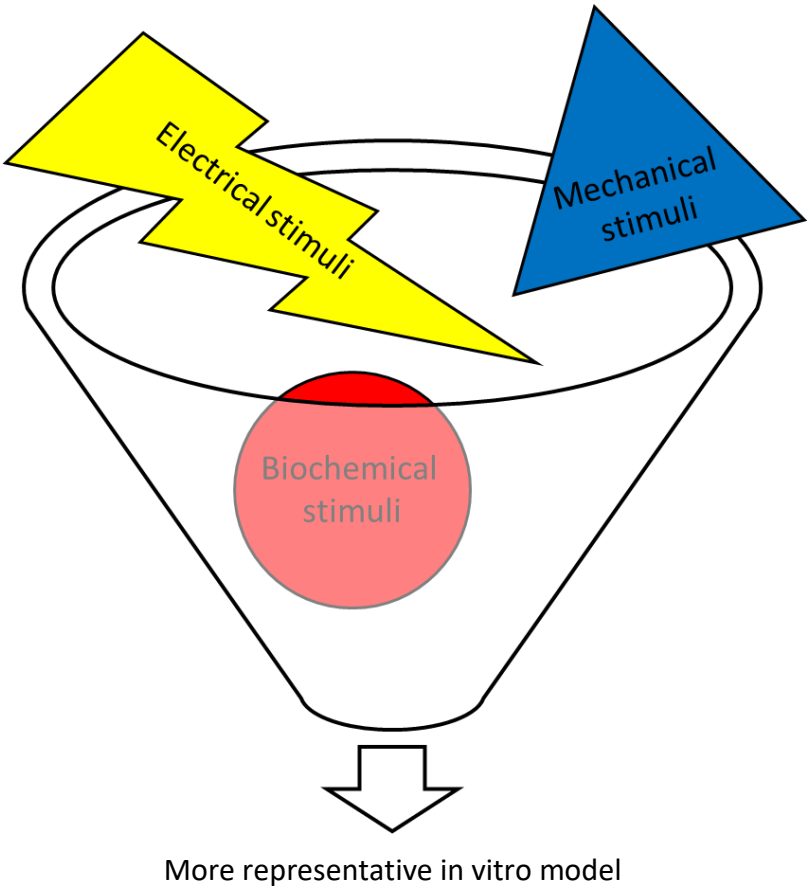

Figure 1.2: A combinatory approach to in vitro models. Utilising the three different stimuli is crucial in the development of in vitro models which better represent the in vivo environment, therefore obtaining better quality data which is more likely to translate from bench to bedside.

1.3 Bioelectronic medicine

Bioelectronic medicine is the merging of electronics with biology, using electrical stimuli to modulate cellular function and treat disease (Olofsson and Tracey, 2017). Originally used to modulate neuronal behaviour, it is now present in the wound healing field; both in vitro (Zhao et al., 2006; Hoare et al., 2015) and in vivo (Long et al., 2018; Liu et al., 2021). To achieve this, an understanding of how electricity influences events ranging from individual organelles to whole organ systems is vital. The interactions of living tissue and electrically mediated signalling are not a new concept. In the 18th century, Luigi and Lucia Galvani observed that the muscles of a frog's leg twitched upon electrical stimulation which led to

the idea of bioelectricity being established (Bresadola, 1998). During the 19th century, building on the work of the Galvanis, Emil Du Bois-Reymond identified that these electrical stimuli were involved in wound healing (Du Bois-Reymond, 1848).

Harnessing electricity as a treatment method – electrotherapy – was first utilised in the 18th century and quickly became a way of preventing muscle wastage by improving restoration via muscle contractions (Licht, 1967). Electrotherapy in the 20th century was most associated with the field of physiotherapy, with few applications in other fields such as psychology. Current day applications of bioelectronic medicine now include pacemakers (Giannoni et al., 2022), allowing clinicians to use electrical stimuli to modulate the rhythm of atrial fibrillation, and cochlear implants (Heiduschka and Thanos, 1998), ensuring deaf patients can interpret sound by exogenously stimulating the auditory nerve. Cancer is also a target for bioelectronic medicine. Proteins which regulate the transportation of ions, and thus electrical current and field effects, have been linked to pro-tumour genes (Levin, 2014), insinuating that the use of electrical stimuli could be used as a therapy. Robinson et al. (2021) utilised the hypothesis that cancer is a cell's malfunctioning bioelectrical circuitry to employ electrical stimuli as a treatment. Tumour treating fields have been shown to increase survival rates for glioblastoma patients (Rominiyi et al., 2021), with a range of mechanisms implicated from anti-mitotic to enhanced membrane permeability. The electrical stimuli's ability to enhance the permeability of cell membranes is called electroporation and has been used in combination with conventional chemotherapy as a way to increase chemotherapeutic agent uptake into cancerous cells (Clover et al., 2019). Modulation of the immune system is used for some cancer therapies. Electrical stimulation has been used in these approaches too, as a way to reduce or eliminate dosing patients with chemical agents and thus reduce side effects (Das et al., 2021). However, it is not only the disease itself that bioelectronic medicine can target. Chemotherapeutic agents used as cancer treatments often lead to nausea and vomiting; exogenous electrical stimulation has

been used as a complementary treatment to manage these side effects (Garcia et al., 2021). The autonomic nervous system is another recent target for bioelectronic medicine, based on the broad range of targets it influences (Cracchiolo et al., 2021). Specifically, stimulation of the vagus nerve can modulate inflammation in rheumatoid arthritis through TNF-α suppression (Koopman et al., 2016), linking reduced inflammation to electrical stimuli via immune cells. The reduction in inflammatory cytokines shown by Koopman et al. (2016) could be a factor in bioelectronic medicine being used in pain management (Hurlow et al., 2012; Coskun Benlidayi, 2020), as well as reducing inflammation in other diseases (Das et al., 2021). Vagus nerve stimulation has also been used to target type 1 diabetes (Dirr et al., 2020).

Wound healing is an emerging field of study within the scope of bioelectronic medicine. Electrical stimuli are known to play a part in the normal wound healing process (Nuccitelli, 2003), potentially being the key orchestrator of the overall process; yet, this is an area that is in desperate need of greater understanding. Given this, even in lieu of a full understanding of the mechanism involved, there are applications which utilise the power of bioelectronic medicine for clinical wound healing applications. Long et al. (2018) reported on the in vivo enhanced healing effects of an electrical bandage, which resulted in wound closure in 3 days compared with 12 days in a control group. The bandage used a nanogenerator to convert kinetic energy from the rat models into periodic biphasic electric field stimulation. The development of this technology led to studies on mice with human skin xenografts as a more human-applicable model (Liu et al., 2021). Similar results were seen; healing within a week compared to within a month in controls allowed to heal without the bioelectronic aid. As well as the obvious benefits of accelerated healing, Liu et al. (2021) reported no undesirable side effects such as irritation, infection, or necrotic regions as a result of the bandage. Liu et al. admit that this research is still in its infancy, with a variety of considerations to investigate in future work including human immune

responses to the device and its action as well as the stimuli not being dynamic, i.e., not tapering off as the healing occurs. Further research will no doubt lead to more effective therapies to combat the ageing global population and the soaring cost of wound care stated previously.

1.3.1 Electrical stimuli

All mammalian cells produce and respond to electrical signals, this is a method of communication to both local and distant environments (Levin, 2014). This communication is through current flow which comes in ionic and faradaic forms, as detailed in Figure 1.3 and the sections below.

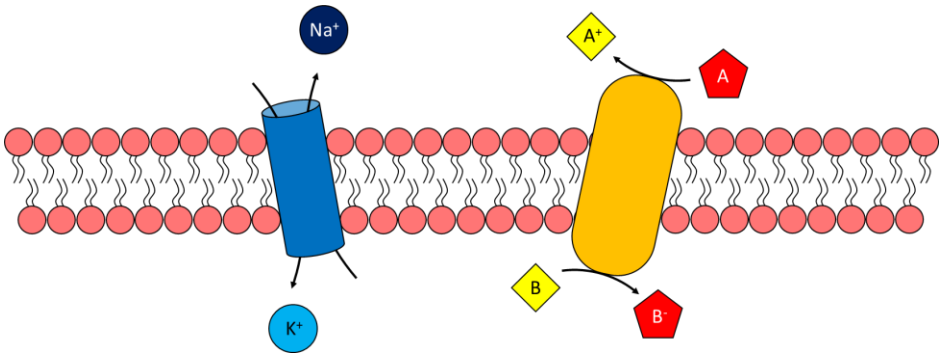

Figure 1.3: Ion and electron movement induces a current, allowing conductivity across membranes of cells and organelles. The passage of ions such as K^+ and Na^+ can be passive or active through transport pumps which utilise ATP to ADP energy transfer. Electron transfer, generated by redoxactive molecules, is achieved through electrochemical reactions occurring on both sides of the membrane. Such communications are not only present via membrane bound channels, intra- or extra-cellular communication can occur with REDOX active molecules and ion gradients. Reproduced with permission from Sanjuan-Alberte et al. (2018).

1.3.1.1 Ionic currents

Membranes surrounding both cells and organelles have a potential difference, or voltage gradient, across them. This is mediated by both the flow of ions through passive channels

and active pumps between the intra- and extracellular spaces (Figure 1.3) and lipid charges within the membrane (McLaughlin, 1989; Ma et al., 2017). The movement of ions is controlled by ion pumps, ligand-gated, or voltage-gated channels. Ion pumps utilise ATP hydrolysis to allow the passage of ions, the sodium-potassium pump is the most understood example of this. Ligand-gated channels open in response to chemical messenger binding, whereas voltage-gated channels respond to electrochemical gradients. Ion concentration gradients on either side of the membrane, as well as the various charged molecules embedded into the lipid bilayer itself, collectively sum up the membrane potential. A resting membrane potential is commonly negative compared to the extracellular space. Ions within the cell which contribute to the resting membrane potential do not reach equilibrium, mainly due to the selective permeability of cell membranes, controlling specific ion concentration intracellularly. Many ions, including calcium and chloride, contribute to the setting of the resting membrane potential, with the main contributing ions being potassium and sodium (Chrysafides et al., 2021). K^+ has a relatively high permeability, given the large number of K^+ passive channels present, meaning that it is closer, compared to Na^+, to equilibrium. Na^+ itself has relatively low permeability and therefore is distant from electrochemical equilibrium. The resting state for a membrane potential differs on cell type, maturity, and thus function, through various means but fundamentally through slight differences in how dominant an ion is in controlling the membrane potential. The more membrane permeable an ion is, the more dominant in influencing the potential said ion is. Changes in the ion concentration across a membrane can depolarise, repolarise or hyperpolarise the membrane, with these states acting as signalling pathways (Hammond, 2015). Different polarisation states driven by ionic currents are responsible for the action potential, which is thought to drive phenotypic macrophage polarisation (Li et al., 2016).

1.3.1.2 Faradaic currents

While ionic currents refer to the movement of ions, faradaic currents describe the movement of electrons. The electrons are carried between two species: electron donors, oxidisers, and electron acceptors, reducers (Bard and Faulkner, 2001), as illustrated in Figure 1.3. These reactions are highly specific and can be referred to as 'REDOX' reactions:

$$\begin{aligned} &\text{Oxidation: } \mathrm{A} \rightarrow \mathrm{A}^{+} + \mathrm{e}^{-} \\ &\text{Reduction: } \mathrm{B} + \mathrm{e}^{-} \rightarrow \mathrm{B}^{-} \end{aligned} \qquad [1.1]$$

A = Electron donor, A^{+} = Cation, e^{-} = Electron, B = Electron acceptor, B^{-} = Anion.

In vivo, REDOX reactions are controlled by electrical stimuli which influence REDOX active molecules such as nicotinamide adenine dinucleotide (Berg, Tymoczko, and Stryer, 2002), glutathione (Pompella et al., 2003), and other reactive oxygen species (ROS) (Holmström and Finkel, 2014). REDOX active molecules have been proposed to play a role in a variety of diseases (Adler et al., 1999; Houstis et al., 2006), as well as wound healing (Sen and Roy, 2008). Growth factors for example, such as platelet-derived growth factor (Sundaresan et al., 1995) and TGFβ (Junn et al., 2000), rely on ROS and REDOX reactions to function. Given the evidence of REDOX involvement across wound healing, the implication is that endogenous electrical stimulation, either lack or overuse of, is a contributory cause of disease.

1.3.1.3 Electric fields

Due to the movement of ions and electrons, electric fields are inherently present in vivo and thus is another tool utilised for cell and tissue signalling. Electric fields are defined as

regions around charged particles within which other charged particles are either attracted or repelled through electrostatic forces. Individual electric fields are a theoretical tool which can be used to anticipate the actions of charges around a single point. Experimentally, electric fields exist and overlap one another leading to electric force, F, effects on point charges, as noted by Coulomb's law:

$$|\mathrm{F}| = \mathrm{k}\frac{|\mathrm{q}_1\mathrm{q}_2|}{\mathrm{r}^2} \qquad [1.2]$$

F = electric force (N), k = Coulomb's constant ($\frac{\mathrm{Nm}^2}{\mathrm{C}^2}$), q_n = point charge (C), r = distance between charges (m)

From Coulomb's law it is possible to determine the magnitude of an electric field, E, by selecting a single point charge and a particular distance from it, r:

$$|\mathrm{E}| = \mathrm{k}\frac{|\mathrm{q}|}{\mathrm{r}^2} \qquad [1.3]$$

E = electric field magnitude ($\frac{\mathrm{N}}{\mathrm{C}}$), k = Coulomb's constant ($\frac{\mathrm{Nm}^2}{\mathrm{C}^2}$), q = point charge (C), r = distance from point charge (m)

Electric fields generated through ion transport are thought to be responsible for orchestrating the entire wound healing complex. Starting with wound generation and the disruption to the transepithelial potential and ending with wound closure due to cell migration, this is a relatively new branch of bioelectronic medicine and so knowledge gaps remain.

1.3.2 Application of electrical stimuli

The literature which utilises electrical stimulation in its methods does so in a few slightly different ways.

1.3.2.1 DC vs. AC

The delivery of a current can occur via two waveforms: alternating and direct. Alternating current (AC) is a bidirectional current flow that reverses direction in regular intervals known as the frequency (Figure 1.4A). Direct current (DC) is a unidirectional current flow and thus has no frequency property attached (Figure 1.4B).

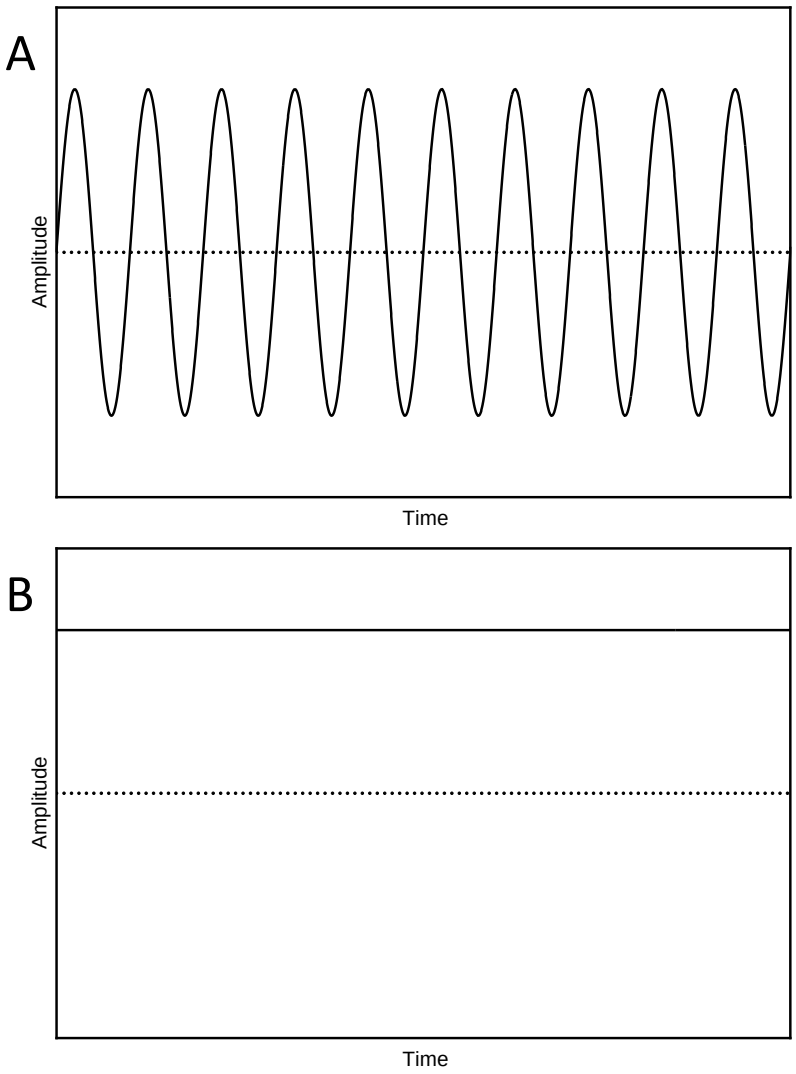

Figure 1.4: Waveforms of alternating and direct current. AC and DC describe two forms of current flow. AC is a current which periodically changes direction, going from positive to negative magnitudes every *x* unit of time which is quoted as the frequency (A). DC is a current which is unidirectional, in that it only ever presents the magnitude as a consistent value meaning it possesses no frequency (B).

In DC circuits the voltage applied is kept constant, whereas AC circuits have a fluctuating voltage from positive to negative values indicating the directionality of the current flow. AC is present in electricity distribution systems as it is transformed from one voltage to another without a high energy loss, whereas DC is utilised by batteries, computing technologies, and the human body. DC is utilised in the transepithelial potential, discussed later, along with other functions in the body. Therefore, it is common to see instances of DC being used in in vivo and in vitro studies as it mimics the endogenous electrical activity

of the body. AC uses are seen in the literature, but not for wound healing applications. It is postulated that this lack of AC stimuli success seen in wound healing is due to an absence of electrical polarity, due to the constant fluctuations of the current direction (Kloth, 2014). This begins to make sense considering that mammalian cells and tissues have evolved to detect and respond to unidirectional stimuli driving behaviours such as migration. The fluctuations in amplitude that AC provides would not be detected in the same way and thus would not result in the same effects. This is not to say that other effects would not appear. AC stimulation is seen in other areas of literature including but not limited to cancer therapy (Robinson et al., 2021), neurobiological processes (Abd Hamid et al., 2015) and cardiomyocyte stimulation (Vaithilingham et al., 2019).

1.3.2.2 Continuous vs. pulsed

Continuous current applications are defined as the flow of charge for longer than 1 s, whereas pulsed current applications are short bursts of current with then a longer period in which little to no current flows (Kloth, 2014). These isolated electrical events cause the current to flow for 1 ms < x < 1 s as a monophasic or biphasic waveform (Figure 1.5). The current can be applied as single or twin events, twin peaks are seen in Figure 1.5A, yet twin peaks are much more commonly seen in applications of high voltages (> 100 V) (Franek et al., 2012). For the biphasic application of current, the amplitude can be applied symmetrically (as seen in Figure 1.5B) or asymmetrically, i.e. have a bias towards either the positive or negative potential values (Baker et al., 1996).

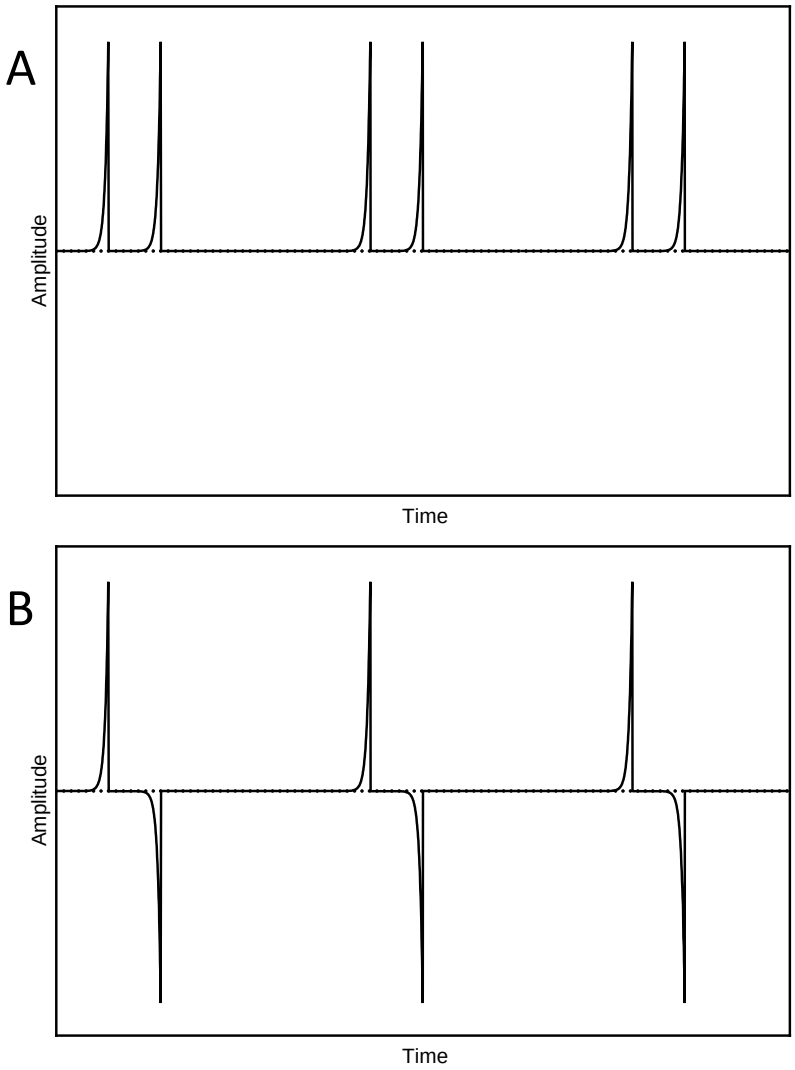

Figure 1.5: Pulse currents. Monophasic pulsed currents are unidirectional in the same way DC is, meaning they are either always positive or always negative amplitude values (A). Biphasic pulsed currents are bidirectional in the same way AC is, in that they fluctuate periodically (B).

The body applies continuous and pulsed current forms depending on the functionality of the tissues it affects. An action potential is an example of a pulsed current, in which there is a depolarisation of the membrane which peaks and then cannot re-peak for a set time. Continuous current flow is present in endogenous wound healing via the transepithelial potential. Ions constantly drive an electric field for relatively long periods post wound generation. However, in wound healing literature studies utilise both forms of the current application. Continuous current flow is present in vivo yet not preferred in vitro, this is because continuous current application over a sufficient voltage can drive the production

of acidic and alkaline compounds at the anode and cathode, respectively (Kloth, 2014). The build-up of these compounds over long periods (> 1 s) can lead to changes in local pH levels and thus lead to undesirable toxicity in vitro and skin irritation in vivo, yet in the pulsed current application the build-up is not as severe and therefore local pH changes are either not as detrimental or dispersed faster. The majority of studies still report significant effects due to electrical stimuli whether they were applied using continuous or pulsed approaches so the decision as to which to use is likely taken depending on the voltages applied.

1.3.2.3 Conducting biomaterials

Given the research indicating that electrical stimuli are a promising avenue for research in many areas, the desire to modulate biological functions through conductivity has elicited growing interest. This is achieved by incorporating conductive elements into materials which interact with biological systems, making conducting biomaterials. Due to the interest in electrical stimuli, the conducting properties of biomaterials have been increasingly modified by the addition of conductive elements (Table 1.2).

Table 1.2: Additives used in biomaterials to primarily enhance conductivity. Studies referenced were selected from journal articles both describing material properties and their recent application for in vitro biomaterial research.

Conductive additive	Form	Conductivity, $S.m^{-1}$	Biocompatibility	References
Black phosphorus	Nanosheets, up to a few layers thick.	~ 10^2	Dependent on functionalisation. Functionalisation with polyethylene glycol improves biocompatibility.	Tao et al., 2017 Wu et al., 2018
Gold	Nanoparticles ranging from 5-60 nm.	4.1×10^7	No overtly toxic effects noted in vitro or in vivo, however results can vary depending on functionalisation and particle size: > 30 nm particles have shown toxic effects.	Kadhim et al., 2021 Kus-Liśkiewicz et al., 2021 MatWeb, 2022a
Graphene	Monolayer sheets in a pure form, < 1 nm thick sheets as an oxide.	$> 1.0 \times 10^2$	Impurities can have an adverse impact on the biocompatibility, yet pure graphene elicits no significant toxic effects.	Stankovich et al., 2006 Liao et al., 2018
Metal carbides, MXenes	Single layer film, ~ 1 nm thick.	10^4 - 10^6	Dependant on composition, concentration, and functionalisation. Conjugation with biocompatible polymers (such as collagen or polyethylene glycol) decreases toxic effects.	Ling et al., 2014 Lim et al., 2021 Lipatov et al., 2021
PEDOT:PSS	Film, < 100 nm thick.	5.9×10^5	No toxic effects were noted in vitro or in vivo, however, results can vary depending on functionalisation.	Luo et al., 2008 Hilal and Han, 2018 Lu et al., 2021
Polyaniline	Studied as an extract from a globular polymer and as 30-35 nm nanoparticles.	$> 4.0 \times 10^1$	Low biocompatibility in salt form while biocompatibility is higher in base form. Viability drops as concentration increases.	Humpolíček et al., 2018 Manaf et al., 2019
Polypyrrole	Presented as nanotubes, globular extracts, nanoparticles, and membranes.	$< 4.2 \times 10^4$	Low biocompatibility in salt form while biocompatibility is higher in base form. In base form, no toxic effects noted in vitro.	Fahlgren et al., 2015 Stejskal et al., 2016 Humpolíček et al., 2018 Cui et al., 2021
Silver	Nanoparticles smaller than 5 nm.	6.3×10^7	High concentrations can impact viability and proliferative behaviours due to cellular uptake. Incorporation into a bulk material can significantly decrease these toxic effects.	Alarcon et al., 2012 Pauksch et al., 2014 MatWeb, 2022b

A group of conductive additives attracting attention from a range of fields, not only that of conducting biomaterials, are carbon nanotubes (CNTs). These are a group of carbon allotropes characterised by their cylindrical structure (Iijima, 1991). They often exhibit a diameter in the nanometre range with a length up to the centimetre range, meaning there is a large surface area. CNTs have high electron mobility, meaning that electrons can move through them with high speed and low resistance (Dürkop et al., 2004). The combination of high surface area, high electron mobility, and low resistance makes CNTs highly conductive; with values over 1×10^6 $S.m^{-1}$ (Wang et al., 2017). They also possess exceptional thermal conductivity, with values between 3000 and 5800 $W.mK^{-1}$ (Balandin et al., 2008). This range in conductivity values rises from the various forms of CNTs available.

Single-walled CNTs (SWCNTs) have only a single layer of hexagonally latticed carbon atoms. Individual SWNCTs possess the best conductive properties, both electrical and thermal, due to their smaller cross-sectional area and differences in electron transport (Yang et al., 2021). Multi-walled CNTs (MWCNTs) have multiple layers of hexagonally latticed carbon atoms which gradually increase in diameter, one nested within another. These layers are bound together via weak van der Waals' forces. Due to the larger area and van der Waal interactions rather than carbon-carbon bonds, individual MWCNTs often have lower conductivity values (Zhang et al., 2016). Another way in which conductivity values can differ is with the configuration of the hexagons within the CNT lattice. Zigzag nanotubes follow the circumference of the tube and turn 60 ° in alternating directions at each atom (Figure 1.6A). Armchair nanotubes take two 60 ° in the same direction before alternating to two 60 ° in the other direction and so on (Figure 1.6B). Chiral CNTs exist in-between these two forms, simply visualised by turning the hexagonal structure < 90 °. This difference in configuration can impact the properties of the CNTs, with armchair nanotubes having greater electrical (Lu and Chen, 2005) and thermal conductivity (Zhou et al., 2013). This is

the reason behind experimental data showing a huge range in conductivity values that overlap between types of CNT, as Cao et al. (2013) report.

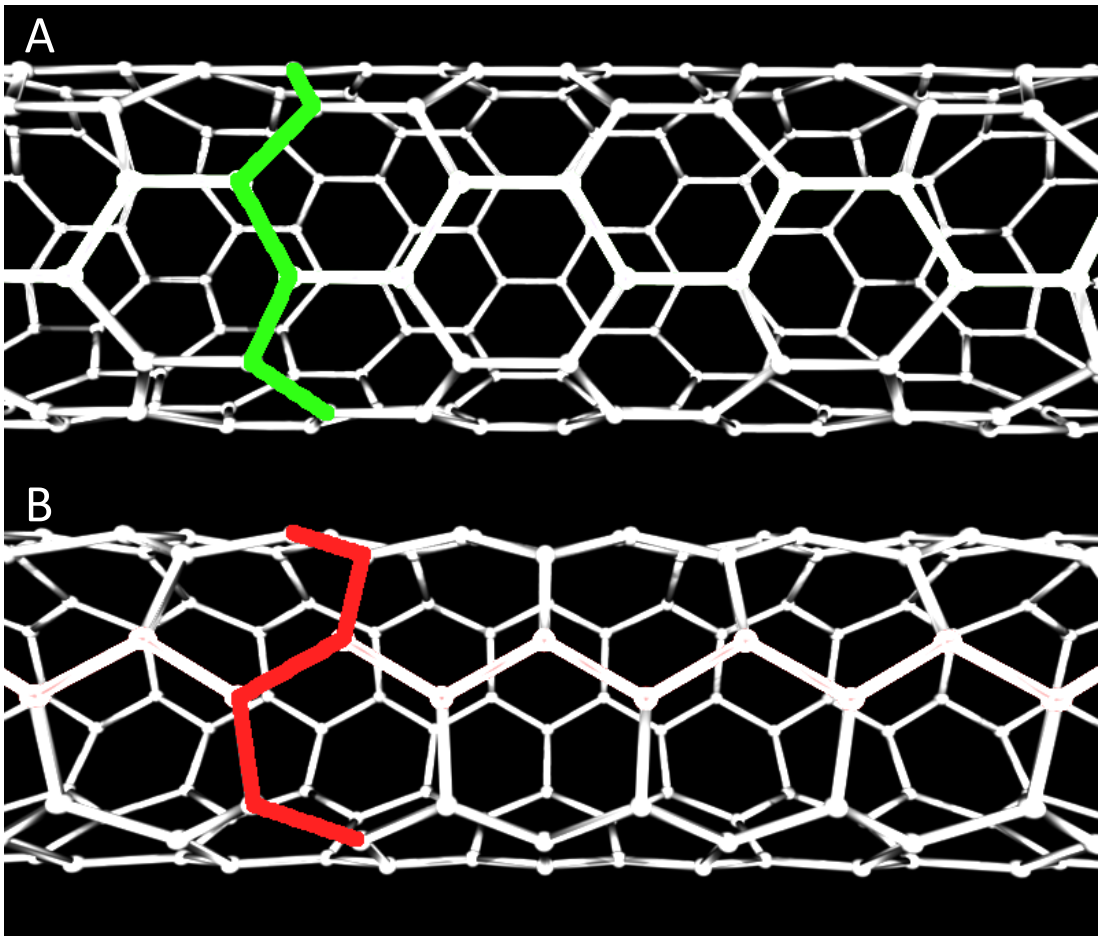

Figure 1.6: Hexagonal configuration within the CNT lattice. Illustrations of the zigzag (A) and armchair (B) configurations seen in CNTs. Images reproduced from Materialscientist via Wikimedia Creative Commons.

CNTs, in their raw form, have been designated as a potential concern to human health. Studies have highlighted that unmodified CNTs can lead to inflammation and even pulmonary fibrosis in both in vitro and in vivo models (Muller et al., 2005; Pauluhn, 2009; Mercer et al., 2011). These effects are similar to those seen from asbestos inhalation. While the shape of CNTs may be a factor in their in vivo incompatibility, for in vitro applications it is heavy metal residues that are the main drivers of poor biocompatibility (Ge et al., 2012). The metals present are mostly transition metals including but not limited to: iron, nickel,

molybdenum, yttrium, cobalt and chromium (Ge et al., 2011). These heavy metals originate from the CNT manufacturing methods in which the metals act as catalysts. Ge et al. (2011) found that across a range of manufacturers that these impurities remained even after complex purification steps, stating that the purification is often costly and incomplete. Purification protocols designed to eliminate as much metal residue as possible have been used in the literature, yet these are resource consuming whilst having the potential of changing the properties of the CNTs themselves through damage (Ge et al., 2012). Functionalisation of CNTs can aid in the biocompatibility of the material (Vardharajula et al., 2012).

Both types of CNT are known to aggregate when dispersed in an aqueous environment (Saleh et al., 2008). This aggregation is due to the hydrophobic surface of the CNTs which promotes the grouping together via weak van der Waal interactions. These aggregates allow MWCNTs to have much more similar properties to SWCNTs, given that cross-sectional surface area is now negligible, and both sets of CNT possess weak van der Waals' forces within them. Therefore, functionalisation is often employed to make the CNTs less hydrophobic and thus increase solubility and dispersion within aqueous environments. CNTs are prone to developing protein corona (Li et al., 2008; Cai et al., 2013). Protein corona is an effect seen when layers of protein adsorb onto a surface from biological fluids. This ability to adsorb proteins will increase the biocompatibility, as cells have less surface area to interact with and any impurities are trapped inside. Additionally, protein corona allows for reservoirs of growth factors and other proteins for local cell populations, thus providing a use as delivery systems within a biomaterial (Karimi et al., 2015; Maheshwari et al., 2019). It is shown that this protein aggregation could alter the conductive properties of the CNTs (Chen et al., 2004).

Alongside their highly conductive properties, CNTs also provide great mechanical enhancing capabilities. CNTs exhibit high tensile strength values (Ruoff, Qian and Liu, 2003; Kim et al., 2017) and are flexible too (Li, 2013; Cai and Wang, 2015). These properties mean that CNTs are ideal for reinforcing weak materials. As with the relationship between CNT structure and electrical properties, the mechanical properties of the CNT also depend on the structural construct (Takakura et al., 2019).

CNTs have been used to propagate electrical stimuli, whilst providing mechanical stability, in the culture of cardiomyocytes in collagen I hydrogels (Yu et al., 2017). Another study investigated the effect of CNT incorporation into a collagen hydrogel on collagen assembly and cell response (Kim et al., 2015). It was found that CNTs interacting with collagen created thicker, more taut fibrils. These fibrils possessed a thicker D-period, essentially stretching out the fibres by ironing out the creases. This structural change in the assembly of collagen produced a cellular response in the form of mediating differentiation in stem cells. Kim et al. (2015) proposed that because functionalised CNTs are negatively charged at their surface, and therefore increased the local ionic strength when in contact with collagen fibres, this caused the changes in fibre assembly leading to downstream physical changes in the structure and thus material characteristics. Cytotoxicity was not noted in any of the collagen-based material studies, nor incorporation into other bulk structures (Shin et al., 2011; Sun et al., 2017; Mihajlovic et al, 2018), indicating that encapsulation within a biomaterial aided in improving the cytocompatibility of the CNTs.

1.3.3 Electrical stimuli in the context of wound healing

The body possesses an electrical-based wound healing detection system: the transepithelial potential (Nuccitelli, 2003). The potential difference across a membrane is often discussed

in terms of single cells, i.e. membrane potential. The transepithelial potential is the potential difference across an epithelium and is the collective total of membrane potentials within the said epithelium. The transepithelial potential has a range of functions including facilitating potassium reabsorption in late proximal tubules of the kidney (DiBartola and De Morais, 2012), a diagnostic marker of cystic fibrosis (Hay and Geddes, 1985), as well as a key role in wound generation and healing progression signalling (Nuccitelli, 2003).

The transepithelial potential at rest is maintained by the movement of Na^+ and K^+. In normal epithelia, Na^+/K^+ ATPase pumps use ATP to maintain a high internal K^+ and a low internal Na^+. This drives K^+ out of the channels in the basolateral membrane and draws in Na^+ from the apical membrane, generating a positive ionic charge at the basolateral membrane. These charges then flow through the highly resistive paracellular pathway to complete the circuit (Figure 1.7A).

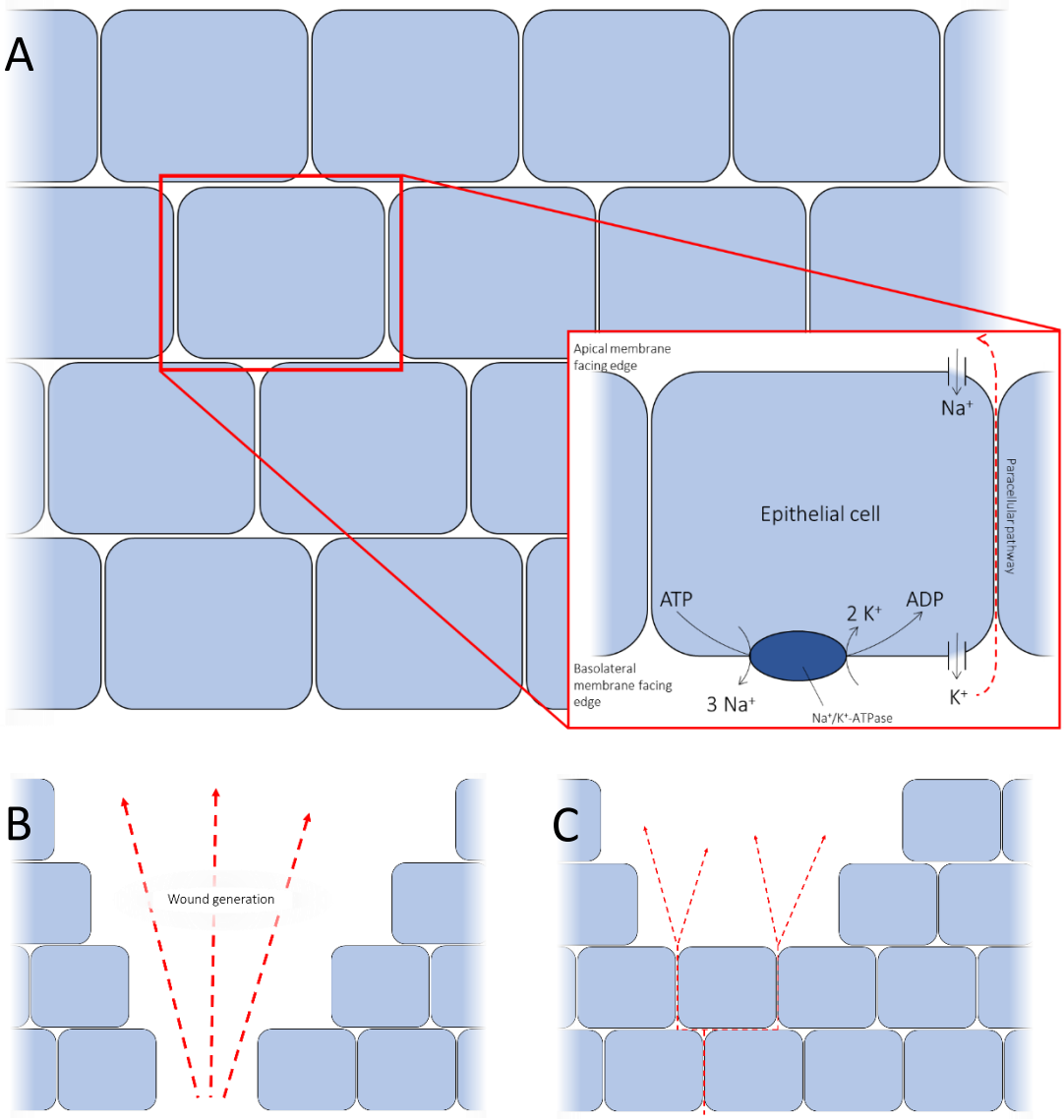

Figure 1.7: Transepithelial potential mechanism. In an epithelial layer (A) the movement of ions into and out of the intracellular spaces and the resultant completion of the circuit via the paracellular pathway (A, inset) generates a default transepithelial potential of 10-100 mV.mm^{-1}. The generation of a wound will create a low resistance route through which ion discharge will take preferentially over the paracellular pathway (B), leading to an increase in potential up to values of 400 mV.mm^{-1}. Over time, as the epithelium is repopulated via migration and proliferation, those highly resistive paracellular pathways are reinstated as the route in which the circuit is completed and therefore the transepithelial potential gradually returns to pre-wound levels (C). Adapted from Nuccitelli (2003).

When a wound occurs, this opens a low resistance pathway in which the ion discharge takes over the paracellular circuit breaking the normal transepithelial potential of 10-100 mV.mm^{-1} leading to a stronger electric field, up to 400 mV.mm^{-1} (Figure 1.7B). Over time, the wound heals and the transepithelial potential strength decreases (Figure 1.7C), eventually returning to pre-wound levels.

While the inset in Figure 1.7A shows the mechanism for the generation of a transepithelial potential over a single cell, this occurs across the entire epithelial layer, meaning a break anywhere in the layer can be identified by surrounding cells using the change in potential. It is this identifiable change in an electrical field strength that is thought to have a large impact on controlling the wound healing complex.

Given the presence of the transepithelial potential and its changes between wound generation and closure, it has been hypothesised that electrical stimuli not only influence but drive parts of the wound healing process. Such hypotheses have been proven to be correct within in vitro studies which are discussed in the following sections, in which exogenous electrical stimuli are applied to cultures.

1.3.3.1 Directed migration

Cell migration occurs in response to a cue. These cues are mainly thought of as: chemotaxis (Singer and Clark, 1999) and mechanical (Fenteany et al., 2000). The former being a cue provided by molecules within the environment, with the latter being a cue provided by the structure of the environment; i.e. the generation of more available space created by the wound void leading to mechanical forces “pushing” cells leading to wound closure. However, more recent studies have come to identify electric fields just as important, if not more than, any of these cues. Publications have demonstrated that cells will respond to electrical signals by migrating (Nuccitelli, 2003; Funk, 2015; Guido et al., 2020; Moarefian et al., 2021).

Zhao et al. (2006) have pioneered this understanding by looking at specific genes that are involved in electrotaxis, sometimes called galvanotaxis, which is the directional movement under the influence of electrical stimuli. It was identified that electric field polarity could garner sole control of the migrational movement of a cultured epithelial monolayer,

essentially modulating the closing and reopening of a scratch assay. This confirmed that electrical stimuli were being detected and thus responding to the directional cues offered by the polarised stimulus. Phosphophatidylinositol-3-kinase gamma (PI(3)Kγ) was shown to be involved in electrotaxis, as when the gene responsible for PI(3)Kγ was inhibited, the directedness of cells was lessened when stimulated with an electric field in comparison to the wild type. This was confirmed via experimentation of corneal epithelia in which genetic disruption of the gene for PI(3)Kγ (p110γ) significantly impaired the directional movement in response to electrical stimuli. It was also shown that, like in vitro, applying an electric field in a polarity which is the reverse of the normal healing direction led to migration away from the wound centre, yet genetic disruption of p110γ led to normal movement towards the wound centre even under the influence of an electric field.

Nakajima et al. (2015) went on to identify that the knockout of the KCNJ15 gene eliminated both anodic and cathodic electrotaxis without affecting cellular motility or directional migration through chemotaxis. KCNJ15 codes for a K^+ channel, $K_{ir}4.2$. This is an inward-rectifier type K^+ channel, meaning the net flow of ions is into the intracellular space. Disruptions to the KCNJ15 gene also disrupt the resting membrane potential. Other types of these K^+ channels, specifically $K_{ir}4.1$ via the KCNJ10 gene, were shown to also influence the resting membrane potential as well as electrotaxis, albeit in a minor way. Authors also analysed directed migration through fluorescent trackers. It was found that a cell polarisation marker, PIP_3, would localise at the leading edge when the cell was undergoing directional migration of any form, either by electrotactic or chemotactic means. The knockdown of KCNJ15 prevented this polarisation marker distribution to the cathode facing edge of the cells stimulated by an electric field, something which the wild type gene could facilitate. The cells used for these experiments were immortalised human corneal epithelial cells, which were known to directionally migrate to the cathode under electric field stimulation, spontaneously immortalised human keratinocytes, and epithelial-like human

breast adenocarcinoma cells, chosen for their anodic directed migration. Both cell lines lost the directed migration response to electric fields when the KCNJ15 gene was knocked down.

A mechanism as to how $K_{ir}4.2$ could be responsible for electrotactic responses was proposed. Intracellular polyamines modulate the activity of K_{ir} channels, these compounds are positively charged and cause a blockage of the channel pores leading to the low outward flow of K^+ while retaining the relatively high inward flow (Lopatin et al., 1995). Nakajima et al. (2015) found that these charged compounds were being moved intracellularly under electrical stimulation and that it was the interactions with $K_{ir}4.2$ which prompted the cellular migration in a particular direction, with polyamines increasing electrotactic responses in a concentration dependent manner until the KCNJ15 gene was knocked down. Hence it was proposed that the mechanism to which cells sense electrical stimuli involved the distribution of positively charged particles, mainly polyamines, via said stimulation which led to changes in K^+ flux due to coupling with the $K_{ir}4.2$ channels.

The movement of macrophages, and their precursory monocytes, is of great importance within the wound healing process given that the epidermis isn't necessarily a region in which macrophage populations are high. Hoare et al. (2015) applied exogenous electric fields similar to that seen in vivo, 150 $mV.mm^{-1}$. It was shown that when exposed to exogenous electrical stimuli macrophages migrate towards the anode, showing they are electrotactic. The pro-anodic electrotaxis has been noted elsewhere in the literature too (Orida and Feldman, 1982). This was the opposite direction of migration to keratinocytes (Zhao et al., 2006) and T cells (Lin et al., 2008; Li et al., 2011). The precursory form of the macrophage, monocytes, migrated away from the anode and towards the cathode. These migration movements arose from a reorganisation of the cytoskeleton via the applied exogenous electric fields as after 2-hours of exposure, the macrophages showed an

elongated morphology that aligned with the field. Hoare et al. (2015) stated in their methods that the electrotaxis experiment was performed using electric fields up to 450 $mV.mm^{-1}$, however they only reference data for 150 $mV.mm^{-1}$. Therefore, it can be speculated that going above 150 $mV.mm^{-1}$ caused an undesirable effect, presumably a reduction in viability, and thus was eliminated from further investigations.

Sun et al. (2019) came to the same conclusions as Hoare et al. (2015), in that macrophages migrate towards the anode under electrical stimulation. However, Sun et al. (2019) inferred that the migration of the macrophage toward the wound site is more heavily directed by chemotaxis rather than electrotaxis, yet the movement away from the wound site by the macrophage is almost entirely controlled by electrotaxis, not chemotaxis. Once differentiated, the direction of migration is driven by chemical markers of damaged tissue and potential infections rather than the electrical stimuli. After the source of the chemical markers has gone, or decreased past a particular level, the electrotaxis takes over and drives macrophage migration away from the wound and toward lymphatic draining pathways.

The migration kinetics of fibroblast cells is also important to note, due to the ability of fibroblasts to relocate to the wound site and begin wound closure. Rouabhia et al. (2013) investigated the effect of electrical stimulation on human skin fibroblasts; using 50 and 200 $mV.mm^{-1}$ to investigate the enhanced migratory effects under the influence of the electrical stimuli. A higher potential applied elicited an increased migratory pace, while the time at which cells were exposed to the stimuli did not seem to impact migration significantly.

1.3.3.2 Proliferative enhancement

The rate of proliferation is increased upon the application of exogenous electrical stimuli (Love et al., 2018; Chen et al., 2019). The exact mechanisms as to how this is achieved remain unknown. Vincente et al. (2003) describe the impact K^+ channels, mainly $K_v1.3$ and $K_{ir}2.1$, have in macrophage proliferation in vivo, with various biochemical components regulating these voltage-dependant channels. Li et al. (2016) then report that the exogenously applied electrical stimuli modulates the activity of a range of cell membrane voltage-dependant ion channels. This indicates that the interactions with ion channels is fundamental to the proliferative enhancement of electrical stimuli, however other mechanisms could influence this too.

In vivo the proliferative phase is not solely limited to the rate at which cells proliferate. The proliferative phase can be split into three subsections: angiogenesis, fibroplasia, and reepithelialisation. These can each be impacted by electrical stimuli leading to a positive net enhancement to the proliferative phase, as explored in the following paragraphs.

It is well understood that angiogenesis is vital for wound healing. Without the growth of new blood vessels into a wound site, any cell migration or division to that site wouldn't have the nutrition required for healthy tissue. Electrical stimulation and increased angiogenesis have been linked since the beginning of the 21st century, with vascular endothelial growth factor (VEGF) being noted as a key compound involved (Amaral et al., 2001). One study showed that the application of in vivo-like electric field strengths directly promoted factors involved in the pre-angiogenic phase (Zhao et al., 2003). Again, it was postulated that these effects were driven by the increase in VEGF release which kickstarted the pro-angiogenic response. More recent research backs this hypothesis up by reporting that VEGF expression was up 120.4% compared to untreated controls (Chen et al., 2018). As expected, this increase in VEGF correlated with increases in downstream signalling

molecules (pVEGFR2, Akt, Erk1/2 and JNK), however, it is unclear whether the electrical stimulation was inducing the production of said factors directly or indirectly through the VEGF alone. Another study investigated several pro-angiogenic proteins both in vitro and in vivo post stimulation and found that VEGF and MCP-1, both associated with angiogenesis, were significantly elevated compared to the controls and also that anti-angiogenic proteins including plasminogen activator inhibitor-1 (PAI-1) were significantly decreased (Beugels et al., 2019). The interaction between the applied exogenous fields and VEGF is not yet understood, however one theory points toward ROS due to the lack of additional VEGF after electrical stimulation in the presence of Vitamin E, a well-known antioxidant (Liu et al., 2018).

Fibroplasia, or the production of fibrous tissue, is performed by fibroblasts. It is well documented in the literature and already in Section 1.3.3.1 that fibroblast migration is promoted by the application of exogenous electric fields (Guo et al., 2010). Therefore, it was hypothesised that such events would correlate with an increase in the amount of fibrotic tissue produced allowing for faster closure of the wound (Ud-Din and Bayat, 2014).

Restoration of the epithelia from an uncovered area is called reepithelialisation. Restoring lost epithelial tissue leads to the closure of wounds. To generate that lost epithelium cell division is critical. Figure 1.8 illustrates reepithelialisation, highlighting the influence electric fields have on migration to the wound centre first and then subsequent differentiation causes re-population of the epidermis. Electrical stimulation has been observed to both suppress and increase cell division at distance-from-the-wound-dependant sites. By using pharmacological compounds, Song et al. (2002) were able to artificially enhance and diminish the endogenous transcellular potential gradient to assess the effects of reepithelisation orientation and rate. Experiments showed that cell division was suppressed at the wound edge yet increased around 500 µm away, with the healing of the

wound occurring faster when the electric field strength was enhanced. Song et al. (2002) reported that it is not possible to attribute their findings to just mechanical forces alone, those that “push” cells into the wound void. The pharmacological factors used also were shown to not affect any growth factor release which could’ve been the cause of the increased reepithelisation. Therefore, they concluded that it is the electric field that is contributing to all these effects. The hypothesis presented for the effects seen centred around how the electric field may affect spindle formation along the electric vector. These spindle interactions could arise from the movement of lipids, receptors and other intracellular components that respond to electric fields (Zhao et al., 2002) which attach to the positive regions of the microtubules and align them, indirectly, due to the electric field aligning the polarised molecules. Interestingly, it is reported that migration and division do not occur simultaneously (Chan et al., 1989; Zagon et al., 2000).

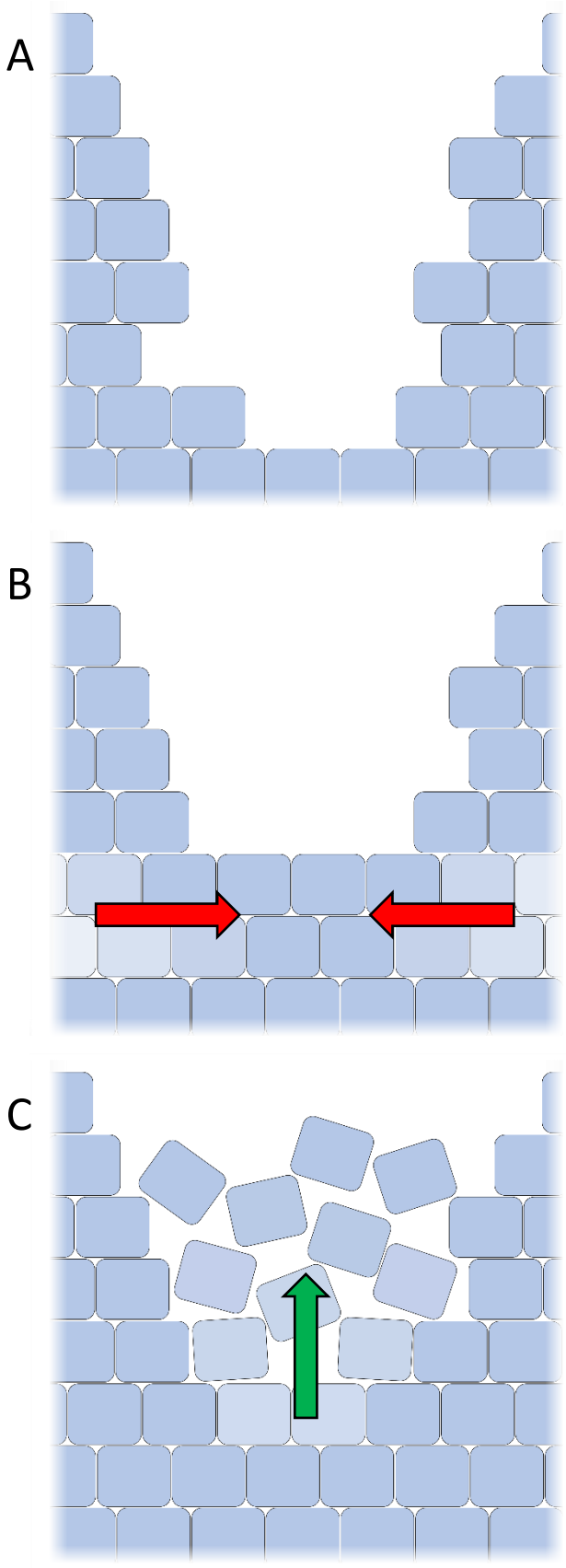

Figure 1.8: A representation of reepithelialisation. Tissue is damaged, creating a void (A). This gap in the epithelium promotes ion release generating a stronger electric field which first drives migration to the base of the wound void (B) before replication and differentiation causes a newly generated cell front which moves up, filling the void (C). Red arrows indicate direction of migration, green arrow indicates the direction of proliferation. Adapted from Moulin et al. (2012).

1.3.3.3 Tissue remodelling

To resolve the inflammation caused by the wound and consequential immune response, T cells are recruited via macrophage chemokine release (Sallusto and Baggiolini, 2008). Endogenous field intensities applied exogenously caused T cell migration towards the cathode (Lin et al., 2008; Li et al., 2011) in the same actin-based pathway as macrophages (Hoare et al., 2015). There is limited literature on other effects of electrical stimuli on neutrophil and T cell function. Studies into neutrophils and T cells would be interesting for the field of chronic wounds as the lack of wound repair has been linked to the overstimulation of inflammatory factors released by neutrophils (Ellis et al., 2018) and the reduction in the pro-immunomodulatory effects of T cells (Havran and Jameson, 2010). Another study showed that electrical stimulation had no detrimental effects on bioactive molecules within in situ tissue explants, rather a reduction in tissue degradation was described (Yuan et al., 2014). This is important for in vitro works because bioactive components are vital cues that aid the retention of cell phenotype and morphology (Bissell and Barcellos-Hoff, 1987; Dozmorov et al., 2006; Timraz et al., 2015). MMPs have a strong influence on tissue remodelling by degrading ECM at the wound site (Kandhwal et al., 2022). Electric stimuli have been shown to enhance the gene expression of these proteases, yet not impact activity (Russo et al., 2008; Sayyah et al., 2022).

1.3.3.4 Phagocytosis

A large part of macrophage function within the wound healing process is the clearance of invading microorganisms and cell debris (Gordon and Plüddemann, 2018). The electric field application by Hoare et al. (2015) promoted this behaviour, with the magnitude of said behaviour being proportional to the field strength. This response was seen with synthetic carboxylate microspheres and with a natural foe, *Candida albicans*. The increase in

phagocytic activity could be due to changes in the surface receptors post-polarisation. Mannose and scavenger receptors, contributors to *C. albicans* and carboxylate microspheres phagocytosis respectively, showed a more clustered distribution on the edge facing the direction of travel. This effect was seen without the total fluorescence of the system increasing, i.e. the increase in activity is down to the positioning of the receptors, not because there are more of them. Cell morphology also took part in affecting phagocytic activity, with more elongated M2-like macrophages contributing more to the overall increase in the internalisation of both foreign objects used (McWhorter et al., 2013). As with migration, phagocytosis is a process that involves actin (May and Machesky, 2001; Ronzier et al., 2022), a group of proteins that form filaments and allow cells to move and facilitate muscle contraction (Dominguez and Holmes, 2011). Actin accumulates at the leading edge of macrophages resulting in the migration in the direction of the leading edge and promoting more receptor binding (Ronzier et al., 2022), both of which are key for the wound healing process.

1.3.3.5 Macrophage polarity

As summarised in Table 1.1, macrophages are phagocytic cells that can be divided into different functional subsets with key functions in maintaining tissue homeostasis post injury or infection. It has been shown that the membrane potential of macrophages is involved in macrophage polarity and, therefore, wound healing modulation. Li et al. (2016) targeted the ligand gated ion channel, ATP sensitive potassium channels. Glibenclamide and pinacidil were used to close and open, respectively, those channels to modulate that resting membrane potential. The results showed that blocking the passage of potassium decreased the expression of M1 markers and increased certain M2 markers, indicating a population shift to more of an M2-like phenotype. This indicates that there is a pathway

through which electrical stimuli, such as the flow of ions within an exogenously applied electric field, could modulate the polarity of a macrophage through changes to the membrane potential. Such therapies have the potential to discourage the continuation of an M1-like response and therefore guide the process towards the latter stages of wound healing.

Kong et al. (2021) also showed that electrical stimulation can drive polarisation, whereby Ca^{2+} flow through voltage-gated channels augmented the release of pro-inflammatory cytokines such as TNF-α and IL-1β, M1 markers. This provided evidence towards the hypothesis that electrical driven polarisation is due to membrane potential changes, as this is the controlling factor in the opening of voltage-gated channels (Catterall, 2011).

1.3.3.6 Fibroblast function

Fibroblasts have some cellular plasticity and, under the correct stimuli, can differentiate into myofibroblasts. Myofibroblasts possess properties of fibroblast and smooth muscle cells, in that they contribute to the production and organisation of ECM proteins within damaged tissues whilst controlling wound closure through contractile action (Darby et al., 2014). These functions are vital in ensuring the wound healing complex is completed and not left open to disruption leading to chronic wounds. Electrical stimuli are thought to promote this differentiation from fibroblasts to myofibroblasts due to, at least partially, Ca^{2+} influx (Li et al., 2019). Whether this is due to increased flow via calcium channels or a release of intracellular calcium from the smooth endoplasmic reticulum is yet to be understood. Rouabhia et al. (2013) described that electrical stimulation enhanced the contractility via fibroblast-myofibroblast transdifferentiation. Contrary to a lot of the migration-based research, the time within which the cells were exposed to the stimuli drove the increased contractility, rather than the strength of the stimuli applied.

Long et al. (2018) and Liu et al. (2021) postulated that accelerated healing due to their electrical bandage in rodents is a result of enhanced fibroblast activity. This response was seen due to electric field effects emitted from the bandage, suggesting that these stimuli are influencing fibroblasts in all their behaviours, i.e. migration, proliferation, and transdifferentiation, not just a singular action. This assumption would further back up the claim that electrical stimuli are the major drivers of the wound healing process, not just a passenger guiding particular sections of it.

Myofibroblasts are thought to be terminally differentiated. To halt the pro-immunomodulatory fibrotic actions, myofibroblast actions need to be stopped at the correct time to avoid fibrotic scarring. If not stopped promptly, prolonged fibrosis can lead to losses in tissue functionality and is linked with up to 45% of deaths in developed countries (Wynn, 2008). Diseases such as liver cirrhosis, kidney disease, pulmonary fibrosis, and cardiovascular disease to name a few, all possess some form of scarring which contributes to the overall mortality of the disease. The mechanisms that modulate the fibrotic response are highlighted by Merkt et al. (2021). There is no literature to suggest that a reduction in myofibroblast functionality is modulated by electrical stimuli. Electrical stimuli can promote apoptosis, but not at the strengths or application types found in wound healing literature (Wang et al., 2012; Geng et al., 2018). This is important to note for future clinical applications of electrical stimulation as a wound healing therapy, as over-stimulation may lead to fibrosis through fibroblasts/myofibroblast functions being overridden to continue.

1.4 Extracellular matrix biomaterials

1.4.1 The extracellular matrix

ECM provide a cell-supportive architecture, as well as possessing bioactive regions which elicit cell-ECM interactions that influence cellular behaviour, from attachment to differentiation (Frantz et al., 2010). The ECM is composed of approximately 300 proteins and polysaccharides, alongside secreted growth factors and other bioactive molecules, all with distinct properties and in tissue-specific amounts (Hynes and Naba, 2011). The unique collection of the macro- and micromolecules enables different ECM to possess different properties, depending on the specific requirements of the local tissue.

The cell-ECM relationship is dynamically reciprocal (Xu et al., 2009). Cells interact with the ECM via surface receptors, with the resultant intracellular cascade leading to alterations in gene expression, hence the changes in cell behaviour. At the same time, changes in gene expression can lead to an increase in ECM secretion or production of MMPs which degrade ECM and release previously trapped bioactive molecules. These bioactive molecules, such as growth factors, go on to influence cellular behaviour, repeating the dynamic reciprocity (Thorne et al., 2015).

1.4.1.1 Composition

The ECM is comprised of macromolecules, fibrous protein and glycosaminoglycans, and micromolecules (Frantz et al., 2010); these are described in the text below and then summarised in Table 1.3.

Collagen, the most abundant fibrous protein in ECM (Lodish et al., 2000), is responsible for tissue integrity and structure, adding both stability and resiliency to stress to tissues, as well as some biochemical cues for specific cell actions. Collagens all contain a triple helix in

their tertiary structure with various modifications, besides type I which is just uninterrupted triple helices, leading to at least 28 sub-types (Ricard-Blum, 2011) which can be categorised into fibrillar, fibril-associated and network (or sheet) forming collagens that differ in structure and function. For humans, 80-90% of collagen content is comprised of types I, II and III, with the remainder mainly being types IV and V. Collagens, specifically the more tissue discrete sub-types, have distinct functions in physiological pathways. An example of this is sub-type X which can impact foetal bone development, during which the haemopoietic niche is established at the chondro-osseous junction (Sweeney et al., 2010; Gudmann and Karsdal, 2016). Another example is the influence sub-type XXIV has on osteoblast differentiation which similarly leads to bone formation (Matsuo et al., 2008; Nielsen and Karsdal, 2016). More abundant collagens, types I, II, III, IV, and V, can affect migration (Chintala et al., 1996; Stejskalová et al., 2021), adhesion (Somaiah et al., 2015; Tang, 2020), and proliferation (Najafi et al., 2008; Edgar et al., 2018).

Collagen fibrillogenesis is the process in which collagen molecules self-assemble into fibrils (Birk and Silver, 1984), instigated by three single soluble precursor monomers of procollagen (Canty and Kadler, 2005). The process begins with the formation of a triple helix structure, in which three collagen molecules align and interact via the C-terminus. Once the helix is formed, the N- and C-termini are cleaved and fibrils can be connected (Canty and Kadler, 2005). The propagation of this process is modulated by other proteins: fibronectin, membrane integrins and collagen V, and proteoglycans (Wenstrup et al., 2004; Kadler et al., 2008; Chen et al., 2020). The resultant fibril morphology is dependent on a variety of environmental factors such as pH, temperature, and collagen concentration (Na et al., 1989; Harris and Reiber, 2007; Li et al., 2009; Shannon et al., 2015).

Elastin's are named due to their elasticity, a unique mechanical property essential for many fundamental functions of the human body. Given the function of the protein, elastin is

most prominent in extendable tissues such as lungs, blood vessels and skin (Kristensen and Karsdal, 2016). Elastin provides low stiffness, high extension, and efficient elastic–energy storage, allowing tissues to return to their original structure post-stretch (Trębacz and Barzycka, 2023). Tissue elasticity does not solely come from the sheer abundance of elastin, but with how it is organised. The elastic property is modulated by associations with collagen fibrils, with elastic integrity supported by glycoproteins, mainly fibrillins (Frantz et al., 2010).

Ubiquitous across the majority of tissues, fibronectin is involved in the cell-ECM interactions. Fibronectin and its influence in cell attachment is the best understood function (Martino et al., 2009; Custódio et al., 2010; Schwarzbauer and DeSimone, 2011). However, there are other functionalities that are just as crucial: such as proliferation, differentiation, clotting, tissue remodelling (Grinnell, 1984; Valenick et al., 2005; Schwarzbauer and DeSimone, 2011).

Laminins, found in the basal lamina, form independent networks. Here, laminin tends to bind to ECM components via the N-terminus and to proteins embedded in cell membranes via the C-terminus (Aumailley, 2013). Expressed by various tissue types, primarily by muscle and epithelial cells (Kular et al., 2014). Through the networks between ECM components and cells, laminins have a noted effect on cell attachment, growth, and differentiation (Paulsson, 1992). They are also thought to have some interactions with cytokines and growth factors, yet this is ill-defined.

Tenascins (TN) are a collection of four proteins, C, R, W, and X: TN-C is up-regulated during embryogenesis, bone remodelling in adult tissue, and inflammation; TN-R is confined to the central nervous system; TN-W is predominantly found in the developing skeleton and adult kidneys; and TN-X is limited to ECM surrounding skeletal muscle fibres, the heart, and skin dermis (Vishwakarma, 2015). Functionality depends on the form of tenascin: TN-C has a

variety of functions from stages of tissue development, or external stimuli such as trauma (Jones and Jones, 2000); TN-R promotes the assembly of ECM in neuronal tissue (Morawski et al., 2014); TN-W is an adhesion modulatory protein that can promote bone development, angiogenesis, cell adhesion and cell migration (Tucker and Degen, 2019); and TN-X is responsible for regulating the structure and stability of elastic fibres (Valcourt et al., 2015).

GAGs are linear polysaccharides formed of repeating disaccharide units (Uyama et al., 2007). They are able to bond to a range of proteins, such as laminins and fibronectins, to make proteoglycans via carboxyl and sulphate groups (Ricard-Blum, 2017). The primary structural function of GAGs is to regulate the osmotic equilibria within the local environment by drawing in water due to their polar, negatively charged chemistry (Wang et al., 2016). This tissue hydration allows for the shock absorbing properties of tissues (Yanagishita, 1993; Raman et al., 2005). Another structural role of GAGs involves the generation of collagen fibrils via collagen fibrillogenesis. It is understood that the physiological GAG concentration relative to collagen has an impact on fibril diameter as well as the rate of fibrillogenesis (Stuart and Panitch, 2008), impacting structural factors such as strength and stiffness. GAGs also possess a huge range of biochemical implications for pathways such as proliferation, cell adhesion, and wound repair (Casale and Crane, 2022). This is performed through binding sites for a variety of growth and other secreted factors, many of which are crucial in supporting the maintenance and growth of the local cell population (Sarrazin et al., 2011; Zhang F. et al., 2019). This allows for the ECM to be analogous to a reservoir of soluble signalling molecules that can impact many physiological pathways, modulated by the exact composition of GAGs within the ECM itself. The most common proteoglycans present in the small intestinal submucosa (SIS), heparan sulphate proteoglycans (Hurst and Bonner, 2001), provide a variety of functions both in the small intestinal submucosa (SIS) and in other tissues around the body (Bishop et al., 2007).

As well as housing growth factors and other signalling molecules, ECM also contain matrix-bound vesicles (MBVs). MBVs are lipid-bound transporters excreted by cells into the extracellular space as a communication method, supplying signalling molecules from cells to the local environment to modulate a variety of pathways (Huleihel et al., 2016). Extracellular vesicles are located in biological fluids and thus are easily identified and extracted. However, in order to get a high yield and purity of MBVs liberase and collagenase digestion is employed to separate the MBVs from their bound proteins (Quijano et al., 2020). Depending on the contents, these MBVs can play a role in various aspects of cellular biology including but not limited to differentiation and macrophage polarisation (Huleihel et al., 2017; Steketee et al., 2017; Hussey et al., 2019). As a relatively recent discovery, the extent to which MBVs influence the matrix environment is not yet known.

Table 1.3: A summary of the components within in vivo extracellular matrix.

Component	Description	Function
Collagens	• Ubiquitous • ≥ 28 sub-types • Triple helix tertiary structure	• Maintenance of tissue integrity and structure • Stability and resilience • Biochemical cues
Elastin	• Allows tissues to return to their original structure post-stretch • Most prominent in extendable tissues	• Responsible for tissue elasticity • Function comes from abundance and spatial arrangement
Fibronectin	• Ubiquitous • Cell-ECM interactions	• Cell attachment is the best understood function • Also involved in proliferation, differentiation, clotting, and tissue remodelling
Laminin	• Found in the basal lamina • Cell-ECM interactions	• Involved in cell attachment, growth, and differentiation • Thought to also interact with small molecules
Tenascins (TN)	• TN are a collection of four protein groups: C, R, W, and X • These forms vary in their location and function	• Tissue development and trauma (TN-C) • Assembly of ECM (TN-R) • Adhesion, bone development, angiogenesis, cell adhesion and cell migration (TN-W) • Regulation of elastic fibres (TN-X)
Glycosaminoglycans	• Linear polysaccharides formed of repeating disaccharide units • Able to bond to a range of proteins to form proteoglycans	• Regulate the osmotic equilibria • Shock absorption • Influences collagen fibrillogenesis, therefore strength and stiffness too • Biochemical cues
Matrix-bound vesicles	• Lipid-bound transporters excreted by cells • Tightly bound to matrix proteins	• Transporting signalling molecules from cells to the local environment • Involved in a wide range of pathways, including differentiation and macrophage polarisation

1.4.1.2 ECM in the context of wound healing

Upon wound generation, tissue is damaged leading to a release of pro-inflammatory cytokines and other signalling molecules. These come from local cell populations, but also the ECM structure. Once damaged, the bioactive molecules trapped within begin to be released, accelerated by proteolytic degradation. MMPs have at least 23 known human

sub-types, separated by their targets and other biochemical differences (Laronha and Caldeira, 2020). Collagenases first act on collagen I, as a way of easing cell migration to the wound site, followed by the degradation of elastin (Potekaev et al., 2021). This initial degradation of the ECM is hypothesised to release inflammatory bioactive molecules which were matrix-bound, accelerating the wound healing process (Huleihel et al., 2016).

Fibronectin binds to the fibrin plug formed during haemostasis, enabling cell migration to more easily occur on the wound surface through enhanced attachment. Fibronectin also stimulates the production of collagens to further promote the wound healing process (Clark, 1990). Extracellular debris is cleared by phagocytic cells to make way for new ECM production, mainly facilitated by fibroblasts, which marks the beginning of the proliferative phase.

The proliferative phase of wound healing is where ECM plays the largest role. Collagen deposition is at first random, with collagen III being the predominant subtype produced (Mathew-Steiner et al. 2021). Enzymatic activity leads to covalent crosslinking, reinforcing the matrix. Collagen remodelling leads to collagen I being the predominant subtype present in post-healing tissues. Cell-ECM interactions have been shown to modulate an M2-like phenotype and drive epithelial cell function (El Masry et al., 2019).

GAGs are involved in the regulation of the ECM. At the wound site, hyaluronic acid (HA) is a component of the fibrin-fibronectin plug and acts as a chemoattractant for growth factors which have a role in advancing the wound healing process. Throughout, HA exhibits both pro- and anti-inflammatory actions; the high molecular weight is often attributed to anti-inflammatory behaviour, while low molecular weight is predominantly pro-inflammatory. Longer HA subunits have been shown to recruit and activate macrophages, endothelial, and epithelial cells, while attracting immunomodulatory cytokines to the wound site, further influencing cell behaviour (D'Agostino et al., 2015), stimulating wound closure (Tolg et al.,

2014), and contributing to proangiogenic pathways (Gao et al., 2010). While shorter HA subunits are involved in macrophage recruitment, the immunomodulatory cytokine recruitment have not been noted and thus inflammatory phenotypes are present, leading to an inhibition of wound closure (Litwiniuk et al., 2016).

As discussed previously in Section 1.3.3.6, a myofibroblast's specialism is contractility. These contractions work similarly to muscle contractions, via actin; with myofibroblasts containing very high concentrations. Myofibroblasts align on the wound edge and contract in unison, requiring not only communication between cells, but also cell-ECM. Cytoplasmic extensions link to fibronectin through actin binding, then drag the collagen matrix causing a tightening effect on the matrix which results in wound closure (Li and Kirsner, 2005). The speed at which closure occurs is dependent on cell number, the amount of collagen present, and the wound site size. The alignment and unified contraction create an aligned matrix along the tension lines generated during wound closure; partially modulated due to the secretion of decorin from myofibroblasts, which establishes uniformity between collagen fibrils because of its C-like shape (Zhang et al., 2007). New ECM post-healing differs from its predecessor in its composition and structure. Collagen fibril alignment leads to structurally weaker skin, with levels of elastin lower than non-wounded skin. Fibrous tissue, or a scar, is physically weaker than normal tissue due to the ECM fibres deposited having this directional bias, compared to that of normal tissue which is somewhat random in formation (Dallon et al., 2000). Therefore, a healed wound will have approximately 80% of the tensile strength of non-wounded skin.

1.4.2 Decellularisation

The ECM plays a significant role in wound healing and tissue homeostasis. Therefore, it is clear that developing biomaterials which can capture properties of ECM would be

advantageous to both in vitro research and in clinical applications to aid healing. Products derived from ECM have been studied for many years now, with products on the market utilising the material discussed in Section 1.4.3.

Mammalian ECM, however, requires processing before it can be utilised as a biomaterial. Pioneered by Professor Stephen Badylak, decellularisation generates natural bioactive materials, or biomaterials, which can act as scaffolds for cell growth in the fields of tissue engineering and regeneration (Saldin et al., 2017). Decellularisation techniques range from mechanically scraping away cellular debris from soft tissues such as small intestine (Badylak et al., 1989), to enzymatic treatment as with liver tissue (Loneker et al., 2016), to chemical approaches to remove the cellular components from hard tissues such as bone (Sawkins et al., 2013). Initial research into decellularisation of animal tissues were the result of a need to solve the large problem of rejection in tissue/organ transplantation (Badylak et al., 1989). Decellularisation ideally eliminates all cellular and nuclear material in order for the product not to cause immunogenic responses upon in vitro culture or in vivo implantation (Crapo et al., 2011). In practice, decellulariation doesn't eliminate all nuclear antigenic material, as harsh processes that would achieve this would negatively impact the desirable ECM architecture and bioactive molecules within. While decellularisation techniques have advanced since they were first investigated, with whole organs now able to be decellularised (Fathi et al., 2021), these materials have also been utilised in a variety of ways allowing their scope to be much more than organ transplantation as discussed in Section 1.4.3.

1.4.2.1 Source

One of the most widely used tissue sources for biomaterials is porcine; this is due to the ease of availability for relatively low cost from butchers and abattoirs, with organs and

tissues obtained larger, compared to rodents, allowing for a higher yield per organ (Zhang et al., 2021). Porcine organs also match human organ physiology better than the alternatives (Meurens et al., 2012). Animal tissue derived ECM contains a plethora of bioactive molecules that can orchestrate particular cellular behaviours, often analogous to the tissues from which they were derived (Freytes et al., 2014; Park et al., 2016; Shridhar et al., 2019). ECM derived from cells grown in culture has been used as an animal alternative, with the cell-derived ECM containing the same matrix composition as the in vivo tissues (Assunção et al., 2020), in theory. Primary cells, not cultured for long periods, are seen as the best option given that they are the most phenotypically similar to in vivo counterparts (Fitzpatrick and McDevitt, 2016) and thus most likely to produce in vivo-like ECM. A disadvantage to cell-derived ECM is that current technology restricts users from obtaining large quantities (Chan et al., 2021), as can be done with animal-derived ECM, and that due to the culture conditions impacting cell phenotypes the ECM obtained is often characteristically different from the ECM it is supposed to mimic (Zhang et al., 2021).

The unique collection of the macro- and micromolecules enables different ECM to possess different properties, depending on the specific requirements of the local tissue. Therefore, each organ or tissue's ECM possesses different characteristics, meaning many animal-derived ECM have been harvested for various research requirements (Saldin et al., 2017). Tissue specific niches elicited specific behaviour depending on the source of cell-derived ECM; for example, matrix deposited by chondrocytes led to the most successful chondrogenic differentiation (Cheng et al., 2009), while embryonic stem cell produced ECM promoted the differentiation of other embryonic stem cells, even when starved of other differentiation cues (Goh et al., 2013).

1.4.3 Biomaterial form

Having an ECM-based material may allow in vitro cell populations to exploit the reservoir of biochemical cues discussed in Section 1.4.1 and thus reside in a more physiologically representative environment. Utilising more naturally occurring matrix molecules may further enhance not only cell survival, but lead to a more representative, in vivo-like cellular phenotype. Synthetic polymers fail to contain analogous ways in which they can influence the cellular response due to the inherent complexity of the naturally-derived ECM, this is explored further in Section 3.1. Natural polymers are often slightly better in terms of possessing multifaceted biochemical cues yet still fall short of the surplus of options ECM-based materials have access to.

Once obtained, there are various forms in which ECM can be used. The form of ECM obtained is dependent on both the source tissue and the decellularisation process. Some decellularisation techniques produce sheets of ECM. Examples of this, harvested from SIS, urinary bladder, and skin, have been used in research in the recent past. OASIS® products are derived from SIS-ECM and are used to enhance wound healing through the structural and bioactive benefits of ECM. Their product line targets general wounds through OASIS® Wound Matrix (Barendse-Hofmann et al., 2007), burn-derived wounds through OASIS® Burn Matrix, and deeper, sometimes surgical in origin, wounds through OASIS® ULTRA Tri-layer Matrix (Cazzell et al., 2015). AlloDerm®, a human skin ECM product, has also been shown to promote the regeneration of the skin after a burn-derived wound (Juhasz et al., 2010).

Decellularised ECM sheets are imperfect for some applications, due to their relatively low surface area. Through extra processing steps, microparticles of varying sizes can be produced. The generation of ECM microparticles allows for a much greater surface area, as well as more exposed bioactive sites available for cell-ECM interactions (Hoganson et al.,

2016). The production of ECM microparticles can occur via simple grinding of decellularised ECM sheets or powders (Mazzitelli et al., 2011; Hoganson et al., 2016), electrospraying solubilised decellularised ECM (Wang et al., 2022), with newer techniques such as using microfluidics being tailored to develop particulate ECM products (Lin et al., 2022). Experimentally, they have been shown to support cells in vitro (Mazzitelli et al., 2011), used as a vehicle for cellular delivery as a healing enhancing therapy (Hoganson et al., 2016) and as a bioactive molecule supply for post-injury regenerative promotor in the heart (Wang et al., 2022).

A key property of ECM materials is that they can be solubilised; through the agitation with pepsin and HCl, the collagen fibres are digested and thus form a viscous liquid, known as ECM digest. This ECM digest can undergo thermo- and pH-responsive self-assembly, via collagen fibrillogenesis, to form hydrogels when neutralised and heated to 37 °C (Freytes et al., 2008). Hydrogels are 3D networks, where the structural components are insoluble in water yet can retain a high degree of water within it. Due to the high water content, ECM hydrogels closely match the environment present in human tissues. Consequently, ECM hydrogels often possess a good degree of biocompatibility, with gas and nutrient exchange being key factors, hence their utilisation as cell culture scaffolds (Tibbitt and Anseth, 2009; Caliari and Burdick, 2016). ECM derived hydrogels retain key bioactive molecules (Saldin et al., 2017) which are known to modulate various cellular processes, and thus are advantageous for in vitro and in vivo applications.

ECM hydrogels have been used for a range of applications. In vitro, they are primarily used as multi-dimensional cell culture substrates (Zhao et al., 2020). Ma et al. (2022) utilised SIS-ECM and augment it through the incorporation of additional extracellular vesicles, containing angiogenic factors, for a larger, more sustained release of bioactive molecules to assess the efficacy in a diabetic wound model. For in vitro applications, ECM hydrogels are

moulded during gelation into simple structures or, due to the thermo-responsive and pH-responsive nature of the ECM components, they are an attractive material for bioinks which can be printed into more complex structures (Kabirian and Mozafari, 2020; Sanjuan-Alberte et al., 2022). The liquid pre-gels are ideal for injectable biomaterials too, which are the main use case for in vivo materials too; treating surface wounds (Lin et al., 2021) as well as other complex diseases such as cardiovascular disease in the heart (Wassenaar et al., 2016), promoting repair in a post-stroke brain (Ghuman et al., 2016), preventing radiation damage to lung tissue (Zhou et al., 2020), and with potential for peripheral nerve repair (Kellaway et al., 2022).

ECM hydrogels are an important biomaterial for in vitro studies. Given their derived sources, they are the best reflection of the in vivo environment currently available in terms of structure and function. Better yet, these properties can be tuned to suit the need of the particular study, as in the Ma et al. (2022) report through functionalisation and via modulation of the material stiffness via crosslinking (Výborný et al., 2019).

1.5 Hypothesis and aims

Much is known regarding the biochemical, physical and, more recently but to a lesser degree, electrical stimuli required for successful and healthy healing to take place. However, these are often studied as sole factors. It is rare to see a study that incorporates two or more of these stimuli into a single study. Therefore, the goal of this research is to combine these stimuli into a model through which to view cellular responses; the expectation being that the whole is greater than the sum of its parts in terms of combinatory stimuli and pro-healing phenotypes. Therefore, the overarching hypothesis of this thesis is that culturing macrophages on an ECM hydrogel and applying an exogenous

electrical stimuli propagated by CNTs will drive macrophage polarisation toward an M2-like phenotype.

To test this hypothesis, the following aim was identified: develop and characterise an ECM hydrogel system, some of which had CNTs incorporated, as a complex model of the in vitro environment which can be used alongside exogenous electrical stimulation to investigate the effects of physical, biochemical, and electrical stimuli on cell populations present in wound healing.

The following objectives presented are intended to achieve the aim and answer the hypothesis stated:

- Utilise decellularisation methods to robustly generate SIS-ECM and subsequent hydrogels, which were fully characterised in terms of decellularisation metrics.
- Determine how the addition of carbon allotropes influences the mechanical and electrical properties of the ECM hydrogels.
- Ascertain the biocompatibility of the carbon allotrope incorporated ECM hydrogels and exogenous electrical stimuli separately.
- Investigate the combined effect of carbon allotrope incorporated ECM hydrogels and exogenous electrical stimuli on macrophage polarity and fibroblast cytokine secretion.

Chapter 2 | Materials and Methods

This chapter outlines the materials used throughout this thesis and the methods used to achieve the data presented. All experiments were performed across the BioDiscovery Institute and the Life Sciences Building, both at the University of Nottingham, UK.

2.1 Materials

Table 2.1: Materials used, and the supplier associated.

Materials	Supplier	
1,9-dimethylmethylene blue	Sigma Aldrich, UK	341088
4',6-diamindino-2-phenylindole	Thermo Fisher Scientific, UK	D1306
Absolute ethanol (200 proof)	Thermo Fisher Scientific, UK	16685992
Agarose	Sigma Aldrich, UK	1168020025
Alexafluor 488, goat anti-rabbit	Thermo Fisher Scientific, UK	A-11008
BSA	Sigma Aldrich, UK	A7284
Calcium chloride	Sigma Aldrich, UK	C1016
Calprotectin mouse antibody, anti-human	Thermo Fisher Scientific, UK	27E10
Chondroitin 1,6 sulphate	Sigma Aldrich, UK	C4384
CyQUANT™ LDH cytotoxicity assay	Thermo Fisher Scientific, UK	C20300
Dimethyl sulfoxide	Sigma Aldrich, UK	D5879
Disodium hydrogen phosphate	Sigma Aldrich, UK	1065851000
Duoset ELISA kits	R&D Systems, UK	
bFGF		DY233
CCL18		DY233
HGF		DY294
IL-6		DY206
IL-10		DY217B
MCP-1		DY279
TNF- α		DY210
Ethylenediaminetetraacetic acid	Sigma Aldrich, UK	E9884
Ethidium bromide	Sigma Aldrich, UK	E7637
Foetal bovine serum	Sigma Aldrich, UK	F2442
Gelatine from porcine skin	Sigma Aldrich, UK	G2500
Glucose solution	Thermo Fisher Scientific, UK	A2494001
GlutaMAX	Thermo Fisher Scientific, UK	35050061
Glycine	Sigma Aldrich, UK	G8898
GM-CSF	Sigma Aldrich, UK	G5035
Goat serum	Sigma Aldrich, UK	G6767
HEPES buffer	Thermo Fisher Scientific, UK	15630080
Hydrochloric acid	Sigma Aldrich, UK	435570
IFN-γ	Sigma Aldrich, UK	I17001
IL-4	Sigma Aldrich, UK	I4269
L-cysteine	Sigma Aldrich, UK	C1276
L-glutamine	Sigma Aldrich, UK	59202C
Lipopolysaccharide (LPS), *E. Coli* O111:B4	Sigma Aldrich, UK	L4391

LIVE/DEAD™ viability kit	Thermo Fisher Scientific, UK	L3224
Mannose receptor rabbit antibody, anti-human	Abcam, UK	ab64693
M-CSF	Sigma Aldrich, UK	M6518
Minimum essential media	Sigma Aldrich, UK	51412C
Mixed nanocarbon	NanoLab, USA	N/A
Molecular ladder (1 kbp)	New England Biolabs, USA	N3232S
Molecular ladder (100 bp)	New England Biolabs, USA	N3231S
MWCNT, OD: 15 nm	NanoLab, USA	PD15L1-5
MWCNT, OD: 30 nm	NanoLab, USA	PD30L5-20
Non-essential amino acids	Sigma Aldrich, UK	M7145
Papain	Sigma Aldrich, UK	P3375
Paraformaldehyde, 4%	Thermo Fisher Scientific, UK	15670799
Penicillin and streptomycin	Sigma Aldrich, UK	P4333
Pepsin	Sigma Aldrich, UK	P7012
Peroxyacetic acid	Thermo Fisher Scientific, UK	257755000
Phenol-chloroform-isoamyl	Sigma Aldrich, UK	77617
Phorbol 12-myristate 13-acetate	Sigma Aldrich, UK	P8139
Phosphate buffered saline	Thermo Fisher Scientific, UK	12899712
Polymer dielectric grey	Sigma Aldrich, UK	902497
Porcine small intestine	R B Elliot and Son, UK	N/A
PrestoBlue assay kit	Thermo Fisher Scientific, UK	A13262
Proteinase K	Invitrogen, UK	25530-049
Quant-iT PicoGreen dsDNA assay kit	Thermo Fisher Scientific, UK	P7589
Rhodamine red x, goat anti-mouse	Thermo Fisher Scientific, UK	R-6393
RPMI-1640 media	Thermo Fisher Scientific, UK	21870076
Sodium acetate	Sigma Aldrich, UK	241245
Sodium chloride	Sigma Aldrich, UK	S9888
Sodium dodecyl sulphate	Sigma Aldrich, UK	L3771
Sodium pyruvate	Thermo Fisher Scientific, UK	11360070
Sulphuric acid	Thermo Fisher Scientific, UK	15644920
TE buffer	Sigma Aldrich, UK	574793
TMB substrate solution	Thermo Fisher Scientific, UK	10647894
ToxiLight™ bioassay kit	Lonza, UK	LT07-217
Tris-EDTA buffer	Sigma Aldrich, UK	93283
Tris-HCl	Thermo Fisher Scientific, UK	77-86-1
Triton-X 100	Sigma Aldrich, UK	93443
Trypan blue	Thermo Fisher Scientific, UK	15250061
TWEEN® 20	Sigma Aldrich, UK	P1379

2.2 Equipment and software

Table 2.2: Equipment and software used, and the supplier associated.

Equipment	Supplier
1 mL TipOne® pipette tips (trimmed manually)	StarLab, UK
Coffee grinder	Krups, UK
CoolSafe freeze drier	Labogene, UK
Countess® Automated Cell Counter	Thermo Fisher Scientific, UK
EC1000SA, Programmable AC/DC power source	NF Systems, Japan
F-4200N 3-Axis Inline Gantry Robot	FISNAR, UK

FEG SEM	JEOL, Japan
FIJI, ImageJ v1.53c	NIH, USA
ImageQuant™ LAS-4000 biomolecular imager	FUJIFILM, UK
LabRAM HR Raman microscope[1] and a xyz automated stage[2]	HORIBA, Japan[1] Märzhäuser, Germany[2]
Office	Microsoft, USA
Orbital shaker	OHAUS, USA
PGSTAT potentiostat, FRA32M module, and NOVA v2.1.4	Metrohm Autolab, Netherlands
Physica MCR 301 Rheometer and Rheoplus v3.40	Anton Paar, UK
PRISM v9.4.1	GraphPad, USA
Tecan infinite 200 plate reader	Tecan, UK
Ultra centrifuge	Eppendorf, UK
ZOE Fluorescent Cell Imager	BioRad, UK

2.3 Chapter 3 methods

The following methods are executed in Chapter 3: CNT-ECM incorporated hydrogels.

2.3.1 DNA analysis

2.3.1.1 Extraction

An adapted methodology to extract and quantify the presence of dsDNA was utilised (Gilbert et al., 2008). Lyophilised and milled samples of known weights were incubated at 50 °C for 24 h in a 0.5% proteinase K buffer containing 1 M tris-HCl, 5 M NaCl, 0.5 M EDTA and 10% SDS. DNA extraction utilised multiple repeating steps of phenol-chrloroform-isoamyl (25:24:1) mixing and 10,000 g, 4 °C centrifugation for 10 min, discarding all but the aqueous phase in between. DNA then crashed out as a precipitate through the addition of 3 M sodium acetate and 100% ethanol while stored at -80 °C until fully frozen. While still frozen, a DNA pellet was formed through 10,000 g, 4 °C centrifugation. The pellet was then washed in 100 and 70% ethanol, dried, and resuspended in TE buffer.

2.3.1.2 PicoGreen

dsDNA was quantified using a PicoGreen assay kit, as per the manufacturer instructions. A standard curve was generated using Lambda dsDNA, from 0-2000 ng.mL^{-1}, to which the total dsDNA of the samples was calculated via fluorescence using a plate reader (Tecan, UK) using excitation and emission wavelengths of 480 and 520 nm respectively, according to manufacturing protocols. Tissue samples were diluted 1:1000 to fit on the standard curve.

2.3.1.3 Gel electrophoresis

Remaining DNA fragment size and distribution was analysed through gel electrophoresis. A 1% agarose gel was produced and 2.5 µL of ethidium bromide added prior to casting. TE buffer was used to submerge the agarose gel. DNA samples were loaded along with two molecular ladders ranging from 100-100 bp and 0.5-10 kbp. Gel electrophoresis was performed at 100 V for 1 h. Agarose gels were then analysed using a biomolecular imager.

2.3.2 Electrical characterisation

200 µL samples of pre-gel were cast into the top of 1 mL pipette tips leading to cylindrical hydrogels of 8 mm in diameter and 3 mm in depth. These were kept in dH_2O water until testing. Samples were placed between two gold coated glass slides (Figure 2.1) which were linked up to a PGSTAT potentiostat incorporated with a FRA32M module. Testing frequencies ranged from 1-100,000 Hz. Analysis was performed using version 2.1.4 of the NOVA software.

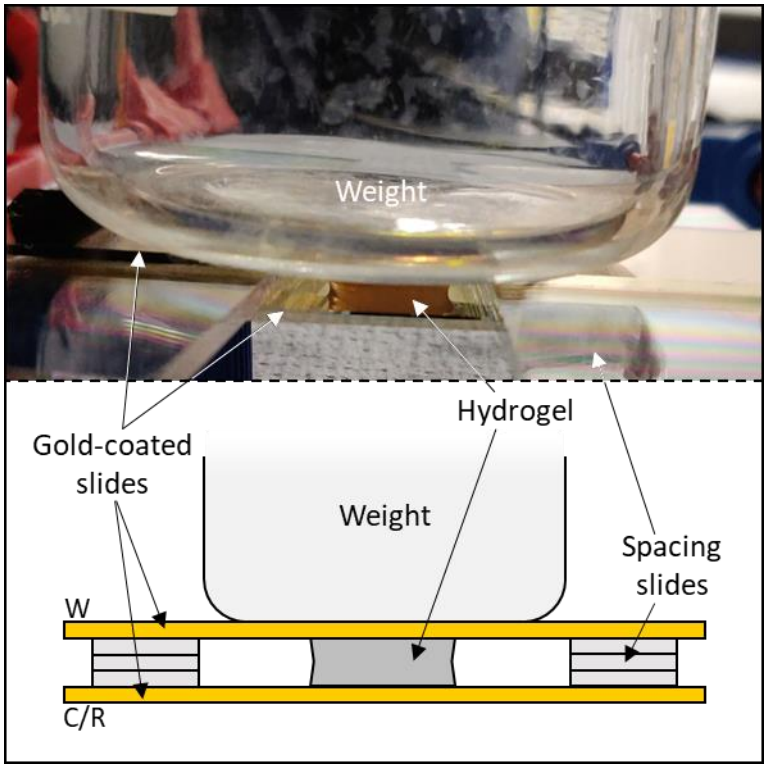

Figure 2.1: Gel-electrode set up during EIS interrogation. The hydrogel is sandwiched between two gold plates which are connected to the working (W) and counter/reference (C/R) electrode respectively. A consistent gap between electrodes is achieved by spacing two glass slides between them. A consistent pressure is applied to keep the whole set up stable using a beaker.

2.3.3 GAG analysis

2.3.3.1 1,9-dimethyl-methylene blue quantification

The method used was adapted from previous literature (Zheng and Levenston, 2015). Lyophilised and milled SIS-ECM of known weights were incubated at 65 °C in a 125 µg.mL^{-1} papain buffer containing 0.1 M disodium phosphate, 10 mM EDTA, and 10 mM L-cysteine until the samples were completely solubilised. 1,9-dimethyl-methylene blue (DMMB) reagent was made by dissolving 4 mg of DMMB in 1.25 mL of 100% ethanol, then volume adjusting to 250 mL with 40 mM glycine and 40 mM NaCl in dH_2O, adjusting to a pH of 1.5 using concentrated HCl. Once made, the DMMB reagent was stored in a foil covered bottle, away from light exposure. A standard curve was generated using chondroitin 1,6 sulphate,

from 0-100 µg.mL^{-1}, to which the total sGAG content was calculated via absorbance at 525 and 595 nm using a plate reader (Tecan, UK).

2.3.3.2 Alcian blue

Alcian blue was employed to visualise the presence of GAGs pre- and post-decellularisation, adapted from Gothard et al. (2015). Both native and decellularised tissues were dehydrated using washes with increasing ethanol concentrations. Tissues were then embedded in paraffin and sliced into sections before rehydrated through decreasing ethanol concentration washes, ending with dH_2O. Tissues were then submerged in Alcian blue solution for 30 min, incubated at 37 °C. Once the tissues were removed from the Alcian blue solution, they were rinsed again with dH_2O prior to imaging.

2.3.4 Material generation

2.3.4.1 SIS-ECM

Porcine small intestines were harvested from animals between 3-6 months old at R B Elliot and Son LTD and delivered the same day (Figure 2.2A). Upon arrival, the organ was washed thoroughly with tap water by squeezing it down the lumen until the water came out clear from the other end (Figure 2.2B). These intestines were then contained and frozen at -20 °C for storage. Prior to processing, organs were defrosted overnight while submerged in tap water at 4 °C. The intestine was then cut into sections approximately 20-25 cm to avoid too much stress leading to tearing (Figure 2.2C). These sections were housed in a container of tap water to avoid drying out prior to being sliced longitudinally using a scalpel (Figure 2.2D). The technique used has been adapted from method previously described (Badylak et al., 1998). These sections were laid flat, luminal side up, and mechanically delaminated

using a rubber scraper until the mucosal layers were removed (Figure 2.2E). Sections were then turned over and the same technique was employed to remove the serosa and muscularis layers until a semi-transparent sheet remained – this was the submucosal layer (Figure 2.2F). Peyer's patches were discarded due to their greater tendency to cause tears across the section. The SIS sheets were rinsed in water to wash away any residual cell-laden layers. SIS sheets had excess moisture removed via wringing through a sieve placed on blue roll to promote further water weight loss. 2 h of disinfection in 0.1% peroxyacetic acid solution (PAA), made up of dH_2O and 100% ethanol at 24:1, at 20:1 v/w ratio followed, with sheets constantly agitated at 200 rpm on an orbital shaker (Figure 2.2G). SIS sheets were then washed twice in both 1x PBS and dH_2O for 15 min periods. Liquid nitrogen was utilised to flash freeze the SIS before lyophilisation and ground down into small pieces using a coffee grinder (Figure 2.2H). This is SIS-ECM.

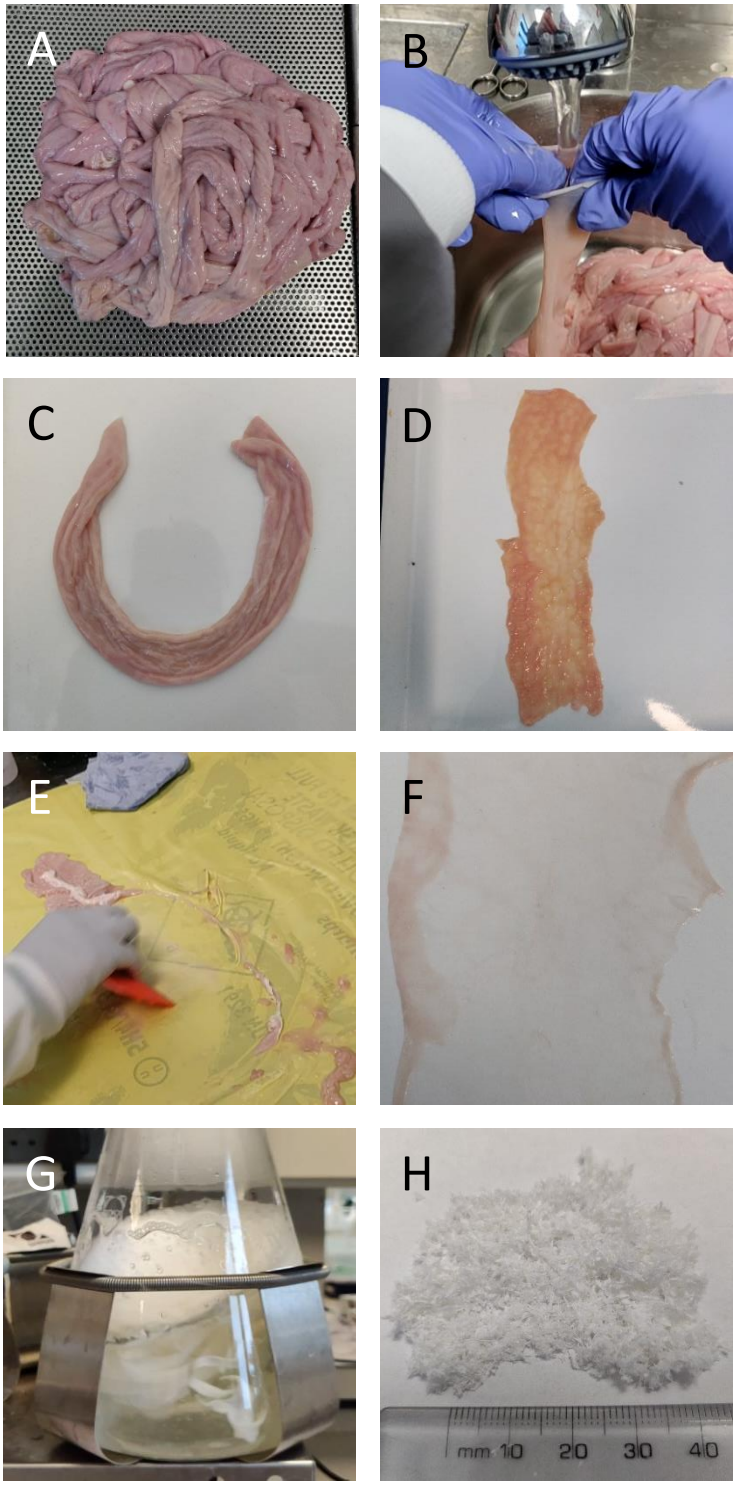

Figure 2.2: Preparation and generation of decellularised small intestinal submucosal ECM. Small intestines as received (A) are washed thoroughly with tap water (B) and cut into sections between 20-25 cm in length (C). These sections are then sliced longitudinally and placed luminal side up (D). A rubber scraper was then employed to mechanically delaminate the lumen before being turned over and repeated on the abluminal side (E). Resultant sheets (F) are washed in 0.1% PAA (G) before being flash frozen, lyophilised, and milled into small pieces (H).

2.3.4.2 ECM-hydrogels

A method used in the literature was replicated to produce ECM hydrogels (Freytes et al., 2008). Lyophilised and milled SIS-ECM was digested using pepsin, at a 10:1 ratio, in 0.01 M HCl to generate a stock solution of ECM digest at 10 $mg.mL^{-1}$. This was incubated at room temperature under constant agitation for 48 h. ECM digests were then centrifuged at 2000 g for 2 min to pellet any undigested pieces and the liquid digests were aliquoted and kept at 2-4 °C for short term storage (< 2 weeks) or frozen at -20 °C for long term storage (> 2 weeks). ECM hydrogels produced via this method are pH and thermoresponsive prior to gelation. Therefore, in order to generate a hydrogel, the ECM digests undergo basic neutralisation, using formulations found in Table 2.3, generating a pre-gel which can then be cast in a mould and incubated at 37 °C for 20 min.

Table 2.3: Formulation table concerning the production of SIS-ECM hydrogels of varying ECM concentrations. Volume values provided are for production of a 200 µL hydrogel, however scaled-up stocks of these neutralisation buffers were made and then used on demand to produce the required number and volumes of hydrogels.

Desired ECM concentration, $mg.mL^{-1}$		8	6	4
ECM digest volume, µL		160	120	80
Neut. Buffer composition, µL	1× PBS	6.22	54.7	103.2
	10× PBS	17.78	13.3	8.8
	0.1 M NaOH	16	12	8
Neut. buffer volume, µL		40	80	120

2.3.4.3 CNT-ECM hydrogels

A range of carbon allotropes were used in this thesis (Figure 2.3). Two forms of MWCNT were used: one with an outer diameter of 15 ± 5 nm and the other 30 ± 15 nm (Figure 2.3A and B, respectively). These had differing length ranges: 1-5 µm for the 15 nm diameter

variety and 5-20 µm for the 30 nm. A third allotrope of carbon used is a mixture containing approximately ~70% amorphous carbon, ~30% MWCNT with a diameter of 5 nm, and trace amounts of SWCNT. These are not depicted in Figure 2.2 as they were sold as SWCNTs yet upon Raman spectra investigation were found to be mostly amorphous carbon. References to carbon allotropes refer to all three forms described throughout, whereas mixed nanocarbon (NC) refers to the ~70% amorphous carbon composition.

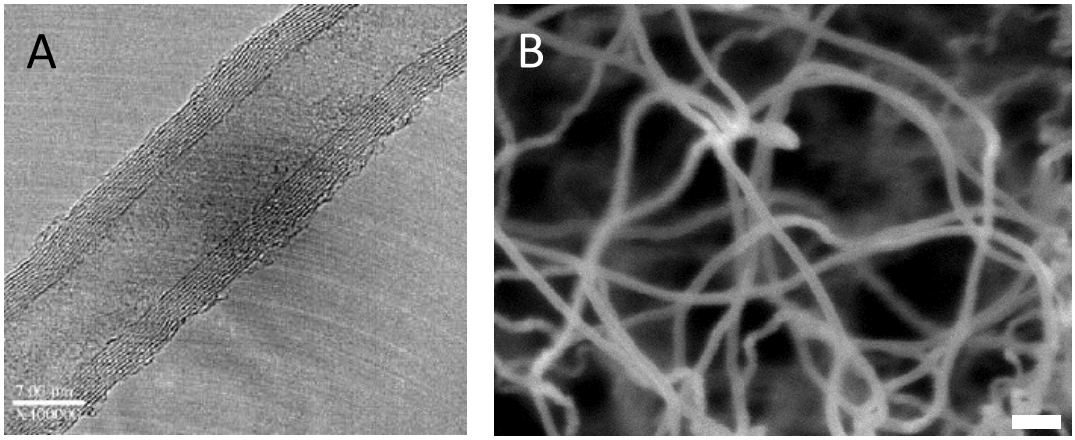

Figure 2.3: Electron micrographs of the two MWCNT forms utilised in this thesis. Images presented were obtained via the supplier's webpage. The outer diameters and length differ between the two, OD: 15 ± 5 nm, L: 1-5 µm (A) and OD: 30 ± 15 nm, L: 5-20 µm (B). Scale bars are 7 nm (A) and 200 nm (B).

Carbon allotropes must be added prior to gelation. The way this is done is by incorporating them into the neutralisation buffer to allow for a homogenous distribution prior to adding to the ECM digests, making it easier to distribute evenly within the pre-gel. Given the differing ratios of ECM digest to neutralisation buffer depending on the desired ECM concentration shown in Table 2.3, discrete amounts of carbon allotropes were added to each ECM concentration specific neutralisation buffer (Table 2.4).

Table 2.4: Formulation table concerning the production of carbon allotrope incorporated SIS-ECM hydrogels of varying concentrations.

Desired ECM concentration, $mg.mL^{-1}$	8	6	4
CNT concentration in neut. buffer, % w/v	1	0.5	0.34
CNT concentration in hydrogel, % w/v	0.2	0.2	0.2

Note: To produce the 0.02% carbon allotrope incorporated hydrogels, the 0.2% carbon allotrope neutralisation buffers were diluted 1:10 with the ECM concentration specific neutralisation buffer.

2.3.5 Mechanical characterisation

2.3.5.1 Time sweep

200 µL samples of pre-gel were added to the Peltier plate of the rheometer, which was pre-cooled to 4 °C. The Peltier hood was used to keep the humidity conditions stable during the experiment. A 22 mm parallel plate was used at a working distance of 0.4 mm as to not under or over trim (Figure 2.4). Once the pre-gel was in place, the temperature of the Peltier plate was rapidly increased to 37 °C and a time sweep was used at a constant angular frequency and amplitude, 1 $rad.s^{-1}$ and 1% respectively, to analyse the gelation kinetics, taking a reading once every 15 s for 20 min.

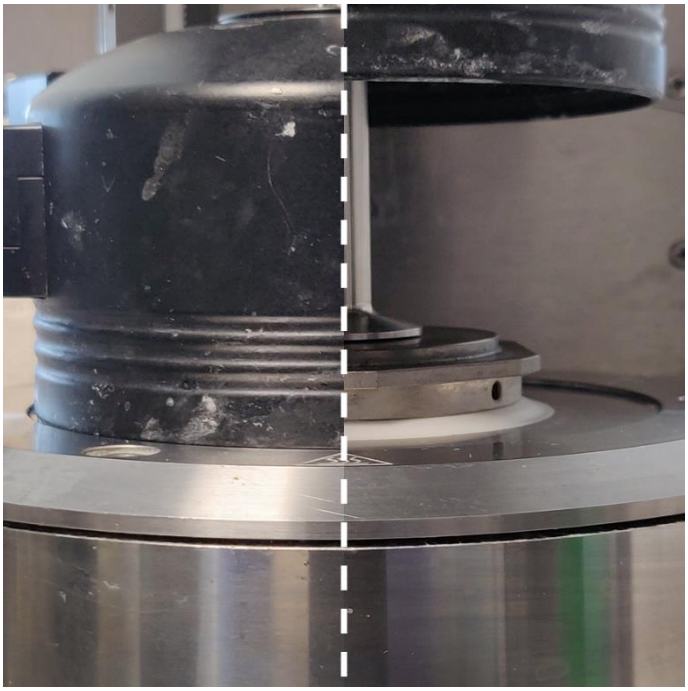

Figure 2.4: Rheometer configuration during experimentation. Showing both the Peltier hood (left) and underneath with the 22 mm parallel plate at the 0.4 mm testing position (right).

2.3.5.2 Amplitude sweep

An amplitude sweep was performed immediately after the time sweep, during which the angular frequency remained 1 rad.s^{-1} but the oscillatory strain ramped from 1-200% to analyse linear viscoelasticity, strain stiffening, and plastic deformation. The temperature remained stable at 37 °C throughout.

2.3.6 Visual characterisation

2.3.6.1 Field emission gun scanning electron microscopy

200 µL samples of pre-gel were cast into the top of 1 mL pipette tips leading to cylindrical gel of 8 mm in diameter and 3 mm in depth. These were kept in dH_2O water. Said gels were then slam frozen, also known as metal mirror freezing, smashed between liquid nitrogen cooled copper plates. This vitrified the top 10 µm of the samples to allow for imaging in its

most natural state possible (Graham, 2008). These samples were then submerged in liquid nitrogen and freeze dried prior to imaging. Dried samples were coated in 4 nm of iridium using a sputter coater and imaged using a 7100F FEG-SEM.

2.3.6.2 Raman spectroscopy

200 µL samples of pre-gel were cast into the top of 1 mL pipette tips leading to cylindrical gel of 8 mm in diameter and 3 mm in depth. These were kept in dH_2O water for up to 5 h prior to Raman prep. Said gels were then slam frozen, also known as metal mirror freezing, smashed between liquid nitrogen cooled copper plates. This vitrified the top 15-30 µm of the samples to allow for imaging in its most natural state possible. These samples were then submerged in liquid nitrogen and freeze dried prior to imaging. Raman spectroscopy and imaging was performed using a LabRAM HR Raman microscope equipped with an automated xyz stage. Spectra were acquired using a 660 nm laser at 24 mW power, a 100x objective and a 50 µm confocal pinhole.

2.4 Chapter 4 methods

The following methods are executed in Chapter 4: Cellular response to ECM and DC stimulation.

2.4.1 Biocompatibility analysis

2.4.1.1 ISO 10993-05

The biological evaluation of medical devices (ISO 10993-05) was used as a guide to determine biocompatibility of the ECM only and CNT-ECM hydrogels, specifically the extract and direct methodologies.

For extract testing, hydrogel samples were incubated at 37 °C for 24 h in minimum essential medium (MEM). The MEM was then aspirated and used on a subconfluent layer of BJ fibroblasts which were incubated for a further 24 h before being subject to LIVE/DEAD™ and ToxiLight™ biocompatibility analysis.

For direct testing, cylindrical hydrogel samples (diameter: 8 mm, height: 3 mm) were placed on top of a subconfluent layer of BJ fibroblasts in a 24-well plate and incubated for 24 h before being subject to LIVE/DEAD™ and ToxiLight™ biocompatibility analysis.

2.4.1.2 LDH

Cell viability was measured using a lactate dehydrogenase (LDH) cell viability assay. 50 µL of media was transferred to a 96-well plate and 50 µL of the LDH assay kit reaction mixture was added, as per manufacturer instructions, before being incubated for 30 min at room temperature protected from light. 50 µL of the stop solution was then added to all wells and samples were quantified via absorbance. LDH activity was determined using a plate reader.

2.4.1.3 LIVE/DEAD™

The LIVE/DEAD viability kit was used to qualitatively analyse cell viability. Cells were prepared for analysis by aspirating the spent media, washed with PBS, and replaced with a

solution of PBS containing 4 µM ethidium homodimer-1 and 2 µM calcein AM, as per the manufacturer instructions. After a 30 min incubation at room temperature protected from light, the cells were imaged using a fluorescence microscope.

2.4.1.4 PrestoBlue

Cell metabolism was measured using a PrestoBlue cell viability assay. The PrestoBlue reagent was added at a 1:10 dilution directly to cells in culture medium and incubated at 37 °C for up to 3 h, protected from light sources. Samples were then quantified via absorbance, utilising 570 nm light normalised to the 600 nm wavelength, using a plate reader.

2.4.1.5 ToxiLight™

Cell viability was measured using the ToxiLight™ non-destructive cytotoxicity kit. Supernatant samples were taken post experimentation and frozen at -20 °C for preservation prior to analysis. Once thawed, the Toxilight™ kit was used as per the manufacturer instructions. 20 µL of supernatant was added to 100 µL of the adenylate kinase detection reagent and incubated at room temperature for 5 min before being quantified via luminescence using a plate reader.

2.4.2 BJ fibroblast culture

2.4.2.1 Routine culture

Human skin BJ fibroblasts (CRL-2522, ATCC) were cultured in MEM with the following supplements: 10% foetal bovine serum, 1% L-glutamine, 1% non-essential amino acids, 1% penicillin-streptomycin, and 1% sodium pyruvate. Fibroblasts were cultured at 37 °C in a 5%

CO_2, humidified atmosphere. In generic subculturing, fibroblasts were cultured until 80-90% confluency and then split 1:4-6 as per ATCC guidelines. Media was refreshed every 2-3 days.

2.4.2.2 Experimental culture

For extract and direct biocompatibility testing, BJ fibroblasts were seeded at 150k cells per well (24-well plate) in order to achieve a sub confluency of ~80% after an overnight incubation, ready for addition of extract media or the presence of hydrogel samples.

Prior to seeding for 4-day cytokine secretion analysis, a 250 µL ECM only or CNT-ECM hydrogel was formed on the surface of a 24 well plate and cured for 40 min. Once gelation had occurred, BJ fibroblasts were seeded at 40k per mL of appropriately supplemented MEM.

2.4.3 Electrical stimulation

In vitro exogenous electrical stimulation experiments were performed using a programmable AC/DC power source. A DC voltage range of 0.6-4.8 V was used in order replicate: the normal transepithelial potential (Nuccitelli, 2003), the physiological range seen in mammalian wounds in vivo, and above (≤ 4.8 V) to determine the upper limit of stimulation for this system as well as purposely causing cell damage as a control that stimulation was occurring. Said voltages were applied using stainless-steel rods 12 mm apart (Figure 2.5). Rods were either exposed stainless-steel, to allow the passage of current in order to analyse current effects, or coated in polymer dielectric grey, to block the current in order to analyse field effects.

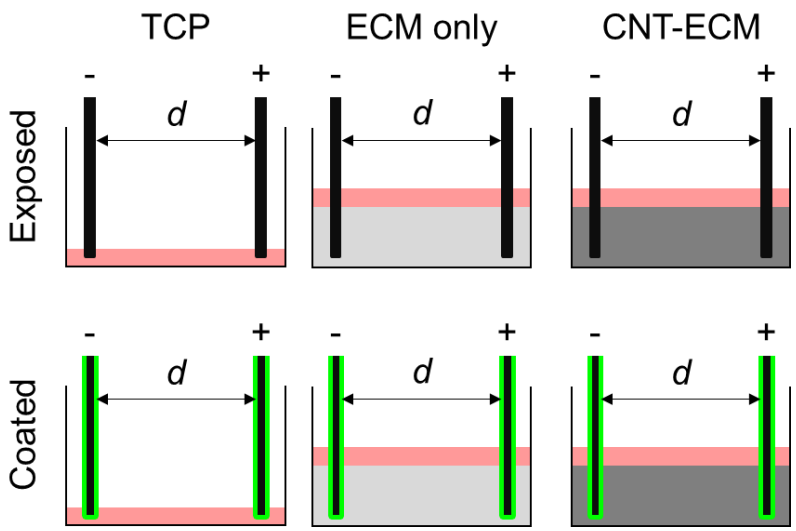

Figure 2.5: Electrical stimulation set-up schematic. Two stainless steel rods, connected to the programmable AC/DC power source, placed in a well d mm apart, where d = 12, containing cells cultured on TCP, ECM, or CNT-ECM hydrogels. These stainless-steel rods were either exposed or polymer dielectric grey-coated in order to allow or prevent the flow of current, respectively.

2.4.3.1 Dielectric electrode generation

Stainless-steel rods were dipped in the polymer dielectric grey ink, with excess scraped off on the edge of the bottle and cured at 130 °C for 20 min to ensure the ink was fully dry. This coating process was then repeated twice more to ensure there was no exposed stainless-steel.

2.4.4 ELISA

Detection of CCL18, TNF-a, IL-6, and IL-1ra secreted into the media by THP-1 cells was achieved through analysis using Duoset enzyme-linked immunosorbent assay (ELISA) kits according to the cytokine-specific manufacturer instructions. Supernatant samples were taken after incubation of 3- or 6-days, centrifuged to eliminate any cellular debris, and frozen at -20 °C for preservation prior to analysis. 96-well plates were coated with the 100 µL of the relevant capture antibody and incubated overnight before they were blocked in 300 µL 3% BSA in PBS for 2 h. 100 µL of the relevant standards and thawed samples were

added and incubated for 2h, followed by the addition of 100 µL of the relevant detection antibody. After another 2 h incubation, 100 µL of working dilution streptavidin-HRP was added and incubated away from direct light for 20 min. 100 µL of the substrate solution was then incubated, also away from direct light, for a further 20 min after which 50 µL of stop solution was added directly, without washing the plates. Plates were then read at 450 nm normalised to 560 nm, using a plate reader. Bar the addition of the stop solution, plates were washed thrice with Tween in-between each step to rinse unbound protein. All incubation steps occurred at room temperature under constant agitation.

2.4.4.1 Cytokine spiking

Three conditions of hydrogel samples were prepared in a 24-well plate (see Section 2.3.4): ECM only, 0.02% CNT-ECM, and 0.2% CNT-ECM hydrogels. Once gelation had occurred, 1 mL cell culture media was added per well. This media was spiked with 150 and 300 $pg.mL^{-1}$ of TNF-α and CCL18 Duoset ELISA kit standards, respectively. These were incubated at 37 °C in a 5% CO_2 atmosphere for 6-days before undergoing analysis via ELISA.

2.4.4.2 Limit of detection calculations

For the ELISA data, the limit of detection (LOD) have been applied to determine whether data can be reliably detected and therefore compared. It is calculated using the limit of blank (LOB) (Equation 2.1), which is the highest apparent analyte concentration expected to be found when replicates of a blank sample containing no analyte are tested. The LOD is the lowest standard concentration which is reliably distinguished from the blank and thus is feasibly detectable (Equation 2.2) (Armbrusher and Pry, 2008).

$$\mathrm{LOB} = Mean_{blank} + (1.645 + SD_{blank}) \quad [2.1]$$

$$\mathrm{LOD} = \mathrm{LOB} + (1.645 + SD_{lowest\ concentration\ standard}) \quad [2.2]$$

2.4.5 Immunocytochemistry

Upon incubation for 3- or 6-days, cells were fixed with 4% paraformaldehyde and permeabilised using 0.2% Tween 20. A 30 min incubation of 3% BSA and 1% glycine in PBS was used to block the samples followed by a 30 min incubation with 5% goat serum. Primary antibodies specific to mannose receptor and calprotectin were then used at 1 and 2 $\mu g.mL^{-1}$ respectively, incubated for 1 h. Another 0.2% Tween 20 wash preceded the secondary antibody incubation, 8 $\mu g.mL^{-1}$ rhodamine red x and Alexafluor 488 for 1 h. After another 0.2% Tween 20 wash, cell nuclei were stained with 4',6-diamindino-2-phenylindole (DAPI) at 200 $ng.mL^{-1}$ for 5 min. All incubations performed at room temperature. Cells were imaged using a ZOE fluorescent cell imager. 3 locations per well were randomly selected for imaging, resulting in 9 representative images per condition.

2.4.6 THP-1 monocyte culture

2.4.6.1 Routine culture

Human monocytes (TIB-202, ATCC) were cultured in RPMI-1640 with the following supplements: 10% foetal bovine serum, 1.25% glucose solution, 1% penicillin-streptomycin, 1% sodium pyruvate, 1% GlutaMAX, and 1% HEPES. THP-1s were cultured at 37 °C in a 5% CO_2, humidified atmosphere. In generic subculturing, THP-1s were cultured to a maximum cell density of 1M cells per mL of media was reached, at which point they were counted and re-seeded at 200k cells per mL.

2.4.6.2 Monocyte differentiation

THP-1 monocytes were seeded at 500k cells per well (24-well plate) in 1 mL of supplemented media. Differentiation was induced immediately by further supplementing RPMI-1640 media with 50 ng.mL^{-1} phorbol 12-myristate 13-acetate (PMA) for 5-6 h. This generated a THP-1 derived macrophage possessing an M0-like state which was allowed to rest overnight prior to polarisation.

2.4.6.3 Macrophage polarisation

To achieve an M1-like state, THP-1 derived M0-like macrophages were exposed to a cytokine cocktail consisting of 50 ng.mL^{-1} GM-CSF, 20 ng.mL^{-1} IFN-γ, and 100 ng.mL^{-1} LPS. To achieve an M2-like state, THP-1 derived M0-like macrophages were exposed to a cytokine cocktail consisting of 50 ng.mL^{-1} M-CSF, and 20 ng.mL^{-1} IL-4. To maintain the M0-like state, exposure to 10 ng.mL^{-1} M-CSF was maintained throughout electrical stimulation and subsequent incubation. Experimentation occurred immediately after the addition of polarisation supplementation.

2.4.6.4 Experimental culture

Prior to seeding for 3- and 6-day cytokine secretion analysis, a 250 µL ECM only or CNT-ECM hydrogel was formed on the surface of a 24 well plate and cured for 40 min. Once gelation had occurred, THP-1 monocytes were seeded at 200k per mL of appropriately supplemented RPMI-1640 media. THP-1 cells were differentiated and polarised whilst in the presence of the hydrogels.

2.5 Chapter 5 methods

The following methods are executed in Chapter 5, Section 5.3: Future work.

2.5.1 Bioprinting

2.5.1.1 Gelatine bath

This method has been adapted from Hinton et al., 2015. 250 mL of milli-Q water was heated to 45 °C then continuously stirred as 4% (w/v) of gelatine from porcine skin and 15 mM of $CaCl_2$ was added. When full dissolved, and the mixture transparent, the solution was cooled at 4 °C for approximately 90 min until a solid puck formed. A 0.16% (w/v) $CaCl_2$ was pre-cooled to 4 °C alongside the gelatine solution. Once solid, the gelatine puck was bathed in the $CaCl_2$ solution and crudely broken up using a spatula before being blended using a homogeniser at 7500 rpm for 2 min. The resultant slurry was then aliquoted into falcon tubes and centrifuged for 5 min at 4200 g, the supernatant was removed and more $CaCl_2$ solution was added and the whole thing vortexed before being spun again. This centrifugation step was repeated until there were no bubbles in the supernatant and the gelatine slurry was pipettable but not runny. The slurry was then chilled for up to 24 h prior to use in printing.

2.5.1.2 FRESH printing

The F-4200N compact benchtop robot was used as an extrusion device to print the ECM inks. Pre-gels were prepared as previously described at ECM concentrations of 4, 6, and 8 $mg.mL^{-1}$ inside a 5 cc barrel and left on ice until printing. The cooled gelatine slurry was pipetted into a petri dish and the F-4200N set up in such a way that it would print into the gelatine. Printing was attempted at around 0.5-1.5 psi, yet this was increased if no

extrusion occurred up to a maximum of 50 psi at which time the needle was changed as it had become blocked. Printed material was left at room temperature for 40 min then incubated at 37 °C for 15 min to melt the gelatine slurry which could then be pipetted away, releasing the hydrogels. These were then rinsed using PBS to remove any residual gelatine.

2.5.2 Room temperature rheology

A gelation profile was produced in a similar method as described previously (see Section 2.3.5), just at 21 °C rather than 37 °C as to not prematurely melt the gelatine bath. Briefly, 200 µL samples of pre-gel were added to the Peltier plate of the rheometer which was pre-cooled to 4 °C. The temperature of the Peltier plate was rapidly increased to 21 °C and a time sweep was used at a constant angular frequency and amplitude, 1 rad.s^{-1} and 1% respectively, to analyse the gelation kinetics, taking a reading once every 60 s for 90 min.

Chapter 3 | CNT-ECM incorporated hydrogels

3.1 Introduction

The dynamics of cell-environment interactions are a vital step in taking research forward. Currently, the relative simplicity of conventional 2D in vitro studies poses issues in reproducibility and translatability. These issues arise due to the non-representative environments generated in 2D cell culture leading to inaccurate conclusions regarding cellular behaviour (Costa et al., 2016). Therefore, more complexity of the in vitro cellular environment is required to enhance how representative a model is compared to the in vivo environment. One aspect of increased complexity that has been studied is increasing the cell's dimensional interactivity. Utilising multi-dimensional structures (2.5/3D) to house cells as a biomimicry method has shown to produce a more in vivo-like cell behaviour for commonly studied readouts such as differentiation and protein synthesis (Antoni et al., 2015; Caliari and Burdick, 2016). A second aspect, which is vital for a better representation of the in vivo environment, stems from an understanding that cells obtain a significant number of cues from their environment, not just surrounding cell populations (Frantz et al., 2010). This is especially important for wound healing research, as the surrounding matrix is a key part of the process itself. A third aspect which has been studied is the understanding that electrical stimuli are key orchestrators in many in vivo processes (Nuccitelli, 2003; Levin, 2014; Li et al., 2016; Chen et al., 2019). This has led to conducting materials being incorporated into cell culture structures to propagate said stimuli, allowing for bioelectronic medicine to become an interesting prospect for a variety of applications as discussed in Section 1.3. Since multi-dimensional structures, bioactive materials, and conductivity, through the application of electrical stimuli, elicit more representative in vivo-like responses, a combinatory approach linking the three could prove beneficial in terms of enhancing how representative in vitro models can be.

Hydrogels are a crosslinked network of hydrophilic polymeric fibres that remain highly absorbent whilst maintaining their structural capabilities (Peppas and Hoffman, 2020). Hydrogels are established as 2- and 3D constructs on, or in, which in vitro cell culture can occur in biomimetic extracellular environments, compared to TCP. These mimetic environments simulate that of the ECM in vivo; thus different, more in vivo-like, behaviours are seen in these experiments (Caliari and Burdick, 2016). There have been a variety of materials from which a hydrogel is generated and used in the literature as structures in which cells are cultured. Hydrogels are advantageous in that they have the potential to fulfil two aspects of the modelling system described: structural and bioactive.

The choice of material is critical in providing the most representative set of structural and bioactive components. Hydrogel composition is categorised into three forms: synthetic, natural, and hybrids. Synthetic hydrogels are derived from synthetic polymers, such as polyethylene glycol (PEG) and polyacrylamide (PAM) (Gyles et al., 2017). These hydrogels possess little batch-to-batch variability and can be produced to be stronger and more durable than the natural alternative. Some synthetic hydrogels have been shown to possess slightly lower biocompatibility compared to natural hydrogels.

Natural hydrogels are derived from proteins, polysaccharides, or acellular tissues produced by decellularisation (Catoira et al., 2019). The advantages of natural hydrogels lie in the inherent biocompatibility within biological systems as well as the positive influence on cellular behaviours: proliferation, differentiation, migration, and other characteristics associated with wound healing for example (Hesse et al., 2010; Lei et al., 2011; Sawkins et al., 2013; Liang et al., 2015; Ho et al., 2017; Chen et al., 2022; Ma et al., 2022).

The simplest natural hydrogels are comprised of a single protein or polysaccharide: the most common, due to its abundance in vivo (Lodish et al., 2000), is collagen (Zhu et al., 2001; Jha and Moore, 2022). These simple natural hydrogels are an improvement on 2D

TCP cell culture models. The hydrogel-cell interactions present elicit differences in the cell behaviour, as mentioned in Section 1.4.3, mimicking the cell-ECM relationship found in vivo. While the simplicity is a positive in terms of batch variability and material homogeneity, there is a concern that these models remain too simplistic and thus these collagen hydrogels are now often modified. Such modifications seek to improve simple biomaterial hydrogels by combining multiple materials to form composite hydrogels. This can achieve enhanced complexity leading to a greater degree of bio-functionality, such as augmenting macrophage immunomodulatory actions via the addition of fibrin (Hsieh et al., 2016), fibronectin (Logie et al., 2021), and hyaluronic acid (Hauck et al., 2021) to collagen hydrogels. Alongside generating composite hydrogels through manually combining proteins, it is possible to obtain multi-protein collagen-based biomaterials through cellular production. A common example of this is Matrigel®, which is an extracellular protein mixture. Compared to collagen-only hydrogels, Matrigel® offers more complexity in terms of composition. Matrigel® is composed of basement membrane proteins: laminin, collagen IV, and entactin, as well as up to seven growth factors at varying concentrations (Aisenbrey and Murphy, 2020; Corning, 2021). It has been commonly used to form hydrogels within regenerative medicine research, given the ability to better mimic the in vivo environment. The application of Matrigel® has led to improved proliferative readouts and noted to promote differentiation (Grefte et al., 2012; Josan et al., 2021). However, Matrigel® has some limitations which hinder the potential of the biomaterial. Besides the lack of compositional definition and economical limitations, it is Engelbreth-Holm-Swarm murine sarcoma-derived. This restricts its desirability in immunology-based research due to the immunogenic impact, as well as excluding the transition into clinical applications due to potential tumorigenicity (Serban et al., 2008; Conboy et al., 2017).

Utilising decellularised ECM derived from mammalian organs and tissues for hydrogel generation is another development in naturally derived hydrogels. Decellularised ECM can

generate hydrogels via solubilisation, as discussed in Section 1.4.3. The major advantage of these hydrogels is their innate dynamic relationship with cells. These interactions arise due to the preservation of bioactive molecules, such as growth factors and matrix-bound vesicles, as well as the fibres themselves possessing bioactive functionality, as previously discussed in Section 1.4.1. Given that a more representative model is the goal, the use of said decellularised tissues as hydrogels is the desired route. Virtually every organ and tissue type has been used to create animal-derived decellularised products for a range of regenerative medicine applications such as organ transplantation (Tapias and Ott, 2014) and tissue engineering (Zhang et al., 2022). The first tissue-derived decellularised biomaterial was SIS, used in 1995 in the repair of the Achilles tendon in canines (Badylak et al., 1995). Those treated with decellularised SIS displayed marked improvements in healing, with SIS-treated tendons possessing superior strength, comparable to a normal tendon. Since then, SIS-ECM has been employed as a pro-healing biomaterial in muscle regeneration (Mase et al., 2010), burn repair (Juhasz et al., 2010), and wound healing applications (Prevel et al., 1995; Barendse-Hofmann et al., 2007; Hodde and Allam, 2007; Cazzell et al., 2015; Chen et al., 2022). SIS-ECM-derived products have also received FDA approval for wound care applications, as noted in Section 1.4.3. Due to this evidence indicating that SIS-ECM retains, and thus can provide, the biochemical capability to promote healing, along with the ability to support an in vivo-like environmental complexity through the generation of a hydrogel, it was selected as the biomaterial of choice for use throughout the work described in this thesis.

Conducting biomaterials, and bioelectronic medicine more generally, have attracted attention from the regenerative medicine field due to the growing interest in electrical stimuli as an orchestrator of a wide range of pathways. Conducting hydrogels have been used to mimic an in vivo-like environment for cardiac tissues (Lee et al., 2022), as well as in other muscle-cell-based applications (Dong et al., 2020). This is due to the fundamental

presence of electrical stimuli as a signalling cue in the muscle contraction pathway (Luo and Ehrlich, 2015). Given the current understanding of electrical stimuli in the wound healing process (see Section 1.3.3), conducting hydrogels now have the potential to be utilised in advancing the understanding of wound healing through more representative means. Various conductive elements used to generate conducting biomaterials were highlighted in Section 1.3.2.4.

CNTs are an attractive option for conducting biomaterials as they can possess an extremely high conductivity (Wang et al., 2017; Zhao et al., 2020) with many studies presenting little cytotoxic impact once incorporated into a bulk material (Shin et al., 2011; Sun et al., 2017; Mihajlovic et al, 2018; Sanjuan-Alberte et al., 2022). However, some studies still describe some cytotoxic effects (Ravanbakhsh et al., 2019). This discrepancy with the biocompatibility likely stems from the sheer variability in length, diameter, functionalisation, and residual heavy metals (Muller et al., 2005; Pauluhn et al., 2009; Ge et al., 2011; Mercer et al., 2011; Ge et al., 2012). The electrical properties of CNTs are well reported (Wang et al., 2017; Zhao et al., 2020), with values over 1×10^6 $S.m^{-1}$ depending on the specific form, dimensions, and degree of functionalisation. Once in a bulk, polymeric network, CNTs are known to adhere to percolation theory. Percolation theory defines the interactions within a network through specific nodes. At a critical number of these nodes, the previously disconnected array of nodes becomes a big network-spanning collection of connections allowing the passage of something through the space (Stauffer and Aharony, 1994). With regards to conducting

biomaterials, this means that above a critical CNT concentration, the conductivity of the whole network significantly increases (Pekcan and Akn, 2011). Enhanced conductivity across the network leads to a greater efficacy of electrical stimuli applied to the material. Alongside the electrical capabilities, CNTs are mechanically strong too whilst being efficient

thermal conductors (Ruoff et al., 2003; Balandin et al., 2008; Kim et al., 2017). These secondary features are important too as they may influence the cell biology aspect of the model, given that the stiffness of a material is known to impact cell behaviour (Wells, 2007; Caliari and Burdick, 2016) and ECM hydrogels utilise temperature changes to initiate gelation (Saldin et al., 2017). Another advantage to incorporating CNTs into biomaterials is their adsorptive properties. It is known that CNTs generate protein corona when interacting with biological matter (Li et al., 2009; Cai et al., 2013); the protein adsorption has been shown to enhance the biocompatibility of the materials by shielding cells from direct CNT/impurity interactions (Karimi et al., 2015; Maheshwari et al., 2019).

CNTs have been used to increase conductivity within natural biomaterials before, primarily in collagen-based materials. Collagen-CNT biomaterials have been noted to change the fibre structure which enhances the mechanical properties of the materials (Li et al., 2022), which has been shown to increase neuronal differentiation (Kim et al., 2015) and improve cardiomyocyte culture in both alignment and performance (Sun et al., 2017). It has been suggested that collagen-CNT materials have such great potential due to the CNT dimensions mimicking that of collagen fibrils, whilst providing additional structural support to cells residing in the materials (Hopley et al., 2014).

As previously discussed, there are a variety of CNTs available with slightly different properties (Section 1.3.2.4). Given that functionalisation is a necessity to decrease the hydrophobicity of the CNTs to incorporate them into a hydrogel, two COOH-functionalised MWCNTs with different outer diameters were selected for this study. Alongside the CNTs, the incorporation of a mixed nanocarbon (NC) was used. Containing approximately ~70% amorphous carbon, ~30% MWCNT with a diameter of 5 nm, and trace amounts of SWCNT, these materials possessed electrical properties similar to that of the MWCNT samples, yet

lacked the same structural definition. This enables the dissection of the enhanced capabilities MWCNTs provide in combination with SIS-ECM hydrogels.

The development and characterisation of a novel in vitro model, combining the structural and bioactive attributes of ECM hydrogels with the electrical, thermal, and mechanical properties of MWCNTs, will be described in this chapter. The objectives of the research reported herein were to utilise decellularisation methods to robustly generate SIS-ECM and subsequent hydrogels, which were fully characterised in terms of decellularisation metrics. All to determine how the addition of MWCNTs influences the mechanical and electrical properties of the SIS-ECM hydrogels.

3.2 Experimental design

Porcine SIS tissue was decellularised using the established delamination protocol (Section 2.3.4) reported by Badylak et al. (1998). The decellularisation process was performed on the whole organ, with representative ECM aliquots taken from this organ used throughout this thesis. SIS was chosen as a tissue of choice for a specific reason, as described in Section 3.1.

3.2.1 Post-decellularisation biochemical quantification

Decellularisation techniques aim to eliminate antigenic molecules as could stimulate an immunogenic response leading to poor cellular behaviour. Examples of antigenic components include pathogens and associated secreted proteins, as well as cellular material, such as nucleic acids and mitochondrial damage-associated molecular patterns (Zhang et al., 2010; Briard et al., 2020), from the intestines themselves. Eliminating these antigens reduces the risk of any immunogenic response and activation when decellularised

materials are used in in vitro cell culture or in vivo transplantation. Therefore, it is key that the removal of antigens is quantified to determine the extent of decellularisation. However, it is impractical, and can be detrimental to the retention of bioactive molecules, to eliminate all antigenic components from the ECM (Chakraborty et al., 2020). Crapo et al. (2011) postulated three criteria for a successful decellularised material, focussing on dsDNA as a representative marker for cellular material retention, as it is responsible for adverse immune reactions (Zheng et al., 2005). The criteria stated are as follows: ≤ 50 ng dsDNA per mg of dried decellularised ECM, with < 200 base pair DNA fragments, and a lack of nuclear material visible via either H&E or DAPI staining techniques (Crapo et al., 2011). However, the literature is not in agreement on the dsDNA threshold that determines decellularisation success due to different tissues possessing different native levels of dsDNA (Chakraborty et al., 2020). While a reduction in dsDNA does not correlate with reductions in all antigenic substances, such as endotoxins and proteases (Aamodt and Grainger, 2016), other analyses to detect these are not assessed consistently within the literature.

The analysis of retained bioactive molecules is an important factor when analysing decellularisation success. Decellularisation should not be so thorough that it is to the detriment of these molecules, as this could diminish the effectiveness of the ECM as a biomaterial (White et al., 2017). Research utilising animal-derived ECM biomaterials often reports levels of GAGs as a marker of bioactive molecule retention (Giobbe et al., 2019; Kellaway et al., 2023). GAG functionality ranges from hydration of tissues to cellular modulation (Bishop et al., 2007; Wang et al., 2016). Therefore, retaining these molecules in a tissue-derived ECM hydrogel makes for a more desirable biomaterial for use in mammalian cell culture. Detection and quantification of GAGs within decellularised ECM is reported using a dimethylmethylene blue (DMMB) assay (Zheng and Levenston, 2015).

3.2.2 FEG SEM preparation

It is important to investigate the physical micro-structures of ECM derived materials to explore mechanical properties, the visualisation of the ECM hydrogel micro-structure allows for this dissection between the physical structure and mechanical data. Ethanol dehydration and critical point drying (CPD) are commonly used (Sawkins et al., 2013; Giobbe et al., 2019). However, CPD is known to cause material artefacts due to the changes in structure produced during the process (Koch and Włodarczyk-Biegun, 2020). Samples dried using CPD fix the samples in 2.5-3% glutaraldehyde prior to imaging, which fundamentally changes the structure and morphology of the materials; fixation therefore leads to images that are not representative of the samples used in other experiments within the same articles.

Environmental SEM (ESEM) would allow for the optimal imaging of the hydrogels, exhibiting a maintained physical structure preserved in a hydrated state. Despite this obvious benefit, ESEM is rarely used in hydrogel imaging due to the limitations concerning the presence of water. Condensation resulting from the high humidity can interfere with image detection. Combined with the more limited resolving power, in comparison to SEM, the materials are more difficult to visualise (Doucet et al., 2005). Another limitation is due to practicality. ESEM with hydrogels is time sensitive, as the constant electron beam and fluctuations in pressure lead to artefacts in the samples (Alcouffe et al., 2020).

Metal mirror freezing, or small freezing, was instead used in this work. Metal mirror freezing vitrifies the top layer of the materials, producing optimal freezing up to 10 µm from the surface (Graham et al., 2008). This ensures that the images collected post-drying are as close to native as possible; without the need for fixation or the development of artefacts due to desiccation as in CPD, nor the beam damage and image quality constraints brought on by ESEM.

3.2.3 Hydrogel mechanical quantification

Viscoelasticity is ubiquitous in ECM (Chaudhuri et al., 2020; Ma et al., 2021). This is a property responsible for both the mechanical and bioactive components of materials which are made of ECM. Given that cells will sense and respond to viscoelasticity (Hosseini and Katbab, 2014; Chaudhuri et al., 2020), it is important to investigate the impact of CNT incorporation into the ECM hydrogels. ECM hydrogels are described as viscoelastic as they display behaviours of both elastic solids and viscous liquids. This dynamic behaviour is a result of energy dissipation due to structural changes within the hydrogel. With regards to ECM hydrogels, these structural changes arising from the bond formation during thermoresponsive fibre assembly and bond breaking during mechanical stress and strain (Ma et al., 2021).

Rheology can be employed to investigate the viscoelastic properties of ECM hydrogels. The storage, G', and loss, G", moduli are two vital measures when characterising viscoelasticity using rheology. G' is a depiction of the elastic part of the viscoelastic property (Mezgher et al., 2021). It can be thought of as a description of the solid-like behaviour of a material. G' is a representation of this energy stored within the material whilst under stress. Conversely, G" is the representation of the viscous part of the viscoelastic property. Contrasting to G', it can be thought of as the liquid-like behaviour of a material. This viscous behaviour is seen when matter flows and causes internal friction within a material, hence the connection between G" and liquids. G" is a representation of the energy collected via internal flow friction when dissipated across the material. Materials with a $G' > G''$ are viscoelastic solids, with some sort of strong bonds present, i.e. hydrogen bonding and/or covalent bonding, to store the elastic energy. On the other hand, materials with a $G' < G''$ are viscoelastic liquids which have little to no strong bonds between individual components of the material. ECM pre-gels possess more viscoelastic liquid features, while post-gelation

ECM hydrogels will display features of a viscoelastic solid, prior to plastic deformation. The use of rheology can capture these measurements during and after gelation.

3.2.3.1 Gelation profile

To fully characterise the viscoelastic properties of ECM hydrogels, the gelation profile was analysed. Prior to gelation, digested ECM undergoes basic neutralisation to form a pre-gel (Freytes et al., 2008). It is this which when heated to 37 °C self-assembles, via collagen fibrillogenesis, into the hydrogel matrix network. However, this may spontaneously start at lower temperatures depending on the concentration of ECM present in the pre-gel (Shannon et al., 2015). Higher concentrations of pre-gel are more likely to initiate self-assembly prior to the optimum conditions being reached.

The loss tangent, tanδ, describes the relationship between G' and G" (Equation 3.1) (Mezgher et al., 2021). For a perfectly elastic material, tanδ value would be 0; for a perfectly viscous material, tanδ would be ∞, as G' = 0. Experimentally, materials are dubbed ideally elastic or ideally viscous if the tanδ value is approximately 0.01 or 100, respectively. Tanδ is a useful visualisation of gelation as it describes the relative relationship between G' and G" without absolute values.

$$\mathrm{Tan}\delta = \frac{\mathrm{G"}}{\mathrm{G'}} \qquad [3.1]$$

$\mathrm{G'} = \text{Storage moduli}, \mathrm{G"} = \text{Loss moduli}.$

3.2.3.2 Amplitude sweep

An amplitude sweep is a method used to determine the dynamic mechanical properties of a material in response to deformation. A sinusoidal deformation is applied to the hydrogel, with a dynamic strain amplitude, yet constant angular frequency. The resultant stress of the hydrogel is then measured as a function of said amplitude (Stojkov et al., 2021). The amplitude sweep is utilised for viscoelastic materials to investigate their specific viscous and elastic properties during a range of applied strain. For this study, amplitude sweeps were performed immediately after gelation.

The first portion of data obtained represents the linear viscoelastic (LVE) region (Mezgher et al., 2021). The LVE region is the strain applied within which the material maintains its structure through G' forces overcoming those G" forces seen in a viscous sample. The LVE region eventually ends at a given strain, known as the linearity limit. The yield point is the storage modulus value at which the LVE region ends, calculated via a ± 5% deviation from the LVE plateau.

Strain stiffening is a property observed in materials derived from protein sources, such as collagen and fibrin (Storm et al., 2005; Rudnicki et al., 2013; Bertula et al., 2019), and describes the increase in G' under increasing strain. It is hypothesised that biological materials possess this property to be more adaptive to the external environment in terms of local mechanical interactions, and thus it is a fundamental property of animal-derived tissues (Humphrey, 2003). Strain stiffening is also thought to have a bioactive role in cell migration, with fibroblasts being shown to stiffen the local substrate upon which they move (Helvert and Friedl, 2016).

Strain stiffening reaches a peak, referred to as the ultimate strength, at which point plastic deformation beings. Plastic deformation occurs when the loss modulus overcomes the

storage modulus, thus the material begins to act more like a viscous flowing liquid and is irreversibly altered.

3.2.4 Hydrogel electrical quantification

The aim is to enhance the electrical properties of the material by increasing their conductivity, through the addition of CNTs to the ECM hydrogels. Electrochemical impedance spectroscopy (EIS) was employed to determine the success of this CNT induced increase in conductivity. EIS investigates the amount of impedance in a system (Bard and Faulkner, 2001; Gamry, n.d.). Ohm's law states that current is directly proportional to the voltage, where resistance (R) blocks said current. Impedance (Z) is complex resistance, in that it has a frequency-dependent relationship (Figure 3.1; Equations 3.2-3.5), unlike resistance which is frequency-independent. Therefore, impedance is the resistance equivalent within an AC circuit. The frequency dependency relates to the presence of reactance (X); described as the imaginary component of the complex impedance of a circuit element (Equation 3.2).

$$\mathrm{Z} = \sqrt{R^2 + X^2} \qquad [3.2]$$

Z = Impedance, R = Resistance, X = Reactance.

Like resistance, reactance describes the opposition of current flow; larger reactance leads to smaller currents for the same applied voltage. Reactance can be further classified into two types: capacitive reactance (X_C) and inductive reactance (X_L) (Equation 3.3). The relationship between reactance and frequency is reversed depending on the type of

reactance: capacitive reactance decreases with increasing frequency, while inductive reactance increases with increasing frequency.

$$X = X_L - X_C \quad [3.3]$$

X = Reactance, X_L = Inductive reactance, X_C = Capacitive reactance.

Capacitive reactance is best described using the capacitor circuit element. A capacitor consists of two conducting plates with a dielectric, or insulating, material between them. When a voltage is applied, an electric field is generated across the insulative material causing electrons to collect on the negatively charged plate. As electrons accumulate, they generate capacitive reactance through like charges repelling one another. Capacitance (C) describes the ability to store charge and thus is used to calculate capacitive reactance (Equation 3.4). In a DC circuit, the capacitor will charge up and then have infinite resistance due to the insulative dielectric material blocking the flow of electrons, hence a lack of capacitance and therefore frequency dependency. In an AC circuit, due to the oscillation of current, the electrons periodically flip their direction of flow, and this allows the capacitor to discharge and recharge each oscillation. The higher the capacitance, the more charge must flow to build up to the peak voltage; therefore, the higher the current. Higher frequencies allow more current to flow, as the capacitor has less time to charge before to oscillation.

$$X_C = \frac{1}{2\pi f C} \quad [3.4]$$

X_C = Capacitive reactance, f = Frequency, C = Capacitance.

Inductive reactance is best described using the inductor circuit element. Inductors consist of insulated wire wound into a coil around a core. When a voltage is applied, a large magnetic field is generated due to the combined magnetic fields of individual wires within the coil. The inductor opposes instantaneous changes in current; this property is referred to as inductance (L) and is used to describe inductive reactance (Equation 3.5). In a DC circuit, an inductor opposes current flow while it charges up by creating a unidirectional magnetic field. After this period, the current will experience no inductive reactance due to the inductor preferring current values to stay constant. In an AC circuit, a time-varying magnetic field will be generated, meaning that the current changes direction depending on the frequency and so the force exerted to oppose current change continually alternates too, meaning there is a continuous opposition to current flow. The higher the frequency, the higher the inductive reactance, and the lower the current flow.

$$X_L = 2\pi f L \qquad [3.5]$$

X_L = Inductive reactance, f = Frequency, L = Inductance.

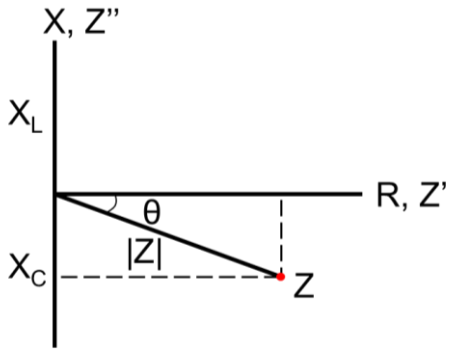

Figure 3.1: Impedance, the result of reactance (X) and resistance (R). Reactance (X) and resistance (R) are variables of impedance (Z). Reactance is composed of inductance (X_L) and capacitance (X_C). The resultant vector describes the magnitude of impedance (|Z|) and the angle between the x-axis and impedance is the phase angle (θ).

Conductance is a frequency independent measure of a lack of resistance in a circuit, therefore is the reciprocal of resistance. Impedance shares that relationship with admittance, making admittance the AC equivalent of conductance.

3.3 Results and discussion

3.3.1 SIS-ECM generation and decellularisation success criteria

SIS-ECM was generated using methods described in Section 2.3.1. DNA is an antigenic marker commonly used to define decellularisation success (Crapo et al., 2011). Therefore, three representative samples of homogenous lyophilised SIS-ECM were used in the detection of dsDNA via PicoGreen (Figure 3.2A) and fragment size via gel electrophoresis (Figure 3.2B). Figure 3.2A shows a significant decrease ($P \leq 0.0001$) in dsDNA by dry weight between the native and decellularised tissues, 13400 $ng.mg^{-1}$ vs. 3300 $ng.mg^{-1}$ respectively, a 75.4% decrease. Gel electrophoresis showed that the remaining dsDNA within the decellularised tissues was below 200 bp, whereas the native dsDNA contains bands across the dsDNA ladder range (Figure 3.2B).

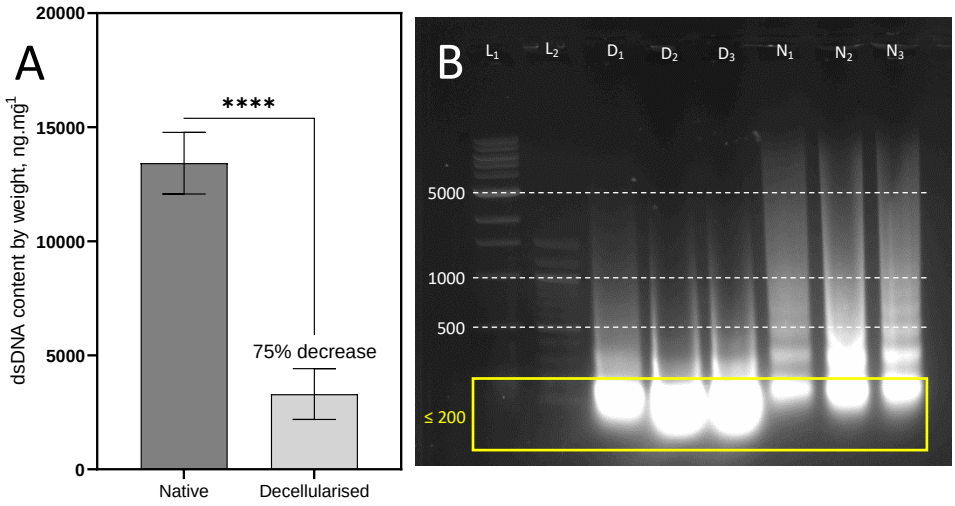

Figure 3.2: Decellularisation success criteria using dsDNA as an indicator. dsDNA content for native SIS and decellularised SIS-ECM (A) and nucleic acid fragment size of purified dsDNA from native, N_x, and decellularised, D_x, sources (B). L_1 is a 1000 bp ladder, L_2 is a 100 bp ladder. Bar graphs represent mean ± SD. N = 1, n = 3, samples were run in triplicate.

Whilst the remaining dsDNA indicates incomplete decellularisation with regards to the criteria stated by Crapo et al. (2011), it could be suggested that a comparison to those values is not the de facto measure of decellularisation success. The criteria set out by Crapo et al. (2011) are based on a wide range of tissue sources and thus differing decellularisation methods. Some tissues undergo chemical and enzymatic decellularisation. These processes involve soaking the native, or partially processed, tissues in decellularising agents such as trypsin-EDTA (Sawkins et al., 2013), or a detergent, such as sodium deoxycholate, triton X-100, or sodium dodecyl sulphate (Ott et al., 2008; Baptista et al., 2011; Fernández-Pérez and Ahearne, 2019; Giobbe et al., 2019; Shahraki et al., 2022). Comparing all the resultant ECM to the SIS-ECM generated via physical mechanical delamination alone is challenging given the difference in techniques used, and thus a criterion for all decellularisation products is therefore restrictive. Mechanical delamination itself is one of the most prone to subjective interpretations; for example, the implement used and the amount of pressure applied during delamination will have an impact on the degree of decellularisation noted

between different research groups; a non-existent issue when referring to a chemical or enzymatic decellularisation, where the protocol is soaking tissues for defined a period.

The presence of DNase use within decellularisation protocols also results in published data non-comparable with the SIS-ECM dsDNA data (Figure 3.2A) (Giobbe et al., 2019; Kobayashi et al., 2020). Tissues treated with DNase before being analysed for dsDNA content after the fact do not elicit any evidence that the decellularisation process itself was successful in removing antigenic components; it only provides proof that DNase degrades DNA.

Another consideration regarding Figure 3.2A is the initial dsDNA concentration. Whilst the dsDNA content remaining in the decellularised tissue was higher than the ≤ 50 ng stated by Crapo et al. (2011), the amount of dsDNA found in the native tissue is far greater than that seen in native tissue of other studies (Giobbe et al., 2019; Kobayashi et al., 2020; Palmosi et al., 2022). Due to this, it could be postulated that one would expect to see a proportionately higher amount of dsDNA in the decellularised tissue stated in Figure 3.2A. The decrease presented in this data is 75.4%, which is a significant decrease ($P \leq 0.0001$).

The remaining dsDNA present in decellularised tissues displayed dsDNA fragments under the 200 bp threshold also set by Crapo et al (2011). This shows that while the dsDNA content was relatively high compared to other decellularised products, the actual decellularisation process was successful in degrading the nucleic acid to a similar degree as seen in apoptotic cells as a result of caspase-activated DNase (Nagata et al., 2010). Given the reduction in dsDNA to below 200 bp, it is unlikely that the DNA content will be responsible for any antigenic responses when used for cell culture (Keane et al., 2012). The cellular response to these materials will be investigated further in Chapter 4.

Though it is important to reduce the antigenic components of tissue throughout the decellularisation process, it should not be to the detriment of the benefits of using ECM as a biomaterial, such as the biochemical and mechanical properties. To demonstrate

biochemical retention, GAGs were analysed in both native and decellularised samples (Figure 3.3). A level of GAGs was retained throughout the decellularisation process, with 617.4 ng.mg^{-1} by dry weight remaining (Figure 3.3A); alcian blue staining confirmed a reduced relative to native tissue, but still present, GAG concentration (Figure 3.3B). Decellularised tissue does not have a higher concentration of GAGs compared to native tissue, the increase in Figure 3.3A is due to a reduction in cellular materials over the decellularisation process meaning that the concentration of GAGs is relatively higher in comparison to the tissue as a whole.

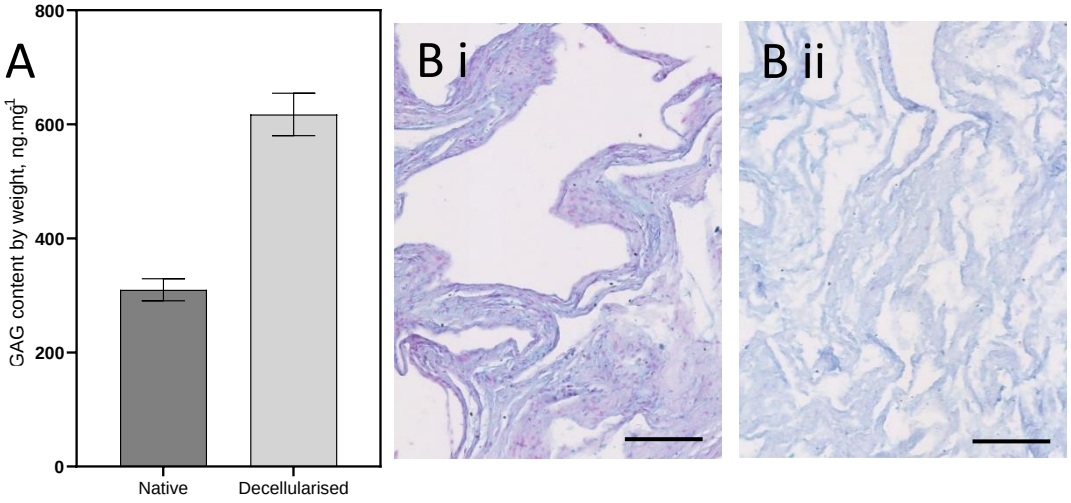

Figure 3.3: GAG retention in decellularised SIS-ECM. Quantification of GAG content for native SIS and decellularised SIS-ECM (A). Alcian blue staining for native small intestine (i) and decellularised SIS (ii) to qualitatively show sGAG content (B), collected by Dr Simon Kellaway. Bar graphs represent mean ± SD. N = 1, n = 3, samples were run in triplicate. Scale bars represent 100 µm.

GAGs have properties which are highly desirable in a biomaterial, as discussed in Section 1.4.1.1. Given this relationship between GAGs and their functions, the incomplete decellularisation indicated by the dsDNA data in Figure 3.2 may be advantageous in relation to GAG content. More complete decellularisation is thought to be responsible for a greater loss of GAGs (Kellaway et al., 2023). Reporting the GAG concentration of decellularised ECM is important in comparing the mechanical properties of resultant hydrogels.

Differences in GAG concentration across various studies may influence the gelation kinetics, and therefore could be a factor in the resultant hydrogels displaying differing mechanical properties (Brightman et al, 2000; Stuart and Panitch, 2008).

3.3.2 SIS-ECM hydrogel generation and macrophotography

SIS-ECM underwent pepsin digestion in the presence of 0.01 M HCl to form an ECM digest (Figure 3.4A). To form an ECM pre-gel, ECM digest underwent basic neutralisation using formulations found in Table 2.4, either as a control or with added allotropes of carbon (Figure 3.4B) ready for incorporation during gelation. Once neutralised, the pre-gel was cast into a mould and incubated at 37 °C for 20 min. This generated SIS-ECM hydrogels. The ECM only, control hydrogels are opaque off-white (Figure 3.4C). At the higher concentration of 0.2% (Figures 3.4, Di to Fi), the hydrogels containing MWCNTs with a diameter of 15 nm and 30 nm (Figures 3.4, Di and Ei) are opaque and black, while the mixed nanocarbon incorporated hydrogel is slightly opaque off-white in comparison (Figure 3.4Fi). The lower carbon allotrope concentration of 0.02% was opaque off-white (Figures 3.4, Dii to Fii). 0.02% MWCNTs produced a speckled look (Figures 3.4 Dii and Eii), whereas the lower concentration mixed nanocarbon had fewer dark specks present (Figure 3.4Fii), more similar to the ECM only control hydrogels. In terms of handling the hydrogels, relative to the ECM only controls, the 0.2% MWCNT hydrogels felt less fragile, an observation not noted with other hydrogels. Prior to further testing hydrogels were stored in PBS. During this time, it was noted that the hydrogels incorporated with all allotropes of carbon used exhibited some leaching as the PBS changed colour. Whether or not this leachate is detrimental to biocompatibility will be assessed in Chapter 4.

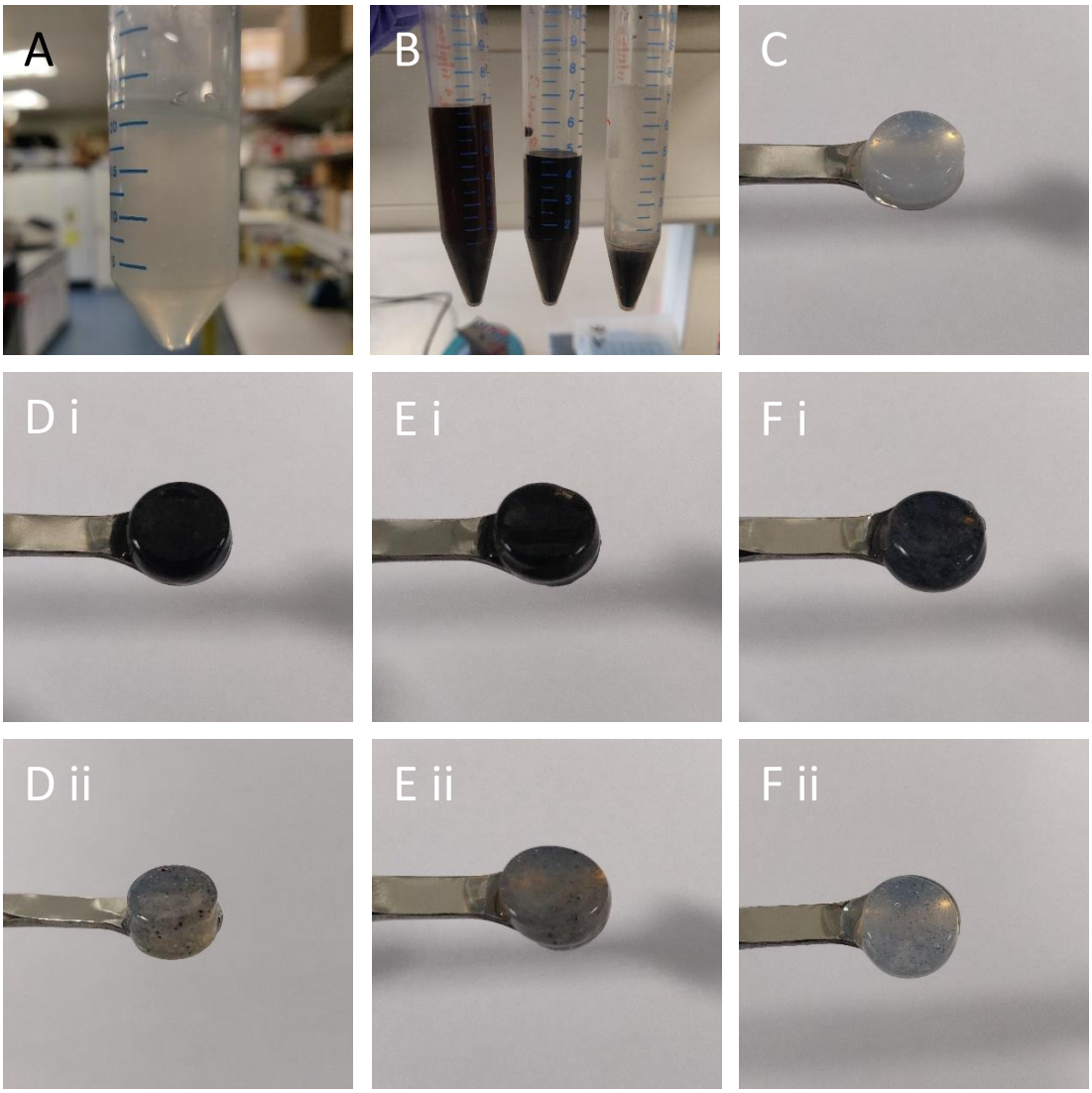

Figure 3.4: Hydrogel formation and macrophotography of the carbon allotrope incorporated hydrogels. SIS-ECM digest is a very viscous, translucent liquid (A) which is then mixed with a neutralisation buffer. Neutralisation buffers made with, from left to right, MWCNT with a diameter of 15 nm (MW15), MWCNT with a diameter of 30 nm (MW30), and a mixed nanocarbon sample made up of ~70% amorphous carbon, ~30% MWCNT with a diameter of 5 nm and trace amounts of SWCNT (NC) (B). Control hydrogels looked like the SIS-ECM digest, in that they are translucent, but with a solid form (C). Hydrogels made with CNT containing neutralisation buffers are pictured, MW15 (D), MW30 (E), and NC (F). These gels are made with 0.2% CNTs (i) and 0.02% CNTs (ii).

3.3.3 Carbon allotrope incorporated SIS-ECM hydrogels microstructure

Investigating the microstructure of composite hydrogels can be insightful characterisation method, as the visual appearance of hydrogels can be used to explain mechanical data presented later in this chapter. Therefore, electron micrographs of SIS-ECM only, and 0.2%

carbon allotrope hydrogels were collated and are presented in Figure 3.5. Figure 3.5A illustrates the ECM only hydrogels; collagen fibres presented as a dense yet homogenous carpet with little alignment, matching that which has been noted in previous literature (Sawkins et al., 2013; Giobbe et al., 2019). Figures 3.5B to D show carbon allotrope incorporated hydrogels, highlighting the presence of aggregated clumps nestled within the fibre carpet. These aggregations are a result of the incorporated allotropes of carbon. The electron micrographs suggest that the ECM fibres encase clusters of hydrophobic CNTs. It is difficult to confirm from these electron micrographs whether there are visible CNTs protruding from the aggregations, given the smallest scale bars are 100 nm and the largest MWCNTs are approximately 30 nm in diameter with a length of 5-20 µm (Figure 2.2B); collagen fibrils are much thicker and have a length in the micron range (Chang and Buehler, 2014).

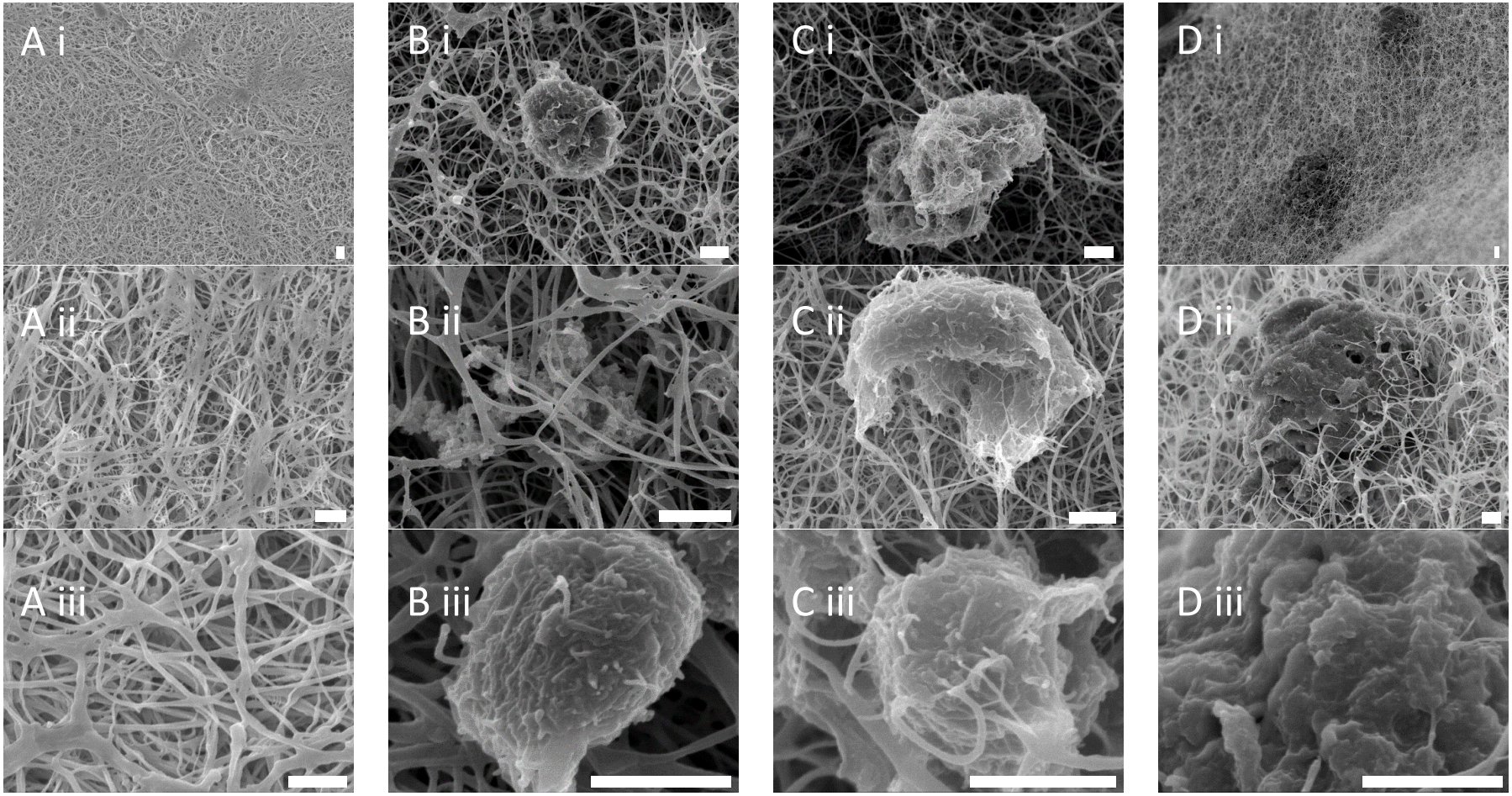

Figure 3.5: Representative microstructures of SIS-ECM hydrogels via FEG-SEM at different magnifications. SIS-ECM hydrogels present as a dense carpet of fibre with no distinct features (A). 15 nm MWCNT (B), 30 nm MWCNT (C), and mixed nanocarbon (D) SIS-ECM hydrogels exhibit aggregations of material throughout the fibre carpet. Scale bars are 1 µm. Collected by Ms Nikki Weston.

The aggregations noted in Figures 3.5B to D are most likely examples of the protein corona, commonly seen in CNT-protein interactions (Cai et al., 2013). This is likely to improve the biocompatibility of the CNTs when in culture, however, could impact the desirable electrical properties of the CNTs. It is reported that SWCNT and collagen type I interactions can lead to alterations in the collagen fibre structure (Kim et al., 2015). This is not replicated here and therefore requires higher resolution SEM, or TEM, to investigate. However, this phenomenon could be an interaction only exhibited by SWCNTs, not MWCNTs as used in the materials presented here. Likewise, it could be masked, or interfered with, by the presence of other ECM proteins present in these SIS-ECM hydrogels, given that Kim et al. (2015) present data using collagen type I hydrogels.

3.3.4 MWCNT incorporation confirmation via Raman spectroscopy

While it is reasonable to assume that incorporated allotropes of carbon are present in the final hydrogels, based on the black colouring (Figure 3.4), Raman spectroscopy was utilised to confirm their presence, distribution, and structure. The spectra of the MWCNT hydrogels show a strong resemblance to the MWCNTs themselves (Figure 3.6*X*i). The G band, attributed to the in-plane motion of the C–C bond (Hodkiewicz, 2010; Jorio and Saito, 2021) within the graphite-like structure of the walls of the MWCNT, can be seen at ~1325 cm^{-1}. The D band, known as the disorder band, highlights disorder within the graphite-like structure (Brown et al., 2001; Hodkiewicz, 2010). This is higher in MWCNTs compared to SWCNTs and can be attributed to the multi-layered composition leading to more defects in the structure. However, functionalisation, with –COOH, of these MWCNTs seen in this work could also attribute to this. The D band is seen at ~1600 cm^{-1}. The G', or 2D, band is not perfectly understood, it is linked to the Raman scattering of six carbons vibrating in a hexagonal lattice (Jorio and Saito, 2021). It is a peak which is known to proportionally

increase with wall number in CNTs, similarly to the G band. G' is seen at ~2650 cm^{-1}. The quoted Raman shift values differ from that seen in the literature; the G band is usually quoted as 1580 cm^{-1} and the D band as 1350 cm^{-1}, for example (Brown et al., 2001; Dresselhaus et al., 2005; Hodkiewicz, 2010). The source of this blueshift of the G band and redshift of the D band is unknown, yet most likely to be attributed to the hydrogel environment surrounding the MWCNTs. Analysis of the peak positions and ratios compared to the spectra released by the manufacturer of the carbon allotropes suggests that hydrogel preparation does not have a significant impact on the structure of the incorporated MWCNTs.

Microscopy (Figure 3.6*X*ii) and subsequent spectroscopic mapping (Figure 3.6*X*iii) show that the aggregates contain the specified MWCNTs while analysis of the surrounding matrix seems to suggest the incorporation of significantly fewer, and often non-detectable levels of MWCNTs. Similar clustering has been seen in previous literature which used the same MWCNTs (Vaithilingam et al., 2019). It is important to note that the lack of spectroscopic evidence for MWCNTs in these locations does not mean that they are not present, more that they are likely below the detection threshold for the instrument.

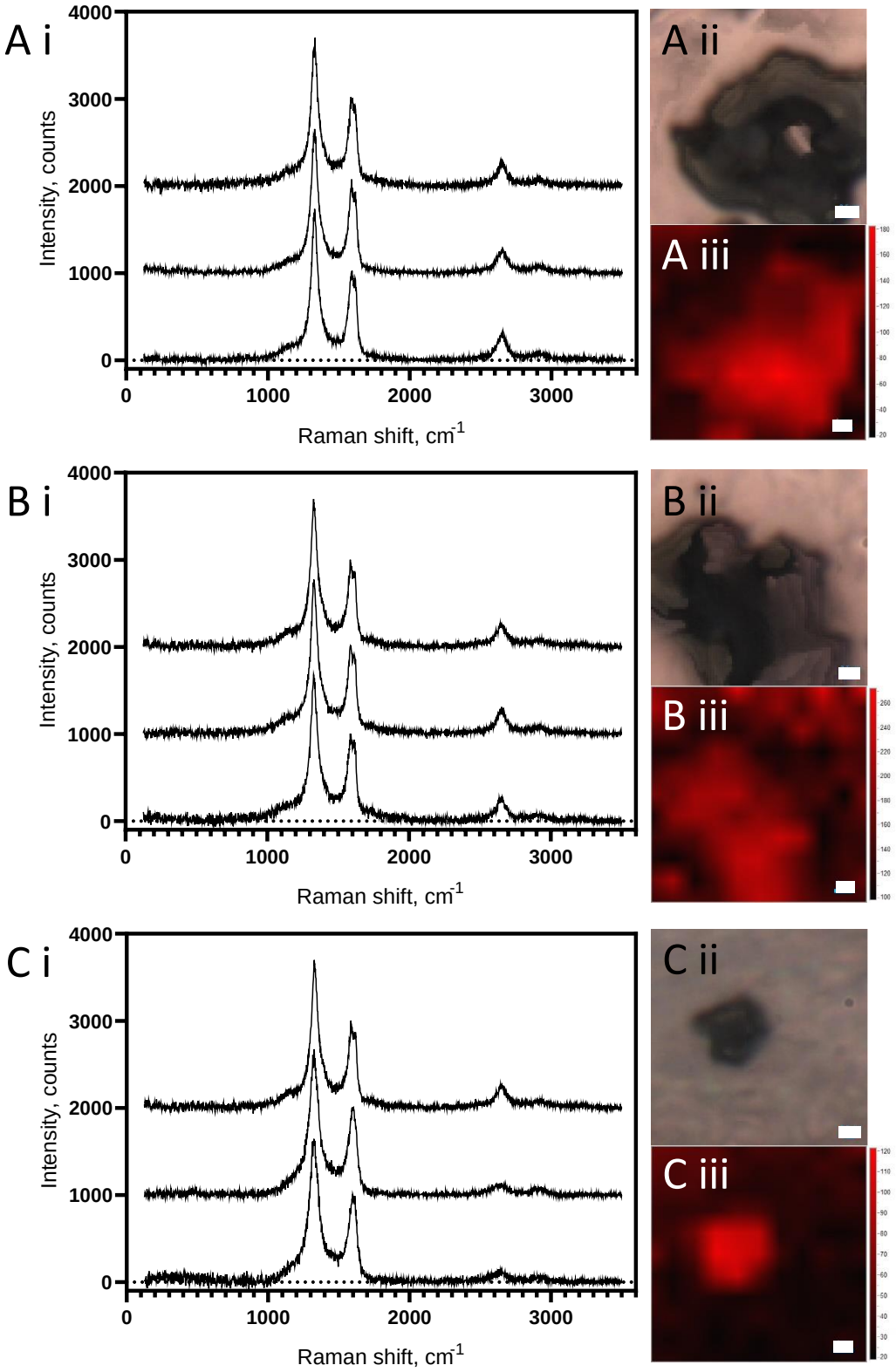

Figure 3.6: Raman spectra and mapping of carbon allotrope incorporated hydrogels. 15 nm MWCNTs (A), 30 nm MWCNTs (B), and mixed nanocarbon (C) hydrogels with Raman spectra (i) and alongside microscopy (ii) and mapping to the D band (iii). The spectra in (i) are collected from separate aggregates in each case and confirm the homogeneity of MWCNT inclusion within the aggregates. Spectra have been shifted on the y-axis for visual clarity. The Raman maps in (iii) confirm the aggregates seen in optical micrographs (ii) as MWCNTs. The intensity scaling corresponds to the intensity of the D band of the MWCNTs, in counts. Scale bars are 1 µm. Collected by Dr Graham Rance.

Attempts to obtain complementary data regarding the spectra of ECM only control hydrogels were tried. However, said spectra were dominated by scattering from water, similar to that seen in previous literature (Amaral et al., 2020) with additional weak photoluminescence. This is likely an inherent property of the hydrogels, given their ECM origins (Shipp et al., 2017), inhibiting any additional chemical information on the hydrogels themselves from being acquired.

3.3.5 Mechanical properties of carbon allotrope incorporated ECM hydrogels

3.3.5.1 Gelation

Due to the influence of a biomaterial's mechanical properties on cell populations, rheology was employed to establish the stiffness of the SIS-ECM hydrogels generated. Figure 3.7 presents the gelation profiles of 0.2% w/v carbon allotrope ECM hydrogels at varying concentrations of SIS-ECM: 4, 6, and 8 $mg.mL^{-1}$ (Figure 3.7A to C). ECM only hydrogels with 4 $mg.mL^{-1}$ of ECM had a gelation point, where G' ≥ G", of 3.7 ± 0.3 min (Figure 3.7A). The mixed nanocarbon ECM hydrogels deviated slightly from this, with a gelation point of 2.6 ± 1.6 min. Both variants of the MWCNT incorporated ECM hydrogels had a lower gelation point: 1.3 ± 0.4 and 1.7 ± 0.2 min respectively for the 15 nm and 30 nm MWCNTs. The ECM only hydrogels with 6 $mg.mL^{-1}$ showed a similar trend; the ECM only gels had their gelation point average at 3.0 ± 1.0 min with mixed nanocarbon deviating slightly again, at 3.6 ± 0.5 min (Figure 3.7B). Both MWCNT incorporated hydrogel gelation points remained lower, like the 4 $mg.mL^{-1}$ samples, with the gelation point for 15 and 30 nm MWCNTs at 1.4 ± 0.5 and 1.1 ± 0.0 min respectively. ECM only hydrogels with 8 $mg.mL^{-1}$ of ECM continued this trend (Figure 3.7C). The ECM only and mixed nanocarbon hydrogels had similar gelation points: 3.8 ± 1.9 and 4.7 ± 0.7 min, respectively. The two MWCNT samples cross-over much quicker, 2.0 ± 0.3 and 1.5 ± 0.5 min for the 15 and 30 nm MWCNT incorporated hydrogels,

respectively. The gelation profile shape across the concentrations remains consistent across the two higher ECM concentrations, besides the reduced ECM concentration reducing the maximum G' the hydrogels reach after 20 min. However, the addition of MWCNTs, regardless of outer diameter size, causes gelation to start much earlier. This jump in gelation acceleration seemingly impacts the strength of the post-gelation product, with MWCNT hydrogels always having a lower G' after 20 min.

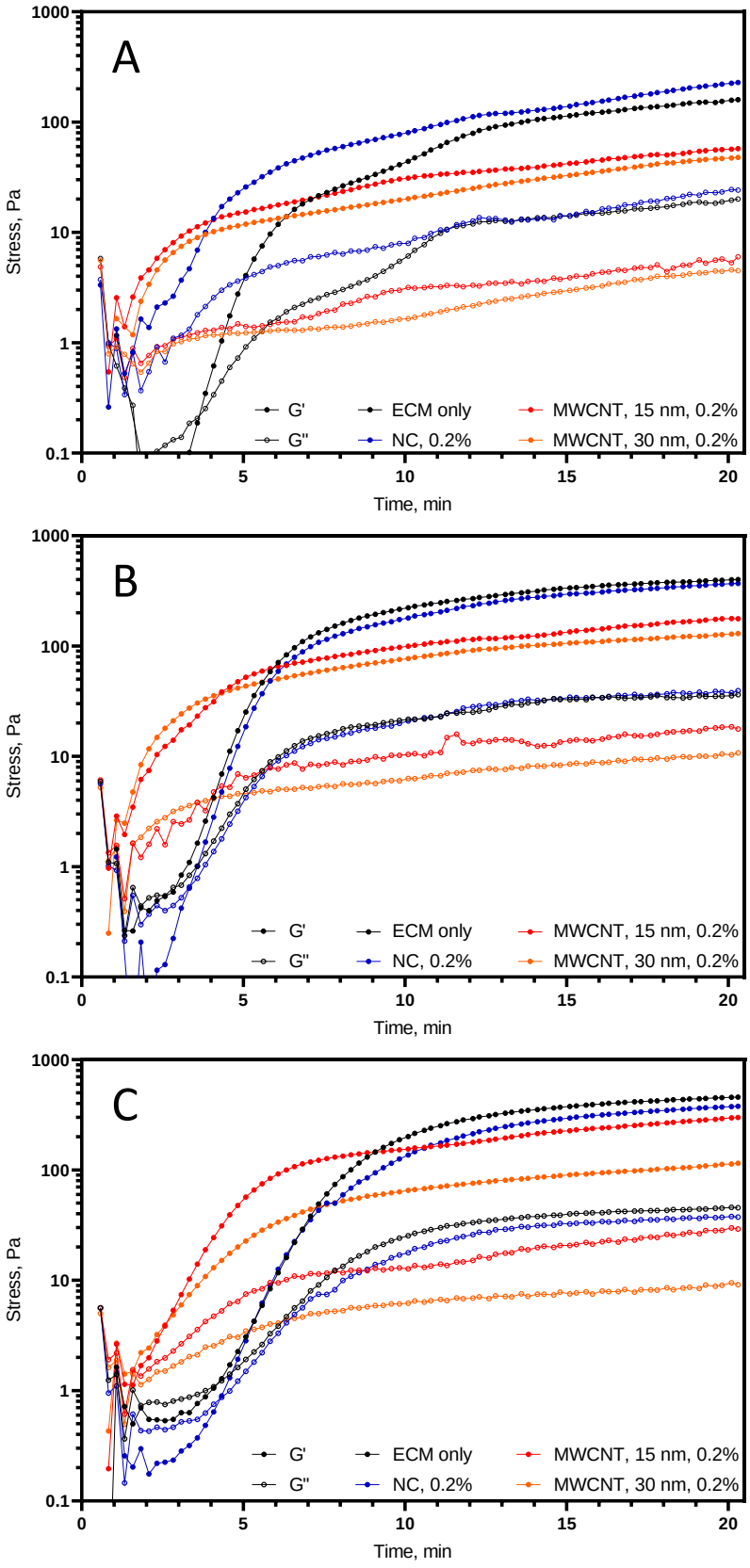

Figure 3.7: Typical gelation profiles of hydrogels containing 0.2% w/v allotropes of carbon. ECM concentrations differ between graphs, from 4 (A), 6 (B), and 8 (C) mg.mL^{-1}. n = 3 independent hydrogels.

Plotting the loss tangent of these data shows this behaviour a little more clearly (Figure 3.8). It shows that the control ECM only hydrogels, those without the incorporation of any carbon allotropes, reach the viscoelastic solid plateau much later compared to the hydrogels with 0.2% w/v MWCNTs. Mixed nanocarbon incorporated ECM hydrogels appear to show no effect on the gelation profile at this concentration, closely tracking the loss tangent of the ECM only hydrogels. Just as Figure 3.7 highlighted the difference in gelation point whilst comparing the MWCNT hydrogels with ECM only and mixed nanocarbon hydrogels, Figure 3.8 also exemplifies the much faster start to gelation. Yet, this doesn't necessarily cause an increase in gelation velocity.

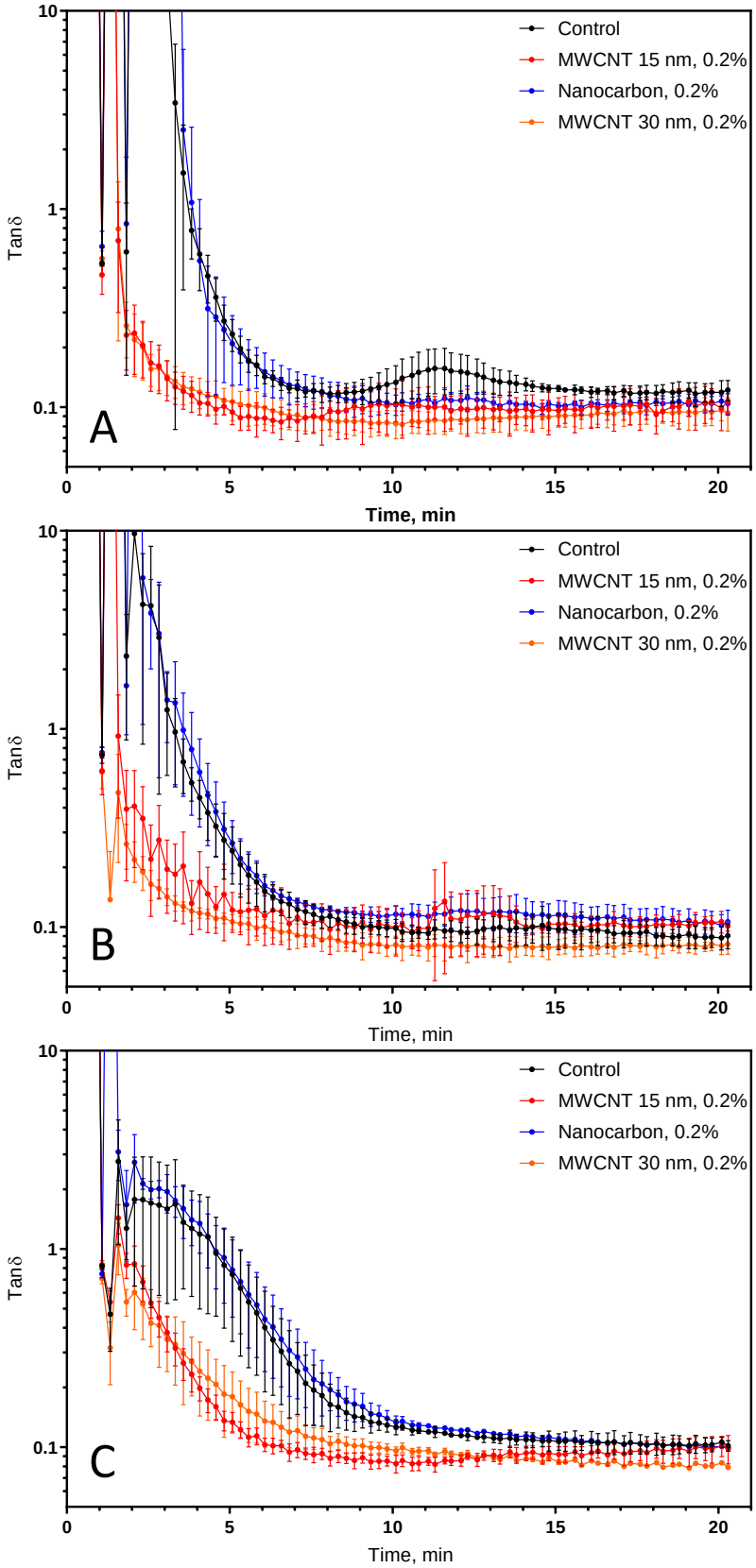

Figure 3.8: Loss tangent transformations of the gelation profiles of hydrogels containing 0.2% allotropes of carbon. ECM concentrations differ between graphs, from 4 (A), 6 (B), and 8 (C) mg.mL^{-1}. Error bars represent mean ± SD. n = 3 independent hydrogels.

Both Figures 3.7 and 8 lead to the assumption that the structure of the MWCNTs, and their interactions with the ECM, are causing this change in gelation. The lower time taken to reach the gelation point is hypothesised to be caused by the fibres within the ECM initiating self-assembly faster. However, the diameter of the MWCNT does not seem to make a difference in this regard. A hypothesis as to why this occurs is that the MWCNTs are better at conducting the heat from the rheometer and thus are more rapidly heating the hydrogel to 37 °C; thus, reaching the point at which thermo-responsive self-assembly occurs faster than hydrogels without MWCNTs. This is supported by the thermal properties of the MWCNTs, as they possess thermal conductivity values of over 22 $W.mK^{-1}$ (Park et al., 2012). This can be higher depending on the diameter, length, and level of functionalisation, but 22 $W.mK^{-1}$ is the lowest value found in the literature. This is over 30 times higher than the thermal conductivity values of both water and collagens, which are approximately 0.61 (Dinçer and Zamfirescu, 2016) and 0.53 $W.mK^{-1}$ (Bhattacharya and Mahajan, 2003) at physiological temperatures, respectively. Given such a large difference, MWCNTs could contribute significantly to getting the local environment up to temperature, allowing for the self-assembly of the collagen fibres to start sooner. The fact that the mixed nanocarbon hydrogels, which contain ~70% amorphous carbon, show no difference from the control would also fit this hypothesis. Studies show that the thermal conductivity of amorphous carbon to be between 0.7-2 $W.mK^{-1}$ (Bullen et al., 2000), meaning the difference would be negligible compared to the MWCNTs. The lack of difference in gelation velocity, but a difference in gelation acceleration, also supports this hypothesis. As once all hydrogels reach the desired temperature, the MWCNTs no longer possess an advantage in terms of fibre self-assembly and therefore the ECM only and mixed nanocarbon hydrogels match the gelation profile shape of the MWCNT incorporated hydrogels, albeit lagging.

The trends observed are confined to SIS-ECM hydrogels, with no literature on the MWCNT-ECM gelation interactions to compare. If the thermal conduction hypothesis stated is

correct, the same trend would be expected in other materials which undergo thermo-responsive gelation. Therefore, other animal-derived ECM hydrogels should display the same behaviours. Kim et al. (2015) described the gelation kinetics of SWCNT-collagen type I hydrogels, describing the incorporation of 0.25% w/w SWCNTs with 1.5 $mg.mL^{-1}$ collagen type I as slowing gelation compared to the collagen alone. With SWCNTs also having exceptional thermal conductivity (Yu et al., 2005), it would be expected that this hypothesis would apply to these hydrogels too. Since this trend is not seen in Kim et al. (2015), there could be a secondary influence in the ECM which, combined with the MWCNT thermal conduction, drives faster gelation. If this is the case, it is likely to be another ECM constituent which plays a role in promoting collagen fibrillogenesis, such as versican or chondroitin sulphate (Chen et al., 2020). However, it could simply be due to the collagen concentration used, since it has been shown that higher concentrations of collagen used in other studies lead to faster gelation (Shannon et al., 2015; Sackett et al., 2018). Other CNT-collagen studies fail to describe the gelation kinetics (Lee et al., 2014; Sun et al., 2017; Yu et al., 2017; Li et al., 2022) and thus additional research would be required to further challenge the hypothesis.

Figure 3.9 shows that the addition of MWCNTs at a 10-fold lower concentration elicits no such change in the gelation acceleration of the ECM hydrogels at 6 and 8 $mg.mL^{-1}$. Figure 3.9A depicts an ECM concentration of 4 $mg.mL^{-1}$ presenting a small deviation from this pattern, with the ECM only hydrogels having a decreased gelation acceleration compared to the allotrope incorporated hydrogels, as $G' \geq G''$ at 4.3 ± 0.5, 3.0 ± 1.7, 2.8 ± 0.3, and 3.1 ± 0.0 min respectively. At 6 $mg.mL^{-1}$, the gelation points for ECM only, mixed nanocarbon, 15 nm MWCNTs, and 30 nm MWCNTs are 4.1 ± 0.9, 4.0 ± 0.9, 3.4 ± 0.4, and 3.2 ± 0.5 min respectively (Figure 3.9B), with no obvious change in gelation acceleration in any samples. Likewise, at 8 $mg.mL^{-1}$, the gelation points are 2.2 ± 0.8, 3.6 ± 0.8, 2.6 ± 0.7, and 3.2 ± 1.4 min respectively (Figure 3.9C).

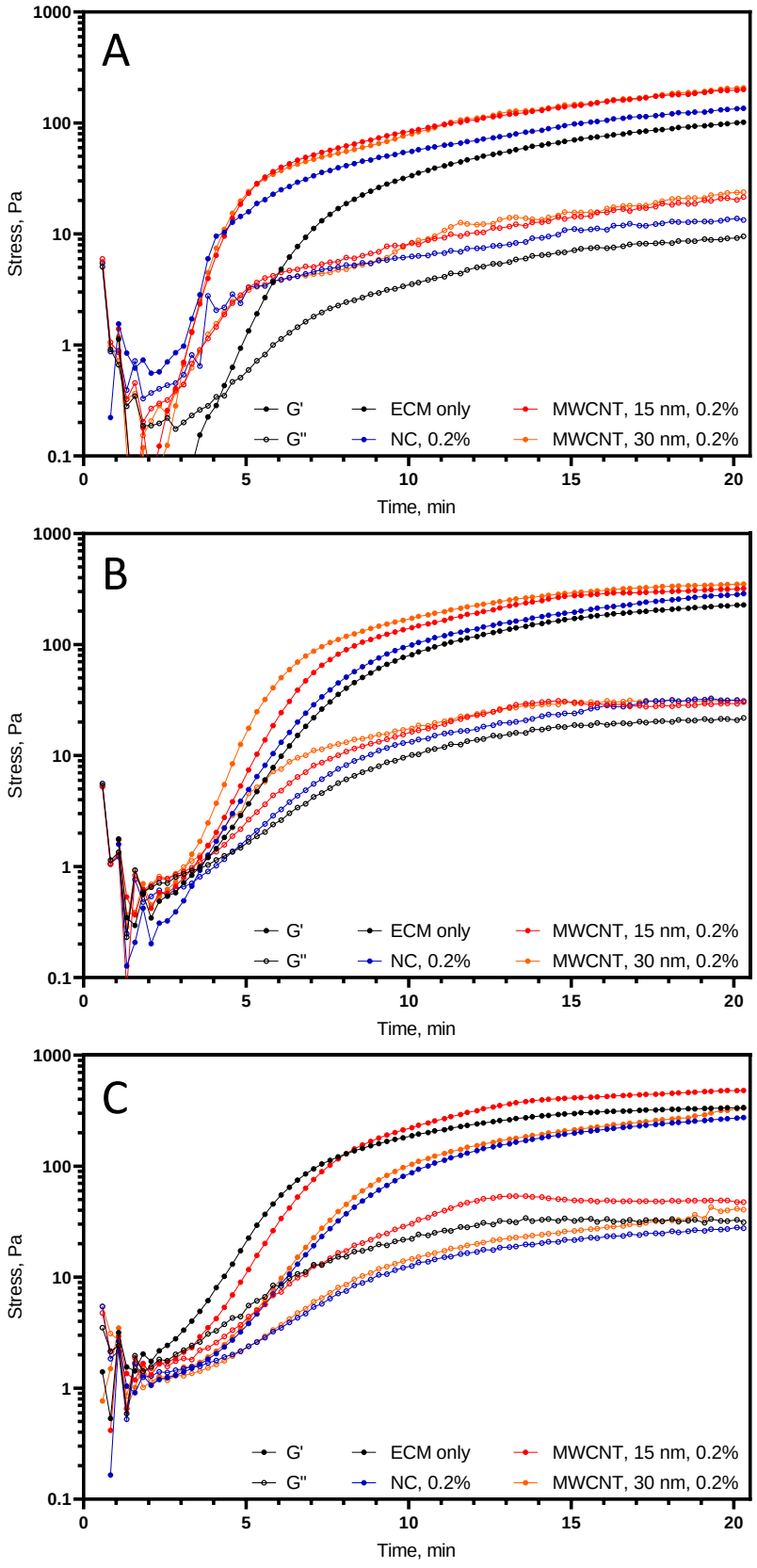

Figure 3.9: Typical gelation profiles of hydrogels containing 0.02% w/v allotropes of carbon. ECM concentrations differ between graphs, from 4 (A), 6 (B), and 8 (C) mg.mL^{-1}. n = 3 independent hydrogels.

These results are confirmed by the loss tangent data presented in Figure 3.10. If the structural and thermal conductivity hypotheses are correct, then there should be a difference between the control and the MWCNT incorporated hydrogels, of both diameters. The lack of difference in Figures 3.9 and 10 could be due to the concentration of MWCNTs being too low to impact gelation to a great enough level to influence gelation.

In Figures 3.8 and 10 there is a decrease in gelation velocity as the ECM concentration decreases, noted by the less steep descending gradient in the first few minutes of each gelation profile. This is similar across all hydrogels, even the ECM only controls. The faster gelation at lower concentrations of ECM has been noted in previous literature (Freytes et al., 2014, Giobbe et al., 2019). This seems counterintuitive in terms of factors which affect rates of reaction and goes against other literature which states that increases in collagen concentration led to faster gelation (Shannon et al., 2015; Sackett et al., 2018). Therefore, a form of competitive inhibition must be occurring, most likely due to a component of the ECM. Due to the evidence that collagen does follow direct proportionality regarding concentration and rate, yet ECM hydrogels do not, it is likely that the competitive inhibitor is a different ECM constituent such as aggrecan or small leucine rich proteoglycans (Chen et al., 2020).

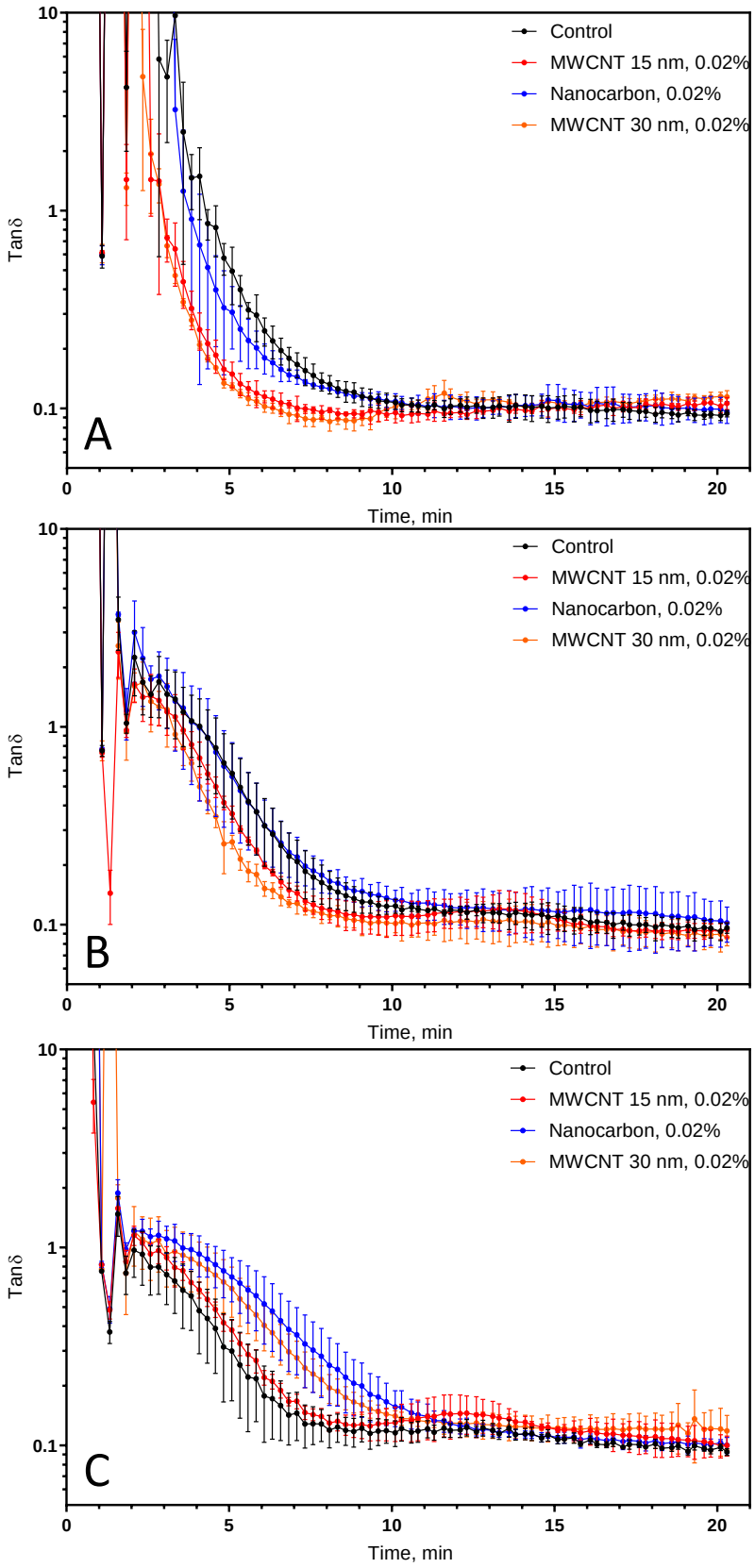

Figure 3.10: Tanδ transformations of the gelation profiles of hydrogels containing 0.02% allotropes of carbon. ECM concentrations differ between graphs, from 4 (A), 6 (B), and 8 (C) mg.mL^{-1}. Error bars represent mean ± SD. n = 3 independent hydrogels.

3.3.5.2 Linear viscoelastic region and strain stiffening

Post-gelation, the hydrogels were interrogated further to investigate their LVE region (Figure 3.11). The LVE region describes the strain which can be applied to the hydrogels without damaging the microstructures. This is important with regards to biomaterials as the viscoelastic properties can influence cell behaviour (Chaudhuri et al., 2020). The generation of a viscoelastic biomaterial is crucial in providing a basic solid-like structure for cells to reside, yet that is also fluid-like, pliable, and therefore dynamic so cells can interact and re-organise the environment (Corominas-Murtra and Petridou, 2021). In these data, the LVE region is found between 1% strain up until the linearity limit. In Figure 3.11A, 0.2% w/v MWCNT hydrogels had a much lower initial LVE storage moduli compared to the control, whereas the mixed nanocarbon samples had a higher storage modulus at the lower ECM concentration, 4 $mg.mL^{-1}$, dropping to match that of the control at the higher ECM concentration, 8 $mg.mL^{-1}$. 30 nm MWCNT incorporated ECM hydrogels had the lowest LVE storage modulus values within each ECM concentration at 0.2% w/v, these were lower than that of the 15 nm variety, except at the low ECM concentration. This is further evidence that the MWCNTs, and not the ~70% amorphous carbon samples, were interacting with the ECM fibres in a way which affects their material properties, as with the gelation data (Figures 3.7 to 10). Despite this trend at 0.2% w/v, no trend was observed at the lower concentration of 0.02% w/v seen in Figure 3.11B; further matching the gelation data seen in Figures 3.7 to 10. The explanation stated for this behaviour seen in the gelation data may also apply here too, in that the MWCNTs are at such a low concentration that they do not cause any discernible differences to the mechanical properties of the ECM hydrogel. Future studies with a larger range of MWCNT concentrations would be required to confirm this relationship.

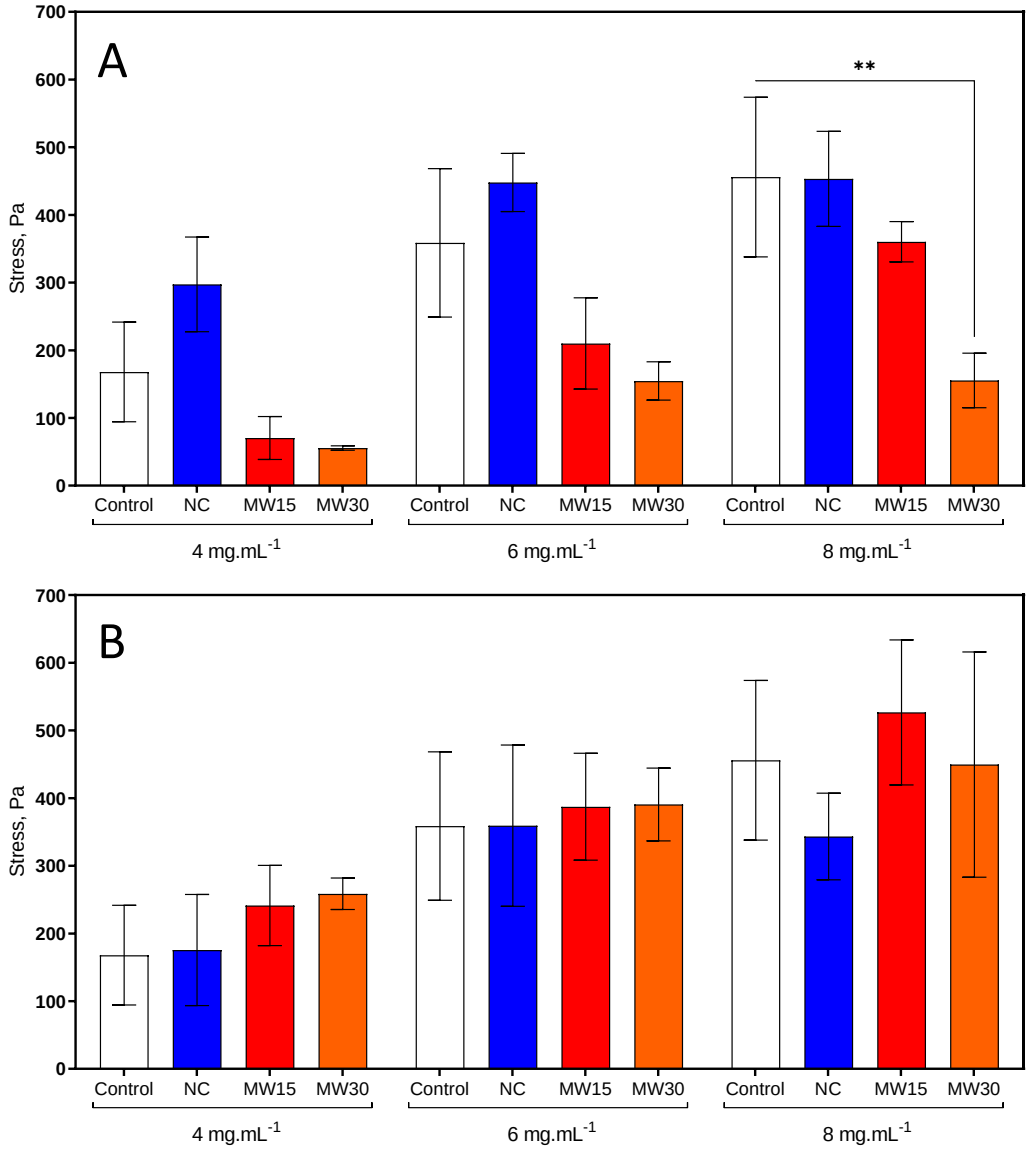

Figure 3.11: G' values at 1% strain of varying ECM and carbon allotrope concentrations. Data taken from the beginning of the LVE regions for each sample, with the carbon allotrope concentrations 0.2 w/v% (A) and 0.02 w/v% (B) and ECM concentration differences are explored. Error bars represent mean ± SD. Statistics obtained through a one-way ANOVA compared to the relevant ECM concentration control; n = 3 independent hydrogels.

Both the control and carbon allotrope incorporated samples show a concentration dependent increase in storage moduli, relative to the ECM concentration. Figure 3.11A shows that the addition of MWCNTs negatively impacts the storage modulus of the hydrogels compared to the control across all ECM concentrations. The fact the addition of MWCNTs causes a lower stiffness value indicates that the MWCNTs themselves are disrupting the ECM network, whereas the mixed nanocarbon does not. This could be due to

the shape of the MWCNTs compared to the mostly amorphous carbon containing mixed nanocarbon allotropes. The effect observed is MWCNT concentration dependent too, with the hydrogels containing 0.02% MWCNTs not displaying any similar decreases in stiffness relative to the ECM only control. This could be a result of the aggregations of carbon allotropes interrupting the organised collagen fibrillogenesis, with the lower concentration of MWCNTs leading to less disruption and therefore a lesser impact on stiffness. However, if this were the case, the expectation would be to see a decrease in stiffness compared to the ECM only hydrogels for the mixed nanocarbon incorporated hydrogels; given that their addition leads to aggregates too (Figure 3.5D). Also, Kim et al. (2015), studying SWCNT-collagen interactions, described SWCNT to be influential in the gelation process in a way that led to more uniform fibres which led to an increase in stiffness proportionally with SWCNT concentration. Future work utilising a wider range of both ECM and MWCNT concentrations would be useful in the investigation as to why MWCNTs at 0.2% are caused a decrease in stiffness.

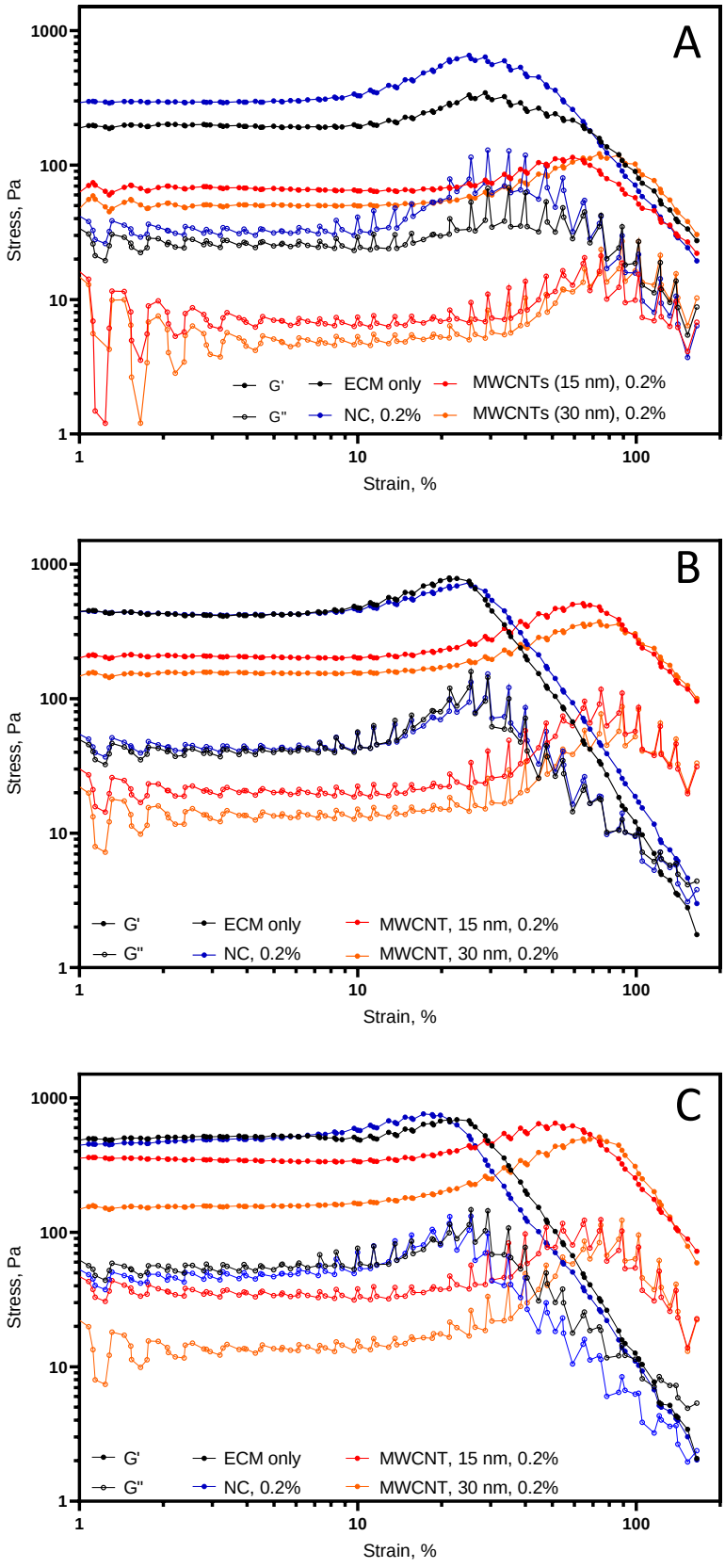

Figure 3.12: Typical amplitude sweeps of hydrogels containing 0.2% w/v allotropes of carbon. ECM concentrations differ between graphs, from 4 (A), 6 (B), and 8 (C) mg.mL^{-1}. n = 3 independent hydrogels.

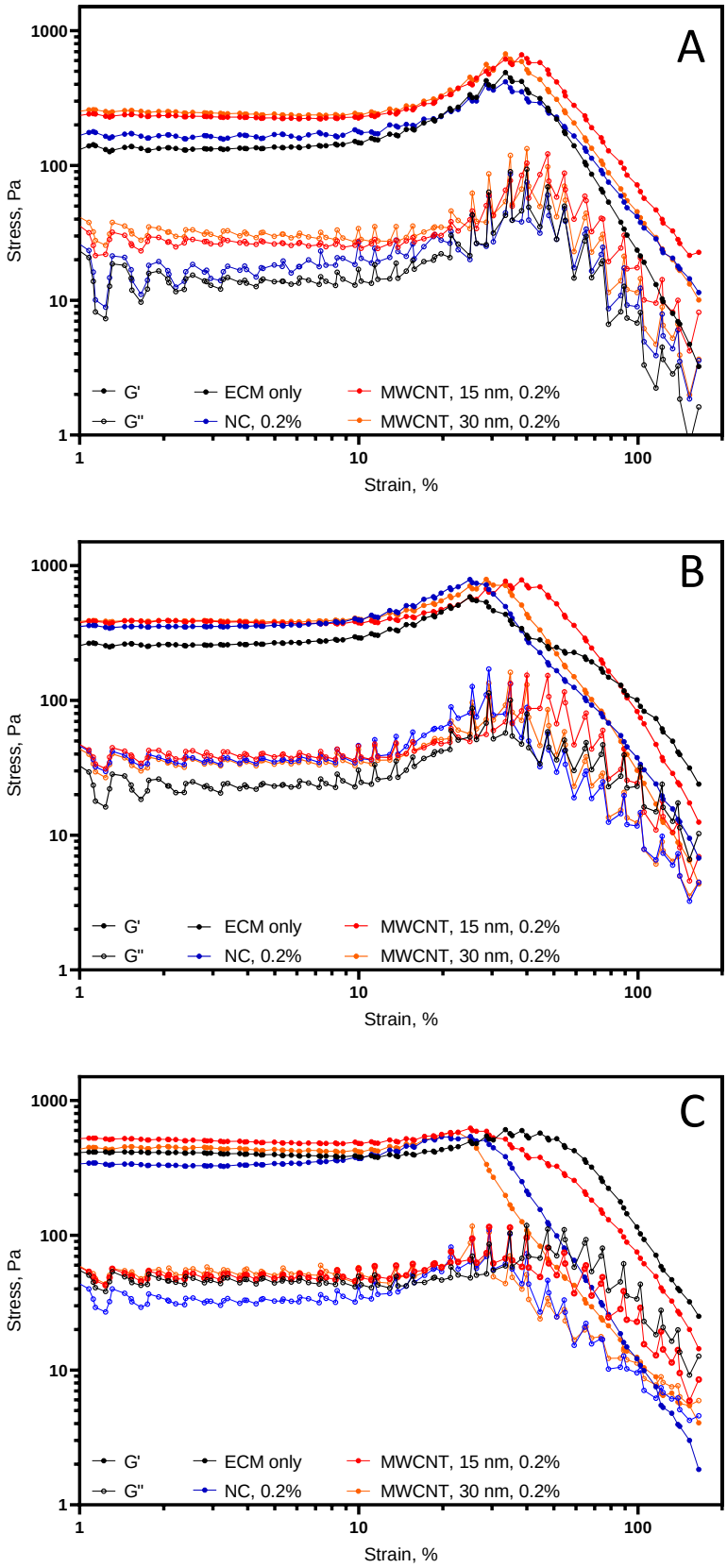

Figure 3.13: Typical amplitude sweeps of hydrogels containing 0.02% w/v allotropes of carbon. ECM concentrations differ between graphs, from 4 (A), 6 (B), and 8 (C) mg.mL^{-1}. n = 3 independent hydrogels.

The LVE region is visible at the linear portion of the trace, on the left-hand side (Figures 3.12 and 13). The LVE region is defined as the region between 1% strain up until the linearity limit, where the linearity limit is a ± 5% deviation from that horizontal trace. Linearity limit and strain stiffening data are tabulated for easier viewing (Table 3.1). Whilst the ECM only and mixed nanocarbon incorporated hydrogels are stiffer during their LVE region, the MWCNT, mainly the 15 nm, hydrogels tend to have a higher linearity limit at high concentrations of ECM at 0.2% w/v. A higher linearity limit suggests that the MWCNT hydrogels can support more strain and thus are more resilient to shear deformation. The higher linearity limits on MWCNT hydrogels could be an indication that the findings from Kim et al. (2015) could be applied here too, in that the MWCNTs were reinforcing the matrix structures and thus increasing their resilience. Though it remains unclear that this hypothesis is correct given the lack of visual organisation from the electron micrographs (Figure 3.5) alongside Kim et al. (2015) observing an increase in stiffness via SWCNT incorporation. In terms of a difference between the two types of MWCNT used, the diameter of the tubes in this data are 15 ± 5 nm and 30 ± 15 nm. Comparatively, the diameter of collagen (type I) molecules is ~1.6 nm (Chang and Buehler, 2014), while collagen fibrils average around 60-300 nm depending on source location (Barton and Marks, 1984; Ushiki, 1992; Chang and Buehler, 2014). Therefore, MWCNT outer diameter difference may indeed be crucial to obtain the optimum mechanical enhancing characteristics of collagen fibrils. On the other hand, collagen fibres range in size from 1-20 µm (Ushiki, 1992; Change and Buehler, 2014) and thus in the context of a fibre, the diameter of the CNT may not be a concerning factor. In terms of length, the MWCNTs used had lengths of 1-5 µm for the 15 nm diameter variety and 5-20 µm for the 30 nm, so are in the realm of collagen fibril length, which is on the scale of microns (Chang and Buehler, 2014).

Table 3.1: Tabulated ECM and carbon allotrope concentration dependant linearity limit and yield point data from Figures 3.12 and 13. Data was collected from the amplitude sweeps regarding the LVE. n = 3 independent hydrogels.

Nomenclature			Linearity limit, %		Strain stiffening, %	
Carbon allotrope, % w/v	ECM, $mg.mL^{-1}$	ID	Mean	S.D.	Mean	S.D.
0.2	4	Control	12.05	3.75	35.00	14.14
		MW15	11.95	11.03	56.47	4.56
		MW30	1.28	0.02	74.03	0.58
		NC	9.14	4.27	28.73	8.46
	6	Control	10.52	0.52	23.83	2.19
		MW15	13.17	6.20	65.73	7.39
		MW30	16.28	7.64	74.90	11.15
		NC	12.10	2.31	25.10	0.00
	8	Control	6.36	0.26	16.72	11.39
		MW15	14.45	6.71	51.63	7.26
		MW30	13.45	3.68	73.70	0.00
		NC	4.45	1.99	18.13	2.89
0.02	4	Control	6.67	1.61	33.97	0.81
		MW15	12.23	5.33	39.77	8.20
		MW30	11.45	5.89	40.00	0.00
		NC	6.82	4.31	35.73	7.89
	6	Control	12.59	10.10	37.53	18.68
		MW15	9.28	5.24	38.77	5.51
		MW30	12.70	1.08	30.23	2.83
		NC	9.06	2.46	25.10	0.00
	8	Control	10.27	5.72	44.13	15.21
		MW15	16.21	9.98	32.80	10.38
		MW30	6.76	2.39	23.03	1.92
		NC	10.01	2.05	24.53	4.48

If the MWCNT incorporation indeed impacts the self-assembly of the fibrils due to its size, then this will impact fibre formation further down the line. Therefore, only a specific size distribution of MWCNT may fit into the fibril formation in such a way that reinforces it. This may also be a key factor in the point made previously, that the MWCNTs direct the self-assembly of the ECM matrix during gelation. As the mixed nanocarbon samples contain ~30% MWCNTs with a diameter of ~5 nm, it is unclear whether it is a low concentration, the combination of MWCNTs with amorphous carbon, or the diameter of the MWCNT that is the cause of them not impacting the mechanical properties.

If the postulation that MWCNTs have a direct organisational effect on the collagen self-assembly as seen in Figure 3.11, this could also be a factor to consider when looking at the strain stiffening values (Table 3.1), as noted by strain % at which the highest G' values were reached at the peak of strain stiffening. Post-LVE region, there is a strain stiffening peak for all hydrogels (Figures 3.12 to 13; Table 3.1), expected given the collagen-heavy composition of ECM. Collagen hydrogels display strain stiffening, to varying degrees depending on the gelation conditions (Motte and Kaufman, 2013). The mechanism for collagen strain stiffening is described by Karunaratne et al. (2018). It involves the extension of fibrils due to an external strain leading to the straightening of previously disordered kinks within the fibril, followed by an elongation of the triple helices before the fibril eventually deforms. The straightening of the kinks can be associated with the incline from the LVE region, with the plateauing at the ultimate strength being attributed to the elongation of the triple helices. The MWCNT hydrogels have a significantly elongated strain stiffening region, defined by higher strain values, compared to the control and mixed nanocarbon hydrogels at 0.2% w/v. Future work could investigate this further by analysing the MWCNT-ECM interface at the nano-scale, both to analyse how the fibrous matrix interacts with the MWCNTs at rest and whilst under strain. This trend exists to a lesser extend in the 0.02% w/v carbon allotrope and 4 $mg.mL^{-1}$ ECM concentration. This suggests that the materials generated via MWCNT incorporation are more structurally stable, with added MWCNTs reinforcing the ECM matrix which enables them to have a better ability to withstand the oscillatory strain, as previously hypothesised. The drop in G' after the strain stiffening peak is due to the creation of microfractures within the material, as the fibrous proteins deform and their bond break, which means the elastic energy stored is lost and broken fragments begin to flow in and around the fracture points and thus are no longer a part of a solid matrix structure. These micro-deformations eventually grow and lead to plastic deformation, where G" > G'.

3.3.6 Electrical properties of carbon allotrope incorporated ECM hydrogels

To determine the success of generating a conducting biomaterial, the electrical properties of the hydrogels generated were analysed. Figures 3.14 and 15 describe the impedance spectra for 0.2 and 0.02% w/v carbon allotrope incorporated SIS-ECM hydrogels respectively. Figure 3.14*X*i demonstrate that the addition of MWCNTs causes a decrease in impedance, most significantly at lower frequencies; indicating the addition of allotropes of carbon enhanced the conductivity via capacitive behaviour due to their high surface area, regardless of ECM concentration.

The mixed nanocarbon samples exhibit similar decreases in impedance, except in the lowest ECM concentration (Figure 3.14Ai). This was as hypothesised, given that MWCNTs possess highly electrically conductive properties (Lau et al., 2008) and the contents of the mixed nanocarbon sample also contain conductive elements, including ~30% MWCNTs (Ogata and Shibutani, 2003; Lau et al., 2008; Zhao et al., 2020). However, at the 0.02% w/v concentration of carbon allotropes, these decreases in impedance are not present (Figure 3.15*X*i). This is a similar result to the rheological characterisation already discussed; a difference was observed in the 0.2% w/v carbon allotrope hydrogels while the 0.02% w/v concentration did not display the same behaviours. This is further evidence that the use of 0.02% w/v carbon allotropes concentrations was too low to elicit an influence over the ECM hydrogels.

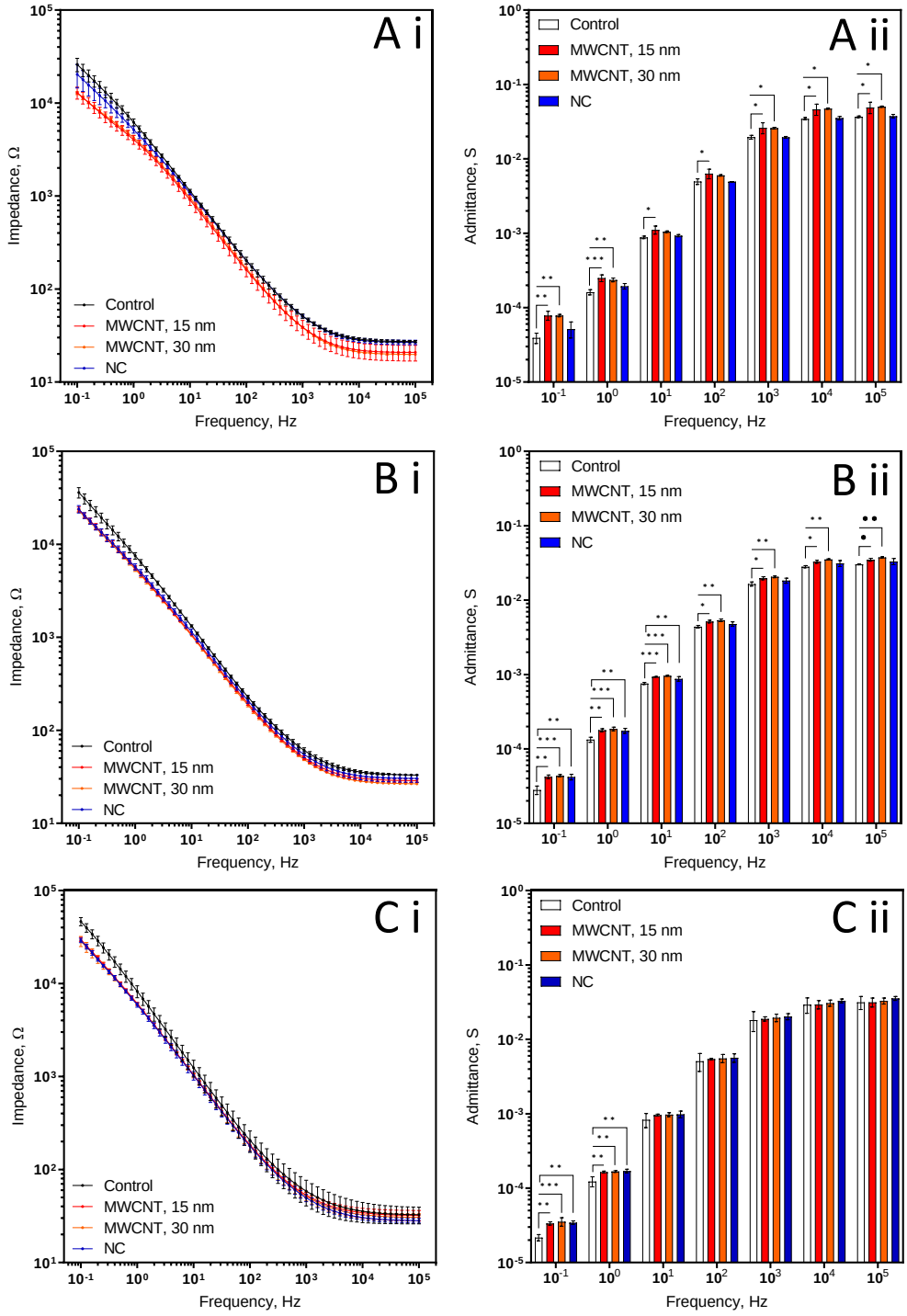

Figure 3.14: Impedance and corresponding admittance spectra of SIS-ECM hydrogels containing 0.2% allotropes of carbon. Impedance spectra (i) obtained from interrogating hydrogels using EIS and admittance data (ii) obtain from using the inverse of those impedance spectra. The ECM concentration range used was 4 (A), 6 (B), and 8 (C) mg.mL^{-1}. All statistical significance relates to comparisons between the carbon allotrope containing hydrogels and the control of that particular frequency. Bar graphs represent mean ± SD. n = 3 independent hydrogels.

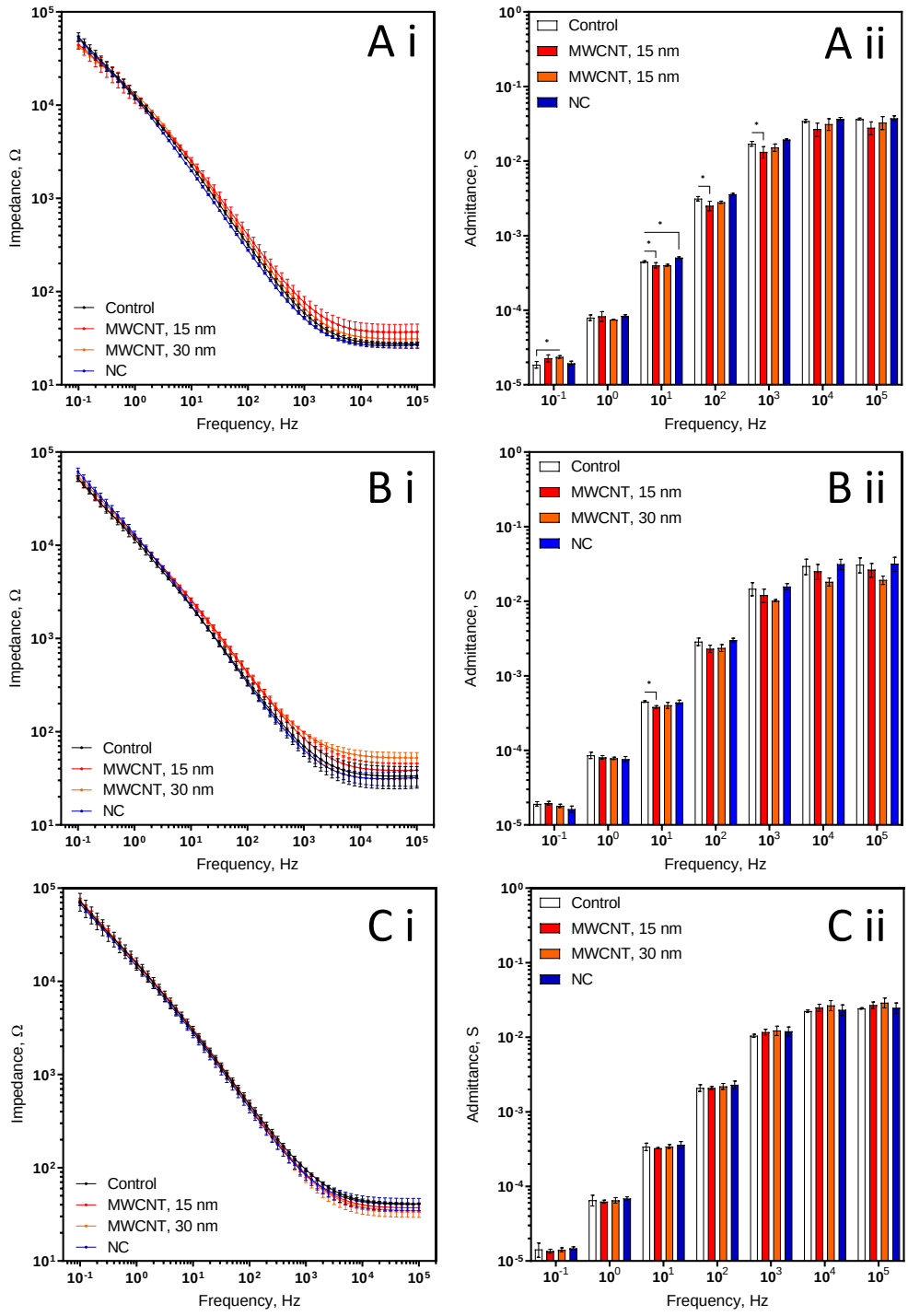

Figure 3.15: Impedance and corresponding admittance spectra of SIS-ECM hydrogels containing 0.02% allotropes of carbon. Impedance spectra (i) obtained from interrogating hydrogels using EIS and admittance data (ii) obtain from using the inverse of those impedance spectra. The ECM concentration range used was 4 (A), 6 (B), and 8 (C) mg.mL^{-1}. All statistical significance relates to comparisons between the carbon allotrope containing hydrogels and the control of that particular frequency. Bar graphs represent mean ± SD. n = 3 independent hydrogels.

Figures 3.14*X*ii and 3.15*X*ii present the admittance at specific frequencies calculated from the impedance data. As discussed, the incorporation of MWCNTs at 0.2% w/v produced significantly higher conductivity at the lower end, up to 10^0 Hz, of the frequency spectra in hydrogels with an ECM concentration of 8 mg.mL^{-1} (Figure 3.14Cii).

This lack of significant increase in admittance at the higher frequencies could be attributed to the capacitive properties of biological materials (Dean et al., 2008). As a lack of charge build up due to the oscillating current negates the high capacitance provided by the MWCNT incorporation. 4 and 6 mg.mL^{-1} hydrogels do exhibit significantly higher admittance values at frequencies beyond 10^0 Hz; this suggests that the capacitive effects of the ECM act in a concentration dependant manner and that 4 mg.mL^{-1}, and therefore 6 mg.mL^{-1} as well, do not hold the charge enough to mask the high capacitance of the MWCNTs. This is important for the experiments in Chapter 4 as the exogenous electrical stimuli applied is DC and thus there will be a build up of charge due to the lack of current alternation. This will influence ion gradients and therefore downstream electro-cellular processes such as voltage-gated ion channels.

The enhanced admittance provided by the mixed nanocarbon hydrogels follows the same trends as MWCNTs up to a point, 10^0 Hz in 8 mg.mL^{-1} hydrogels and 10^1 Hz in 6 mg.mL^{-1}, before falling back to being not significantly different to the control; likely a result of the overall conductivity of the mixed nanocarbon being lower than that of both MWCNT types. Interestingly, the 0.2% w/v mixed nanocarbon is not significantly different from the control at any frequency in 4 mg.mL^{-1} hydrogels (Figure 3.14Aii).

The incorporation of 0.02% w/v allotropes of carbon had no significant impact on the admittance of the 8 mg.mL^{-1} hydrogels (Figure 3.15Cii). The same applies to the hydrogels with an ECM concentration of 6 mg.mL^{-1}, except for a drop in admittance noted at 10^1 Hz ($P \leq 0.05$) (Figure 3.15Bii). At 4 mg.mL^{-1}, there are more significant ($P \leq 0.05$) differences

(Figure 3.15Aii). 15 nm MWCNTs significantly decrease the admittance relative to the control at 10^1, 10^2, and 10^3 Hz, 30 nm MWCNTs significantly increased the admittance relative to the control at 10^{-1} Hz, while the mixed nanocarbon increased the admittance relative to the control at 10^1 Hz. This extra significance at the lowest ECM concentrations links with the capacitive biomaterial rationale up to a point, but that doesn't explain the decreases in admittance caused by the 15 nm MWCNTs.

Such low concentrations of carbon allotropes, 0.02% w/v, may not impact conductivity due to not developing a percolating pathway. Coelho and Morales (2014) calculated that the percolation threshold, the critical node number, for the MWCNTs used in their report is 0.2% w/v. This corroborates with what is seen between Figures 3.14 and 15, however experimentally the percolation threshold will differ depending on varying CNT properties such as outer diameter, length, functionalisation, and protein adsorption, as well as the type of polymeric network used in the system (Watt and Gerhardt, 2020). To discuss the percolation threshold here, it would need to be calculated for this specific system; however, the two concentrations used offer a relatively clear estimate as to what the percolation threshold is. In the data presented, 0.2% w/v of MWCNTs possesses such a comparative decrease in impedance, and thus an increase in conductivity, that it could be suggested such a percolating pathway exists, enabling a less resistive route. Whereas 0.02% w/v MWCNTs is most likely below this critical number of nodes, meaning that the MWCNTs are too sparse for this to occur, leading to a lack of significant change in impedance between the ECM only hydrogels and the MWCNT incorporated hydrogels.

3.4 Conclusions

SIS-ECM was successfully decellularised, with GAGs retained, while 75% of the dsDNA was eradicated and much of the remaining nucleic acid present only as small, non-immunogenic fragments of < 200 bp. Three allotropes of carbon were incorporated into the ECM hydrogels generated which led to aggregations within the microstructure of the hydrogels. The aggregates are thought to have implications for the mechanical properties of the hydrogels. The thermal conductivity properties provided by the incorporation of the MWCNTs accelerated the start of the gelation process, but to the detriment of the stiffness within the LVE region. However, the MWCNT incorporation allows the hydrogels to undergo higher strains before plastic deformation. The suggestion as to why this occurs is that the MWCNTs are somehow reinforcing the collagen fibrils, and therefore collagen fibres, during the self-assembly process. The mixed nanocarbon incorporated hydrogels do not cause such changes in the mechanical properties, indicating that they are inert in terms of matrix interactions. The integration of the higher allotropic concentration enhanced the electrical properties of the ECM hydrogels as hypothesised. EIS revealed that 0.2% w/v carbon allotropes decreased the impedance of the hydrogels, especially at lower frequencies. The 0.02% w/v equivalent hydrogels presented no such decrease, this is hypothesised to be due to a lack of percolation network of MWCNTs within the ECM hydrogels.

Experiments in Chapter 4 will not proceed with mixed nanocarbon incorporated ECM hydrogels; this is because they offer no changes in mechanical properties and have weak electrical properties in comparison to MWCNTs. One of the two MWCNTs, 15 nm outer diameter, will proceed to cell interaction experiments. While both forms present slightly different properties, the literature suggests that the relatively small difference in diameter is unlikely to present significant differences in biocompatibility (Nagai et al., 2011).

The MWCNT incorporated SIS-ECM hydrogels have been characterised mechanically and electrically, showing that the products are soft and conducting, whilst retaining key bioactive properties. The next chapter utilises these biomaterials in immune cell culture to determine the collective impacts of mechanical, biochemical, and electrical stimuli on macrophage polarisation.

Chapter 4 | Cellular response to ECM coupled with DC stimulation

4.1 Introduction

Electrical stimuli have been shown to influence and drive various in vivo processes (Nuccitelli, 2003; Levin, 2014; Li et al., 2016; Chen et al., 2019); this includes the emergence of bioelectronic medicine as a promising approach in the promotion of wound healing (Section 1.3.3). The idea of electricity having some command of the wound healing complex has long been established (Du Bois-Reymond, 1848), with more recent research identifying both the origins of relevant electrical stimuli in vivo (Nuccitelli, 2003) and specific interactions within the wound healing process, such as migration and proliferation for example (Sections 1.3.3.1 and 1.3.3.2, respectively). The vast majority of bioelectronic wound healing research has been performed using traditional 2D culture methods. In Chapter 3 a CNT-ECM hydrogel biomaterial was characterised in terms of its biochemical, physical, and electrical properties. Introducing this multi-dimensional biomaterial to cell populations is postulated to promote a more in vivo-like behaviour given the representative environment. The use of biomaterials in cell culture has become an increasingly employed convention to modulate cellular behaviour, as discussed in Sections 1.4.3 and 3.1. To determine this material's impact with regards to wound healing, macrophages and fibroblasts were selected to be studied due to their persistent presence throughout each stage of the wound healing process. The influence electrical stimulation alone has on macrophage and fibroblast populations has been discussed previously in section 1.3.3. The combination of ECM biomaterials, with bioactive functionality, and exogenous electrical stimuli provides a novel platform to test cellular responses in a microenvironment that can be tailored to mimic parts of the wound healing complex.

In this chapter, the ECM only and 0.2% w/v 15 nm MWCNT-ECM hydrogels were studied in terms of their ability to modulate cellular behaviours. Combined with exogenous electrical stimuli, the hypothesis is that culturing electrically stimulated macrophages on an ECM hydrogel, propagated by CNT networks, will drive macrophage polarisation toward an M2-like phenotype. As stated in Section 1.7, the objectives for this chapter are as follows:

- Ascertain the biocompatibility of the MWCNT incorporated ECM hydrogels and exogenous electrical stimuli separately.
- Investigate the combined effect of MWCNT incorporated ECM hydrogels and exogenous electrical stimuli on macrophage polarity and fibroblast cytokine secretion.

4.2 Experimental design

As characterised in Chapter 3, 0.2% 15 nm outer diameter MWCNT incorporated SIS-ECM hydrogels were selected as the material to utilise for cellular experiments, alongside an SIS-ECM only control. Given that cell experiments were performed in 24-well plates, 250 µL hydrogels were generated across the whole well surface to ensure no TCP was accessible. Presented here is the reasoning behind experimental decisions made in this chapter.

4.2.1 Macrophages and fibroblasts

The wound healing process is a convoluted array of specific pathways implemented by a variety of cell types. It is understood that the major cell types involved in wound healing are platelets, neutrophils, macrophages, and fibroblasts (Yussof et al., 2012). Platelets have a role in haemostasis; impeding the loss of fluid and the creation of a temporary barrier to stop opportunistic pathogens (Periayah et al., 2017). While that is a vital part of the

process, platelet response does not span the wound healing process and therefore is not a focus in this chapter. Similarly, neutrophils function as part of the innate immune response (Wilgus et al., 2013). This presents as the release of inflammatory cytokines, ROS, MMPs, and antimicrobial proteins. However, in healthy wounds, they undergo apoptosis at the end of the inflammation phase and therefore do not appear further in this chapter.

Macrophages are present throughout the wound healing process. Understanding their behaviour and responses to stimuli is vital for wound healing research as many comorbidities and the resultant poor healing has been linked to lingering inflammatory macrophages halting wound healing progression (Zhao et al., 2016; Hesketh et al., 2017). Macrophages provide a range of activity including: the consumption and digestion of foreign bodies and cellular debris, and act as signalling factories that release cytokines to orchestrate other local cell behaviours (Krzyszczyk et al., 2018). Macrophages originate from monocytes which circulate in the vasculature. They are recruited from the blood into tissues following wound generation due to an increase in chemotactic cytokines (Shi and Pamer, 2011). Electrical stimuli have been shown to influence macrophages and their progenitors at this stage (Hoare et al., 2015), demonstrating the ability of these cells to detect, interact with, and act on electrical signals. Cytokines are also a driver of macrophage differentiation and polarisation. However, Li et al (2016) describe the pathway via which electrical stimuli play a role in macrophage polarisation, indicating it is not exclusively a result of cytokine interactions. K^+ channels were affected by the electrical stimulus and influenced macrophage polarisation; hyperpolarisation of said channels resulted in a more M1-like response, while blocking them led to the opposite M2-like phenotype. Electric fields were also shown to increase the influx of Ca^{2+}, leading to a promotion in phagocytic abilities of macrophages (Lévêque et al., 2018). The summary from this research, and others discussed in Section 1.3.3, is that electrical stimuli play a role

in a range of pathways and resultant behaviours present in macrophage biology. This led to the selection of macrophages as a focal point of study in this thesis.

Fibroblasts are also present throughout the wound healing process, with both excessive activity and dysfunction linked to delayed wound resolution and therefore potential chronic or complex wound development (Lerman et al., 2003; Hinz, 2016). Acting in response to a range of cues, fibroblasts are key mediators of the wound healing process, serving as signalling secreting and ECM modulating cells (Dick et al., 2022). Fibroblasts begin to impact the wound site by adhering to the fibrin plug through integrins and initiate the degradation by releasing MMPs, replacing the haemostasis temporary plug with ECM proteins (Laurens et al., 2006). This degradation is regulated by MMP inhibitors also released by fibroblasts (Soo et al., 2000). Initially, the majority of ECM proteins produced are collagen III due to the speed at which it can be synthesised. Subsequently, the collagen III is mostly remodelled into collagen I as it is mechanically stronger, despite requiring more time to synthesise (Witte and Barbul, 1997). Fibroblasts can undergo transdifferentiation to myofibroblasts, a phenotypic state in which cells are specialised to controlling the contraction of ECM fibres, leading to wound closure, due to the upregulation of α-smooth muscle actin (Bainbridge, 2013). Rouabhia et al. (2013) described that this transdifferentiation was enhanced through electrical stimuli, leading to enhanced contractility and therefore faster healing. Given the interactions with electrical stimuli and prevalence in wound healing, fibroblasts were selected a secondary cell type for the studies in this chapter.

4.2.1.1 Primary monocytes vs. THP-1 monocytes

The macrophage precursor, monocytes, circulates in the vasculature in vivo, ready to act when the body's first line of defence is breached. Once removed from the body via a buffy

coat preparation, these are the gold standard primary cells for macrophage research (Murray et al., 2014; Tedesco et al., 2018).

THP-1 cells are an immortalised monocyte cell line harvested from the blood of a one-year-old acute monocytic leukaemia patient (Tsuchiya et al., 1980). Due to the large proportion of monocytic cells, they are able to be differentiated into macrophage-like populations and polarised toward both the M1- and M2-like phenotypes. THP-1 cells have been used heavily in the literature to represent monocytes and macrophages (Bosshart and Heinzelmann, 2016). Utilisation of the THP-1 cell line has some distinct advantages (Chanput et al., 2014); for example, due to all populations being derived from the same lineage the data obtained is much more easily replicable due to the lack of donor-to-donor variability seen in peripheral blood primary monocytes. The speed at which cell numbers can be accumulated for large-scale experiments is much faster, cells can be cultured for much longer, and cells can even be frozen in liquid nitrogen for multiple years without impacting the phenotypic features or cell survival. THP-1 cells are inherently safer for laboratory staff too, as no evidence has been shown for populations to host infectious pathogens which is not always the case with the primary equivalent.

But the use of THP-1 cells for data regarding monocyte and macrophage research should ideally be preliminary and be further validated by studies with peripheral blood primary monocytes due to the following disadvantages towards THP-1. THP-1 and primary monocytes have been found to vary significantly, approximately 20%, at the chromosomal level (Liu et al., 2021). These genetic differences, due to the isolation and immortalisation, are likely to drive differences between the two cell types downstream in their structure and function. For example, chromosomal alterations can impact gene expression and thus protein expression which may be the root cause of THP-1 cells possessing a much more muted response to chemical stimuli, specifically LPS (Bosshart and Heinzelmann, 2016),

compared to the primary equivalent. While THP-1s are a more stable cell line than primary monocytes in terms of variability, there have been studies to show that significant genetic drift has occurred between isolation and investigations across two different biorepositories, linked to the instability of tumour cell lines (Noronha et al., 2020). Alongside genetic changes caused by time in culture leading up to senescence, this can lead to some large discrepancies in data that can go unrecognised.

The macrophage-based work presented in this chapter is performed solely using THP-1 derived macrophages. This was chosen for the reasons presented above with any future work targeting reproduction of said data using peripheral blood primary monocytes.

4.2.2 Cellular readouts

ECM hydrogels (Saldin et al., 2017) and electrical stimuli (Section 1.3.3) have been shown to be biocompatible with a range of cell types. However, cell viability and metabolism analyses were performed throughout to ensure both the strength of the electrical stimuli used and the addition of MWCNTs did not negatively impact cell health. Cell viability is a commonly used measure of determining the health of a cell population in response to extracellular change due to a form of stimulation. Two forms of viability analysis were selected. LIVE/DEAD staining was used to obtain qualitative fluorescent microscopy data; determining the degree of cell lysis via ethidium homodimer-1 binding to DNA, whilst simultaneously indicating live cells through metabolism of calcein AM through intracellular esterase activity. The detection of adenylate kinase was also utilised as a quantitative measure of the degree of cell lysis. Cell metabolism refers to the large complex of reactions required for a living cell to remain alive. It is linked with, but not analogous to, viability. Viability is a binary measure of a cell being alive or not, whereas metabolism is a dynamic measure reflecting biosynthesis and catabolism. To determine cell metabolism, a resazurin-

based assay was selected when viability measures weren't appropriate. The resazurin gets reduced to resorufin in live cells, resulting in a fluorescent signal.

There is a growing body of research indicating that electrical stimuli are involved in many cellular behaviours, such as migration, proliferation, and others discussed in Section 1.3.3. Given this prior research, these were not included in this thesis as the resulting outcome has been reported elsewhere. However, macrophage polarity has not been investigated to the same extent. As discussed in 1.3.3.5, macrophage polarity is known to be influenced by ion channels and thus influenceable through electrical stimuli (Catterall, 2011; Li et al., 2016; Kong et al., 2021). Therefore, investigations into the polarisation surface and secreted markers were selected to track discrepancy in phenotypic shifts over the culture period whilst exposed to both the biomaterial and post-stimulation. Immunocytochemistry was used as a qualitative analysis method to determine macrophage polarisation: investigating the degree of heterogeneity of a population in terms of surface marker expression and morphology of individual cells, as well as the distribution of the population. Calprotectin has previously been used as an M1 surface marker (Bartneck et al., 2010; Rostam et al., 2017). Mannose receptor, CD206, is expressed in high amounts in the M2 phenotype (Gordan and Martinez, 2010). ELISA-based immunoassays were used as a quantitative analysis to detect inflammatory and immunomodulatory-related cytokine secretion in both macrophage and fibroblast supernatant. IL-6 and TNF-α are well established markers for M1 polarisation (Idriss and Naismith, 2000; Johnson et al., 2020), likewise with IL-10 and CCL18 for the M2-like populations (Schraufstatter et al., 2012; King et al., 2014). ELISA was initially used to quantify these concentrations over a period of 3- and 6-days post differentiation, to monitor secretion throughout culture. However, it was noted that most cytokine expression was insignificant at the 3-day mark and therefore subsequent experiments just analysed the 6-day supernatants. Regarding the fibroblast cytokine secretion analysis, IL-6 and MCP-1 were selected to investigate inflammatory

fibroblast responses (Deshmane et al., 2009; Johnson et al., 2020), while bFGF, often referred to as FGF-2, and HGF selected for the anti-inflammatory counterpart (Kobayashi et al., 2015; Miyagi et al., 2018). These analyses were performed after 4-days post-seeding.

4.2.3 Culture dimensions

3D cell culture is more representative of the in vivo environment compared to conventional 2D culture, as discussed in Section 1.2. This is due to the cells being able to interact in all directions with the substrate and other cell populations, mimicking the in vivo environment more closely. Pairing this with an in vivo-like material such as ECM proteins leads to cell morphology all but matches that of the in vivo cell shape (Ravi et al., 2014). Data collection from cell populations in 3D culture, however, is more challenging. From sample preparation pre-imaging being a much more complex affair, such as requiring a sectioning protocol which doesn't allow for dynamic analysis; to protein and nucleic acid retrieval requiring different techniques, such as Trizol™, as well as retrieving the cells themselves (Khetan and Burdick, 2010). 3D culture, due to the increased complexity of the system, is difficult to reproduce (Hickman et al., 2014). Combining these factors with the incorporation of CNTs into the work presented here, it was decided that 3D would not be a factor of this work presently, as 2.5D could be utilised to generate some results which can then determine conditions to pursuit in future work. It is important to note that 2.5D culture is still a marked improvement on conventional 2D culture, whilst also bringing challenges not noted for 2D culture.

4.2.4 Electrical stimuli

4.2.4.1 Current type

Continuous DC stimulation was chosen as the form of electrical stimulation for the work presented in this chapter. This is the form of endogenous stimulation exerted during the transepithelial potential (Figure 1.7), the suspected source of electrical stimuli caused by wound generation and present throughout the wound healing process, and therefore the most appropriate to simulate the effects on macrophage polarisation for these experiments.

4.2.4.2 Electrical stimuli strength

Given that previous studies have shown a range of electrical stimuli applied to cell populations, a range was used in some initial experimentation to determine the cellular tolerance range (Table 4.1). The array of stimulation strength applied ranged from 0.6 to 4.8 V. Due to the distance between the electrodes, 12 mm, this corresponds to an equivalent field strength range of 50 to 400 $mV.mm^{-1}$, calculated for comparison to studies using a variety of experimental set-ups. This is a large range that encompasses the normal in vivo wound healing strengths of < 200 $mV.mm^{-1}$ (Dubé et al., 2010) and above to determine cellular tolerance.

Table 4.1: Relationship between stimuli strength applied across the well and the resultant field strength. Voltages were applied using stainless steel electrodes placed 12 mm apart for 10 min.

Stimuli strength, V	Applied field, $mV.mm^{-1}$
0.6	50
0.9	75
1.2	100
1.5	125
1.8	150
2.1	175
2.4	200
2.7	225
3.0	250
3.3	275
3.6	300
3.9	325
4.2	350
4.5	375
4.8	400

4.2.4.3 Current vs. field effects

As discussed in Section 1.3.1, electricity can be split into electric currents and electric fields. Within the body, both are associated with various aspects of biology across all organ systems. For in vivo wound healing, specifically the transepithelial potential, ionic currents and electric fields are the key endogenous forms identified. Current effects are characterised by current flowing in solution, whereas field effects are a force exerting field that surround electrically charged particles. Electric fields are known to influence biology, tumour treating fields (Kirson et al., 2007) and electroporation (Gehl, 2003) are examples of this.

Two techniques are employed to apply electrical stimuli, depending on the output of current or field effects. To obtain a flow of current, bare electrodes contact culture media and a voltage is applied; thus, allowing electrochemical reactions at the electrode-media interface which drives current through the solution, providing a stimulus to local cell populations. To select for field effects, insulated electrodes are used to deny current flow. Dielectric inks possess insulative properties due to a lack of free electrons, meaning that

current is blocked when a dielectric material is utilised in a circuit. While the current is blocked, electric fields are not. The dielectric materials are instead polarised, producing their own electric field which repels the original field yet propagates the new one throughout the remainder of the circuit, albeit at a lower strength dependant on the dielectric constant of the material. Dielectric ink was used to coat the electrodes used for the final cytokine expression experiments. Combined with the uncoated electrodes, it enabled a comparison between current and field effects, discussed in section 1.3.1. In current only experimenting, the electric field exists but decays exponentially due to the generation of the double layer capacitance at the electrode surface. When this current flow is blocked in field only experimenting, this double layer cannot form and thus the electric field can penetrate further and be sensed by cells in culture (Shchukin et al., 2001).

4.3 Results and discussion

4.3.1 Hydrogel biocompatibility

Given that a range of ECM concentrations were tested in Chapter 3, their effect on cell metabolism was analysed to determine which concentration to proceed with in subsequent experiments. Figure 4.1 shows that each concentration of hydrogel produces a more metabolically active M0-like macrophage, compared to the TCP control. The increase in metabolism in 3D cultures vs. 2D cultures has been shown previously in with cells cultured in a silica scaffold and in a spheroid form (Ikari et al., 2021; Tidwell et al., 2022). It is speculated that the increase in resazurin metabolism shown in Figure 4.1, even though it is 2.5D culture, is in alignment with those studies in that cell-substrate interactions and a lack of oxidative stress due to stiff materials are the cause of enhanced metabolism. This is an indicator of a comparatively heathier cell, postulated to be due to the more closely representation of the in vivo environment. Given that there is little distinction between the

hydrogel concentrations in terms of metabolism, it was decided that the ECM concentration of 4 mg.mL^{-1} would be utilised. This conclusion was drawn as 4 mg.mL^{-1} ECM hydrogels led to a less stiff hydrogel across the ECM only and MWCNT variety compared to the other ECM concentrations (Figure 3.11), with softer substrates having been noted as being more biocompatible (Cavo et al., 2016). Alongside this, utilisation of a lower concentration of ECM enabled the generation of Chapter 4's data to be performed on the same batch of SIS characterised in Chapter 3. This eliminated organ variability from the equation when discussing the biological responses in terms of the characterised properties previously analysed.

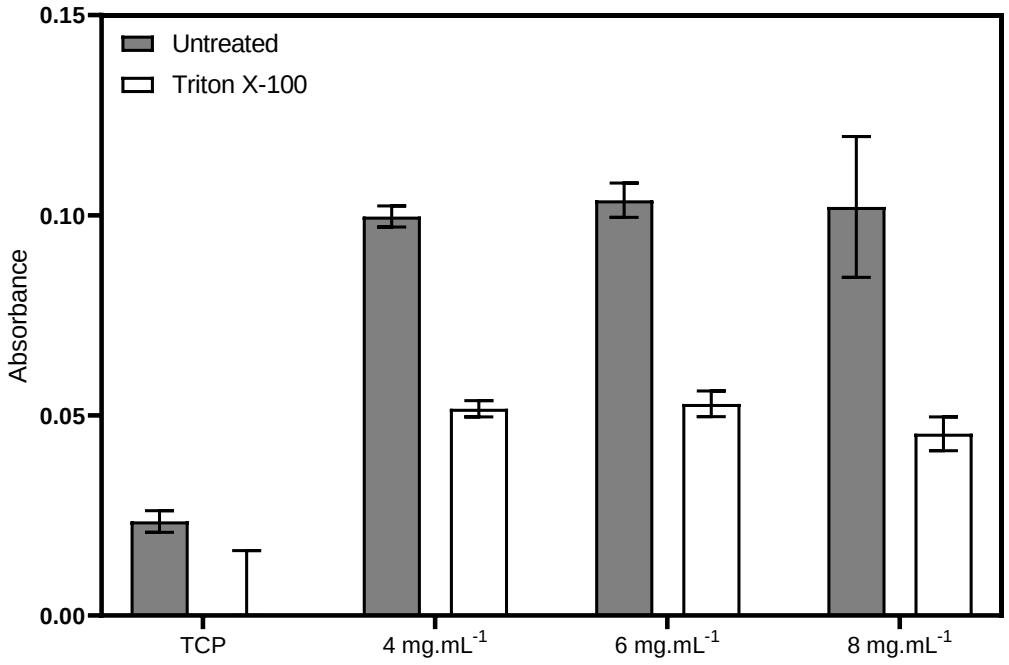

Figure 4.1: Metabolism of THP-1 derived M0-like macrophages (ATCC® TIB-202™) after 24 h post-differentiation growth on TCP vs. SIS-ECM hydrogels of varying concentrations. Metabolism of pre-polarised THP-1 derived macrophages grown on TCP and SIS-ECM hydrogels consisting of 4, 6, and 8 mg.mL^{-1} (w/v) of dry ECM. Bar graphs represent mean ± SD. n = 3, with each well tested in triplicate.

An increased metabolism was observed for cells cultured on ECM hydrogels which were also treated with triton X-100. Triton X-100 was used as a positive control as it acts to lyse cells. In doing so, it disrupts cell membrane integrity and thus renders them unviable with little to no metabolic activity present. Yet cells cultured on the SIS-ECM hydrogel samples seemingly exhibit a relatively high metabolism even when treated with Triton X-100. The elevated metabolism in these wells cannot be attributed to non-specific interactions with the ECM hydrogels themselves as cell-free hydrogel blanks were subtracted from the absorbance reading of the cell-laden samples. It could be postulated that this relatively high degree of metabolism in lysed, triton X-100 treated cells is due to a protective effect from the hydrogels; a portion of the macrophages cultured will have penetrated deeper into the matrix more than others, therefore some will be exposed more readily to attack from the triton X-100 while others will be unreachable. However, given that surfactants such as triton X-100 are used in the decellularisation of native tissues (Loneker et al., 2016), it can be assumed that they can penetrate ECM hydrogels and thus invalidates that hypothesis.

An optimised CNT-ECM hydrogel was brought forward from the characterisation described in Chapter 3. This consisted of MWCNTs of an outer diameter of 15 ± 5 nm and a length of 1-5 μm, these were at a 0.2% w/v concentration within the SIS-ECM hydrogels. Biocompatibility of said biomaterials was first analysed via a metabolism assay. The metabolism of M0-like macrophages was analysed whilst cultured on the three main substrates used in this chapter: TCP, ECM only, and CNT-ECM hydrogels (Figure 4.2). Like metabolism in relation to hydrogel concentration, the addition of 0.2% w/v multi-walled CNTs did not significantly change the metabolism of cells cultured in 2.5D upon them, yet the amount of metabolism remained higher than those cultured on TCP.

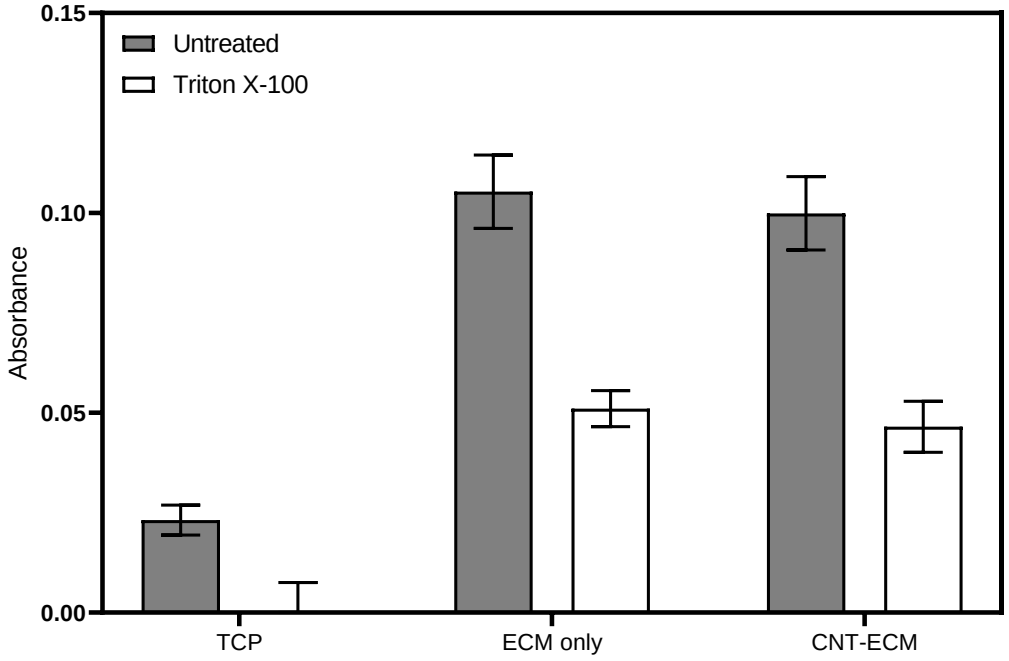

Figure 4.2: Metabolism of THP-1 derived M0-like macrophages (ATCC® TIB-202™) after 24 h post-differentiation growth on three substrates. Metabolism of pre-polarised THP-1 derived macrophages grown on TCP, ECM only, and CNT-ECM hydrogels. The ECM concentration for both the ECM only and CNT-ECM hydrogels was 4 $mg.mL^{-1}$ (w/v) and the CNT concentration was 0.2% (w/v). Bar graphs represent mean ± SD. n = 3, with each well tested in triplicate.

The biological evaluation of medical devices (ISO 10993-05) was used as a guide to further determine the biocompatibility, in terms of cytotoxicity, of the ECM and 0.2% w/v CNT-ECM hydrogels (Figure 4.3). Both extract and direct contact tests were performed. Live (Figure 4.3A) and triton X-100 (Figure 4.3B) controls, grown in 2D on TCP, provide the benchmark of which to compare the 2.5D ECM-only and 0.2% w/v CNT-ECM hydrogels with (Figure 4.3C to D). Extract testing showed that neither hydrogel had any impact on cell viability with respect to LIVE/DEAD staining (Figure 3Ci to ii). This is reflected in the quantification of cytotoxicity, where extract testing with both types of hydrogel lead to an enhanced viability (Figure 4.3Ciii). The lack of decreased viability via extract testing indicates that there are no cytotoxic products that leach out from the ECM-only and 0.2% w/v CNT-ECM hydrogels over a 24 h period, in fact the enhanced viability suggests that hydrogels provide cell supporting bioactive molecules via leaching into the local

environment. With various bioactive molecules from ECM products (Voytik-Harbin et al., 1998; McDevitt et al., 2003) having been shown to modulate cell behaviour (Saldin et al., 2017), it is likely that these are continually released over time into their surrounding environment. It can be alluded to that this is the cause of the enhanced viability, because of fibroblast proliferation, without the cells having direct ECM contact.

With regards to the CNT-ECM hydrogels (Figure 4.3Dii-iii), it can be speculated that the CNTs themselves are unable to leach any potential cytotoxic products, given the lack of increase in cell death. CNTs are often shown to release heavy metals (Bennett et al., 2013), remnants of the CNT manufacture process, however no ill-effects are observed in the data presented in this study. This could be a result of two ideas. The first being that the CNT leachate is somehow blocked, intercepted, or adsorbed by the ECM fibres encasing the CNTs themselves (Kim et al., 2015); thus not able to influence cell fate. The second idea is that these contaminants are indeed present, but at a non-toxic concentration and thus no effects are noted at this concentration of CNTs. Of course, both of these could be in play simultaneously, however without any negative impact noted it was not investigated further in this thesis.

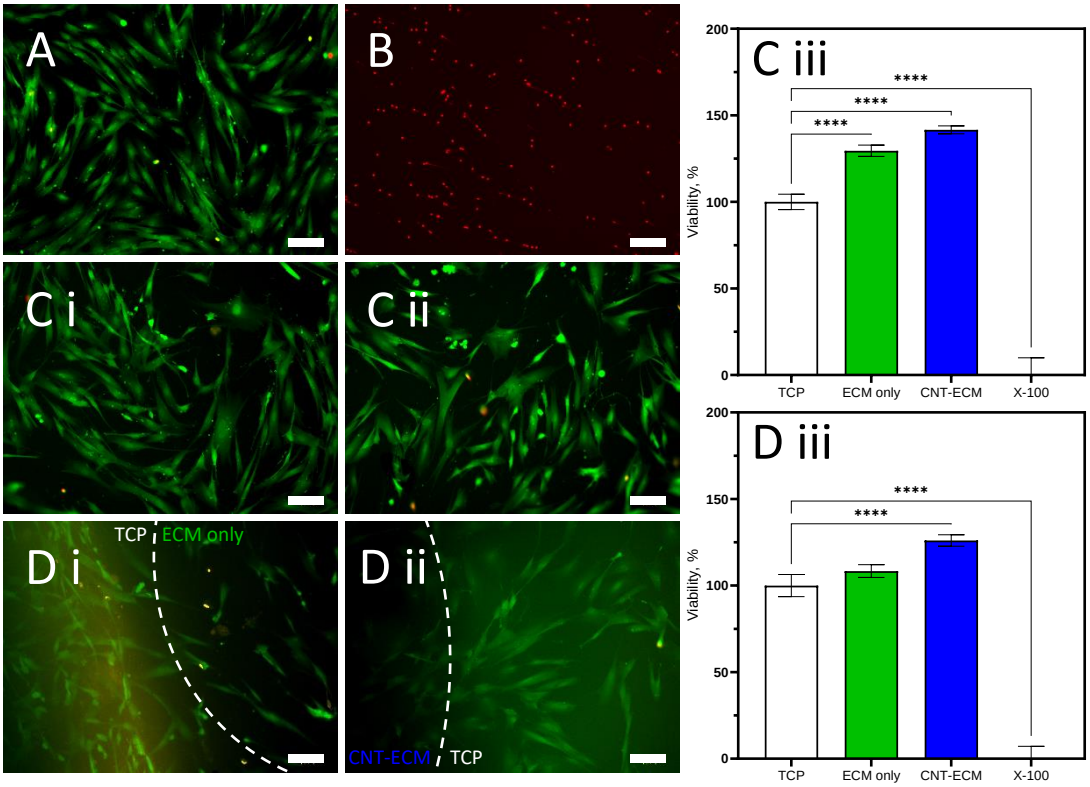

Figure 4.3: Fluorescent microscopy and quantitative analysis of hydrogel cytotoxicity on BJ fibroblasts (ATCC® CRL-2522™). Cytotoxicity investigations followed international standard biological evaluation of medical devices, part 5: tests for *in vitro* cytotoxicity (ISO 19903-5). Untreated (A) and triton X-100 treated (B) fibroblasts grown on TCP acted as controls. Both extract (C) and direct (D) assays were performed on ECM only (i) and CNT-ECM hydrogels (ii) using LIVE/DEAD staining, with calcein-AM (green) and ethidium homodimer-1 (red). Quantitative analysis via the detection adenylate kinase, a product of cell lysis, was performed for both assay types on the three substrates (iii). Scale bar = 100 µm. Bar graphs represent mean ± SD. Statistics obtained through a one-way ANOVA; n = 3, with each well tested in triplicate.

Direct contact testing showed that there were few cells present underneath the ECM-only hydrogels (Figure 4.3Di), yet the surrounding cells look no different to those cells in extract testing or the live control. The 0.2% w/v CNT-ECM hydrogels, similarly to the ECM-only, showed no change in cell viability surrounding the hydrogels (Figure 4.3Dii). However, it is difficult to assess the relative ratio of cells residing underneath them due to the opacity of the hydrogels. Upon removal of the 0.2% w/v CNT-ECM hydrogels there seemed to be no cells present underneath. However, this is not necessarily true as those cells cultured underneath the hydrogels may have attached to the ECM fibres and thus come away with them during hydrogel removal. Quantification of the direct contact testing shows no reduction in viability compared to the TCP control (Figure 4.3Diii). The difference in viability

between the TCP and ECM only hydrogel is not significant; however, the CNT-ECM hydrogels retain their significantly increased viability compared to Figure 4.3Ciii, yet to a lesser degree. Based on the available evidence, it could be speculated that the reduction in viability between indirect and direct experiments could be attributed to a relative reduction in cell number. This could be due to the smaller available growth space within the gel dimensions and a reduced growth underneath the hydrogel. The leached products, both from the ECM hydrogels and CNTs, discussed in the extract testing would be present for the direct testing but at a lower concentration given the shorter time the hydrogels are in the media. Therefore, this could also be a reason for the relatively lower viability compared to the extract testing.

The result of these cytotoxic assays on ECM-only hydrogels is unsurprising, given that the literature suggests that viability is comparable to other hydrogel options across various cell types on a range of ECM hydrogels (Liang et al., 2015; Saldin et al., 2017; Giobbe et al., 2019; Sanjuan-Alberte et al., 2022). However, it is of interest that the incorporation of CNTs does not impact this viability at 0.2% w/v, as CNTs and ECM hydrogels have not yet been used in combination at this concentration. Bare CNTs have been shown to reduce viability, lead to inflammatory and fibrotic cell phenotypes, and even carcinogenic effects (Luanpitpong et al., 2014). Yet incorporated into bulk structures, this cytotoxic tendency seemingly disappears, as seen in this work and in the literature (Shin et al., 2011; Sun et al., 2017; Mihajlovic et al, 2018), except at relatively high concentrations (Ravanbakhsh et al., 2019). This is hypothesised to be linked to the fact that the CNTs are encapsulated by the ECM fibres (Kim et al., 2015) and thus the cells cannot directly interact with the CNTs.

4.3.2 Impact of growth substrate on macrophage polarisation

To determine macrophage phenotype expressed as a result of culturing on the specified substrates microscopy was employed to analyse morphology, expressed surface markers, and information on cell distribution. Figure 4.4 highlights the lack of clarity in which the cells cultured in 2.5D can be visualised under the microscope, compared to conventional TCP cell culture. When grown on TCP, there is a singular plane upon which cell growth can occur and therefore the focal point when imaging these cells is also a singular plane (Figure 4.4A). Microscopy of 2.5D culture on ECM only hydrogels presented the challenge of there being many focal planes to settle on, due to the undulations of the hydrogel surface. This led to images collected being out of focus for much of the frame (Figure 4.4B). However, you can still compare cell morphologies. In this M0-like state, and after only 18 h post-differentiation, there is little difference between cells grown on the different substrates. Despite the short time in culture post-differentiation, the heterogeneity of the population is present. At 18 h post-differentiation and pre-polarisation, there are mostly classic M0-like cells present which have a small, rounded morphology. However, there are some cells with M1-like features such as elongated morphologies with multiple short, spindle-like cytoplasmic protrusions (Bertani et al., 2017). Similarly, there are signs of M2-like cells present, noted by their larger, more rounded shape. These M2-like cells can be multinucleated, yet this isn't clear from brightfield microscopy. The addition of CNTs into the ECM introduces another challenge to imaging cells grown on these biomaterials (Figure 4.4C). Due to the CNTs being black (Figures 3.4, Di to Fi) light is absorbed and therefore the obtained images are very dark. Increasing the brightness did not alleviate this, thus making it difficult to clearly make out morphological differences between cells. In Figure 4.4C, you can see some of the classic M0-like rounded cells as well as the larger M2-like cells relatively clearly due to their size.

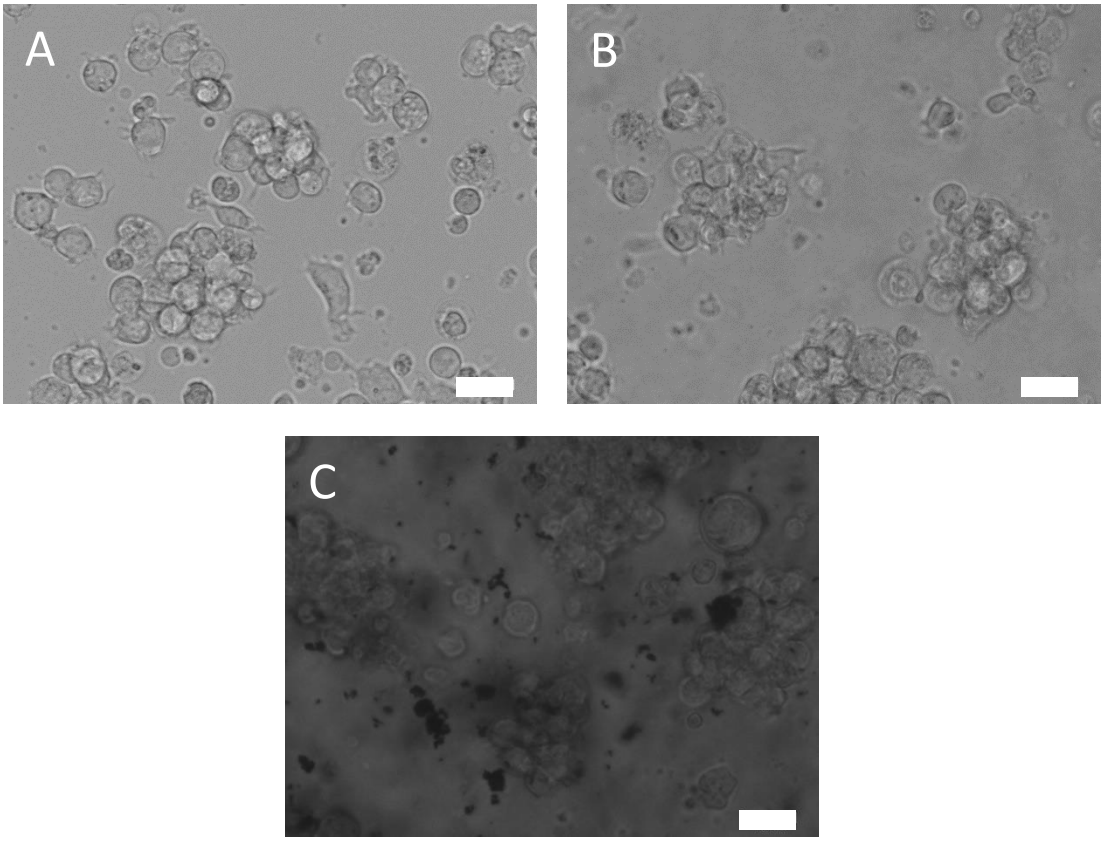

Figure 4.4: Brightfield microscopy of M0 THP-1 derived macrophages (ATCC® TIB-202™) grown for 3 days in 2.5D culture on three substrates. on TCP, ECM hydrogels, and 0.2% w/v CNT-ECM hydrogels. Cells grown on (A) TCP, (B) ECM-only, and (C) CNT-ECM hydrogels were imaged prior to polarisation. Scale bar = 25 µm.

As a result of the poor brightfield microscopy, fluorescence microscopy was used to better identify macrophage polarity compared to morphology alone. Immunocytochemistry staining, and time in culture, allows for a better analysis between the macrophage phenotypes. Figure 4.5 looks at the presence of the nuclear stain DAPI (blue) along with an M1 and M2 surface marker: calprotectin (red) and mannose receptor (green), respectively. The fluorescent tagging of said markers shows that M0-like cells, cultured with the M0 cytokine cocktail, present relatively little calprotectin or mannose receptor 3 days post-polarisation. The cells are evenly distributed across the frame, with the odd cell presenting high amounts of calprotectin or mannose receptor; further confirming the heterogeneity of the cell population. The image showing M0 cells cultured on ECM only hydrogels is like that

of TCP growth, however with seemingly higher amounts of calprotectin and DAPI present. However, this cannot be directly compared to the TCP frame. Images of ECM only hydrogels were taken at a higher contrast and gain on the green and red channels in order to reduce a green hue, speculated to be caused by background fluorescence of non-specific binding from within the hydrogels themselves. There is a sea of green pixels in the background of the ECM only images, most clear on the M1 frame. This is suspected to be the source of the green hue present in both ECM-based substrates; however, it is unknown what the exact cause is. M0 cells grown on CNT-ECM hydrogels still possess that green background fluorescence, as attempts to reduce its effects during image capture caused the images to be too dark to see any features or fluorescence due to the light absorbing properties of the CNTs. Therefore, the CNT-ECM images were collected with the same microscope settings as the TCP samples. Even with the green hue present, some conclusions can still be drawn. Some slight calprotectin expression is visible as well as the dispersion of cells seen in the other substrates too. The expression of mannose receptor is unclear given that it is the green channel through which the non-specific binding has occurred.

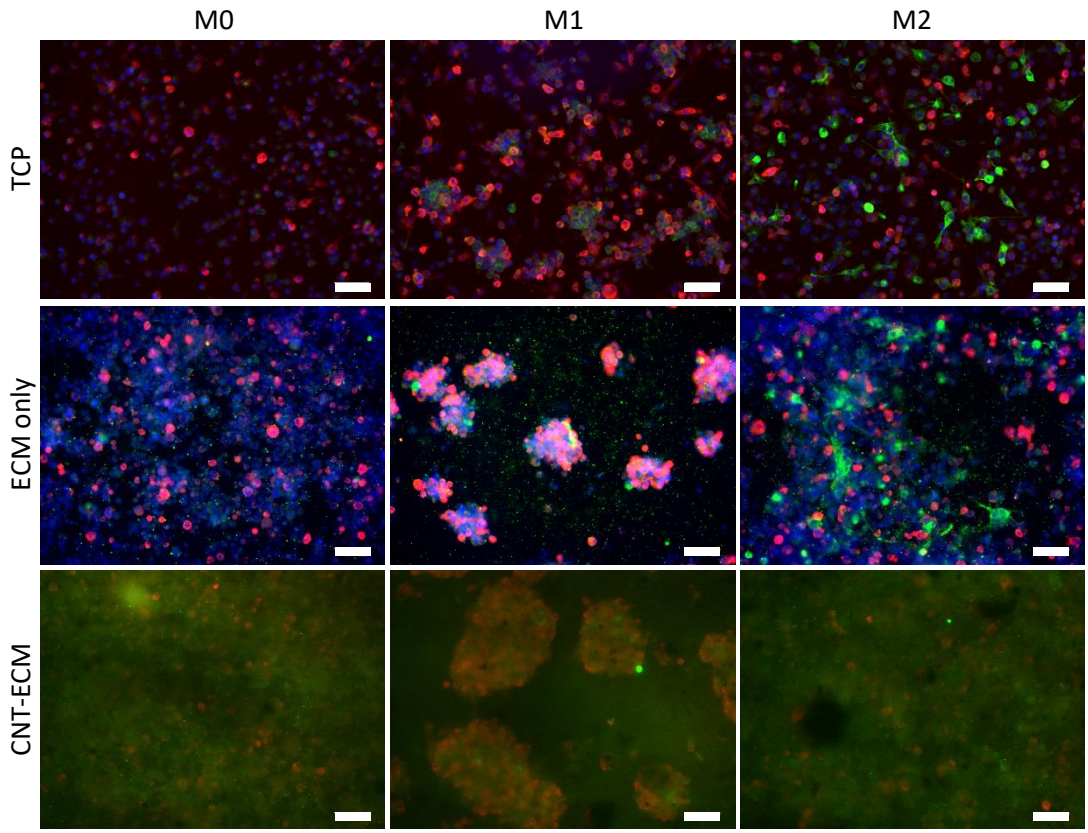

Figure 4.5: Fluorescent microscopy of THP-1 derived macrophages (ATCC® TIB-202™) grown on three substrates 3 days post-PMA differentiation. Immunocytochemistry staining of different phenotypes of THP-1 derived macrophages grown TCP, ECM only, and CNT-ECM hydrogels. Calprotectin (red) and mannose receptor (green) were used as respective M1 and M2 cell surface markers, with DAPI (blue) as a nuclear stain. Images of the ECM only macrophages were taken using a higher contrast on the green and red channels alongside a higher gain value in order to eliminate the green background fluorescence caused by the hydrogels, this was attempted with the CNT-ECM hydrogels too but just caused the image to be too dark. These images are representative of n = 3, 3 images per well. Scale bar = 100 µm.

The M1 frame denoted cells grown on the three substrates for 3 days with cultured media supplemented with the M1 cytokine cocktail. When cultured on TCP, there is an increase in the amount of calprotectin present with some of cells still expressing the M2 mannose receptor. The distribution of cells is not as even, with a few clusters of cells present compared to the M0 TCP image. This clustering is much more apparent in the M1 ECM-only image. Here, the clusters are large and very defined with few cells in-between as shown by the rare spot of DAPI outside of an aggregation. Within the clusters there is a large expression of calprotectin, as expected after the cytokine cocktail. This could be due to an increased ease in migration across the soft ECM surface compared to the stiff TCP surface.

However, this is unlikely as macrophage motility lies between approximately 5-25 μm.min^{-1} depending on the polarisation status (Hind et al., 2016), meaning that cells would have ample time to cluster over the 3 days post-differentiation prior to these images being taken. The enhanced aggregation in M1 macrophages cultured on ECM-only hydrogels could be a result of the hydrogels containing antigenic molecules which activate the macrophages even more. Nevertheless, if this were the case, you'd expect to see activation in at least the M0 frame as well as the M2 frame of the ECM-only hydrogels, meaning the chances of the ECM hydrogels causing antigenic activation in these samples alone are low. The lack of instantaneous activation of M0 macrophages arising from the SIS-ECM hydrogel frame on day 3 is a strong indicator that the materials are in fact free from, or possess low, antigenic concentrations of nucleic acids. This was expected given the reduction in dsDNA to below 200 bp (Figure 3.2) (Keane et al., 2012). It can also be proposed that other immunogenic molecules which weren't quantified, such as endotoxins, also have minimal effect on macrophage activation.

The M1 CNT-ECM frame shows even larger aggregates than the ECM only equivalent, with high expression of calprotectin bleeding through the non-specific binding impacting the green channel. With the aggregation displayed in only M1-like macrophages cultured on both hydrogels, said aggregates must be due to the presence of the hydrogel, regardless of CNT incorporation.

The M2 cytokine cocktail elicited a large expression of mannose receptor in the cells cultured on TCP, with the calprotectin levels mimicking that of the M0 TCP image. There is no clustering present in the M2 ECM only frame, unlike the M1 counterpart. This is very similar to the TCP equivalent in that there is a high expression of mannose receptor, and the expression of calprotectin is similar to that of the M0 frame of the same substrate.

The M2 CNT-ECM image is the most difficult to decipher. It looks strikingly similar to the M0 frame of the same substrate yet without the high levels of mannose receptor seen in the cells grown on TCP or ECM only hydrogels. It would be expected that the mannose receptor expression is present, but masked by the non-specific binding cause by the biomaterial itself.

The cytokine release at day 3 post-polarisation, the same time point shown in Figure 4.5, showed a relatively low release of both M1 and M2 secreted markers (Figure 4.6). IL-6 release was all below the limit of detection with no significant analysis available and thus nothing can be gleamed at this time point (Figure 4.6). TNF-α exhibited a relatively high secretion from both M1- and M2-like cells, however these were not significant from one another and thus it is impossible to use these as reference controls to compare the TNF-α release of either hydrogel substrates (Figure 4.6B). The only cytokine with a relatively strong release was IL-10 (Figure 4.6C). While the M1- and M2-like controls were similarly unsignificant from one another as with TNF-α, the release from the ECM-only hydrogels was almost 3-fold of the reference controls, indicating that the hydrogels themselves play a functional role in driving M2 polarisation which acts via a different, and faster acting, pathway to the cytokine cocktail. Elevated IL-10 has been noted previously in studies culturing macrophages on GelMa (Cha et al., 2017). CCL18, however, was like IL-6 in that there was no detectable release from any cells on any substrate (Figure 4.6D).

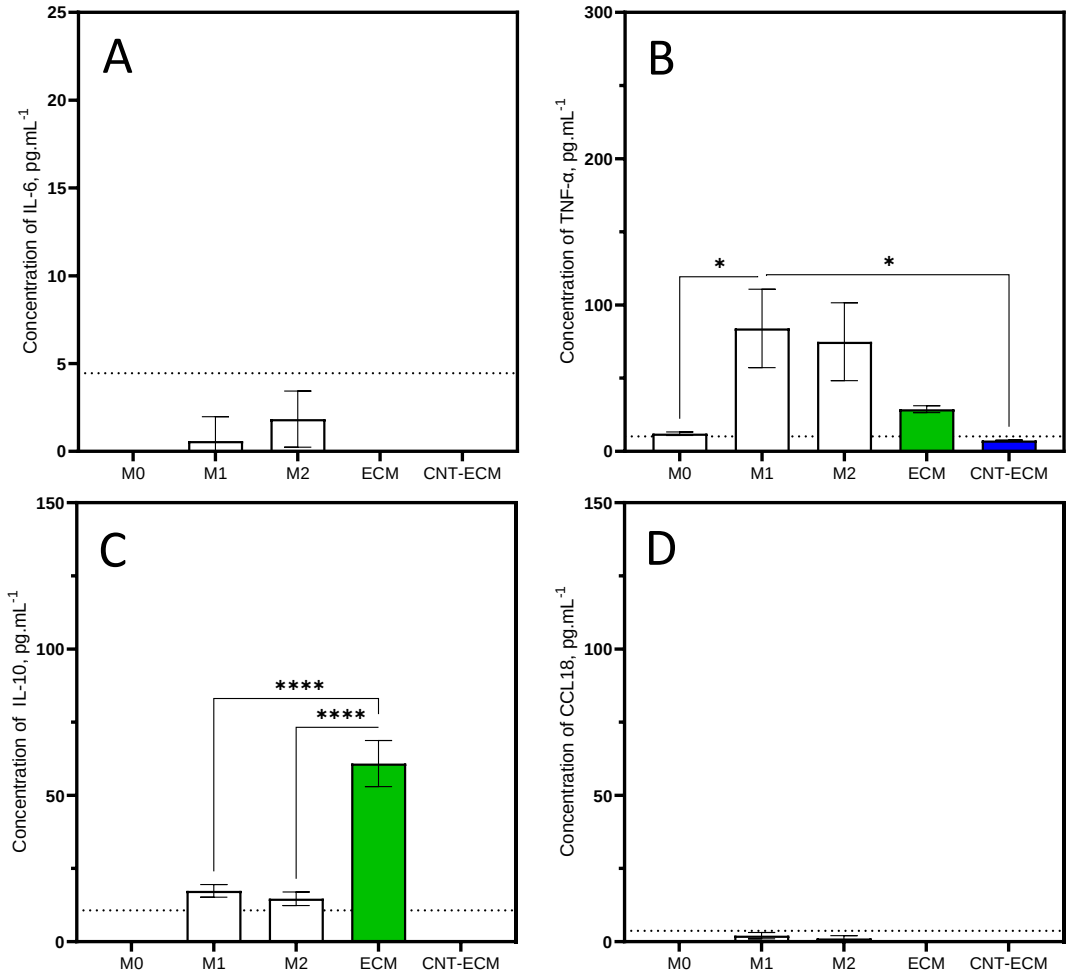

Figure 4.6: Cytokine profiles of THP-1 derived macrophages (ATCC® TIB-202™) grown on three substrates 3 days, post-PMA differentiation. Cytokine profiles of M1 and M2 secreted markers collated via ELISA analysis of different phenotypes of THP-1 derived macrophages grown TCP, ECM only, and CNT-ECM hydrogels. M1 markers used were (A) IL-6 and (B) TNF-α, while M2 markers used were (C) IL-10 and (D) CCL18. The horizontal dotted lines represent the limit of detection calculated for each ELISA kit. Bar graphs represent mean ± SEM. Statistics obtained through a one-way ANOVA; N = 2, n = 3, with each well tested in duplicate.

Immunocytochemistry staining after 6 days post-polarisation (Figure 4.7) is very different to the 3-day equivalent in some frames, shown in Figure 4.5. Macrophages maintained as M0 and cultured on TCP show a slight reduction in calprotectin expression. The M0 ECM only hydrogel frame is different, there is a large decrease in calprotectin present compared to 3 days earlier. The CNT-ECM frames for all three macrophage phenotypes are difficult to interpret due to the green hue present. It is suspected that the reason for this different image quality between day 3 and day 6 for CNT-ECM hydrogels is due to the cultured cells

embedding themselves deeper into the hydrogel which, alongside the background fluorescence and lack of available light, results in a less clear image. However, the trend between day 3 and day 6 imaging for M0 macrophages is that there is a reduction in the expression of calprotectin, and it can be extrapolated that this occurs in the CNT-ECM hydrogels too given that there are fewer cells stained red. It is impossible to determine the level of mannose receptor in this frame given the green hue as discussed earlier, and the lack of visible DAPI means no comparisons in terms of cell number can be made.

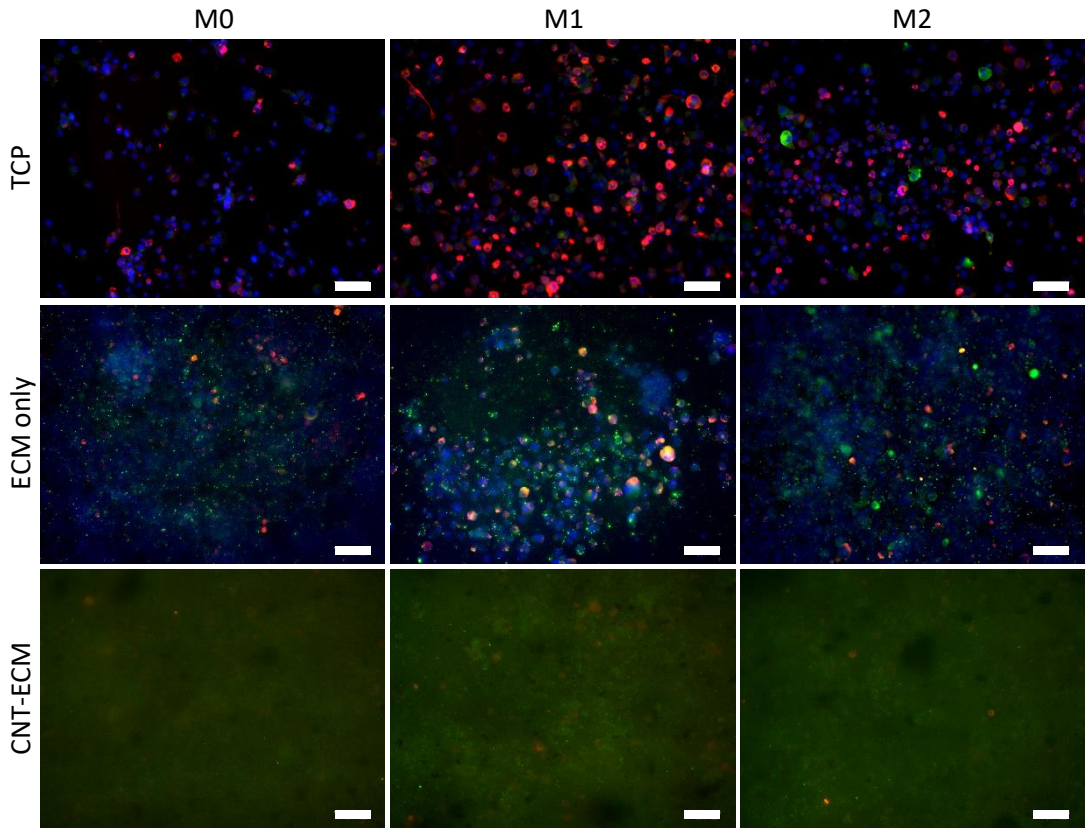

Figure 4.7: Fluorescent microscopy of THP-1 derived macrophages (ATCC® TIB-202™) grown on three substrates 6 days post-PMA differentiation. Immunocytochemistry staining of different phenotypes of THP-1 derived macrophages grown TCP, ECM only, and CNT-ECM hydrogels. Calprotectin (red) and mannose receptor (green) were used as respective M1 and M2 cell surface markers, with DAPI (blue) as a nuclear stain. Images of the ECM only macrophages were taken using a higher contrast on the green and red channels alongside a higher gain value in order to eliminate the green background fluorescence caused by the hydrogels, this was attempted with the CNT-ECM hydrogels too but just caused the image to be too dark. These images are representative of n = 3, 3 images per well. Scale bar = 100 µm.

Cells stimulated with the inflammatory cytokine cocktail, thus M1-like, maintain their strong expression of calprotectin when cultured for 6 days on TCP. They are slightly more dispersed compared to the day 3 counterpart however that is not as apparent as in the day 6 M1 ECM only hydrogel frame, where the clustering is seemingly not present as it was at day 3. There is also a distinct lack of calprotectin expression, the opposite of what you expect when stimulated with GM-CSF, LPS, and IFN-γ. It can be presumed this is due to the immunomodulatory properties of the ECM biomaterial (Slivka et al., 2014; Cha et al., 2017; Sacitri et al., 2020), however this is difficult to confirm due to the disruption in the green channel caused by the speckles of non-specific binding present across the frame. Due to the clustering of the cells in the day 3 equivalent, it is impossible to qualitatively compare cell number between day 3 and 6 in the M1 frames. As mentioned, it is very hard to confirm much with the CNT-ECM images, but it does seem clear that the clustering of the M1 cells had also lessened at day 6. Immunomodulatory, M2, macrophages cultured on TCP show a decrease expression of mannose receptor at day 6, similarly when cultured on the ECM only hydrogels. The M2 CNT-ECM macrophages looked as similar as possible, given the imaging obstacles, to the day 6 M0 equivalent.

All surface marker expression is decreased between day 3 and day 6, regardless of cell phenotype or growth substrate. Purcu et al. (2022) reported that mRNA expression for surface markers, including mannose receptor, peaked at 72 h post-polarisation. This could corroborate what is noted between Figures 4.5 and 4.7, however, their study was limited to a maximum timepoint of 72 h.

Rostam et al. (2017) studied THP-1 derived macrophages for 6 days post PMA treatment and report similar results in that M1-like macrophages possess elevated calprotectin and likewise for mannose receptor and M2-like cells. Due to their only being day 6 data there, any differences on days between the PMA and day 6, like in this study, cannot be

distinguished. Similarly, Rostam et al. (2017) performed their experiments on TCP and therefore the only comparison that can be made is against the similar morphology to the images shown in Figures 4.5 and 4.7 for TCP, and not to the aggregations of M1 polarised cells seen in 2.5D culture.

The day 6 cytokine profiles (Figure 4.8) showed the much greater release compared to the day 3 profiles. IL-6 release was highest in M1-like cells and significantly lower in M0- and M2-like cells (Figure 4.8A). The ECM and CNT-ECM hydrogel IL-6 release remained below the limit of detection. A similar trend is seen for TNF-α release, in that M1-like cells exhibit a significantly elevated release compared to the M0- and M2-like cells as well as the M0-like cells cultured on ECM and CNT-ECM hydrogels (Figure 4.8B). M0-like cells showed no difference in release when grown on TCP and ECM-only hydrogels, however the M0-like cells cultured on CNT-ECM hydrogels displayed a release below the limit of detection and thus significantly lower than the M0-like cells grown on different substrates. From day 3 to day 6, there was a small increase in IL-10 release for M0-like cells cultured on ECM-only hydrogels, whereas the secretion from M0- and M2-like cells on TCP increased to match that ECM-only release (Figure 4.8C). M1-like cells remained low in terms of their IL-10 release and cells cultured on CNT-ECM hydrogels showed minimal release, on the boundary of the limit of detection. CCL18 cytokine profiles for day 6 showed a small secretion in the M0- and M1-like cells (Figure 4.8D), with the M2-like cells having a 5-fold increase in their release compared to the day 3 equivalent. The ECM-only hydrogel grown cells released a third as much as the M2-like cells while the cells cultured on the CNT-ECM hydrogels had a secretion profile below the limit of detection.

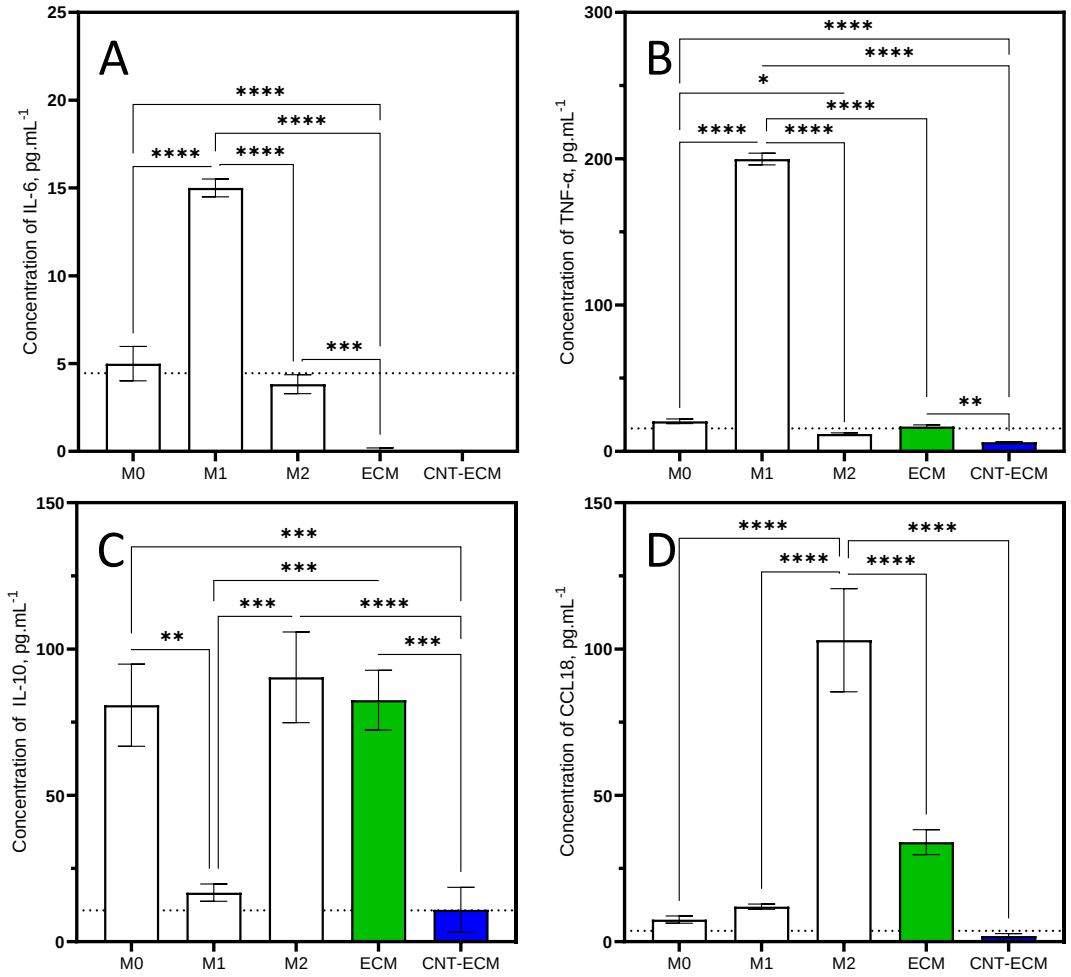

Figure 4.8: Cytokine profiles of THP-1 derived macrophages (ATCC® TIB-202™) grown on three substrates 6 days, post-PMA differentiation. Cytokine profiles of M1 and M2 secreted markers collated via ELISA analysis of different phenotypes of THP-1 derived macrophages grown TCP, ECM only, and CNT-ECM hydrogels. M1 markers used were (A) IL-6 and (B) TNF-α, while M2 markers used were (C) IL-10 and (D) CCL18. The horizontal dotted lines represent the limit of detection calculated for each ELISA kit. Bar graphs represent mean ± SEM. Statistics obtained through a one-way ANOVA; N = 2, n = 3, with each well tested in duplicate.

ECM hydrogels have been shown in the literature to induce an M2-like phenotype (Sacitri et al., 2020), therefore the response from THP-1 derived macrophages cultured on ECM only hydrogel is not unexpected. It has been seen that, specifically in urinary bladder matrix hydrogels, soluble components, such as matrix-embedded growth factors and matrix-bound vesicles, are key to enhancing a range of macrophage functions such as: increasing phagocytic capabilities of THP-1 derived macrophages and supressing the secretion of inflammatory markers (Slivka et al., 2014; Huleihel et al., 2017; White et al., 2018).

Therefore, it is hypothesised that it is the soluble fraction of ECM hydrogels which are mainly responsible for driving the M2-like shift seen in this data. That isn't to say that the structural fraction is not useful in driving macrophage behaviour; structural properties are shown to determine chemotactic migration independently from soluble factors (Hsieh et al., 2019).

The lack of cytokine detection in CNT-ECM hydrogels seen in Figures 4.7 and 9 was expected, due to the understanding that CNTs have a tendency to develop protein corona (Zhang T. et al., 2019; Pinals et al., 2020). Yet it was not expected that these would be below the limit of detection, especially at day 6. This will be discussed further on in the chapter.

4.3.3 Electrical stimulation cytocompatibility

To study ECM hydrogels and electrical stimulation in tandem, preliminary electrical stimulation viability analyses are required first. Cell viability post-stimulation was analysed via cytotoxicity, denoted by the amount of cell lysis across the well (Figure 4.9A). The quantification of the degree of cell lysis, detected by release of adenylate kinase, was as expected at the lower end of the stimulation strength range (≤ 2.4 V). Mammalian wounds experience electric fields up to 200 $mV.mm^{-1}$ (Nuccitelli, 2003; Dubé et al., 2010), which corresponds to 2.4 V in this experimental set-up. Similar studies confirm that low stimulation strengths elicit no significant difference in cytotoxicity; Mobini et al. (2016) reported no signs of cellular toxicity up to 100 $mV.mm^{-1}$, which is equivalent to 1.2 V in this work, which they confirmed again in later work (Mobini et al., 2017). It would therefore be expected that stimuli of this strength would be tolerable for mammalian cells, which is the case given that the degree of cytotoxicity is not significantly different from, or in some cases more cytocompatible than, the untreated control. There is then a large change in the

adenylate kinase release profile noted at a stimulation strength of 2.7 V. Given that 200 $mV.mm^{-1}$ has been shown to be the maximum field strength in vivo then you would likely expect that above this (> 2.4 V) cytocompatibility in vitro may begin to wane. This increased level of cytotoxicity, detected by adenylate kinase release, then begins to drop at 3.3 V and continues to decrease until it is significantly below that of the untreated control. This is unexpected as high stimulation strengths are known to have a detrimental impact on cell viability (Meng, Rouabhia, and Zhang, 2021).

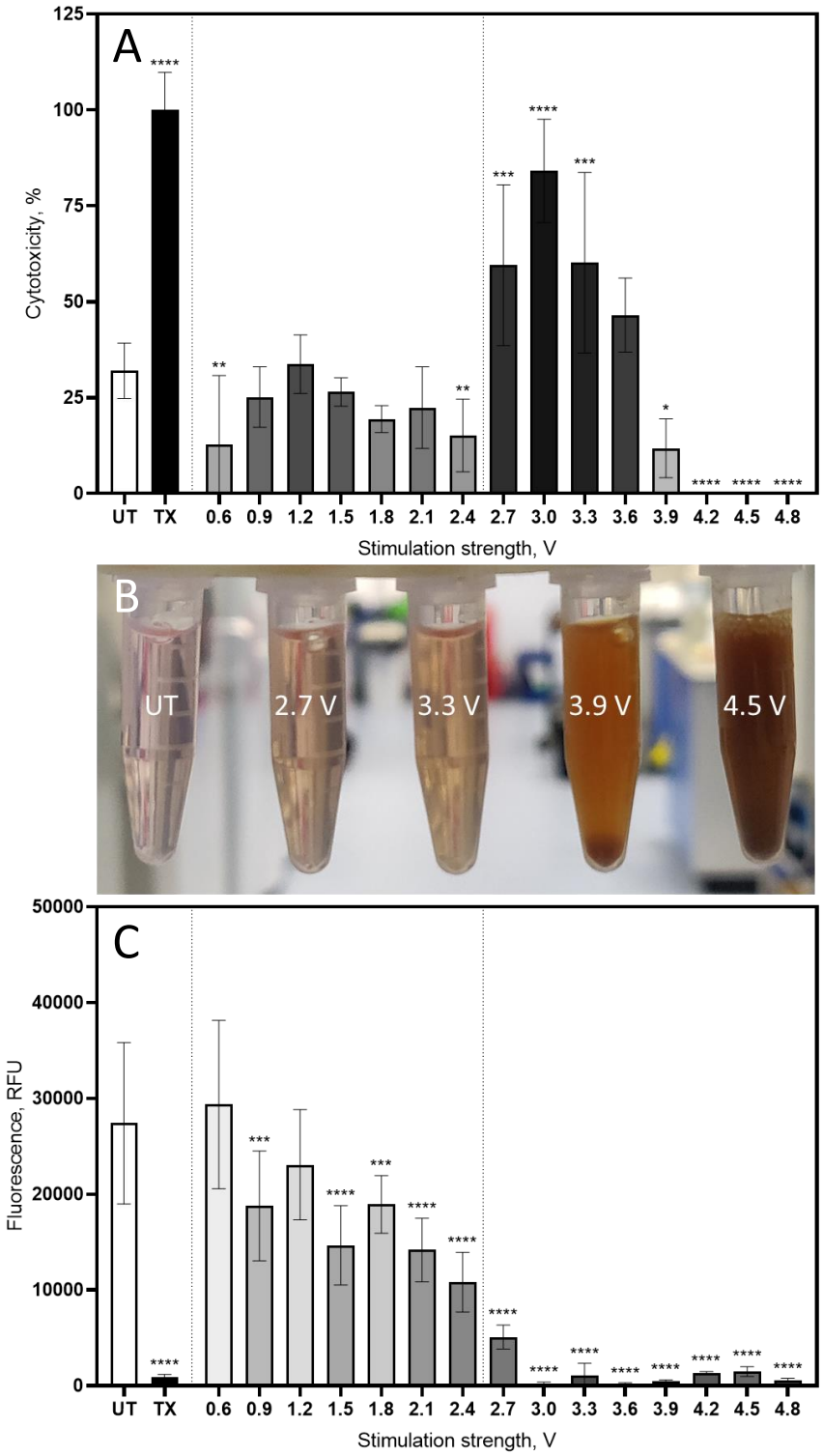

Figure 4.9: Analysis of cell lysis and metabolism of THP-1 derived M0-like macrophages (ATCC® TIB-202™) after 24 h post-differentiation growth on TCP when exposed to electrical stimulation. Pre-polarised THP-1 derived macrophages grown on TCP were subjected to DC electrical stimulation, across a range of voltages, through exposed electrodes for 10 min. Quantitative analysis via the detection adenylate kinase, a product of cell lysis, was performed (A), however the REDOX precipitates generated unexpected readings at higher strengths (B), leading to a change in assay design. Washing these precipitates away with PBS allowed for a more expected pattern of cell metabolism (C). Vertical dashed lines split the data up into two smaller experiments due to logistical constraints as well as separating the controls from the test samples; where UT = untreated, TX = triton X-100 treated. Bars are shaded depending how close they are to the UT, in white, or TX, in black. n = 3, with each well tested in triplicate.

The passage of a current through a material causes the alterations of oxidative states of the material constituents characterised by REDOX reactions. In this system likely water electrolysis, approximately > 2.3 V (Senftle et al., 2010), which is observed by bubbling at the electrode surface, and electrode REDOX, at higher voltages. The appearance of colour changes due to the formation of precipitates indicates that this is occurring at the higher end of the stimulation strength range (Figure 4.9B). The strength dependant decreases in metabolism that are expected is a result of these REDOX effects. These REDOX reactions were suspected to involve the electrodes themselves, given the orange precipitate resembling rust and the observed corrosion of the electrodes themselves. Due to the presentation of the precipitate matching the decline in cytotoxicity between 3.3 and 3.9 V (Figure 4.9A), it is proposed that the precipitates formed are interfering with a part of the luciferase reaction which detects adenylate kinase release via the enzymatic phosphorylation of ADP to ATP. This led to an artificial decrease in cytotoxicity at higher stimulation strengths. Therefore, the use of this method of measuring viability is not suited to this study; an alternative quantitative method of cytocompatibility was required for analysis of cultures in 2.5D post-stimulation.

The solution was to rinse the cells of the precipitates and discoloured media and analyse the metabolism of the remaining cell population. While not analogous to cell viability, cell metabolism can, and has, been used as a reflection of cytotoxicity in THP-1 cells previously (Wathiong et al., 2019; Shukla et al., 2022). Resazurin metabolism post-stimulation presents the expected profile, an overall decrease in cell metabolism as stimulation strength increases (Figure 4.9C). Given that 0.6 V in this system corresponds to the field strength seen in vivo, it is unsurprising that this strength elicits no difference to the untreated control. Significant decreases in metabolism begin sooner than expected given the stimulation ranges exhibited in previous studies (Nuccitelli, 2003; Dubé et al., 2010; Mobini et al., 2016; Mobini et al., 2017), however this discrepancy could be a result of

analysing viability indirectly via metabolism. 3.0 V and upwards displays a large decrease in metabolism, with similar values to that of the Triton X-100 treated controls indicating that such stimulation strengths were detrimental to cellular metabolism. Decreased metabolism and resultant suspected decreases in viability at high stimulation strengths are most likely due to the change in pH as a result of REDOX activity within the system (Saulis et al., 2005), as such little work is reported for high (> 2.4 V/200 $mV.mm^{-1}$) continuous DC stimulation.

The time which cell experience the respective stimulation is not a relevant factor when comparing timescales which are achievable given the logistics of the experimental set up (Figure 4.10). Whether the stimulation period is 10- or 60-min, the difference in cytotoxicity as measured by adenylate kinase release, at a stimulation strength not significantly influenced by precipitate disruption, remains non-significant. Therefore, the larger-scale experiments utilised the shorter stimulation time to obtain a higher throughput of sample analysis.

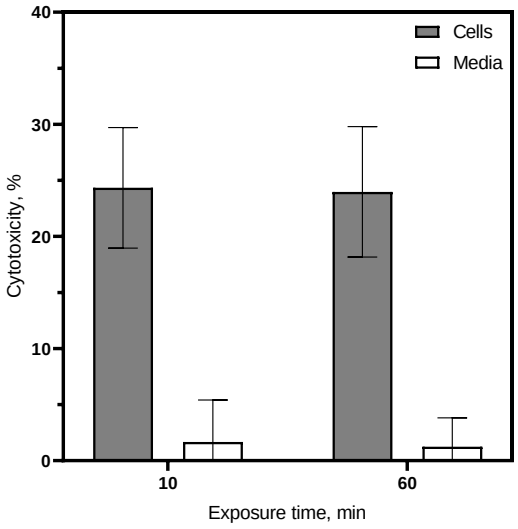

Figure 4.10: Analysis of cell lysis products of THP-1 derived M0-like macrophages (ATCC® TIB-202™) after 24 h post-differentiation growth on TCP when exposed to 2.4 V DC electrical stimulation for two exposure durations. Quantitative detection of lactate dehydrogenase, a product of cell lysis, comparing stimulation exposure times of 10- and 60-min. n = 3, with each well tested in triplicate.

Metabolism of M0-like cells after 24 h of culture has been shown to be unchanged regardless of them being cultured on ECM only or CNT-ECM hydrogels (Figure 4.2). However, Figure 4.11 describes the metabolic activity of M0-like cells cultured on the three substrates 6-days post-stimulation. Firstly, there is a significant increase in metabolism between M1 and M2 reference cells ($P \leq 0.001$). This would be expected given that THP-1 derived macrophages stimulated via inflammatory cytokines end up less viable compared to M0-like cells (Genin et al., 2015). Looking at stimulated cells cultured on TCP, those stimulated with exposed electrodes, and thus producing electric current effects, exhibits a significantly lower metabolism compared to the insulated, field effect, electrode equivalent at low and medium stimuli strengths ($P \leq 0.0001$). Yet at the higher stimuli strength, 2.4 V, the two are not significantly different. Given that Figure 4.9 reported that 2.4 V led to a decreased metabolism in comparison to 0.6 and 1.2 V, the reason for this increased metabolism at 2.4 V in Figure 4.11 is unpredicted. Mobini et al. (2017) report an elevated metabolism in murine adipose tissue-derived mesenchymal stem cells when exposed to electrical stimuli. However, Mobini et al. (2017) only utilised one stimuli strength, 100 $mV.mm^{-1}$, and thus the trend shown in this thesis cannot be compared. Alongside this limitation, Mobini et al. (2017) also presented data displaying a decrease in metabolism with murine bone marrow-derived mesenchymal stem cells, therefore increases in metabolism after electrical stimulation are not universal.

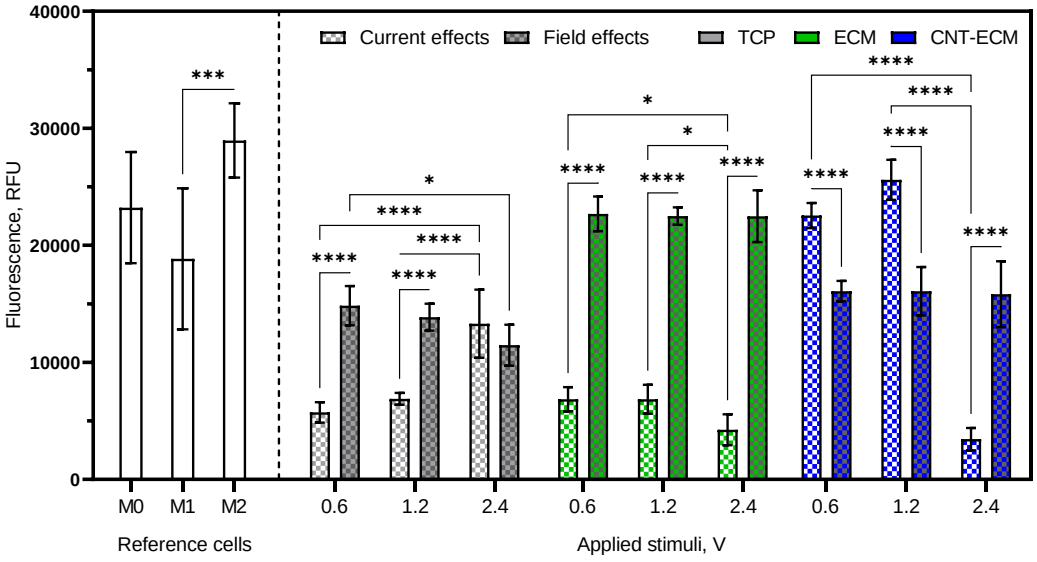

Figure 4.11: Metabolism of THP-1 derived M0-like macrophages (ATCC® TIB-202™) grown on three substrates, 6 days post-stimulation. Metabolism of M0-like cells both grown on different substrates and exposed to varying DC electrical stimulation strengths and types. The substrates used were TCP, ECM only, and CNT-ECM hydrogels. The DC electrical stimulation was applied at 0.6, 1.2, and 2.4 V using either exposed or dielectric ink insulated electrodes to decouple current and field effects. The reference cells were cultured on TCP, supplemented with the relevant cytokine cocktails. Bar graphs represent mean ± SD. Statistics comparing the reference cells was obtained through a one-way ANOVA, while comparing intra-substrate data was achieved through a two-way ANOVA; n = 3, with each well tested in triplicate.

Stimulated cells on ECM only hydrogels present a very clear trend. Exposed electrodes exerting current effects of increasing stimuli strength cause little change in metabolism, until 2.4 V where the drop in metabolism is significant ($P \leq 0.05$). Yet the overall metabolism is lower than that of the reference cells cultured on TCP, contrary to Figure 4.2 where culturing on ECM hydrogels increased metabolism. Likewise, field effect stimulation of increasing strength caused no significant change in metabolism. However, the difference between current and field effects within the same strength are significantly different ($P \leq 0.0001$), with field effects driving a much higher metabolic activity. A hypothesis for this behaviour could be linked to cell viability, in that current effect stimulation leads to more detrimental damage to the cell populations and thus decreasing cell number, hence a decreased metabolic response. However, the evidence shown in Figure 4.9A suggests that this decrease in viability at 2.4 V doesn't exist. The data presented in Figure 4.9C is from

cells only 24 h post-stimulation too, yet the data from ECM only hydrogel current effect stimulation in Figure 4.11 shows a similar pattern of decreasing metabolic activity after spending an extra 5 days in culture post-stimulation. This indicates that the impact on metabolism must be due to the type of stimulation used. Literature reporting electrical stimuli in vitro usually examines either current or field stimulatory effects, not both forms in a comparative fashion. The result of this means that it is difficult to use the literature as a supportive tool due to the large discrepancies between experimental variables across studies investigating the impacts of electrical stimuli in mammalian biology. Further investigations would be key to supporting these findings as well as unlocking the mechanisms behind them.

Culturing on top of the CNT-ECM hydrogels flips the trend seen on ECM hydrogels, with current effect stimulation provoking a stronger metabolic response, until a significant decrease at 2.4 V ($P \leq 0.0001$). Field effect stimulation caused a stable metabolic response, as with the ECM only hydrogels, yet at a lower metabolic rate. The addition of CNTs into the ECM biomaterial seemingly plays a role in how the cells respond to the two types of electrical stimuli: elevating metabolic responses to low and medium strength current effect stimulation, whilst decreasing the metabolic activity of field effect stimulated cells in comparison to those cultured on ECM only hydrogels.

4.3.4 Combinatory impact of growth substrate and electrical stimulation

4.3.4.1 Macrophage polarisation

TNF-α and IL-6 were used to investigate the polarisation towards M1 for M0 cells grown in 2.5D post stimulation (Figure 4.12). The secretion of TNF-α by M0-like cells cultured on TCP post-stimulation does not differ depending on the type of stimulation exposure until the

highest voltage tested range (Figure 4.12A). However, this large increase in TNF-α at 2.4 V ($P \leq 0.0001$) is only present after stimulation via exposed electrodes exuding electrical current effects. The field effect equivalent is not significantly different from the 0.6 V and slightly significant ($P \leq 0.05$) compared to the 1.2 V counterpart. When cultured on ECM-only hydrogels, there is a large amount of TNF-α secretion at all strengths of electrical stimuli for current effects. These are not voltage dependant but are stimulation type dependant, with field effect stimulation significantly decreasing the release for all 3 strengths ($P \leq 0.0001$). Again though, the voltage strength is not a factor in the release for cells cultured on the ECM-only substrate. When compared to the metabolism profile (Figure 4.11), it is clear to see that the high TNF-α release corresponds to the decreased metabolism. It can be postulated that the high TNF-α release is a resultant effect of the electrical stimuli, leading to inflammatory responses and thus reduced metabolic activity (Genin et al., 2015). M0-like cells cultured on CNT-ECM hydrogels generated no detectable TNF-α.

IL-6 secretion of cells cultured on TCP and stimulated with current effects was elevated in comparison to the M0-like reference cells, however the release post-field effects stimulation was below the limit of detection (Figure 4.12B). This trend was also seen in THP-1 derived M0-like macrophages grown on ECM-only and CNT-ECM hydrogels, in that the current effects stimulation produced a detectable, but not voltage dependant elevation of IL-6 whereas the field effect stimulation saw no detectable IL-6 6 days after stimulation.

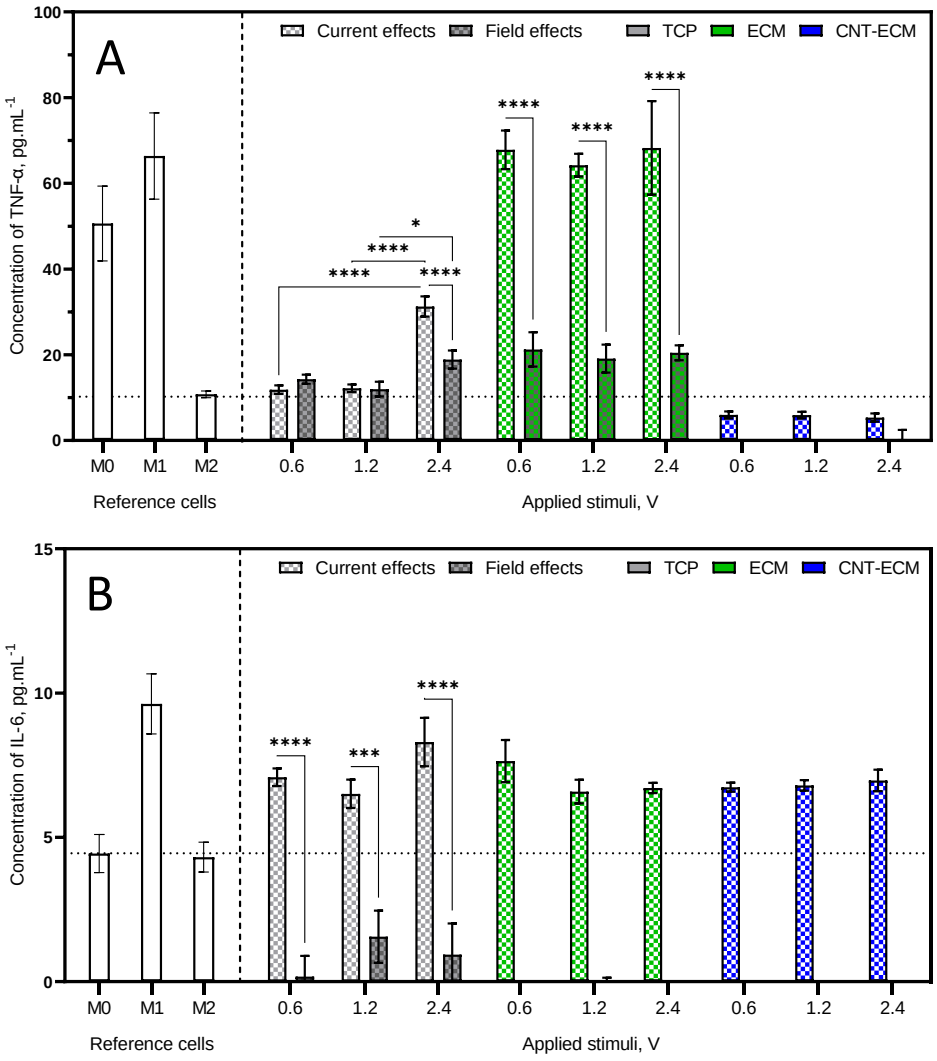

Figure 4.12: Cytokine profiles for M1 markers of THP-1 derived M0-like macrophages (ATCC® TIB-202™) grown on three substrates, 6 days post-stimulation. Cytokine profiles of M1 secreted markers collated via ELISA analysis, TNF-α (A) and IL-6 (B), of cells both grown on different substrates and exposed to varying DC electrical stimulation strengths and types. The substrates used were TCP, ECM only, and CNT-ECM hydrogels. The DC electrical stimulation was applied at 0.6, 1.2, and 2.4 V using either exposed or dielectric ink insulated electrodes to decouple current and field effects. The reference cells were cultured on TCP, supplemented with the relevant cytokine cocktails. The horizontal dotted lines represent the limit of detection calculated for each ELISA kit. Bar graphs represent mean ± SEM. Statistics, comparing intra-substrate data, obtained through a two-way ANOVA; N = 2, n = 3, with each well tested in duplicate.

CCL18 and IL-10 were used to investigate the polarisation towards M2 for M0 cells grown in 2.5D post stimulation (Figure 4.13). The generation of CCL18 in the reference cells was conclusively higher in M2-like THP-1 derived macrophages (Figure 4.13A). Post stimulation, cells cultured on TCP and stimulated with current effects had an elevated level of CCL18 compared to the M0-like reference cell, yet this was inversely proportional to the

stimulation strength, with CCL18 release at 0.6 V being almost twice that of the release at 2.4 V (68.4 vs. 37.5 pg.mL^{-1}). However, field effect stimulation was significantly higher than the current effect counterpart of the same strength; following the same trend of 0.6 V having the highest release and 2.4 V having the lowest (0.6 V, $P \leq 0.0001$; 1.2 V, $P \leq 0.001$; 2.4 V, $P \leq 0.05$). Culturing on ECM-only hydrogels replicated the same trends too, with the current effect stimulation generating similar CCL18 concentrations to the current effect stimulation on TCP. However, the CCL18 release post-field effects was elevated greatly compared to the even the M2-like reference cells. Here, the 0.6 V field effect stimulation released 224.6 pg.mL^{-1}, down to 127.9 pg.mL^{-1} at 2.4 V. The cells grown on CNT-ECM hydrogels produced detectable levels of CCL18, however these remained incredibly low and less than that of the M0- and M1-like reference cells, with no significant difference between the two stimulation conditions or stimulation strength.

The IL-10 profile is similar to the CCL18 profile, in that the field effect stimulation generated a greater IL-10 release in both the TCP and ECM-only substrates (Figure 4.13B). However, in the TCP samples, the IL-10 concentration remained relatively stable across all the voltages except for the field effect 2.4 V stimuli which had a significant increase ($P \leq 0.01$). As with the CCL18 profile, cells cultured on ECM-only hydrogels and stimulated with field effects possessed the greatest IL-10 concentration after 6 days. Following the CCL18 trend still, it is a voltage dependant relationship in which the increased stimulation strength results in a lesser IL-10 concentration.

The data shown for ECM only hydrogels in Figure 4.13 demonstrates that culturing on the ECM hydrogels elicits a large M2-like response, confirming what has been noted previously (Slivka et al., 2014; Cha et al., 2017; Sacitri et al., 2020). However, this is seemingly stifled via the application of current effect stimuli. This lines up with data shown in Figure 4.12 where current effect stimulation elevated the levels of anti-inflammatory TNF-α. Therefore,

it could be suggested that current and field effect stimulation do play a role in THP-1 derived macrophage polarisation, with one driving inflammatory and the other immunomodulatory phenotypes.

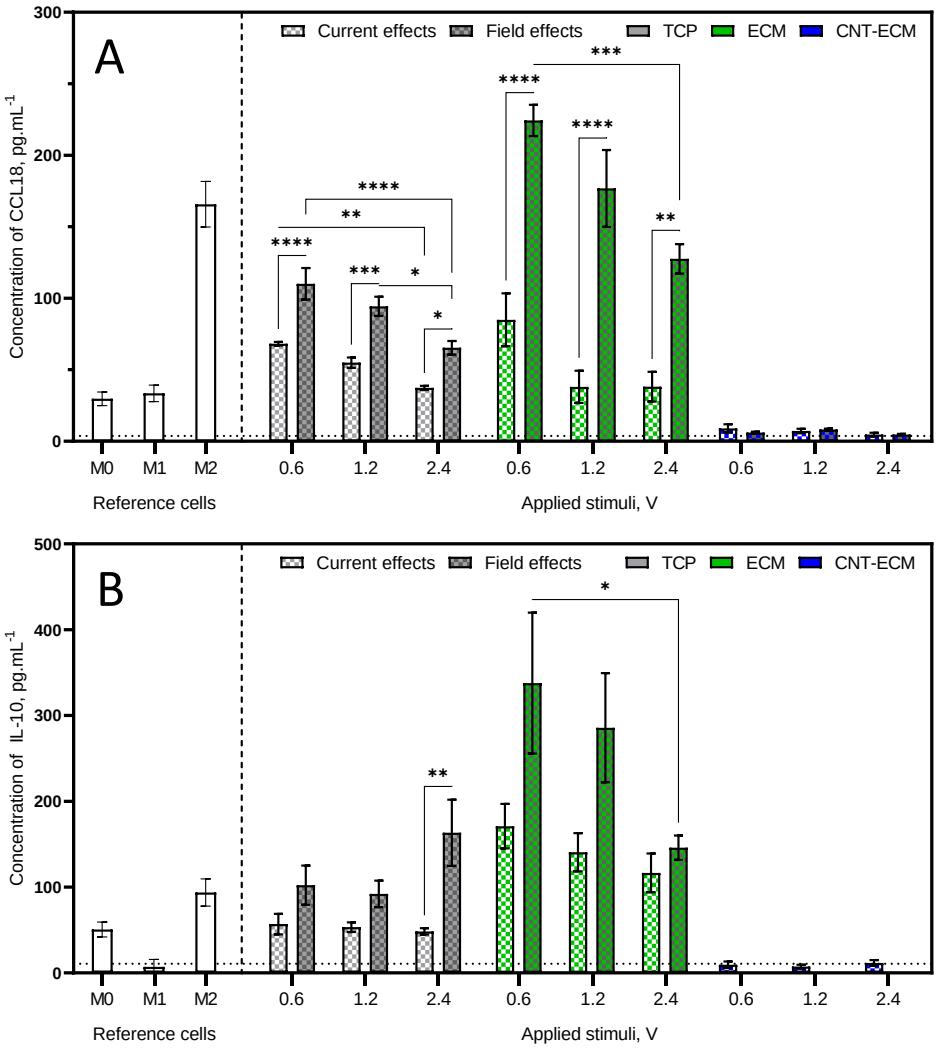

Figure 4.13: Cytokine profiles for M2 markers of THP-1 derived M0-like macrophages (ATCC® TIB-202™) grown on three substrates, 6 days post-stimulation. Cytokine profiles of M2 secreted markers collated via ELISA analysis, CCL18 (A) and IL-10 (B), of cells both grown on different substrates and exposed to varying DC electrical stimulation strengths and types. The substrates used were TCP, ECM only, and CNT-ECM hydrogels. The DC electrical stimulation was applied at 0.6, 1.2, and 2.4 V using either exposed or dielectric ink insulated electrodes to decouple current and field effects. The reference cells were cultured on TCP, supplemented with the relevant cytokine cocktails. The horizontal dotted lines represent the limit of detection calculated for each ELISA kit. Bar graphs represent mean ± SEM. Statistics, comparing intra-substrate data, obtained through a two-way ANOVA; N = 2, n = 3, with each well tested in duplicate.

4.3.4.2 Fibroblast cytokine release

bFGF and HGF were used to investigate the immunomodulatory fibroblast phenotype shown from cells grown in 2.5D post stimulation (Figure 4.14). Unstimulated fibroblasts secrete low levels of bFGF, below that of the limit of detection (Figure 4.14A). Current effect stimulated fibroblasts on TCP show a low, below detection release of bFGF at 0.6 and 1.2 V then a large significant increase at 2.4 V ($P \leq 0.0001$). This trend is not replicated for the field effect stimulation, where bFGF release is above the limit of detection across all three voltages, yet no significant change between them is present. The overall profile of bFGF secretion for cells cultured on TCP is replicated for cells grown on ECM only hydrogels, in that there is little release at 0.6 and 1.2V but relatively large amounts at 2.4 V. This suggests that the addition of a culture substrate has no impact on bFGF secretion whereas electrical stimulation does. CNT-ECM hydrogels stimulated with 2.4 V also possess a higher release profile compared to the other stimuli strengths, yet this is neither significant or above the limit of detection therefore no conclusions can be drawn from this.

Unstimulated fibroblasts secrete low levels of HGF, below that of the limit of detection (Figure 4.14B). This is similar for the stimulated fibroblasts cultured on TCP, however those exposed to 1.2 V current effects show a significant increase ($P \leq 0.05$) which sits above the limit of detection. There is a possibility that this increase in HGF concentration at 1.2 V is linked to a stimulation strength dependant relationship which is then reduced due to the decreased metabolism at the higher strength of 2.4 V. This is unlikely due to no similar impact noted in bFGF release, however, further study would have to be performed to investigate this effect further. The field effect equivalent of 1.2 V stimulation is significantly lower ($P \leq 0.01$), below the limit of detection, and does not fit the same trend. In contrast, the release of HGF by fibroblasts cultured on ECM only hydrogels is consistently higher, indicating that the culture substrate does influence HGF secretion. This is an opposite trend as is seen from the bFGF ELISA, where ECM hydrogels did not seem to influence cytokine

secretion (Figure 4.14A). CNT-ECM hydrogel secretion profiles match that of the TCP release, in that all conditions studied remain below the limit of detection expect for the 1.2 V current effect stimulation.

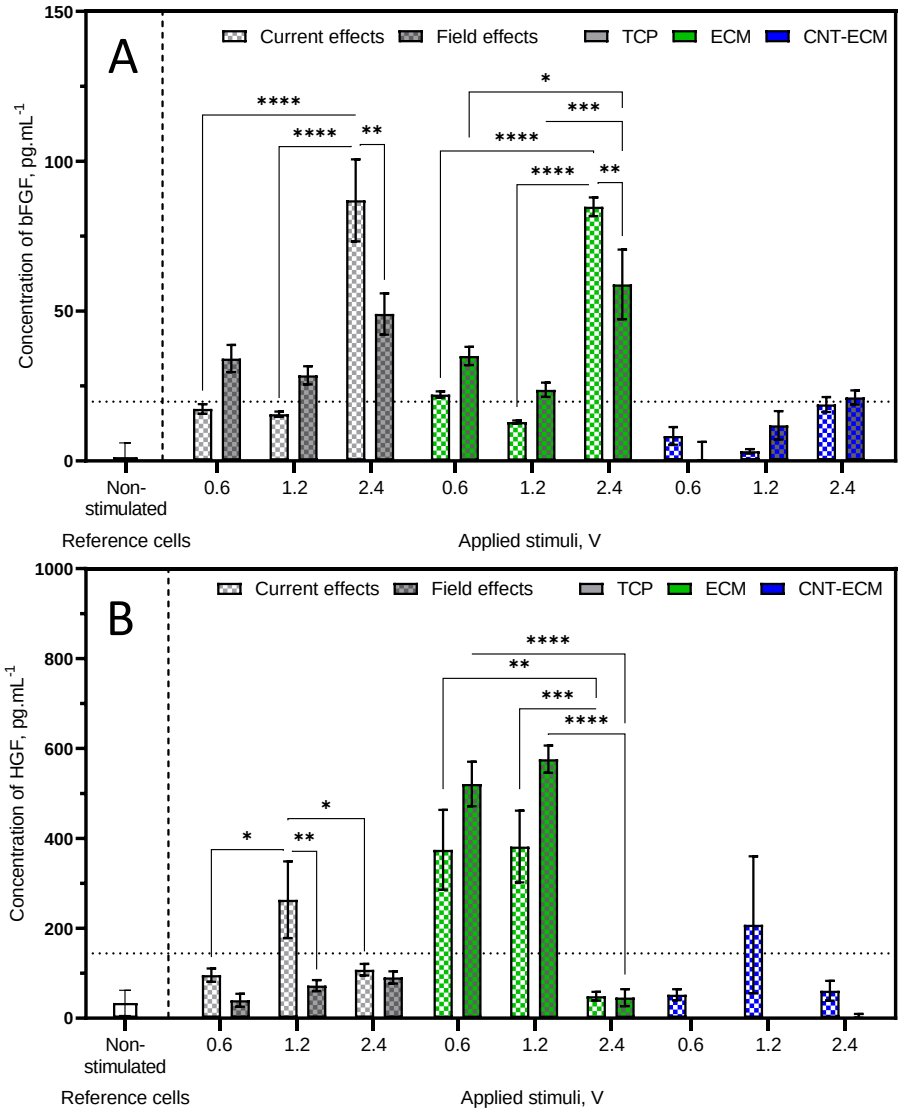

Figure 4.14: Cytokine profiles for pro-immunomodulatory markers of BJ fibroblasts (ATCC® CRL-2522™) grown on three substrates, 4 days post-stimulation. Cytokine profiles of pro-immunomodulatory, anti-fibrotic secreted markers collated via ELISA analysis, bFGF (A) and HGF (B), of cells both grown on different substrates and exposed to varying DC electrical stimulation strengths and types. The substrates used were TCP, ECM only, and CNT-ECM hydrogels. The DC electrical stimulation was applied at 0.6, 1.2, and 2.4 V using either exposed or dielectric ink insulated electrodes to decouple current and field effects. The reference cells were cultured on TCP. The horizontal dotted lines represent the limit of detection calculated for each ELISA kit. Bar graphs represent mean ± SEM. Statistics, comparing intra-substrate data, obtained through a two-way ANOVA; N = 2, n = 3, with each well tested in duplicate.

IL-6 and MCP-1 were used to investigate the inflammatory fibroblast phenotype shown from cells grown in 2.5D post stimulation (Figure 4.15). Non-stimulated fibroblasts secrete more of these inflammatory cytokines relative to the non-inflammatory counterparts, which sit below the limit of detection. IL-6 release of stimulated cells cultured on TCP displays no change in comparison to the unstimulated cells until 2.4 V, for both stimulation types (Figure 4.15A). However, due to the large error within the 2.4 V data there is no significance between this and the lower stimuli strengths. This pattern appears in the IL-6 secretion of cells stimulated with exposed electrodes, cultured on ECM only hydrogels. However, when stimulated with field effects only this large increase at 2.4 V disappears and becomes non-significant in comparison to 0.6 and 1.2 V. The CNT-ECM hydrogel substrate seems to elicit a decrease in IL-6 secretion because of increased current effect stimuli strength, with a significant difference between 0.6 and 2.4 V ($P \leq 0.01$). This trend is not replicated when exposed to field effects.

There is no significance in the secretion of MCP-1 from cells stimulated with current effects on TCP (Figure 4.15B). However, field effect stimulation presents a stimulation strength dependant relationship in which a higher stimulus generates a larger release of MCP-1, with 2.4 V being significantly larger than the current effect equivalent ($P \leq 0.05$). Culture on ECM only and CNT-ECM hydrogels elicited a similar release profile, where current effects decreased MCP-1 release as stimulus strength increased and the stimulation with field effects only elicited no significant difference in secretion.

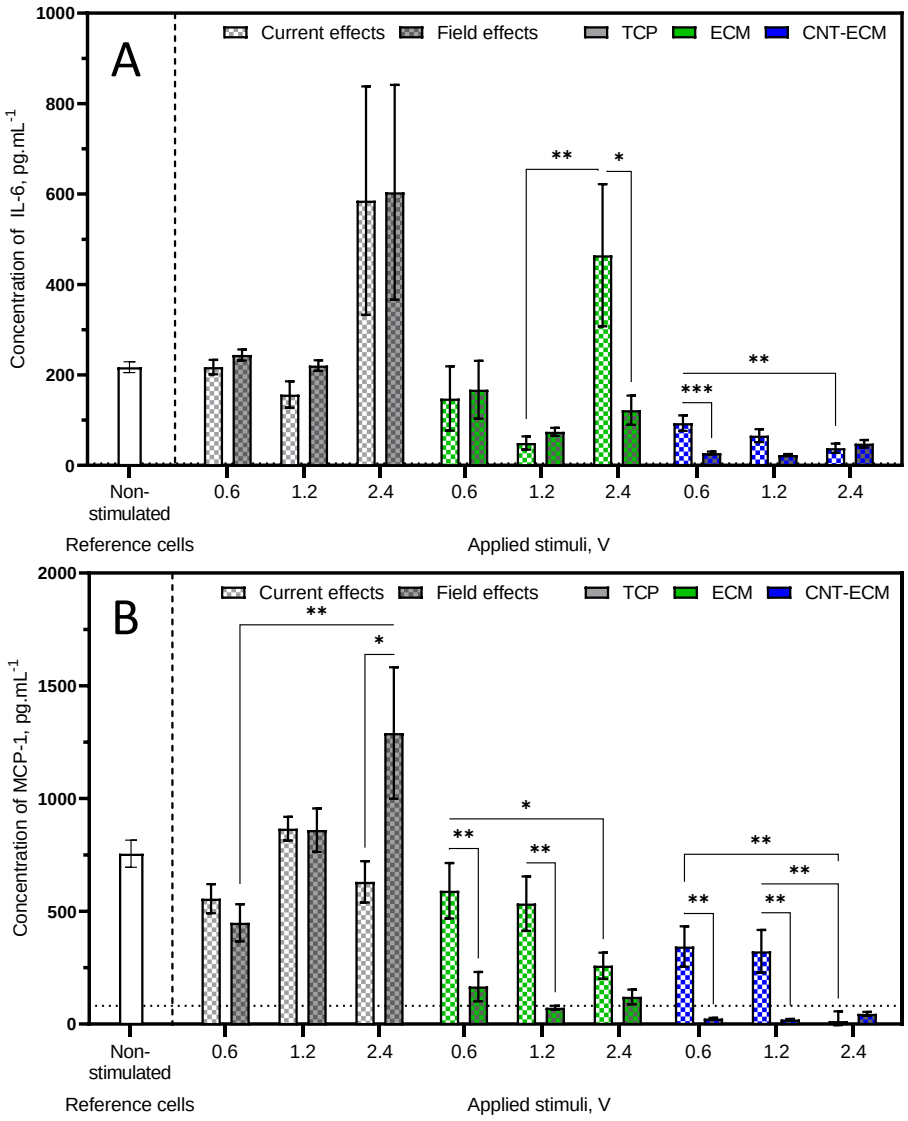

Figure 4.15: Cytokine profiles for pro-inflammatory markers of BJ fibroblasts (ATCC® CRL-2522™) grown on three substrates, 4 days post-stimulation. Cytokine profiles of pro-inflammatory, pro-fibrotic secreted markers collated via ELISA analysis, IL-6 (A) and MCP-1 (B), of cells both grown on different substrates and exposed to varying DC electrical stimulation strengths and types. The substrates used were TCP, ECM only, and CNT-ECM hydrogels. The DC electrical stimulation was applied at 0.6, 1.2, and 2.4 V using either exposed or dielectric ink insulated electrodes to decouple current and field effects. The reference cells were cultured on TCP. The horizontal dotted lines represent the limit of detection calculated for each ELISA kit. Bar graphs represent mean ± SEM. Statistics, comparing intra-substrate data, obtained through a two-way ANOVA; N = 2, n = 3, with each well tested in duplicate.

4.3.5 Impact of growth substrate on cytokine release

As noted in the discussion surrounding Figures 4.12 to 15, there is a large difference in cytokine release compared to cells cultured on ECM only and CNT-ECM hydrogels. Many of the CNT-ECM hydrogel release profiles are below the limit of detection. When viewed

alongside the data in cell viability and metabolism at the relevant stimulation strengths in Figures 4.9 and 11, the lack of cytokine release is unexpected.

Figure 4.16 investigates the cytokine presence of spiked culture media incubated with ECM only and CNT-ECM hydrogels, compared to a TCP control. As expected, the cytokine concentration after 6 days of incubation matches the initial concentration in the spiked media, 150 and 300 $pg.mL^{-1}$ for TNF-α (Figure 4.16A) and CCL18 (Figure 4.16B) respectively. There is a significant difference between these TCP values and the ECM only hydrogel samples (TNF-α, $P \leq 0.01$; CCL18, $P \leq 0.001$). The difference present is likely to be due to protein entrapment within, or adherence to, the ECM fibres or other bioactive molecules within the hydrogels. Whether or not the cytokines which escape detection are active in the sense that cells can interact with them is unknown. Due to this discrepancy between the cytokine concentration of cells cultured on TCP and ECM only hydrogels, the data presented in Figures 4.12 to 15 are not comparable between the substrates. The cytokine release from the CNT-ECM hydrogels used throughout this chapter, at a concentration of 0.2% w/v, is non-existent. However, CNT-ECM hydrogels containing a lower concentration of CNTs does have a detectable level of both TNF-α and CCL18. This is an indication that the reduction of cytokines is a result of the CNTs being present; and is a concentration dependant relationship. CNTs, both single- and multi-walled, are known to form protein corona (Zhang T. et al., 2019; Pinals et al., 2020). Ge et al. (2011) even propose that this adsorption of protein reduces the cytotoxic effects of the CNTs (Luanpitpong et al., 2014). As the actual concentration of cytokines present in CNT-ECM hydrogels throughout this chapter is speculated to be masked by this protein adsorption, it is impossible to draw any conclusions from said data. As previously mentioned, caution is given to data regarding cytokine release from cells cultured on ECM only hydrogels as the results are artificially deflated due to protein adsorption within the hydrogels themselves.

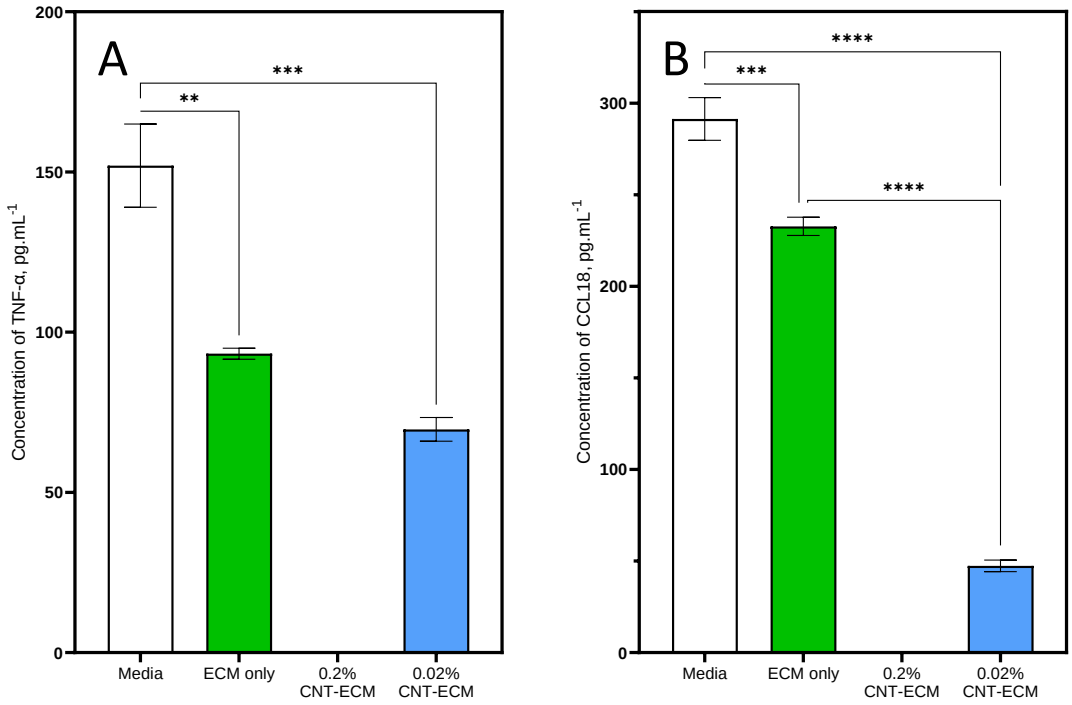

Figure 4.16: Cytokine profiles of spiked cell culture media incubated on four different substrates. Cytokine profiles of TNF-α (A) and CCL18 (B), two secreted markers used to identify M1- and M2-like macrophages, respectively, quantified via ELISA. Cell culture media spiked with 150 and 300 pg.mL^{-1} of each respective marker was incubated for 6 days on TCP (spiked media alone), ECM only hydrogels, and two concentrations of CNT within CNT-ECM hydrogels: 0.2 and 0.02% (w/v). Bar graphs represent mean ± SD. Statistics obtained through a one-way ANOVA; n = 3, with each well tested in duplicate.

4.4 Conclusions

The SIS-ECM only and CNT incorporated hydrogels used in this chapter are a suitable substrate for 2.5D culture of THP-1 derived macrophages, as they provide a biocompatible in vivo-like environment. Culturing macrophages the ECM only substrates, rather than in 2D on TCP, over 6 days shows that inflammatory cytokine induced M1-like phenotypes diminish in their presentation of surface calprotectin while M0 macrophages exhibit very low levels of M1 secreted markers throughout. On the contrary, mannose receptor presentation persists while M2 secreted marker IL-10 presented as significantly higher than those of M0 and M2 macrophages cultured on TCP after 3 days. Field effect electrical stimulation superficially appeared to elicit a pro-immunomodulatory response in THP-1 derived macrophages, shown by the release of both M2 markers used. Opposite effects

were seen with current effect stimuli, with inflammatory markers elevated when employed.

Immunomodulatory cytokines released from fibroblasts display few trends between the stimuli type; only voltage specific significance which would require a larger range of voltage strengths to interpret. Inflammatory markers secreted from TCP cultured fibroblasts do not differ between the stimuli type, yet when paired with an ECM culture substrate the current effect stimuli drives a higher concentration of said markers; indicating, like in the macrophage data, that current effect stimulation drives inflammatory phenotypes.

It is difficult to draw conclusions between the TCP and ECM only hydrogel data, given that it is shown that partial protein entrapment is present in ECM hydrogels, but not in 2D TCP culture. However, it can be speculated that the cytokine release data is artificially lower due to this. Therefore, relative to the TCP data, ECM only hydrogels are suspected to elicit a stronger cytokine response than displayed. This would likely present as increases in both M1 and M2 markers, however it is unknown if all four cytokines analysed would be trapped at consistent rates or whether cytokines are trapped at the same rate regardless of actual concentration. Investigations into CCL18 and TNF-α suggest not, yet more analysis is required before this can be validated.

THP-1 derived macrophage culture on CNT-ECM hydrogels elicited little qualitative data regarding macrophage phenotype due to the opacity of the material, whilst producing relatively low concentrations of secreted markers for both THP-1 derived macrophage and BJ fibroblast populations. This is hypothesised to be due to the formation of protein corona around the CNTs themselves at this concentration, thus no conclusive evidence is noted as to whether the CNT-ECM hydrogel and electrical stimuli in combination promotes an immunomodulatory response.

Chapter 5 | Discussion, future work, and conclusions

Wound care budgets are required to rise consistently, with the increasing proportion of comorbidities in an ageing population (Nussbaum et al., 2018; Storey et al., 2018; Guest et al., 2020). Wound healing research is increasing to combat the cost increase (Figure 5.1). However, most of the research is performed in not settings not representative of the complex in vivo environment. Therefore, the use of modelling systems which include a range of stimuli known to influence the wound healing process is vital in generating data which is more representative and therefore more likely to translate from in vitro to in vivo.

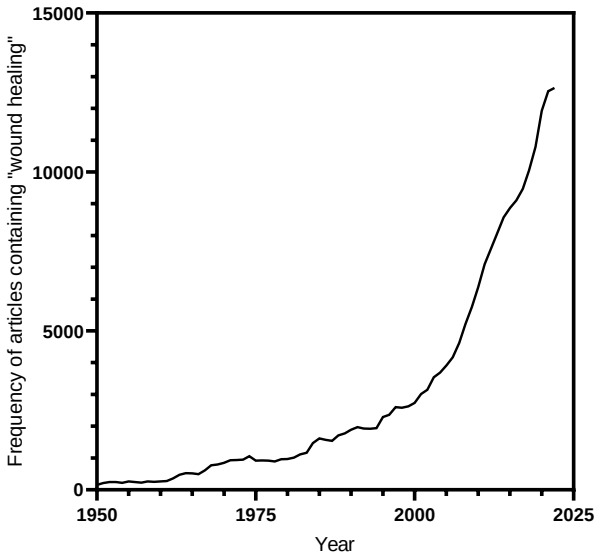

Figure 5.1: The number of publications featuring the phrase "wound healing" between 1950-present. Data acquired via PubMed. 2023 was excluded given an incomplete count.

The goal of this thesis was to investigate the effects of combinatory stimuli on macrophage polarisation. The hypothesis stated that culturing macrophages on an ECM hydrogel and applying an exogenous electrical stimuli propagated by CNTs will drive macrophage polarisation toward an M2-like phenotype. This thesis has combined conducting CNT-ECM hydrogels with exogenous electrical stimuli. In doing so, some inherent complications in

analysing the impact on cellular behaviour, due to inherent properties the CNTs bring, were discovered: the colour and opacity of the generated CNT-ECM hydrogels limiting imaging opportunities, and protein adsorption limiting readouts from ELISA.

5.1 Discussion

5.1.1 SIS decellularisation methods are robust, yet the criteria governing "success" require attention

Within the first results of Chapter 3, SIS was successfully utilised as an organ-derived ECM to generate hydrogels. The protocols used to achieve this did not differ from those previously used in the literature, as the methods had been optimised previously (Badylak et al., 1998). However, subsequent biochemical quantification revealed a remaining dsDNA concentration above that which is stated in the decellularisation criteria published by Crapo et al. (2011). Their summations of the data presented in this thesis would deem the decellularisation ineffective. The reasoning given for this dsDNA quantification to determine effectiveness relates to both comparisons between different ECM products and eliminating antigenic responses because of residual dsDNA. Both reasons are illogical. Firstly, comparisons between ECM products are a challenge that dsDNA quantification fails to tackle. Decellularisation methods can range from mechanical, as with the SIS, to chemical and enzymatic. This can lead to the same tissue type possessing similar amounts of dsDNA yet with varying degrees of matrix damage depending on the technique used (Ji et al., 2018). Said damage could be a key factor when interpreting cellular responses down the line more so than dsDNA content (White et al., 2018; Fernández-Pérez and Ahearne, 2019). Secondly, it was shown in Chapter 4 that regardless of the relatively high dsDNA concentration, the biocompatibility was not impacted. Furthermore, the THP-1 derived macrophages did not activate as a result of the ECM hydrogels. The criteria set out by

Crapo et al. (2011) is wide-spread in the decellularisation community; examples of articles utilising DNases to artificially reduce the dsDNA content is commonplace, negating the point of the analysis. Crapo et al. (2011) also discuss the inclusion of dsDNA fragmentation in the decellularisation success criteria. It could be suggested that this analysis is more appropriate, as this is more valuable in predicting cellular responses in culture (Keane et al., 2012). The data displayed in Chapter 3 demonstrated that while the dsDNA content was relatively high compared to Crapo et al.'s (2011) criteria, the majority of said dsDNA was indeed below 200 bp and thus unlikely to lead to antigenic responses, as noted in viability analysis featured in Chapter 4. To develop an improved set of criteria to determine decellularisation success, more emphasis on non-DNA biochemical analysis would provide a more holistic picture of the decellularisation effectiveness and any resultant damages caused by over-processing tissues.

5.1.2 CNT incorporation influences hydrogel characterisation

The remainder of Chapter 3 presents the impact of allotropes of carbon on the gelation process and subsequent difference in material properties. It was shown that the allotropes do affect the ECM hydrogels in various ways; from the change in colour, to the aggregates formed. The latter of which displayed via electron micrographs and Raman spectral mapping. The rheology data suggests that these aggregates are responsible for a change in the gelation profile of MWCNT-ECM hydrogels; the thermal conductivity of the MWCNTs causes the gelation to initiate quicker, yet also disrupt the gelation process leading to less stiff hydrogels. Hydrogels produced with mixed nanocarbon incorporated did not see this accelerated gelation. However, further analysis identified that these less stiff MWCNT incorporated hydrogels possessed a higher linearity limit, indicating an enhanced resilience upon increased strains. Similarly to gelation, the mixed nanocarbon incorporated exhibited

little deviation from the ECM only hydrogels in comparison to the MWCNTs. This supports the theory that allotrope structure plays a role in the resultant mechanical properties, as mixed nanocarbons displayed no reinforcing properties. These effects were identified as MWCNT concentration dependant properties, with less notable changes exhibited at 0.02% w/v. As desired, the incorporation of MWCNTs into the ECM hydrogels generated a more conductive material. This, like with the mechanical interrogation, was a MWCNT concentration dependant property; hypothesised to be due to no percolation network formed at the 0.02% w/v concentration. This confirms the development of a novel conducting ECM-based biomaterial.

5.1.3 CNT-ECM hydrogels are biocompatible while electrical stimuli are biocompatible at strengths noted in vivo

Chapter 4 began with data confirming that the biomaterials generated in Chapter 3 were biocompatible, utilising both THP-1 derived macrophage and BJ fibroblasts to investigate. This supported what has been noted previously in the literature (see Section 4.3.1). The effect on cell health after a variety of electrical stimuli strengths was assessed and found to follow a strength dependant trend, this was expected given the strengths present in vivo and also through various studies utilising electrical stimuli on mammalian cells (see Section 4.3.3).

5.1.4 ECM hydrogels promote M2 polarity, electrical stimuli influence both phenotypes

Chapter 4 then detailed the impact of hydrogels, MWCNTs, and electrical stimuli on macrophage polarisation. The 2.5D culture on ECM only hydrogels elicited a pro-

immunomodulatory response, with M2 markers enduring while inflammatory surface markers and cytokines decreasing in comparison to TCP controls. This supports previous literature describing the anti-inflammatory properties of the ECM hydrogel (Sacitri et al., 2020).

Field effect stimuli also promoted an anti-inflammatory response from M0 THP-1 derived macrophages, elevating IL-10 and significantly elevating CCL18 relative to the current effect equivalent on both TCP and ECM only hydrogels. Conversely, current effect stimuli saw a rise in IL-6 secretion and TNF-α, the latter of which was significantly elevated during stimulation on ECM only hydrogels. This is suspected to be a result of the stimuli overriding the pro-immunomodulatory effects of the ECM hydrogel. Cytokine release from fibroblasts showed no clear trend regarding substrate type nor type of electrical stimulus.

The data obtained from the CNT-ECM hydrogels was mostly below the limit of detection and thus no conclusions can be drawn, hampering the ability to fully answer the overarching hypothesis. This is hypothesised to be a result of a protein adsorbing property of CNTs. Due to this protein adsorption, which was also observed but to a much lesser degree in ECM only hydrogels, direct comparisons between the different substrates in terms of their cytokine profiles is difficult, as the actual cytokine concentrations are predicted to be artificially lower in ECM only and CNT-ECM hydrogels samples.

5.2 Limitations within the results

The thesis presented contains a novel composite material which demonstrates both a representative environment and the ability to conduct exogenous electrical stimuli. However, this model has limitations which held back the amount of analysis presented as well as the conclusions which can be drawn from this work alone.

CNT-ECM hydrogels are a novel material and therefore have their own challenges when first experimented with. Firstly, the initial ECM product is not homogenous. Due to the animal-based source of the organ, there are inherent variables that differ for both intra- and inter-organ characteristics. Precautions such as selecting the organs from animals of a certain age were employed but these fail to defend against the natural variability. Because of this organ variability, batch-to-batch variability of ECM generated in fundamentally variable too; displayed in the variance shown in the decellularisation metrics presented in Section 3.3.1, and in the rheological and impedance analysis in Sections 3.3.5 and 3.3.6. Given that heterogenous ECM products produce characteristic variable hydrogels, it can be speculated that this variation is likely to influence the cellular response too. Whilst the decellularisation process performed according to protocols established by Badylak et al. (1998), there is a degree of subjectivity regarding how complete it is. Due to the protocol requiring manual delamination, there is always going to be variation between materials decellularised by different research groups as the decellularisation metrics cannot be performed dynamically to analyse decellularisation progress. This is amplified further by the organ variability previously discussed.

The result the organ variability and subjectivity during the decellularisation process can be noted in Figure 5.2, which describes the different concentrations of dsDNA and GAG across three different organ batches. Each batch contains different native concentrations of the decellularisation metrics, with different amounts of variance within the samples per batch.

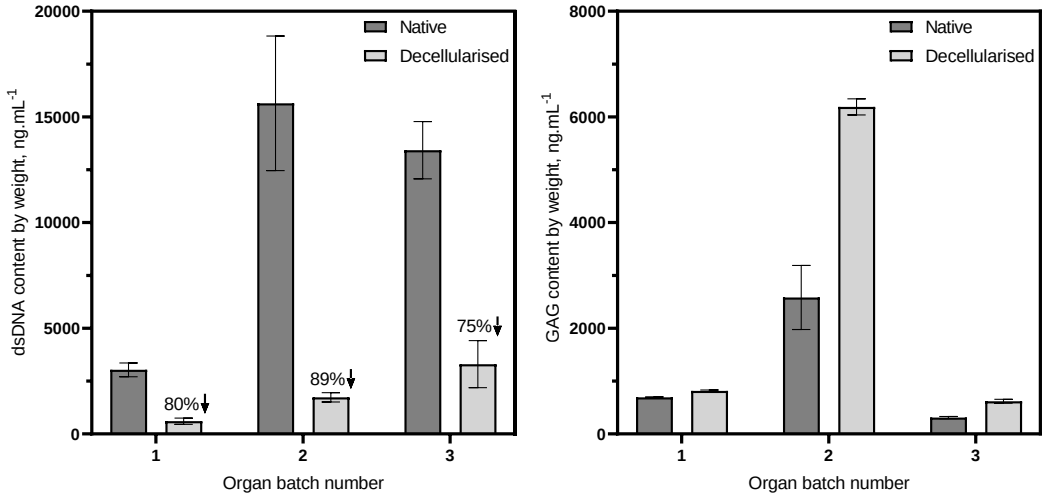

Figure 5.2: Quantification of decellularisation metrics across three separate small intestines. Batch three was used throughout this thesis. Each batch number is N = 1, n = 3, samples were run in triplicate.

A similar limitation arises in the generation of ECM hydrogels. A protocol established by Freytes et al. (2008) was utilised in this work which states that the ECM powder was stirred constantly for ~48 h. However, it was observed in the generation of ECM digest for this thesis that this often generated slightly different products in terms of undigested particulates and therefore viscosity, which led to a downstream impact on the stiffness of the hydrogels generated. Whilst there is no empirical data presented to show for this, it remains a variable to consider when interpreting the data and attempting to produce these materials for future work. Regarding the limitations surrounding the organs and ECM variability, all efforts were made to eliminate variability across the whole thesis. Whilst the decellularisation process was performed three times, the final batch was used throughout the thesis to ensure that the hydrogels generated were as consistent as possible.

Regarding the carbon allotropes, incorporation led to black and opaque hydrogels which had an impact on the ability to perform cell imaging. This, compounded by the challenges in imaging on hydrogels themselves, meant the immunocytochemistry data shown in

Section 4.2 could not be used to determine the substrate influence on macrophage polarity as per surface markers. ELISA, the other polarisation analysis technique used, also had some limitations concerning ECM only and CNT-ECM hydrogels. CNTs are known to adsorb proteins to their surface (Cai et al., 2013), which is suspected to be the cause of the aggregations noted in the FEG SEM micrographs. This also had an effect in the ELISA too, as cytokines secreted by the cells were undetectable in the CNT-ECM hydrogel wells; confirmed to be partially CNT-dependant using cell-free cytokine-spiked media. Whilst the CNT-ECM hydrogels experienced the greatest reduction in cytokine concentrations, ECM only hydrogels also displayed a drop compared to the TCP control. This has implications when drawing conclusions between the growth substrates seen in Section 4.3, as the three are not comparable due to artificially deflated cytokine concentrations to varying degrees. Conclusions can be drawn from the ECM only hydrogel data as most of the cytokines were present above the limit of detection concentration, therefore comparisons can be drawn from within each ECM hydrogel group between the two types of electrical stimuli.

Regardless of the inclusion of CNTs, results obtained from culture on ECM hydrogels alone were difficult to corroborate with the literature. Experiments performed to investigate electrical stimuli in vitro are in their infancy still, with variables inconsistent across the board; from a range of electrical stimuli strengths and exposure times applied via various stimulus types, to a variety of cell types and readouts presented. More standardised experimental design is required across the field to make more confident, and easily supportable advances in this area of research.

Due to the impact of the COVID-19 pandemic, time constraints did not allow for the preliminary cell line experiments to be repeated with primary cells. As reviewed in Section 4.2.1, primary monocytes are the gold standard for macrophage research. They do have limitations themselves, such a donor variability, but given that the rationale of this work

was to develop a more representative, in vivo-like wound healing model the insertion of these therapeutically relevant cells would have been desirable.

5.3 Future work

This section outlines work that either was either being performed or planned yet was halted by the time constraints brought about by the COVID-19 pandemic, whilst also discussing some additional experimental work that would address particular limitations noted in section 5.2, building complimentary data to strengthen the current data, or efforts to further improve the model itself.

5.3.1 Primary cells and co-culture

Primary cells are crucial to enhance this in vivo-like model. Therefore, the incorporation of primary peripheral blood mononuclear cells isolated from whole blood via a buffy coat would greatly improve the model itself. Co-culture is another crucial component not explored in this thesis. Cells do not just interact with other cells of the same type and their environment when in vivo, they communicate to a wide range of cells through a variety of channels. This is especially significant in the wound healing process given that many of the biochemical cues discussed in Section 1.1 arise from cell secreted cytokines which go onto influence the progression of wound healing phases. As discussed in Section 1.1, combining the three major cell types, excluding platelets, involved in the wound healing process would provide the most complete picture of how the cell-cell, cell-ECM, and cell-electrical stimuli interactions co-exist and result in wound healing.

5.3.2 PCR

Investigations into gene expression were planned but halted due to time constraints as a direct result of the COVID-19 pandemic. RNA extraction was made more complex given the 2.5D culture: cells could not be simply harvested, the ECM hydrogels first had to be digested. The results from PCR would be of great interest as they may reveal more information as to the polarisation of macrophages cultured in CNT-ECM hydrogels, given that the inputs are nucleic acid-based and not protein-based. While protein corona would not be an issue here, CNTs are known to interact with nucleic acids too and so further obstacles may disrupt these analyses too (Johnson et al., 2009; Alidori et al., 2013).

5.3.3 Adding further complexity to the wound healing model

Whilst this thesis describes generating a biomaterial which combines the physical and biochemical stimuli provided by an ECM hydrogel, alongside the electrical stimuli applied exogenously yet propagated locally by CNTs, there are some improvements that could be made to further enhance how representative the model is compared to the in vivo environment. Sarmin et al. (2022) demonstrated a hydrogel wound healing model which utilises two separate hydrogel materials, one of decellularised ECM and another of fibrinogen. Utilising two distinct materials in one model generated a “healthy” and “wound” environment, an improvement on the single environment utilised in this thesis. This transition would aim to simulate the transition from healthy tissue to the fibrin plug generated in haemostasis. Therefore, this would be important in further understanding migratory and recruitment kinetics as well as the tissue remodelling phase in which the fibrin plug is replaced with collagen III and then collagen I. A set up proposed in Figure 5.3 may be appropriate as the central hydrogel cylinder would mimic a “wound” environment, with cells recruited from “healthy” ECM, represented by the outer cylinder.

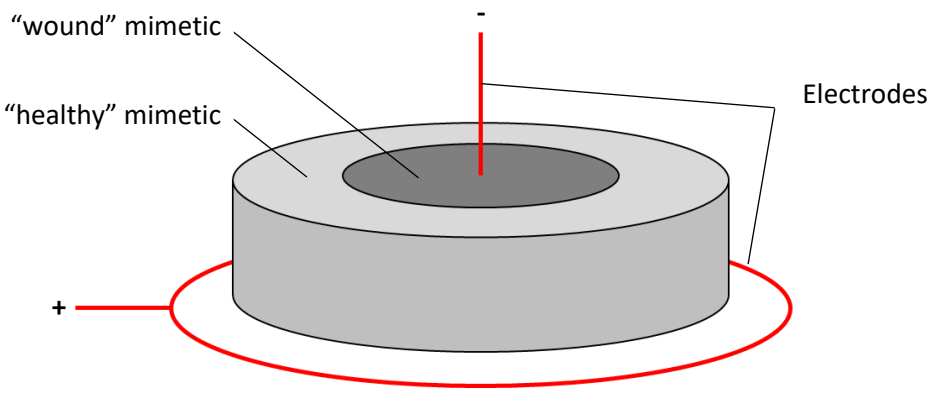

Figure 5.3: A schematic presenting an improved experimental model.

The exogenous electrical stimuli applied in this thesis is quite basic in the sense that it is a static application of a stimuli for a time-period which suited outcomes and logistics rather than purpose. Future work would utilise a dynamic application of an electrical stimuli, one which diminished over time as the elevation in the transepithelial potential during healing does to analyse the modulatory effects on final stage healing, such as contractility. Combining the more sophisticated model with improvements to the way the electrical stimuli were applied would result in much greater insight to the in vivo wound healing process compared to both this thesis and current literature. Figure 5.3 demonstrates this too, with electrodes positioned to best replicate the electric fields propagated from in vivo wounds (Zhao et al., 2006; Long et al., 2018).

5.3.4 Bioinks and 3D bioprinting

The transition from preliminary experimentation to high throughput analysis is required for efficient multi-variable, high sample number analyses. One way of achieving this is through 3D printing. As a result, regenerative medicine and biomaterial research is adopting this technique more and more (Jamee et al., 2021). A considerable amount of work regarding

ECM-based bioprinting has already been published; describing the application of ECM-based bio inks, as reviewed by Wang et al. (2022). However, utilising decellularised matrices is more niche. Currently adipose, cartilage, cardiac, and dermal ECM have been utilised as successful bio inks (Pati et al., 2014; Won et al., 2019). SIS-ECM has been shown to be bioprintable (Sanjuan-Alberte et al., 2022). For this work, Sanjuan-Alberte et al. (2022) used the freeform reversible embedding of suspended hydrogels (FRESH) extrusion bioprinting method. FRESH is a common technique utilised in the bioprinting of hydrogels, given the low viscosity and lack of structural support until gelation is complete (Histon et al., 2015). FRESH also negates the need for UV curing, which is advantageous in relation to the viability of cultures seeded within the bio inks (Jang et al., 2016). Sanjuan-Alberte et al. (2022) conclude that the MWCNT incorporated SIS-ECM hydrogels are not suited to the bioprinting methods described; the following data details the discussion surrounding that conclusion, hypothesises an explanation as to why it occurs, and proposes a future work solution to it.

Figure 5.4 shows the attempts made to print with the three varying concentrations of ECM within the hydrogels: 4, 6, and 8 $mg.mL^{-1}$, as used throughout Chapter 3. None of the prints were successful, nor consistent in the volumes of bio ink extruded (Figures 5.4A to C). Samples were incubated at room temperature to undergo gelation for 40 min, and then at 37 °C for 15 min to melt the gelatine bath. It is clear from Figures 5.4D to F that gelation had not occurred fully, meaning the circular shapes intended ended up as amorphous cohesion of semi-formed CNT-ECM hydrogel. Observations showed that prints were disrupted due to needle blockages (Figure 5.4G); these led to inconsistent extrusion, with some areas of no material and then others with large volumes extruded all at once due to an increased pressure dislodging the blockage. It was this that led to the conclusions that these conducting materials were not suited to these specific bioprinting methods.

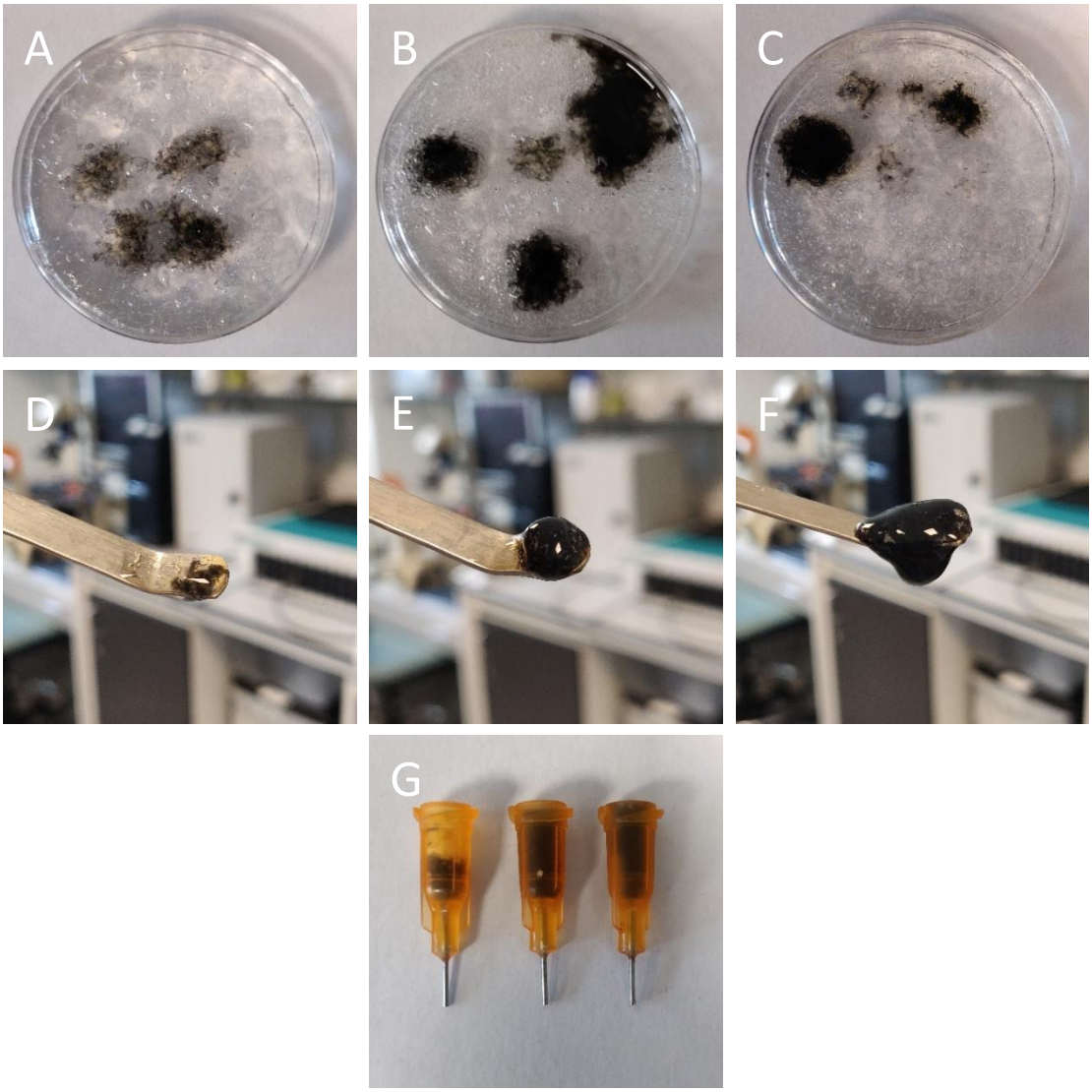

Figure 5.4: Macrophotography of printed CNT-ECM pre-gels in a gelatine bath and the resultant hydrogels created. Pre-gels are mixed in a cartridge on ice and kept there until printing. Three concentrations of ECM were used in the prints: 4 (A), 6 (B), and 8 (C) $mg.mL^{-1}$. The variety of final products produced was quite large. Blockages in the needle mid-print led to small, messy prints (D). Some prints completed without blockages interrupting the extrusion process (E). Other prints were produced with too much extrusion due to an increased pressure used to eject previous blockages. The needles used were 23-gauge (inner diameter: 0.34 mm) and consistently clogged up, leading to material wastage as seen (G).

Regarding the blockages, it was hypothesised that the enhanced thermal conductivity capabilities of the CNT-ECM compared to the ECM only hydrogels (see Section 3.3.5.1) led to gelation beginning in the needle itself prior to, and during, extrusion. This hypothesis explains why SIS-ECM pre-gel was noted as printable (Sanjuan-Alberte et al., 2022), yet CNT-ECM pre-gel is not. The blocking of the extrusion orifice was not noted previously in

the pipette-based technique utilised throughout Chapters 3 and 4, this is suspected to be due to a combination of two factors: diameter and material. Firstly, the inner diameter of the needles used is much smaller than that of the pipette tip. The needles used here have an inner diameter of 0.34 mm vs. 0.83 mm for a 1000 µL TipOne® tip. This means any gelation that may occur will cause a blockage much faster in the needles compared to the tips. Secondly, the needles are metallic and therefore conduct heat much more than the polypropylene of the TipOne® tip. This means that while both are kept on ice prior to extrusion, the metallic needle is much more likely to acclimatise to room temperature faster than that of the polypropylene tips. This then begins to increase the temperature of the pre-gel, initiating gelation sooner.

The incomplete gelation detailed in Figure 5.4D to F must be a result of the CNT-ECM interactions, as complete gelation is noted for ECM only samples (Sanjuan-Alberte et al., 2022). To confirm this suspicion, an adapted rheological analysis was performed (Figure 5.5). Here, the Peltier plate was heated to 21 °C, rather than 37 °C, as room temperature conditions were required for gelation to maintain the gelatine bath. Gelation was shown to occur in both ECM only and CNT-ECM samples, even occurring quicker in CNT-ECM hydrogels as in the analyses performed at 37 °C (Figure 3.7C). The cooler environment led to weaker products after 40 min: 23.7 and 124 Pa for ECM only and CNT-ECM hydrogels, respectively. This is much lower than the stiffnesses noted in Figure 3.7C after only 20 min.

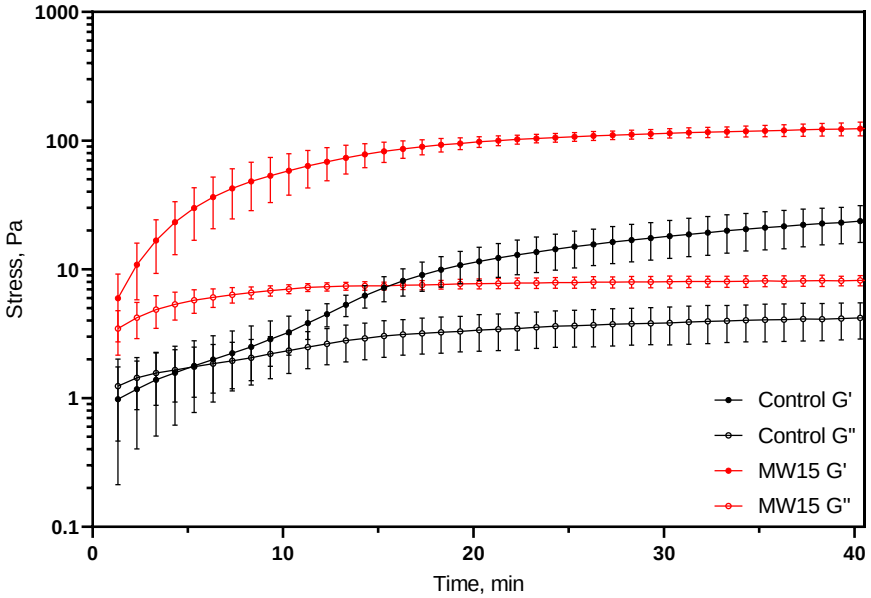

Figure 5.5: Gelation profiles of 8 mg.mL^{-1} ECM only and 0.2% w/v CNT-ECM hydrogels produced at 21 °C. Gelation profile shown as a factor of stress on the storage and loss moduli. n = 3 independent hydrogels.

Figure 5.5 shows that CNT-ECM hydrogels do undergo gelation when incubated at 21 °C, albeit creating a weaker hydrogel. Therefore, the alterations to the gelation temperature are not responsible for the poor printability of the CNT-ECM biomaterial displayed in Figure 5.4D to F. This indicates that the poor printability of the CNT-ECM hydrogels could be a result of the blockages themselves; the partial gelation in the needle prior to extrusion being the cause of incomplete gelation once extruded. This wouldn't be detected by Figure 5.5 given that rheological analysis of the pre-gel within the needle was not investigated.

The way to confirm this hypothesis would be to eliminate the blockages to see if the overall printability improves. This could be achieved in a few ways. Most simply, a lower concentration of MWCNTs incorporated into the ECM hydrogel. This would diminish the thermal properties of the pre-gel and lead to fewer blockages; however, this is to the detriment of the conductive properties as noted between Figures 3.14 and 15. Another workaround could be to use a larger diameter extrusion needle. This may produce less blockages and therefore lead to more consistent prints. However, the larger orifice means

the technique has a reduced resolution, and thus weakens one of the key advantages of printing over pipetting. The solution which would gleam the most comparable data to that already collected would be to use a polypropylene-based needle to extrude from. This way it matches the material of the pipette tip used throughout Chapters 3 and 4, and thus should maintain a lower temperature during the extrusion process. It would clear to determine whether the orifice diameter was a limiting factor too if it were the equivalent 23-gauge used for Figure 5.4.

Utilising the methods laid out, CNT-ECM hydrogels are currently not an ideal biomaterial for bioprinting. However, an alternative ECM hydrogel generation method may be a more suitable way to generate printable ECM hydrogels with or without CNT incorporation. Ultrasonic cavitation describes the generation of an extrudable ECM-based material at temperatures lower than 25 °C (Hussey et al., 2020); ideal for printing using FRESH. This would eliminate the obstacle of gelation occurring at room temperature, as with hydrogel generation via enzymatic digestion. Hussey et al. (2020) demonstrate that this methodology generates a biocompatible hydrogel, with evidence to show that it also drives M2 polarisation. To date no bioprinting or CNT incorporation has been performed using ultrasonic cavitation as a hydrogel generation method.

5.4 Conclusions

The main hypothesis of this thesis was that culturing macrophages on an ECM hydrogel and applying an exogenous electrical stimuli propagated by CNTs will drive macrophage polarisation toward an M2-like phenotype. The data presented in this thesis confirm that ECM hydrogel culturing promotes M2-like responses, while demonstrating that the type of stimuli applied also plays a role in the macrophage phenotypic response. Unfortunately,

the experiments performed to test the CNT aspect of the hypothesis were inconclusive due to several obstacles resulting from the colour and adsorptive properties of the CNT-ECM hydrogels.

This thesis demonstrated that SIS decellularisation success does not rely on the dsDNA content as heavily as the guidelines stated in the literature suggest; this only promotes 'over-decellularisation' as well as the use of DNase. The incorporation of CNTs into an ECM hydrogel generated a novel biomaterial, with softer mechanical and enhanced electrical properties. Whilst the polarisation-based assays failed to capture cell responses to the CNT-ECM hydrogels, the materials themselves at least proved to be biocompatible. The results presented were consistent with previous work in that both THP-1 culture on ECM hydrogels and exogenous electric field stimuli applied separately promoted M2-like phenotypes. This thesis went onto describe, for the first time, the greater M2-like promotion when the two were combined. This was the case even though the degree to which this occurred was artificially masked; with the cytokine release suppressed when cells were culture on the ECM hydrogels.

The experimental data presented here demonstrates the importance of increasing how representative the microenvironment is when it comes to obtaining cellular readouts. Further optimisation of experimental methods would be required to delve deeper into the specific impact of the CNT-laden ECM hydrogels, however this thesis highlights obstacles for the next stage of research to overcome in order to progress. It was always known that the development of more complex cell culture models would lead to more complicated experimental design, data acquisition, and interpretation; the hope is that the continued development of said models leads to more efficient research performed using highly representative in vivo-like mimetics.

References

Aamodt, J. and Grainger, D., 2016. Extracellular matrix-based biomaterial scaffolds and the host response. Biomaterials, 86, pp.68-82.

Abd Hamid, A., Gall, C., Speck, O., Antal, A. and Sabel, B., 2015. Effects of alternating current stimulation on the healthy and diseased brain. Frontiers in Neuroscience, 9.

Adler, V., Yin, Z., Tew, K.D., Ronai, Z., 1999. Role of redox potential and reactive oxygen species in stress signaling. Oncogene 18, pp.6104–6111.

Ahmed, S., Johnson, Robert.T., Solanki, R., Afewerki, T., Wostear, F., Warren, Derek.T., 2022. Using polyacrylamide hydrogels to model physiological aortic stiffness reveals that microtubules are critical regulators of isolated smooth muscle cell morphology and contractility. Frontiers in Pharmacology 13.

Aisenbrey, E.A., Murphy, W.L., 2020. Synthetic Alternatives to matrigel. Nature Reviews Materials 5, pp.539–551.

Alarcon, E.I., Udekwu, K., Skog, M., Pacioni, N.L., Stamplecoskie, K.G., González-Béjar, M., Polisetti, N., Wickham, A., Richter-Dahlfors, A., Griffith, M., Scaiano, J.C., 2012. The biocompatibility and antibacterial properties of collagen-stabilized, photochemically prepared silver nanoparticles. Biomaterials 33, pp.4947–4956.

Alidori, S., Asqiriba, K., Londero, P., Bergkvist, M., Leona, M., Scheinberg, D.A., McDevitt, M.R., 2013. Deploying RNA and DNA with functionalized carbon nanotubes. The Journal of Physical Chemistry C 117, 5982–5992.

Amaral, D., de Souza Salomão Zanette, R., Torres de Souza, G., Augusto da Silva, S., Adriano Kopke de Aguiar, J., Fortes Marcomini, R., Márcio Resende do

Carmo, A., Valentim Nogueira, B., José da Silva Barros, R., de Sá Silva, F., de Oliveira Santos, M., Munk, M., de Mello Brandão, H. and Magno da Costa Maranduba, C., 2020. Induction of osteogenic differentiation by demineralized and decellularized bovine extracellular matrix derived hydrogels associated with barium titanate. Biologicals, 66, pp.9-16.

Amaral, S., Linderman, J., Morse, M. And Greene, A., 2001. Angiogenesis Induced by Electrical Stimulation Is Mediated by Angiotensin II and VEGF. Microcirculation, 8(1), pp.57-67.

Antoni, D., Burckel, H., Josset, E., and Noel, G., 2015. Three-dimensional cell culture: a breakthrough in vivo. Int. J. Mol. Sci. 16, 5517–5527.

Armbruster, D.A., Pry, T., 2008. Limit of Blank, Limit of Detection and Limit of Quantitation. The Clinical Biochemist Reviews 29.

Assunção, M., Dehghan-Baniani, D., Yiu, C.H., Später, T., Beyer, S., Blocki, A., 2020. Cell-derived extracellular matrix for tissue engineering and Regenerative Medicine. Frontiers in Bioengineering and Biotechnology 8.

Atri, C., Guerfali, F. and Laouini, D., 2018. Role of Human Macrophage Polarization in Inflammation during Infectious Diseases. International Journal of Molecular Sciences, 19(6), p.1801.

Aumailley, M., 2013. The laminin family. Cell Adhesion & Migration 7, 48–55.

Badylak, S., Freytes, D. and Gilbert, T., 2009. Extracellular matrix as a biological scaffold material: Structure and function. Acta Biomaterialia, 5(1), pp.1-13.

Badylak, S., Lantz, G., Coffey, A. and Geddes, L., 1989. Small intestinal submucosa as a large diameter vascular graft in the dog. Journal of Surgical Research, 47(1), pp.74-80.

Badylak, S., Record, R., Lindberg, K., Hodde, J. and Park, K., 1998. Small intestinal submucosa: a substrate for in vitro cell growth. Journal of Biomaterials Science, Polymer Edition, 9(8), pp.863-878.

Badylak, S.F., Tullius, R., Kokini, K., Shelbourne, K.D., Klootwyk, T., Voytik, S.L., Kraine, M.R., Simmons, C., 1995. The use of xenogeneic small intestinal submucosa as a biomaterial for Achille's tendon repair in a dog model. Journal of Biomedical Materials Research 29, 977–985.

Bainbridge, P., 2013. Wound healing and the role of fibroblasts. Journal of Wound Care 22, pp.407–412.

Baker, L., Rubayi, S., Villar, F. and Demuth, S., 1996. Effect of electrical stimulation waveform on healing of ulcers in human beings with spinal cord injury. Wound Repair and Regeneration, 4(1), pp.21-28.

Balandin, A., Ghosh, S., Bao, W., Calizo, I., Teweldebrhan, D., Miao, F. and Lau, C., 2008. Superior Thermal Conductivity of Single-Layer Graphene. Nano Letters, 8(3), pp.902-907.

Baptista, P.M., Siddiqui, M.M., Lozier, G., Rodriguez, S.R., Atala, A., Soker, S., 2011. The use of whole organ decellularization for the generation of a vascularized liver organoid. Hepatology 53, 604–617.

Bard, A. and Faulkner, L. (2001). Electrochemical methods and applications. 2nd ed. New York: Wiley-Interscience

Barendse-Hofmann M., Steenvoorde P., van Doorn L., Jacobi C., Oskam J., Hedeman P., 2007. Extracellular wound matrix (OASIS®): exploring the contraindications. Results of its use in 32 consecutive outpatient clinic cases. Wounds, 19(10), pp.258-263.

Bartneck, M., Schulte, V., Paul, N., Diez, M., Lensen, M. and Zwadlo-Klarwasser, G., 2010. Induction of specific macrophage subtypes by defined micro-patterned structures. Acta Biomaterialia, 6(10), pp.3864-3872.

Barton, S. and Marks, R., 1984. Measurement of collagen-fibre diameter in human skin. Journal of Cutaneous Pathology, 11(1), pp.18-26.

Bashir, S., Hina, M., Iqbal, J., Rajpar, A.H., Mujtaba, M.A., Alghamdi, N.A., Wageh, S., Ramesh, K., Ramesh, S., 2020. Fundamental concepts of hydrogels: Synthesis, properties, and their applications. Polymers 12, 2702.

Baum, C.L., Arpey, C.J., 2006. Normal cutaneous wound healing: Clinical correlation with cellular and molecular events. Dermatologic Surgery 31, pp.674–686.

Bennett, S., Adeleye, A., Ji, Z. and Keller, A., 2013. Stability, metal leaching, photoactivity and toxicity in freshwater systems of commercial single wall carbon nanotubes. Water Research, 47(12), pp.4074-4085.

Berg, J., Tymoczko, J. and Stryer, L., 2002. Biochemistry. 5th ed. New York: WH Freeman, Section 25.5: Nucleotide Mono-, Di-, and Triphosphates Are Interconvertible.

Bertani, F., Mozetic, P., Fioramonti, M., Iuliani, M., Ribelli, G., Pantano, F., Santini, D., Tonini, G., Trombetta, M., Businaro, L., Selci, S. and Rainer, A., 2017. Classification of M1/M2-polarized human macrophages by label-free hyperspectral reflectance confocal microscopy and multivariate analysis. Scientific Reports, 7(1).

Bertula, K., Martikainen, L., Munne, P., Hietala, S., Klefström, J., Ikkala, O., Nonappa, 2019. Strain-stiffening of agarose gels. ACS Macro Letters 8, 670–675.

Beugels, J., Molin, D., Ophelders, D., Rutten, T., Kessels, L., Kloosterboer, N., Grzymala, A., Kramer, B., van der Hulst, R. and Wolfs, T., 2019. Electrical

stimulation promotes the angiogenic potential of adipose-derived stem cells. Scientific Reports, 9(1).

Bhattacharya, A. and Mahajan, R., 2003. Temperature dependence of thermal conductivity of biological tissues. Physiological Measurement, 24(3), pp.769-783.

Birk, D.E., Silver, F.H., 1984. Collagen fibrillogenesis in vitro: Comparison of types I, II, and III. Archives of Biochemistry and Biophysics 235, 178–185.

Bishop, J., Schuksz, M. and Esko, J., 2007. Heparan sulphate proteoglycans fine-tune mammalian physiology. Nature, 446(7139), pp.1030-1037.

Bissell, M. and Barcellos-Hoff, M. (1987). The Influence of Extracellular Matrix on Gene Expression: Is Structure the Message? Journal of Cell Science, 1987(Supplement 8), pp.327- 343.

Bosshart, H. and Heinzelmann, M., 2016. THP-1 cells as a model for human monocytes. Annals of Translational Medicine, 4(21), pp.438-438.

Bresadola, M., 1998. Medicine and science in the life of Luigi Galvani (1737–1798). Brain Research Bulletin, 46(5), pp.367-380.

Briard, B., Place, D.E., Kanneganti, T.-D., 2020. DNA sensing in the innate immune response. Physiology 35, 112–124.

Brightman, A.O., Rajwa, B.P., Sturgis, J.E., McCallister, M.E., Robinson, J.P., Voytik-Harbin, S.L., 2000. Time-lapse confocal reflection microscopy of collagen fibrillogenesis and extracellular matrix assembly in vitro. Biopolymers 54, 222–234.

Brown, S., Jorio, A., Dresselhaus, M. and Dresselhaus, G., 2001. Observations of theD-band feature in the Raman spectra of carbon nanotubes. Physical Review B, 64(7).

Bullen, A., O'Hara, K., Cahill, D., Monteiro, O. and von Keudell, A., 2000. Thermal conductivity of amorphous carbon thin films. Journal of Applied Physics, 88(11), pp.6317-6320.

Burdick, J.A., Prestwich, G.D., 2011. Hyaluronic acid hydrogels for biomedical applications. Advanced Materials 23.

Cai, L. and Wang, C., 2015. Carbon Nanotube Flexible and Stretchable Electronics. Nanoscale Research Letters, 10(1).

Cai, X., Ramalingam, R., Wong, H., Cheng, J., Ajuh, P., Cheng, S. and Lam, Y., 2013. Characterization of carbon nanotube protein corona by using quantitative proteomics. Nanomedicine: Nanotechnology, Biology and Medicine, 9(5), pp.583-593.

Caliari, S., Vega, S., Kwon, M., Soulas, E. and Burdick, J., 2016. Dimensionality and spreading influence MSC YAP/TAZ signaling in hydrogel environments. Biomaterials, 103, pp.314-323.

Caliari, S.R., Burdick, J.A., 2016. A practical guide to hydrogels for cell culture. Nature Methods 13, 405–414.

Canty, E.G., Kadler, K.E., 2005. Procollagen trafficking, processing and fibrillogenesis. Journal of Cell Science 118, 1341–1353.

Cao, Q., Yu, Q., Connell, D. and Yu, G., 2013. Titania/carbon nanotube composite (TiO2/CNT) and its application for removal of organic pollutants. Clean Technologies and Environmental Policy, 15(6), pp.871-880.

Carragher, N.O., Levkau, B., Ross, R., Raines, E.W., 1999. Degraded collagen fragments promote rapid disassembly of smooth muscle focal adhesions that correlates with cleavage of pp125fak, paxillin, and Talin. Journal of Cell Biology 147, pp.619–630.

Casale, J., Crane, J., 2022. Glycosaminoglycans. In: Biochemistry. StatPearl [Internet], Treasure Island, FL.

Catoira, M.C., Fusaro, L., Di Francesco, D., Ramella, M., Boccafoschi, F., 2019. Overview of natural hydrogels for Regenerative Medicine Applications. Journal of Materials Science: Materials in Medicine 30.

Catterall, W., 2011. Voltage-Gated Calcium Channels. Cold Spring Harbor Perspectives in Biology, 3(8), pp.a003947-a003947.

Cavo, M., Fato, M., Peñuela, L., Beltrame, F., Raiteri, R., Scaglione, S., 2016. Microenvironment complexity and matrix stiffness regulate breast cancer cell activity in a 3D in vitro model. Scientific Reports 6.

Cazzell S., Lange D., Dickerson Jr. J., Slade H., 2015. The management of diabetic foot ulcers with porcine small intestine submucosa tri-layer matrix: A randomized controlled trial. Advances in Wound Care, 4(12), pp.711–718.

Cha, B.H., Shin, S.R., Leijten, J., Li, Y.C., Singh, S., Liu, J.C., Annabi, N., Abdi, R., Dokmeci, M.R., Vrana, N.E., Ghaemmaghami, A.M., Khademhosseini, A., 2017. Integrin-mediated interactions control macrophage polarization in 3D hydrogels. Advanced Healthcare Materials 6, 1700289.

Chakraborty, J., Roy, S. and Ghosh, S., 2020. Regulation of decellularized matrix mediated immune response. Biomaterials Science, 8(5), pp.1194-1215.

Chan, K., Patton, D. and Cosgrove, Y., 1989. Time-lapse video microscopic study of in vitro wound closure in rabbit corneal cells. Investigative Ophthalmology & Visual Science, 30(12), pp.2488-2498.

Chan, W.W., Yu, F., Le, Q.B., Chen, S., Yee, M., Choudhury, D., 2021. Towards biomanufacturing of cell-derived matrices. International Journal of Molecular Sciences 22, 11929.

Chang, S. and Buehler, M., 2014. Molecular biomechanics of collagen molecules. Materials Today, 17(2), pp.70-76.

Chanput, W., Mes, J. and Wichers, H., 2014. THP-1 cell line: An in vitro cell model for immune modulation approach. International Immunopharmacology, 23(1), pp.37-45.

Chaudhuri, O., Cooper-White, J., Janmey, P.A., Mooney, D.J., Shenoy, V.B., 2020. Effects of extracellular matrix viscoelasticity on cellular behaviour. Nature 584, pp.535–546.

Chen, C., Bai, X., Ding, Y. and Lee, I., 2019. Electrical stimulation as a novel tool for regulating cell behavior in tissue engineering. Biomaterials Research, 23(1).

Chen, D., Smith, L.R., Khandekar, G., Patel, P., Yu, C.K., Zhang, K., Chen, C.S., Han, L., Wells, R.G., 2020. Distinct effects of different matrix proteoglycans on collagen fibrillogenesis and cell-mediated collagen reorganization. Scientific Reports 10.

Chen, D., Smith, L.R., Khandekar, G., Patel, P., Yu, C.K., Zhang, K., Chen, C.S., Han, L., Wells, R.G., 2020. Distinct effects of different matrix proteoglycans on collagen fibrillogenesis and cell-mediated collagen reorganization. Scientific Reports 10.

Chen, R.J., Choi, H.C., Bangsaruntip, S., Yenilmez, E., Tang, X., Wang, Q., Chang, Y.-L., Dai, H., 2004. An investigation of the mechanisms of electronic sensing of

protein adsorption on carbon nanotube devices. Journal of the American Chemical Society 126, 1563–1568.

Chen, X., Wang, Y., Ma, S., Huang, Y., Jing, W., Wei, P., Yu, X. and Zhao, B., 2022. Mechanically active small intestinal submucosa hydrogel for accelerating chronic wound healing. Journal of Materials Chemistry B, 10(33), pp.6279-6286.

Chen, Y., Ye, L., Guan, L., Fan, P., Liu, R., Liu, H., Chen, J., Zhu, Y., Wei, X., Liu, Y. and Bai, H. (2018). Physiological electric field works via the VEGF receptor to stimulate neovessel formation of vascular endothelial cells in a 3D environment. Biology Open, 7(9), pp.1-8.

Cheng, H.-W., Tsui, Y.-K., Cheung, K.M.C., Chan, D., Chan, B.P., 2009. Decellularization of chondrocyte-encapsulated collagen microspheres: A three-dimensional model to study the effects of acellular matrix on Stem cell fate. Tissue Engineering Part C: Methods 15, pp.697–706.

Chia, H.N., Vigen, M., Kasko, A.M., 2012. Effect of substrate stiffness on pulmonary fibroblast activation by TGF-β. Acta Biomaterialia 8, pp.2602–2611.

Chintala, S., Sawaya, R., Gokaslan, Z. and Rao, J., 1996. The effect of type III collagen on migration and invasion of human glioblastoma cell lines in vitro. Cancer Letters, 102(1-2), pp.57-63.

Chrysafides SM, Bordes S, Sharma S. Physiology, Resting Potential. “Physiology, Resting Potential”, in StatPearls [Internet], 2021, Accessed on 25/05/2023. Available from: ncbi.nlm.nih.gov/books/NBK538338/

Clark, R.A., 1990. Fibronectin matrix deposition and fibronectin receptor expression in healing and normal skin. Journal of Investigative Dermatology 94.

Clover, A.J.P., Salwa, S.P., Bourke, M.G., McKiernan, J., Forde, P.F., O'Sullivan, S.T., Kelly, E.J., Soden, D.M., 2020. Electrochemotherapy for the treatment of primary basal cell carcinoma; a randomised control trial comparing electrochemotherapy and surgery with five year follow up. European Journal of Surgical Oncology 46, pp.847–854.

Coelho, P.H., Morales, A.R., 2014. Electrical conductivity, percolation threshold and dispersion properties of PMMA nanocomposites of hybrid conducting fillers. 14th IEEE International Conference on Nanotechnology.

Conboy, I., Freimer, J., Weisenstein, L., Liu, Y., Mehdipour, M., Gathwala, R., 2017. 6.13 tissue engineering of muscle tissue. Comprehensive Biomaterials II 216–235.

Corning, 2021. Corning® Matrigel® Matrix: Frequently asked questions. [Online] Available at: <https://www.corning.com/catalog/cls/documents/faqs/CLS-DL-CC-026.pdf> [Accessed 12/11/2022].

Corominas-Murtra, B., Petridou, N.I., 2021. Viscoelastic networks: Forming cells and tissues. Frontiers in Physics 9.

Coskun Benlidayi, I., 2020. The effectiveness and safety of electrotherapy in the management of fibromyalgia. Rheumatology International, 40(10), pp.1571-1580.

Costa, E. C., Moreira, A. F., de Melo-Diogo, D., Gaspar, V. M., Carvalho, M. P., and Correia, I. J., 2016. 3D tumor spheroids: an overview on the tools and techniques used for their analysis. Biotechnol. Adv. 1427–1441.

Cracchiolo, M., Ottaviani, M., Panarese, A., Strauss, I., Vallone, F., Mazzoni, A. and Micera, S., 2021. Bioelectronic medicine for the autonomic nervous

system: clinical applications and perspectives. Journal of Neural Engineering, 18(4), p.041002.

Crapo, P., Gilbert, T. and Badylak, S., 2011. An overview of tissue and whole organ decellularization processes. Biomaterials, 32(12), pp.3233-3243.

Cui, S., Mao, J., Rouabhia, M., Elkoun, S., Zhang, Z., 2021. A biocompatible polypyrrole membrane for biomedical applications. RSC Advances 11, pp.16996–17006.

Custódio, C., Alves, C., Reis, R. and Mano, J., 2010. Immobilization of fibronectin in chitosan substrates improves cell adhesion and proliferation. Journal of Tissue Engineering and Regenerative Medicine, 4(4), pp.316-323.

D'Agostino, A., Stellavato, A., Busico, T., Papa, A., Tirino, V., Papaccio, G., La Gatta, A., De Rosa, M., Schiraldi, C., 2015. In vitro analysis of the effects on wound healing of high- and low-molecular weight chains of hyaluronan and their hybrid H-HA/L-HA complexes. BMC Cell Biology 16.

Dallon, J., Sherratt, J., Maini, P. And Ferguson, M., 2000. Biological implications of a discrete mathematical model for collagen deposition and alignment in dermal wound repair. IMA Journal of Mathematical Control and Information, 17(4), pp.379-393.

Darby, I., Laverdet, B., Bonté, F. and Desmouliere, A., 2014. Fibroblasts and myofibroblasts in wound healing. Clinical, Cosmetic and Investigational Dermatology, p.301.

Das, R., Langou, S., Le, T.T., Prasad, P., Lin, F., Nguyen, T.D., 2022. Electrical stimulation for immune modulation in cancer treatments. Frontiers in Bioengineering and Biotechnology 9.

Dean, D., Ramanathan, T., Machado, D. and Sundararajan, R., 2008. Electrical impedance spectroscopy study of biological tissues. Journal of Electrostatics, 66(3-4), pp.165-177.

Deshmane, S., Kremlev, S., Amini, S. and Sawaya, B., 2009. Monocyte Chemoattractant Protein-1 (MCP-1): An Overview. Journal of Interferon & Cytokine Research, 29(6), pp.313-326.

DiBartola, SP. and De Morais, HA., 2012. Fluid, Electrolyte, and Acid-Base Disorders in Small Animal Practice. 4th ed. Missouri: Saunders Elsevier, pp.92-119.

Dick MK, Miao JH, Limaiem F. Histology, Fibroblast, in StatPearls [Internet], 2022, Accessed on 25/05/2023. Available from: ncbi.nlm.nih.gov/books/NBK541065/

Dinçer, I. and Zamfirescu, C., 2016. Drying Phenomena: Theory and Applications. 1st ed. John Wiley & Sons Inc, Appendix B.

DiPietro, L.A., 2016. Angiogenesis and wound repair: When enough is enough. Journal of Leukocyte Biology 100, 979–984.

Dirr, E., Urdaneta, M., Patel, Y., Johnson, R., Campbell-Thompson, M. and Otto, K., 2020. Designing a bioelectronic treatment for Type 1 diabetes: targeted parasympathetic modulation of insulin secretion. Bioelectronics in Medicine, 3(2), pp.17-31.

Dominguez, R. and Holmes, K. (2011). Actin Structure and Function. Annual Review of Biophysics, 40(1), pp.169-186.

Dong, R., Ma, P.X., Guo, B., 2020. Conductive biomaterials for muscle tissue engineering. Biomaterials 229, 119584.

Doucet, F.J., Lead, J.R., Maguire, L., Achterberg, E.P., Millward, G.E., 2005. Visualisation of natural aquatic colloids and particles – A comparison of conventional

high vacuum and environmental scanning electron microscopy. Journal of Environmental Monitoring 7, 115.

Dowsett, C., Bielby, A., Searle, R., 2014. Reconciling increasing wound care demands with available resources. Journal of Wound Care 23, 552–562.

Dozmorov, M., Kyker, K., Saban, R., Knowlton, N., Dozmorov, I., Centola, M. and Hurst, R. (2006). Analysis of the interaction of extracellular matrix and phenotype of bladder cancer cells. BMC Cancer, 6(1).

Dresselhaus, M., Dresselhaus, G., Saito, R. and Jorio, A., 2005. Raman spectroscopy of carbon nanotubes. Physics Reports, 409(2), pp.47-99.

Du Bois-Reymond, E., 1848. Untersuchungen über die thierische Elektrizität [Investigations into Animal Electricity]. Reimer.

Dubé, J., Rochette-Drouin, O., Lévesque, P., Gauvin, R., Roberge, C.J., Auger, F.A., Goulet, D., Bourdages, M., Plante, M., Germain, L., Moulin, V.J., 2010. Restoration of the transepithelial potential within tissue-engineered human skin in vitro and during the wound healing process in vivo. Tissue Engineering Part A 16, pp.3055–3063.

Dürkop, T., Getty, S.A., Cobas, E., Fuhrer, M.S., 2003. Extraordinary mobility in semiconducting carbon nanotubes. Nano Letters 4, 35–39.

Duval, K., Grover, H., Han, L., Mou, Y., Pegoraro, A., Fredberg, J. and Chen, Z., 2017. Modeling Physiological Events in 2D vs. 3D Cell Culture. Physiology, 32(4), pp.266-277.

Edgar, S., Hopley, B., Genovese, L., Sibilla, S., Laight, D. and Shute, J., 2018. Effects of collagen-derived bioactive peptides and natural antioxidant compounds on proliferation and matrix protein synthesis by cultured normal human dermal fibroblasts. Scientific Reports, 8(1).

Edmondson, R., Broglie, J., Adcock, A. and Yang, L., 2014. Three-Dimensional Cell Culture Systems and Their Applications in Drug Discovery and Cell-Based Biosensors. ASSAY and Drug Development Technologies, 12(4), pp.207-218.

Ellis, S., Lin, E.J., Tartar, D., 2018. Immunology of wound healing. Current Dermatology Reports 7, 350–358.

El Masry, M.S., Chaffee, S., Das Ghatak, P., Mathew-Steiner, S.S., Das, A., Higuita-Castro, N., Roy, S., Anani, R.A., Sen, C.K., 2018. Stabilized collagen matrix dressing improves wound macrophage function and epithelialization. The FASEB Journal 33, pp.2144–2155.

Fahlgren, A., Bratengeier, C., Gelmi, A., Semeins, C.M., Klein-Nulend, J., Jager, E.W., Bakker, A.D., 2015. Biocompatibility of polypyrrole with human primary osteoblasts and the effect of Dopants. PLOS ONE 10.

Fathi, I., Imura, T., Inagaki, A., Nakamura, Y., Nabawi, A., Goto, M., 2021. Decellularized whole-organ pre-vascularization: A novel approach for organogenesis. Frontiers in Bioengineering and Biotechnology 9.

Fenteany, G., Janmey, P. and Stossel, T. (2000). Signaling pathways and cell mechanics involved in wound closure by epithelial cell sheets. Current Biology, 10(14), pp.831-838.

Fernández-Pérez, J. and Ahearne, M., 2019. The impact of decellularization methods on extracellular matrix derived hydrogels. Scientific Reports 9.

Ferrante, C. and Leibovich, S., 2012. Regulation of Macrophage Polarization and Wound Healing. Advances in Wound Care, 1(1), pp.10-16.

Ferrante, C.J., Pinhal-Enfield, G., Elson, G., Cronstein, B.N., Hasko, G., Outram, S., Leibovich, S.J., 2013. The adenosine-dependent angiogenic switch of

macrophages to an M2-like phenotype is independent of interleukin-4 receptor alpha (il-4rα) signaling. Inflammation 36, 921–931.

Ferreira, M., Tuma Júnior, P., Carvalho, V. and Kamamoto, F., 2006. Complex wounds. Clinics, 61(6), pp.571-578.

Fitzpatrick, L.E., McDevitt, T.C., 2015. Cell-derived matrices for tissue engineering and regenerative medicine applications. Biomaterials Science 3, pp.12–24.

Franek, A., Kostur, R., Polak, A., Taradaj, J., Szlachta, Z., Blaszczak, E., Dolibog, P., Dolibog, P., Koczy, B. and Kucio, C., 2012. Using high-voltage electrical stimulation in the treatment of recalcitrant pressure ulcers: results of a randomized, controlled clinical study . Ostomy/Wound Management, 58(3), pp.30-44.

Frantz, C., Stewart, K. and Weaver, V., 2010. The extracellular matrix at a glance. Journal of Cell Science, 123(24), pp.4195-4200.

Freytes, D., Martin, J., Velankar, S., Lee, A. and Badylak, S., 2008. Preparation and rheological characterization of a gel form of the porcine urinary bladder matrix. Biomaterials, 29(11), pp.1630-1637.

Freytes, D., O'Neill, J., Duan-Arnold, Y., Wrona, E. and Vunjak-Novakovic, G., 2014. Natural Cardiac Extracellular Matrix Hydrogels for Cultivation of Human Stem Cell-Derived Cardiomyocytes. Methods in Molecular Biology, pp.69-81.

Frykberg, R.G., Banks, J., 2015. Challenges in the treatment of chronic wounds. Advances in Wound Care 4, 560–582.

Funk, R., 2015. Endogenous electric fields as guiding cue for cell migration. Frontiers in Physiology, 6.

Gamry, n.d. Basics of Electrochemical Impedance Spectroscopy. [Online] Available at <https://www.gamry.com/application-notes/EIS/basics-of-electrochemical-impedance-spectroscopy/> [Accessed 12/11/2022].

Gao, F., Liu, Y., He, Y., Yang, C., Wang, Y., Shi, X., Wei, G., 2010. Hyaluronan oligosaccharides promote excisional wound healing through enhanced angiogenesis. Matrix Biology 29, pp.107–116.

Ge, C., Li, W., Li, Y., Li, B., Du, J., Qiu, Y., Liu, Y., Gao, Y., Chai, Z. and Chen, C., 2011. Significance and Systematic Analysis of Metallic Impurities of Carbon Nanotubes Produced by Different Manufacturers. Journal of Nanoscience and Nanotechnology, 11(3), pp.2389-2397.

Ge, C., Li, Y., Yin, J., Liu, Y., Wang, L., Zhao, Y. and Chen, C., 2012. The contributions of metal impurities and tube structure to the toxicity of carbon nanotube materials. NPG Asia Materials, 4(12), pp.e32-e32.

Gehl, J., 2003. Electroporation: Theory and methods, perspectives for drug delivery, gene therapy and research. Acta Physiologica Scandinavica 177, 437–447.

Geng, L., Wang, Z., Cui, C., Zhu, Y., Shi, J., Wang, J. and Chen, M., 2018. Rapid Electrical Stimulation Increased Cardiac Apoptosis Through Disturbance of Calcium Homeostasis and Mitochondrial Dysfunction in Human Induced Pluripotent Stem Cell-Derived Cardiomyocytes. Cellular Physiology and Biochemistry, 47(3), pp.1167-1180.

Genin, M., Clement, F., Fattaccioli, A., Raes, M. and Michiels, C., 2015. M1 and M2 macrophages derived from THP-1 cells differentially modulate the response of cancer cells to etoposide. BMC Cancer, 15(1).

Ghuman, H., Massensini, A.R., Donnelly, J., Kim, S.-M., Medberry, C.J., Badylak, S.F., Modo, M., 2016. ECM hydrogel for the treatment of stroke: Characterization of the host cell infiltrate. Biomaterials 91, pp.166–181.

Giannoni, A., Gentile, F., Passino, C., 2022. Bioelectronic medicine and its applications in Cardiology. European Heart Journal.

Gilbert, T., Freund, J. and Badylak, S., 2009. Quantification of DNA in Biologic Scaffold Materials. Journal of Surgical Research, 152(1), pp.135-139.

Giobbe, G., Crowley, C., Luni, C., Campinoti, S., Khedr, M., Kretzschmar, K., De Santis, M., Zambaiti, E., Michielin, F., Meran, L., Hu, Q., van Son, G., Urbani, L., Manfredi, A., Giomo, M., Eaton, S., Cacchiarelli, D., Li, V., Clevers, H., Bonfanti, P., Elvassore, N. and De Coppi, P., 2019. Extracellular matrix hydrogel derived from decellularized tissues enables endodermal organoid culture. Nature Communications, 10(1).

Goh, S.-K., Olsen, P., Banerjee, I., 2013. Extracellular matrix aggregates from differentiating embryoid bodies as a scaffold to support ESC proliferation and differentiation. PLoS ONE 8.

Gordon, S. and Plüddemann, A., 2018. Macrophage Clearance of Apoptotic Cells: A Critical Assessment. Frontiers in Immunology, 9.

Gothard, D., Smith, E.L., Kanczler, J.M., Black, C.R., Wells, J.A., Roberts, C.A., White, L.J., Qutachi, O., Peto, H., Rashidi, H., Rojo, L., Stevens, M.M., El Haj, A.J., Rose, F.R., Shakesheff, K.M., Oreffo, R.O., 2015. In vivo assessment of bone regeneration in alginate/bone ECM hydrogels with incorporated skeletal stem cells and single growth factors. PLOS ONE 10.

Graham, B., Austin, J.R., Kaech, A., Heuser, J.E., 2008. Freezing Techniques: History, comparisons, and applications. Microscopy Today 16, pp.12–17.

Gray, J. and Farber, D., 2022. Tissue-Resident Immune Cells in Humans. Annual Review of Immunology, 40(1), pp.195-220.

Grefte, S., Vullinghs, S., Kuijpers-Jagtman, A.M., Torensma, R., Von den Hoff, J.W., 2012. Matrigel, but not collagen I, maintains the differentiation capacity of muscle derived cells in vitro. Biomedical Materials 7, 055004.

Grinnell, F., 1984. Fibronectin and wound healing. Journal of Cellular Biochemistry, 26(2), pp.107-116.

Gudmann, N. and Karsdal, M., 2016. Chapter 10 - Type X Collagen in Biochemistry of collagens, laminins and elastin. 1st ed. Academic Press, pp.73-76.

Guest, J., Fuller, G. and Vowden, P., 2020. Cohort study evaluating the burden of wounds to the UK's National Health Service in 2017/2018: update from 2012/2013. BMJ Open, 10(12), p.e045253.

Guido, I., Diehl, D., Olszok, N.A., Bodenschatz, E., 2020. Cellular velocity, electrical persistence and sensing in developed and vegetative cells during electrotaxis. PLOS ONE 15.

Guo, A., Song, B., Reid, B., Gu, Y., Forrester, J., Jahoda, C. and Zhao, M. (2010). Effects of Physiological Electric Fields on Migration of Human Dermal Fibroblasts. Journal of Investigative Dermatology, 130(9), pp.2320-2327.

Guo, S., DiPietro, L.A., 2010. Factors affecting wound healing. Journal of Dental Research 89, 219–229.

Gushiken, L., Beserra, F., Bastos, J., Jackson, C. and Pellizzon, C., 2021. Cutaneous Wound Healing: An Update from Physiopathology to Current Therapies. Life, 11(7), p.665.

Gyles, D.A., Castro, L.D., Silva, J.O., Ribeiro-Costa, R.M., 2017. A review of the designs and prominent biomedical advances of natural and synthetic hydrogel formulations. European Polymer Journal 88, 373–392.

Hammond, C., 2015. Cellular and molecular neurophysiology. 4th ed. Amsterdam: Elsevier, Chapter 3 - Ionic gradients, membrane potential and ionic currents.

Harrington, C., Zagari, M., Corea, J. and Klitenic, J., 2000. A cost analysis of diabetic lower-extremity ulcers. Diabetes Care, 23(9), pp.1333-1338.

Harris, J.R., Reiber, A., 2007. Influence of saline and ph on collagen type I fibrillogenesis in vitro: Fibril polymorphism and colloidal gold labelling. Micron 38, 513–521.

Hauck, S., Zager, P., Halfter, N., Wandel, E., Torregrossa, M., Kakpenova, A., Rother, S., Ordieres, M., Räthel, S., Berg, A., Möller, S., Schnabelrauch, M., Simon, J.C., Hintze, V., Franz, S., 2021. Collagen/hyaluronan based hydrogels releasing sulfated hyaluronan improve dermal wound healing in diabetic mice via reducing inflammatory macrophage activity. Bioactive Materials 6, pp.4342–4359.

Havran, W.L., Jameson, J.M., 2010. Epidermal T cells and wound healing. The Journal of Immunology 184, 5423–5428.

Hay, J. and Geddes, D., 1985. Transepithelial potential difference in cystic fibrosis. Thorax, 40(7), pp.493-496.

Heiduschka, P., Thanos, S., 1998. Implantable bioelectronic interfaces for lost nerve functions. Progress in Neurobiology 55, pp.433–461.

Hesketh, M., Sahin, K., West, Z. and Murray, R., 2017. Macrophage Phenotypes Regulate Scar Formation and Chronic Wound Healing. International Journal of Molecular Sciences, 18(7), p.1545.

Hesse, E., Hefferan, T.E., Tarara, J.E., Haasper, C., Meller, R., Krettek, C., Lu, L., Yaszemski, M.J., 2010. Collagen type I hydrogel allows migration, proliferation, and osteogenic differentiation of rat bone marrow stromal cells. Journal of Biomedical Materials Research Part A 94(2), 442-449.

Hickman, J., Graeser, R., de Hoogt, R., Vidic, S., Brito, C., Gutekunst, M., van der Kuip, H. and IMI PREDECT consortium, 2014. Three-dimensional models of cancer for pharmacology and cancer cell biology: Capturing tumor complexity in vitro/ex vivo. Biotechnology Journal, 9(9), pp.1115-1128.

Hilal, M., Han, J.I., 2018. Improving the conductivity of PEDOT:PSS to nearly 1 million S/m with graphene on an ITO-glass substrate. Synthetic Metals 245, pp.276–285.

Hind, L.E., Lurier, E.B., Dembo, M., Spiller, K.L., Hammer, D.A., 2016. Effect of M1–M2 polarization on the motility and traction stresses of primary human macrophages. Cellular and Molecular Bioengineering 9, 455–465.

Hinton, T., Jallerat, Q., Palchesko, R., Park, J., Grodzicki, M., Shue, H., Ramadan, M., Hudson, A. and Feinberg, A., 2015. Three-dimensional printing of complex biological structures by freeform reversible embedding of suspended hydrogels. Science Advances, 1(9).

Hinton, T.J., Jallerat, Q., Palchesko, R.N., Park, J.H., Grodzicki, M.S., Shue, H.-J., Ramadan, M.H., Hudson, A.R., Feinberg, A.W., 2015. Three-dimensional printing of complex biological structures by freeform reversible embedding of suspended hydrogels. Science Advances 1.

Hinz, B., 2016. The role of myofibroblasts in wound healing. Current Research in Translational Medicine 64, 171–177.

Ho, S.S., Keown, A.T., Addison, B., Leach, J.K., 2017. Cell migration and bone formation from mesenchymal stem cell spheroids in alginate hydrogels are regulated by adhesive ligand density. Biomacromolecules 18, 4331–4340.

Hoare, J., Rajnicek, A., McCaig, C., Barker, R. and Wilson, H. (2015). Electric fields are novel determinants of human macrophage functions. Journal of Leukocyte Biology, 99(6), pp.1141- 1151.

Hodde, J. and Allam, R., 2007. Small intestinal submucosa wound matrix for chronic wound healing. Wounds, 19(6), pp. 157-162.

Hodkiewicz, J., 2010. Characterizing Carbon Materials with Raman Spectroscopy. Madison, WI, USA: Thermo Fisher Scientific. Application note: 51901.

Hoganson, D.M., Owens, G.E., Meppelink, A.M., Bassett, E.K., Bowley, C.M., Hinkel, C.J., Finkelstein, E.B., Goldman, S.M., Vacanti, J.P., 2016. Decellularized extracellular matrix microparticles as a vehicle for cellular delivery in a model of anastomosis healing. Journal of Biomedical Materials Research Part A 104, pp.1728–1735.

Holmström, K. and Finkel, T. (2014). Cellular mechanisms and physiological consequences of redox-dependent signalling. Nature Reviews Molecular Cell Biology, 15(6), pp.411-421.

Hopley, E.L., Salmasi, S., Kalaskar, D.M., Seifalian, A.M., 2014. Carbon nanotubes leading the way forward in New Generation 3D tissue engineering. Biotechnology Advances 32, 1000–1014.

Hosseini, M-S. and Katbab, A.A., 2014. Effects of surface viscoelasticity on cellular responses of endothelial cells. Rep Biochem Mol Biol. 3(1), 20-28.

Houstis, N., Rosen, E.D., Lander, E.S., 2006. Reactive oxygen species have a causal role in multiple forms of insulin resistance. Nature 440, pp.944–948.

Hsieh, C.-H., Chen, Y.-D., Huang, S.-F., Wang, H.-M., Wu, M.-H., 2015. The effect of primary cancer cell culture models on the results of drug chemosensitivity assays: The application of perfusion Microbioreactor system as cell culture vessel. BioMed Research International 2015, 1–10.

Hsieh JY, Tran TN, Bovtinick EL and Liu WF, 2016. Investigating the effects of fibrin/collagen composite gels on macrophage phenotype polarization. Front. Bioeng. Biotechnol. Conference Abstract: 10th World Biomaterials Congress

Hsieh, J.Y., Keating, M.T., Smith, T.D., Meli, V.S., Botvinick, E.L., Liu, W.F., 2019. Matrix crosslinking enhances macrophage adhesion, migration, and inflammatory activation. APL Bioengineering 3, 016103.

Huleihel, L., Bartolacci, J., Dziki, J., Vorobyov, T., Arnold, B., Scarritt, M., Pineda Molina, C., LoPresti, S., Brown, B., Naranjo, J. and Badylak, S., 2017. Matrix-Bound Nanovesicles Recapitulate Extracellular Matrix Effects on Macrophage Phenotype. Tissue Engineering Part A, 23(21-22), pp.1283-1294.

Huleihel, L., Dziki, J.L., Bartolacci, J.G., Rausch, T., Scarritt, M.E., Cramer, M.C., Vorobyov, T., LoPresti, S.T., Swineheart, I.T., White, L.J., Brown, B.N., Badylak, S.F., 2017. Macrophage phenotype in response to ECM bioscaffolds. Seminars in Immunology 29, 2–13.

Huleihel, L., Hussey, G., Naranjo, J., Zhang, L., Dziki, J., Turner, N., Stolz, D. and Badylak, S., 2016. Matrix-bound nanovesicles within ECM bioscaffolds. Science Advances, 2(6).

Humphrey, J.D., 2003. Review Paper: Continuum Biomechanics of soft biological tissues. Proceedings of the Royal Society of London. Series A: Mathematical, Physical and Engineering Sciences 459, 3–46.

Humpolíček, P., Kašpárková, V., Pacherník, J., Stejskal, J., Bober, P., Capáková, Z., Radaszkiewicz, K.A., Junkar, I., Lehocký, M., 2018. The biocompatibility of polyaniline and polypyrrole: A comparative study of their cytotoxicity, embryotoxicity and impurity profile. Materials Science and Engineering: C 91, pp.303–310.

Hurlow, A., Bennett, M., Robb, K., Johnson, M., Simpson, K. and Oxberry, S., 2012. Transcutaneous electric nerve stimulation (TENS) for cancer pain in adults. Cochrane Database of Systematic Reviews,.

Hurst, R. and Bonner, R., 2001. Mapping of the distribution of significant proteins and proteoglycans in small intestinal submucosa by fluorescence microscopy. Journal of Biomaterials Science, Polymer Edition, 12(11), pp.1267-1279.

Hussey, G., Dziki, J., Lee, Y., Bartolacci, J., Behun, M., Turnquist, H. and Badylak, S., 2019. Matrix bound nanovesicle-associated IL-33 activates a pro-remodeling macrophage phenotype via a non-canonical, ST2-independent pathway. Journal of Immunology and Regenerative Medicine, 3, pp.26-35.

Hussey, G.S., Nascari, D.G., Saldin, L.T., Kolich, B., Lee, Y.C., Crum, R.J., El-Mossier, S.O., D'Angelo, W., Dziki, J.L., Badylak, S.F., 2020. Ultrasonic cavitation to prepare ECM hydrogels. Acta Biomaterialia 108, pp.77–86.

Hynes, R. and Naba, A., 2011. Overview of the Matrisome--An Inventory of Extracellular Matrix Constituents and Functions. Cold Spring Harbor Perspectives in Biology, 4(1), pp.a004903-a004903.

Idriss, H. and Naismith, J., 2000. TNF alpha and the TNF receptor superfamily: Structure-function relationship(s). Microscopy Research and Technique, 50(3), pp.184-195.

Iijima, S., 1991. Helical microtubules of Graphitic Carbon. Nature 354, 56–58.

Ikari, R., Mukaisho, K., Kageyama, S., Nagasawa, M., Kubota, S., Nakayama, T., Murakami, S., Taniura, N., Tanaka, H., Kushima, R.P., Kawauchi, A., 2021. Differences in the central energy metabolism of cancer cells between conventional 2D and novel 3D Culture Systems. International Journal of Molecular Sciences 22, 1805.

InformedHealth, 2006 [Updated 2018]. What are the treatment options for chronic wounds? [Online] Available at: <ncbi.nlm.nih.gov/books/NBK326436/> [Accessed 21 November 2021].

Italiani, P. and Boraschi, D., 2014. From Monocytes to M1/M2 Macrophages: Phenotypical vs. Functional Differentiation. Frontiers in Immunology, 5.

Jamee, R., Araf, Y., Naser, I.B., Promon, S.K., 2021. The promising rise of bioprinting in Revolutionalizing Medical Science: Advances and Possibilities. Regenerative Therapy 18, 133–145.

Jang, J., Kim, T.G., Kim, B.S., Kim, S.-W., Kwon, S.-M., Cho, D.-W., 2016. Tailoring mechanical properties of decellularized extracellular matrix bioink by vitamin B2-induced photo-crosslinking. Acta Biomaterialia 33, 88–95.

Jha, A., Moore, E., 2021. Collagen-derived peptide, DGEA, inhibits pro-inflammatory macrophages in biofunctional hydrogels. Journal of Materials Research 37, pp.77–87.

Ji, Y., Zhou, J., Sun, T., Tang, K., Xiong, Z., Ren, Z., Yao, S., Chen, K., Yang, F., Zhu, F., Guo, X., 2018. Diverse preparation methods for small intestinal submucosa (SIS): Decellularization, components, and Structure. Journal of Biomedical Materials Research Part A.

Johnson, B., Stevenson, A., Prêle, C., Fear, M. and Wood, F., 2020. The Role of IL-6 in Skin Fibrosis and Cutaneous Wound Healing. Biomedicines, 8(5), p.101.

Johnson, R.R., Johnson, A.T., Klein, M.L., 2009. The nature of DNA-base-carbon-nanotube interactions. Small 6, 31–34.

Jones, P.L., Jones, F.S., 2000. Tenascin-C in development and disease: Gene regulation and cell function. Matrix Biology 19, 581–596.

Jorio, A. and Saito, R., 2021. Raman spectroscopy for carbon nanotube applications. Journal of Applied Physics, 129(2), p.021102.

Josan, C., Kakar, S., Raha, S., 2021. Matrigel® enhances 3T3-L1 cell differentiation. Adipocyte 10, 361–377.

Juhasz, I., Kiss, B., Lukacs, L., Erdei, I., Peter, Z., Remenyik, E., 2010. Long-term followup of dermal substitution with acellular dermal implant in Burns and Postburn Scar Corrections. Dermatology Research and Practice 2010, pp.1–7.

Junn, E., Lee, K.N., Ju, H.R., Han, S.H., Im, J.Y., Kang, H.S., Lee, T.H., Bae, Y.S., Ha, K.S., Lee, Z.W., Rhee, S.G., Choi, I., 2000. Requirement of hydrogen peroxide generation in TGF-β1 signal transduction in human lung fibroblast cells:

Involvement of hydrogen peroxide and CA2+ in TGF-β1-induced IL-6 expression. The Journal of Immunology 165, 2190–2197.

Kabirian, F. and Mozafari, M., 2020. Decellularized ECM-derived bioinks: Prospects for the future. Methods, 171, pp.108-118.

Kadhim, R.J., Karsh, E.H., Taqi, Z.J., Jabir, M.S., 2021. Biocompatibility of gold nanoparticles: In-vitro and in-vivo study. Materials Today: Proceedings 42, pp.3041–3045.

Kadler, K.E., Hill, A., Canty-Laird, E.G., 2008. Collagen fibrillogenesis: Fibronectin, integrins, and minor collagens as organizers and nucleators. Current Opinion in Cell Biology 20, 495–501.

Kandhwal, M., Behl, T., Singh, S., Sharma, N., Arora, S., Bhatia, S., Al-Harrasi, A., Sachdeva, M., Bungau, S., 2022. Role of matrix metalloproteinase in wound healing. American Journal of Translational Research 14, 4391–4405.

Karimi, M., Solati, N., Ghasemi, A., Estiar, M., Hashemkhani, M., Kiani, P., Mohamed, E., Saeidi, A., Taheri, M., Avci, P., Aref, A., Amiri, M., Baniasadi, F. and Hamblin, M., 2015. Carbon nanotubes part II: a remarkable carrier for drug and gene delivery. Expert Opinion on Drug Delivery, 12(7), pp.1089-1105.

Karunaratne, A., Li, S., Bull, A.M., 2018. Nano-scale mechanisms explain the stiffening and strengthening of ligament tissue with increasing strain rate. Scientific Reports 8.

Kausar, A., Ilyas, H. and Siddiq, M., 2017. Current Research Status and Application of Polymer/Carbon Nanofiller Buckypaper: A Review. Polymer-Plastics Technology and Engineering, 56(16), pp.1780-1800.

Keane, T.J., Londono, R., Turner, N.J., Badylak, S.F., 2012. Consequences of ineffective decellularization of biologic scaffolds on the host response. Biomaterials 33, 1771–1781.

Kellaway, S.C., Roberton, V., Jones, J.N., Loczenski, R., Phillips, J.B., White, L.J., 2023. Engineered neural tissue made using hydrogels derived from decellularised tissues for the regeneration of peripheral nerves. Acta Biomaterialia 157, 124–136.

Khetan, S. and Burdick, J., 2010. Patterning network structure to spatially control cellular remodeling and stem cell fate within 3-dimensional hydrogels. Biomaterials, 31(32), pp.8228-8234.

Kim, H., Wang, M., Lee, S., Kang, J., Nam, J., Ci, L. and Suhr, J., 2017. Tensile properties of millimeter-long multi-walled carbon nanotubes. Scientific Reports, 7(1).

Kim, T., Sridharan, I., Zhu, B., Orgel, J. and Wang, R., 2015. Effect of CNT on collagen fiber structure, stiffness assembly kinetics and stem cell differentiation. Materials Science and Engineering: C, 49, pp.281-289.

King, A., Balaji, S., Le, L., Crombleholme, T. and Keswani, S., 2014. Regenerative Wound Healing: The Role of Interleukin-10. Advances in Wound Care, 3(4), pp.315-323.

Kirson, E.D., Dbalý, V., Tovaryš, F., Vymazal, J., Soustiel, J.F., Itzhaki, A., Mordechovich, D., Steinberg-Shapira, S., Gurvich, Z., Schneiderman, R., Wasserman, Y., Salzberg, M., Ryffel, B., Goldsher, D., Dekel, E., Palti, Y., 2007. Alternating electric fields arrest cell proliferation in animal tumor models and human brain tumors. Proceedings of the National Academy of Sciences 104, 10152–10157.

Kloth, L., 2014. Electrical Stimulation Technologies for Wound Healing. Advances in Wound Care, 3(2), pp.81-90.

Kobayashi, F., Matsuzaka, K. and Inoue, T., 2015. The effect of basic fibroblast growth factor on regeneration in a surgical wound model of rat submandibular glands. International Journal of Oral Science, 8(1), pp.16-23.

Kobayashi, M., Kadota, J., Hashimoto, Y., Fujisato, T., Nakamura, N., Kimura, T., Kishida, A., 2020. Elastic modulus of ECM hydrogels derived from decellularized tissue affects capillary network formation in endothelial cells. International Journal of Molecular Sciences 21, 6304.

Koch, M. and Włodarczyk-Biegun, M.K., 2020. Faithful scanning electron microscopic (SEM) visualization of 3D printed alginate-based scaffolds. Bioprinting 20.

Komi, D., Khomtchouk, K. and Santa Maria, P., 2019. A Review of the Contribution of Mast Cells in Wound Healing: Involved Molecular and Cellular Mechanisms. Clinical Reviews in Allergy & Immunology, 58(3), pp.298-312.

Kong, Y., Liu, F., Ma, B., Duan, J., Yuan, W., Sang, Y., Han, L., Wang, S. and Liu, H., 2021. Wireless Localized Electrical Stimulation Generated by an Ultrasound-Driven Piezoelectric Discharge Regulates Proinflammatory Macrophage Polarization. Advanced Science, 8(13), p.2100962.

Koopman, F.A., Chavan, S.S., Miljko, S., Grazio, S., Sokolovic, S., Schuurman, P.R., Mehta, A.D., Levine, Y.A., Faltys, M., Zitnik, R., Tracey, K.J., Tak, P.P., 2016. Vagus nerve stimulation inhibits cytokine production and attenuates disease severity in rheumatoid arthritis. Proceedings of the National Academy of Sciences 113, pp.8284–8289.

Koyama, H., Raines, E.W., Bornfeldt, K.E., Roberts, J.M., Ross, R., 1996. Fibrillar collagen inhibits arterial smooth muscle proliferation through regulation of CDK2 inhibitors. Cell 87, pp.1069–1078.

Krzyszczyk, P., Schloss, R., Palmer, A., Berthiaume, F., 2018. The role of macrophages in acute and chronic wound healing and interventions to promote pro-wound healing phenotypes. Frontiers in Physiology 9.

Kudva, A.K., Luyten, F.P., Patterson, J., 2017. RGD-functionalized polyethylene glycol hydrogels support proliferation and in vitro chondrogenesis of human periosteum-derived cells. Journal of Biomedical Materials Research Part A 106, 33–42.

Kular, J.K., Basu, S., Sharma, R.I., 2014. The extracellular matrix: Structure, composition, age-related differences, tools for analysis and applications for tissue engineering. Journal of Tissue Engineering 5, 204173141455711.

Kuo, I.Y., Ehrlich, B.E., 2015. Signaling in muscle contraction. Cold Spring Harbor Perspectives in Biology 7.

Kus-Liśkiewicz, M., Fickers, P., Ben Tahar, I., 2021. Biocompatibility and cytotoxicity of gold nanoparticles: Recent advances in methodologies and regulations. International Journal of Molecular Sciences 22, 10952.

Krzyszczyk, P., Schloss, R., Palmer, A., Berthiaume, F., 2018. The role of macrophages in acute and chronic wound healing and interventions to promote pro-wound healing phenotypes. Frontiers in Physiology 9.

Landén, N., Li, D. and Ståhle, M., 2016. Transition from inflammation to proliferation: a critical step during wound healing. Cellular and Molecular Life Sciences, 73(20), pp.3861-3885.

Laronha, H., Caldeira, J., 2020. Structure and function of human matrix metalloproteinases. Cells 9, 1076.

Lau, C., Cervini, R., Clarke, S., Markovic, M., Matisons, J., Hawkins, S., Huynh, C. and Simon, G., 2008. The effect of functionalization on structure and electrical conductivity of multi-walled carbon nanotubes. Journal of Nanoparticle Research, 10(S1), pp.77-88.

Laurens, N., Koolwijk, P., de Maat, M.P., 2006. Fibrin structure and wound healing. Journal of Thrombosis and Haemostasis 4, pp.932–939.

Lee, J., Wang, Y.-L., Ren, F., Lele, T.P., 2010. Stamp wound assay for studying coupled cell migration and cell debris clearance. Langmuir 26, pp.16672–16676.

Lee, J.H., Lee, J.-Y., Yang, S.H., Lee, E.-J., Kim, H.-W., 2014. Carbon nanotube–Collagen three-dimensional culture of mesenchymal stem cells promotes expression of neural phenotypes and secretion of neurotrophic factors. Acta Biomaterialia 10, 4425–4436.

Lee, M., Kim, M.C., Lee, J.Y., 2022. Nanomaterial-based electrically conductive hydrogels for cardiac tissue repair. International Journal of Nanomedicine Volume 17, 6181–6200.

Lei, Y., Gojgini, S., Lam, J., Segura, T., 2011. The spreading, migration and proliferation of mouse mesenchymal stem cells cultured inside hyaluronic acid hydrogels. Biomaterials 32, 39–47.

Lerman, O.Z., Galiano, R.D., Armour, M., Levine, J.P., Gurtner, G.C., 2003. Cellular dysfunction in the diabetic fibroblast. The American Journal of Pathology 162, 303–312.

Lévêque, M., Penna, A., Le Trionnaire, S., Belleguic, C., Desrues, B., Brinchault, G., Jouneau, S., Lagadic-Gossmann, D., Martin-Chouly, C., 2018.

Phagocytosis depends on TRPV2-mediated calcium influx and requires TRPV2 in lipids rafts: Alteration in macrophages from patients with cystic fibrosis. Scientific Reports 8.

Levin, M., 2014. Molecular bioelectricity: How endogenous voltage potentials control cell behavior and instruct pattern regulation in vivo. Molecular Biology of the Cell 25, pp.3835–3850.

Li, C., Levin, M. and Kaplan, D., 2016. Bioelectric modulation of macrophage polarization. Scientific Reports, 6(1).

Li, J., Kirsner, R., 2014. Chapter 7 - Wound Healing. In: Surgery of the Skin (3 Ed.). Saunders, Philadelphia, Pennsylvania, pp. 97–115.

Li, J., Nandagopal, S., Wu, D., Romanuik, S., Paul, K., Thomson, D. and Lin, F., 2011. Activated T lymphocytes migrate toward the cathode of DC electric fields in microfluidic devices. Lab on a Chip, 11(7), p.1298.

Li, Q., Yue, C., Chen, T., Ding, C., Zhang, H., 2022. Construction and characterization of conductive collagen/multiwalled carbon nanotube composite films for Nerve Tissue Engineering. AIP Advances 12, 055124.

Li, S., Lu, D., Tang, J., Min, J., Hu, M., Li, Y., Liu, Y., Wang, L., Liu, C. and Hong, L., 2019. Electrical Stimulation Activates Fibroblasts through the Elevation of Intracellular Free Ca2+: Potential Mechanism of Pelvic Electrical Stimulation Therapy. BioMed Research International, 2019, pp.1-10.

Li, X., 2013. Carbon Nanotubes as Biomaterials. Encyclopedia of Biophysics, pp.238-240.

Li, X., Gao, H., Uo, M., Sato, Y., Akasaka, T., Feng, Q., Cui, F., Liu, X., Watari, F., 2008. Effect of carbon nanotubes on cellular functions in vitro. Journal of Biomedical Materials Research Part A 91A, 132–139.

Li, Y., Asadi, A., Monroe, M.R., Douglas, E.P., 2009. Ph effects on collagen fibrillogenesis in vitro: Electrostatic interactions and phosphate binding. Materials Science and Engineering: C 29, 1643–1649.

Li, Z., Bratlie, K.M., 2021. Macrophage phenotypic changes on FN-coated physical gradient hydrogels. ACS Applied Bio Materials 4, pp.6758–6768.

Liang, C.-C., Park, A.Y., Guan, J.-L., 2007. In vitro scratch assay: A convenient and inexpensive method for analysis of cell migration in vitro. Nature Protocols 2, pp.329–333.

Liang, R., Yang, G., Kim, K., D'Amore, A., Pickering, A., Zhang, C. and Woo, S., 2015. Positive effects of an extracellular matrix hydrogel on rat anterior cruciate ligament fibroblast proliferation and collagen mRNA expression. Journal of Orthopaedic Translation, 3(3), pp.114-122.

Liao, C., Li, Y., Tjong, S., 2018. Graphene nanomaterials: Synthesis, biocompatibility, and cytotoxicity. International Journal of Molecular Sciences 19, 3564.

Licht, SH., "History of Electrotherapy", in Therapeutic Electricity and Ultraviolet Radiation, 2nd ed., ed. Sidney Licht, New Haven: E. Licht, 1967, Pp. 1-70.

Lim, G.P., Soon, C.F., Ma, N.L., Morsin, M., Nayan, N., Ahmad, M.K., Tee, K.S., 2021. Cytotoxicity of mxene-based nanomaterials for biomedical applications: A mini review. Environmental Research 201, 111592.

Lin, F., Baldessari, F., Gyenge, C., Sato, T., Chambers, R., Santiago, J. and Butcher, E., 2008. Lymphocyte Electrotaxis In Vitro and In Vivo. The Journal of Immunology, 181(4), pp.2465- 2471.

Lin, K., Zhang, D., Macedo, M.H., Cui, W., Sarmento, B., Shen, G., 2018. Advanced collagen-based biomaterials for regenerative biomedicine. Advanced Functional Materials 29, 1804943.

Lin, S., He, X., He, Y., 2021. Co-culture of ASCS/EPCs and dermal extracellular matrix hydrogel enhances the repair of full-thickness skin wound by promoting angiogenesis. Stem Cell Research & Therapy 12.

Lin, Z., Rao, Z., Chen, J., Chu, H., Zhou, J., Yang, L., Quan, D., Bai, Y., 2022. Bioactive decellularized extracellular matrix hydrogel microspheres fabricated using a temperature-controlling microfluidic system. ACS Biomaterials Science & Engineering 8, pp.1644–1655.

Ling, Z., Ren, C.E., Zhao, M.-Q., Yang, J., Giammarco, J.M., Qiu, J., Barsoum, M.W., Gogotsi, Y., 2014. Flexible and conductive mxene films and nanocomposites with high capacitance. Proceedings of the National Academy of Sciences 111, pp.16676–16681.

Lipatov, A., Goad, A., Loes, M.J., Vorobeva, N.S., Abourahma, J., Gogotsi, Y., Sinitskii, A., 2021. High electrical conductivity and breakdown current density of individual monolayer Ti3C2Tx MXene flakes. Matter 4, pp.1413–1427.

Litwiniuk, M., Krejner, A., Speyrer, M., Gauto, A., Grzela, T., 2016. Hyaluronic Acid in Inflammation and Tissue Regeneration. Wounds 28, pp.78–88.

Liu, F., Mih, J.D., Shea, B.S., Kho, A.T., Sharif, A.S., Tager, A.M., Tschumperlin, D.J., 2010. Feedback amplification of fibrosis through matrix stiffening and cox-2 suppression. Journal of Cell Biology 190, pp.693–706.

Liu, Y., Li, H., Czajkowsky, D. and Shao, Z., 2021. Monocytic THP-1 cells diverge significantly from their primary counterparts: a comparative examination of the chromosomal conformations and transcriptomes. Hereditas, 158(1).

Liu, Z., Ren, Z., Zhang, J., Chuang, C., Kandaswamy, E., Zhou, T. and Zuo, L., 2018. Role of ROS and Nutritional Antioxidants in Human Diseases. Frontiers in Physiology, 9.

Lodish, H., Berk, A. and Zipursky, S., 2000. Molecular Cell Biology. 4th ed. New York: W H Freeman, p.Collagen: The Fibrous Proteins of the Matrix.

Logie, C., van Schaik, T., Pompe, T., Pietsch, K., 2021. Fibronectin-functionalization of 3D collagen networks supports immune tolerance and inflammation suppression in human monocyte-derived macrophages. Biomaterials 268, 120498.

Loneker, A., Faulk, D., Hussey, G., D'Amore, A. and Badylak, S., 2016. Solubilized liver extracellular matrix maintains primary rat hepatocyte phenotypein-vitro. Journal of Biomedical Materials Research Part A, 104(4), pp.957-965.

Long, Y., Wei, H., Li, J., Yao, G., Yu, B., Ni, D., Gibson, A.L.F., Lan, X., Jiang, Y., Cai, W., Wang, X., 2018. Effective wound healing enabled by discrete alternative electric fields from wearable nanogenerators. ACS Nano 12, pp.12533–12540.

Lopatin, A., Makhina, E. and Nichols, C., 1995. The mechanism of inward rectification of potassium channels: "long-pore plugging" by cytoplasmic polyamines. Journal of General Physiology, 106(5), pp.923-955.

Love, M., Palee, S., Chattipakorn, S. and Chattipakorn, N., 2018. Effects of electrical stimulation on cell proliferation and apoptosis. Journal of Cellular Physiology, 233(3), pp.1860-1876.

Lu, X. and Chen, Z., 2005. Curved Pi-Conjugation, Aromaticity, and the Related Chemistry of Small Fullerenes (<C60) and Single-Walled Carbon Nanotubes. Chemical Reviews, 105(10), pp.3643-3696.

Lu, Y., Liu, R., Hang, X.-C., Young, D.J., 2021. Biocompatible, flexible and conductive polymers prepared by biomass-derived ionic liquid treatment. Polymer Chemistry 12, pp.2115–2121.

Luanpitpong, S., Wang, L. and Rojanasakul, Y., 2014. The effects of carbon nanotubes on lung and dermal cellular behaviors. Nanomedicine, 9(6), pp.895-912.

Luo, S.-C., Mohamed Ali, E., Tansil, N.C., Yu, H.-hua, Gao, S., Kantchev, E.A., Ying, J.Y., 2008. Poly(3,4-ethylenedioxythiophene) (PEDOT) nanobiointerfaces: Thin, ultrasmooth, and functionalized pedot films with in vitro and in vivo biocompatibility. Langmuir 24, pp.8071–8077.

Ma, S., Hu, H., Wu, J., Li, X., Ma, X., Zhao, Z., Liu, Z., Wu, C., Zhao, B., Wang, Y., Jing, W., 2022. Functional extracellular matrix hydrogel modified with MSC-derived small extracellular vesicles for chronic wound healing. Cell Proliferation 55.

Ma, Y., Han, T., Yang, Q., Wang, J., Feng, B., Jia, Y., Wei, Z., Xu, F., 2021. Viscoelastic Cell Microenvironment: Hydrogel-based strategy for recapitulating dynamic ECM Mechanics. Advanced Functional Materials 31, 2100848.

Ma, Y., Poole, K., Goyette, J., Gaus, K., 2017. Introducing membrane charge and membrane potential to T cell signaling. Frontiers in Immunology 8.

Maheshwari, N., Tekade, M., Soni, N., Ghode, P., Sharma, M., Deb, P. and Tekade, R., 2019. Functionalized Carbon Nanotubes for Protein, Peptide, and Gene Delivery. Biomaterials and Bionanotechnology, pp.613-637.

Manaf, A., Hafizah, M.A., Riyadi, A.F., Andreas, 2019. Electrical conductivity of polyaniline (PANI) assisted by anionic surfactant through emulsion polymerization technique. Journal of Physics: Conference Series 1153, 012067.

Martin, P. and Leibovich, S., 2005. Inflammatory cells during wound repair: the good, the bad and the ugly. Trends in Cell Biology, 15(11), pp.599-607.

Martino, M., Mochizuki, M., Rothenfluh, D., Rempel, S., Hubbell, J. and Barker, T., 2009. Controlling integrin specificity and stem cell differentiation in 2D and 3D environments through regulation of fibronectin domain stability. Biomaterials, 30(6), pp.1089-1097.

Mase, V.J., Hsu, J.R., Wolf, S.E., Wenke, J.C., Baer, D.G., Owens, J., Badylak, S.F., Walters, T.J., 2010. Clinical application of an acellular biologic scaffold for surgical repair of a large, traumatic quadriceps femoris muscle defect. Orthopedics 33.

Masson-Meyers, D.S., Andrade, T.A., Caetano, G.F., Guimaraes, F.R., Leite, M.N., Leite, S.N., Frade, M.A., 2020. Experimental models and methods for cutaneous wound healing assessment. International Journal of Experimental Pathology 101, 21–37.

Matei, A.-E., Chen, C.-W., Kiesewetter, L., Györfi, A.-H., Li, Y.-N., Trinh-Minh, T., Xu, X., Tran Manh, C., van Kuppevelt, T., Hansmann, J., Jüngel, A., Schett, G., Groeber-Becker, F., Distler, J.H., 2019. Vascularised human skin equivalents as a novel in vitro model of skin fibrosis and platform for testing of antifibrotic drugs. Annals of the Rheumatic Diseases 78, pp.1686–1692.

Mathew-Steiner, S.S., Roy, S., Sen, C.K., 2021. Collagen in wound healing. Bioengineering 8, 63.

Matsuo, N., Tanaka, S., Yoshioka, H., Koch, M., Gordon, M. and Ramirez, F., 2008. Collagen XXIV (Col24a1) Gene Expression is a Specific Marker of Osteoblast Differentiation and Bone Formation. Connective Tissue Research, 49(2), pp.68-75.

MatWeb, 2022a. MatWeb Material Property Data: Gold, Au. [Online] Available at: < https://www.matweb.com/search/DataSheet.aspx?MatGUID=d2a2119a08904a0fa706e9408cddb88e> [Accessed 15 October 2022].

MatWeb, 2022b. MatWeb Material Property Data: Silver, Ag. [Online] Available at: < https://www.matweb.com/search/DataSheet.aspx?MatGUID=63cbd043a31f4f739ddb7632c1443d33> [Accessed 15 October 2022].

May, R. and Machesky, M., 2001. Phagocytosis and the actin cytoskeleton. Journal of Cell Science, 114(6), pp.1061-1077.

Mazzitelli, S., Luca, G., Mancuso, F., Calvitti, M., Calafiore, R., Nastruzzi, C., Johnson, S., Badylak, S.F., 2011. Production and characterization of engineered alginate-based microparticles containing ECM powder for Cell/tissue engineering applications. Acta Biomaterialia 7, pp.1050–1062.

McDevitt, C.A., Wildey, G.M., Cutrone, R.M., 2003. Transforming growth factor-beta1 in a sterilized tissue derived from the pig small intestine submucosa. Journal of Biomedical Materials Research 67A, 637–640.

McWhorter, F., Wang, T., Nguyen, P., Chung, T. and Liu, W., 2013. Modulation of macrophage phenotype by cell shape. Proceedings of the National Academy of Sciences, 110(43), pp.17253-17258.

Meng, S., Rouabhia, M. and Zhang, Z., 2021. Electrical Stimulation and Cellular Behaviors in Electric Field in Biomedical Research. Materials, 15(1), p.165.

Mercer, R., Hubbs, A., Scabilloni, J., Wang, L., Battelli, L., Friend, S., Castranova, V. and Porter, D., 2011. Pulmonary fibrotic response to aspiration of multi-walled carbon nanotubes. Particle and Fibre Toxicology, 8(1), p.21.

Merkt, W., Zhou, Y., Han, H. and Lagares, D., 2021. Myofibroblast fate plasticity in tissue repair and fibrosis: Deactivation, apoptosis, senescence and reprogramming. Wound Repair and Regeneration,.

Meurens, F., Summerfield, A., Nauwynck, H., Saif, L., Gerdts, V., 2012. The pig: A model for human infectious diseases. Trends in Microbiology 20, pp.50–57.

Mezger, T.G., Sprinz, C., Green, A., 2021. Applied rheology: With Joe Flow on rheology road. A. Paar, Graz.

Mihajlovic, M., Mihajlovic, M., Dankers, P., Masereeuw, R. and Sijbesma, R., 2018. Carbon Nanotube Reinforced Supramolecular Hydrogels for Bioapplications. Macromolecular Bioscience, 19(1), p.1800173.

Mirastschijski, U., Schnabel, R., Claes, J., Schneider, W., Ågren, M.S., Haaksma, C., Tomasek, J.J., 2010. Matrix metalloproteinase inhibition delays wound healing and blocks the latent transforming growth factor-β1-promoted myofibroblast formation and function. Wound Repair and Regeneration 18, 223–234.

Miyagi, H., Thomasy, S., Russell, P. and Murphy, C., 2018. The role of hepatocyte growth factor in corneal wound healing. Experimental Eye Research, 166, pp.49-55.

Moarefian, M., Davalos, R.V., Burton, M.D., Jones, C.N., 2021. Electrotaxis-on-chip to quantify neutrophil migration towards electrochemical gradients. Frontiers in Immunology 12.

Mobini, S., Leppik, L. and Barker, J., 2016. Direct current electrical stimulation chamber for treating cells in vitro. BioTechniques, 60(2), pp.95-98.

Mobini, S., Leppik, L., Thottakkattumana Parameswaran, V. and Barker, J., 2017. In vitro effect of direct current electrical stimulation on rat mesenchymal stem cells. PeerJ, 5, p.e2821.

Morawski, M., Dityatev, A., Hartlage-Rübsamen, M., Blosa, M., Holzer, M., Flach, K., Pavlica, S., Dityateva, G., Grosche, J., Brückner, G., Schachner, M., 2014. Tenascin-R promotes assembly of the extracellular matrix of perineuronal nets via clustering of Aggrecan. Philosophical Transactions of the Royal Society B: Biological Sciences 369, 20140046.

Motte, S., Kaufman, L.J., 2012. Strain stiffening in collagen I networks. Biopolymers 99, 35–46.

Moulin, V., Dubé, J., Rochette-Drouin, O., Lévesque, P., Gauvin, R., Roberge, C., Auger, F., Goulet, D., Bourdages, M., Plante, M. and Germain, L., 2012. Electric Potential Across Epidermis and Its Role During Wound Healing Can Be Studied by Using an In Vitro Reconstructed Human Skin. Advances in Wound Care, 1(2), pp.81-87.

Muller, J., Huaux, F., Moreau, N., Misson, P., Heilier, J., Delos, M., Arras, M., Fonseca, A., Nagy, J. and Lison, D., 2005. Respiratory toxicity of multi-wall carbon nanotubes. Toxicology and Applied Pharmacology, 207(3), pp.221-231.

Murray, P.J., Allen, J.E., Biswas, S.K., Fisher, E.A., Gilroy, D.W., Goerdt, S., Gordon, S., Hamilton, J.A., Ivashkiv, L.B., Lawrence, T., Locati, M., Mantovani, A., Martinez, F.O., Mege, J.-L., Mosser, D.M., Natoli, G., Saeij, J.P., Schultze, J.L., Shirey, K.A., Sica, A., Suttles, J., Udalova, I., van Ginderachter, J.A.,

Vogel, S.N., Wynn, T.A., 2014. Macrophage activation and polarization: Nomenclature and experimental guidelines. Immunity 41, 14–20.

Na, G.C., Phillips, L.J., Freire, E.I., 1989. In vitro collagen fibril assembly: Thermodynamic studies. Biochemistry 28, 7153–7161.

Nagai, H., Okazaki, Y., Chew, S.H., Misawa, N., Yamashita, Y., Akatsuka, S., Ishihara, T., Yamashita, K., Yoshikawa, Y., Yasui, H., Jiang, L., Ohara, H., Takahashi, T., Ichihara, G., Kostarelos, K., Miyata, Y., Shinohara, H., Toyokuni, S., 2011. Diameter and rigidity of multiwalled carbon nanotubes are critical factors in mesothelial injury and carcinogenesis. Proceedings of the National Academy of Sciences 108.

Nagata, S., Hanayama, R., Kawane, K., 2010. Autoimmunity and the clearance of Dead Cells. Cell 140, 619–630.

Najafi, M., Vahedi, F., Ahmadi, S., Madani, R. and Mehrvarz, M., 2008. Effect of Collagen Type I (Rat Tail) on Cell Proliferation and Adhesion of BHK-21. IFMBE Proceedings, pp.806-809.

Nakajima, K., Zhu, K., Sun, Y., Hegyi, B., Zeng, Q., Murphy, C., Small, J., Chen-Izu, Y., Izumiya, Y., Penninger, J. and Zhao, M., 2015. KCNJ15/Kir4.2 couples with polyamines to sense weak extracellular electric fields in galvanotaxis. Nature Communications, 6(1).

Nielsen, S. and Karsdal, M., 2016. Chapter 24 - Type XXIV Collagen in Biochemistry of collagens, laminins and elastin. 1st ed. Academic Press, pp.143-145.

Noronha, N., Ehx, G., Meunier, M., Laverdure, J., Thériault, C. and Perreault, C., 2020. Major multilevel molecular divergence between THP-1 cells from different biorepositories. International Journal of Cancer, 147(7), pp.2000-2006.

Nuccitelli, R., 2003. A Role for Endogenous Electric Fields in Wound Healing. Current Topics in Developmental Biology, pp.1-26.

Nussbaum, S., Carter, M., Fife, C., DaVanzo, J., Haught, R., Nusgart, M. and Cartwright, D., 2018. An Economic Evaluation of the Impact, Cost, and Medicare Policy Implications of Chronic Nonhealing Wounds. Value in Health, 21(1), pp.27-32.

Ogata, S. and Shibutani, Y., 2003. Ideal tensile strength and band gap of single-walled carbon nanotubes. Physical Review B, 68(16).

Ogle, M.E., Segar, C.E., Sridhar, S., Botchwey, E.A., 2016. Monocytes and macrophages in tissue repair: Implications for immunoregenerative biomaterial design. Experimental Biology and Medicine 241, 1084–1097.

Olofsson, P.S., Tracey, K.J., 2017. Bioelectronic Medicine: Technology targeting molecular mechanisms for therapy. Journal of Internal Medicine 282, 3–4.

Olsson, M., Järbrink, K., Divakar, U., Bajpai, R., Upton, Z., Schmidtchen, A. and Car, J., 2018. The humanistic and economic burden of chronic wounds: A systematic review. Wound Repair and Regeneration, 27(1), pp.114-125.

Orida, N. and Feldman, J., 1982. Directional protrusive pseudopodial activity and motility in macrophages induced by extracellular electric fields. Cell Motility, 2(3), pp.243-255.

Ott, H.C., Matthiesen, T.S., Goh, S.-K., Black, L.D., Kren, S.M., Netoff, T.I., Taylor, D.A., 2008. Perfusion-decellularized matrix: Using Nature's platform to engineer a Bioartificial Heart. Nature Medicine 14, 213–221.

Palmosi, T., Tolomeo, A.M., Cirillo, C., Sandrin, D., Sciro, M., Negrisolo, S., Todesco, M., Caicci, F., Santoro, M., Dal Lago, E., Marchesan, M., Modesti, M., Bagno, A., Romanato, F., Grumati, P., Fabozzo, A., Gerosa, G., 2022. Small

intestinal submucosa-derived extracellular matrix as a heterotopic scaffold for cardiovascular applications. Frontiers in Bioengineering and Biotechnology 10.

Park, H., Copeland, C., Henry, S. and Barbul, A., 2010. Complex Wounds and Their Management. Surgical Clinics of North America, 90(6), pp.1181-1194.

Park, J., Cheng, Q., Lu, J., Bao, J., Li, S., Tian, Y., Liang, Z., Zhang, C. and Wang, B., 2012. Thermal conductivity of MWCNT/epoxy composites: The effects of length, alignment and functionalization. Carbon, 50(6), pp.2083-2090.

Park, K., Hussein, K., Hong, S., Ahn, C., Yang, S., Park, S., Kweon, O., Kim, B. and Woo, H., 2016. Decellularized Liver Extracellular Matrix as Promising Tools for Transplantable Bioengineered Liver Promotes Hepatic Lineage Commitments of Induced Pluripotent Stem Cells. Tissue Engineering Part A, 22(5-6), pp.449-460.

Pati, F., Jang, J., Ha, D.-H., Won Kim, S., Rhie, J.-W., Shim, J.-H., Kim, D.-H., Cho, D.-W., 2014. Printing three-dimensional tissue analogues with decellularized extracellular matrix bioink. Nature Communications 5.

Pauksch, L., Hartmann, S., Rohnke, M., Szalay, G., Alt, V., Schnettler, R., Lips, K.S., 2014. Biocompatibility of silver nanoparticles and silver ions in primary human mesenchymal stem cells and osteoblasts. Acta Biomaterialia 10, pp.439–449.

Paulsson, M., 1992. The role of laminin in attachment, growth, and differentiation of cultured cells: a brief review. Cytotechnology, 9(1-3), pp.99-106.

Pauluhn, J., 2009. Subchronic 13-Week Inhalation Exposure of Rats to Multiwalled Carbon Nanotubes: Toxic Effects Are Determined by Density of

Agglomerate Structures, Not Fibrillar Structures. Toxicological Sciences, 113(1), pp.226-242.

Peers, S., Alcouffe, P., Montembault, A., Ladavière, C., 2020. Embedment of liposomes into chitosan physical hydrogel for the delayed release of antibiotics or anaesthetics, and its first ESEM characterization. Carbohydrate Polymers 229, 115532.

Pekcan, O., Akn, G., 2011. Conductivity percolation of carbon nanotubes in polyacrylamide gels. Carbon Nanotubes - Polymer Nanocomposites.

Peppas, N.A., Hoffman, A.S., 2020. Hydrogels. Biomaterials Science 153–166.

Periayah, M.H., Halim, A.S., Saad, A.Z.M., 2017. Mechanism Action of Platelets and Crucial Blood Coagulation Pathways in Hemostasis. Int J Hematol Oncol Stem Cell Res 11, pp.319–327.

Pinals, R., Yang, D., Rosenberg, D., Chaudhary, T., Crothers, A., Iavarone, A., Hammel, M. and Landry, M., 2020. Quantitative Protein Corona Composition and Dynamics on Carbon Nanotubes in Biological Environments. Angewandte Chemie International Edition, 59(52), pp.23668-23677.

Pompella, A., Visvikis, A., Paolicchi, A., Tata, V. and Casini, A. (2003). The changing faces of glutathione, a cellular protagonist. Biochemical Pharmacology, 66(8), pp.1499-1503.

Potekaev, N.N., Borzykh, O.B., Medvedev, G.V., Pushkin, D.V., Petrova, M.M., Petrov, A.V., Dmitrenko, D.V., Karpova, E.I., Demina, O.M., Shnayder, N.A., 2021. The role of extracellular matrix in skin wound healing. Journal of Clinical Medicine 10, 5947.

Prevel, C., Eppley, B., Summerlin, D., Sidner, R., Jackson, J., McCarty, M. and Badylak, S., 1995. Small intestinal submucosa: utilization as a wound dressing in full-thickness rodent wounds. Annals of Plastic Surgery, 35(4), pp.381-388.

Raman, R., Sasisekharan, V. and Sasisekharan, R., 2005. Structural Insights into Biological Roles of Protein-Glycosaminoglycan Interactions. Chemistry & Biology, 12(3), pp.267-277.

Ravanbakhsh, H., Bao, G., Latifi, N. and Mongeau, L., 2019. Carbon nanotube composite hydrogels for vocal fold tissue engineering: Biocompatibility, rheology, and porosity. Materials Science and Engineering: C, 103, p.109861.

Ravi, M., Paramesh, V., Kaviya, S., Anuradha, E. and Solomon, F., 2014. 3D Cell Culture Systems: Advantages and Applications. Journal of Cellular Physiology, 230(1), pp.16-26.

Ricard-Blum, S., 2011. The Collagen Family. Cold Spring Harbor Perspectives in Biology, 3(1), pp.a004978-a004978.

Ricard-Blum, S., 2017. Glycosaminoglycans: major biological players. Glycoconjugate Journal, 34(3), pp.275-276.

Rilla, K., Mustonen, A., Arasu, U., Härkönen, K., Matilainen, J. and Nieminen, P., 2019. Extracellular vesicles are integral and functional components of the extracellular matrix. Matrix Biology, 75-76, pp.201-219.

Robinson, A.J., Jain, A., Sherman, H.G., Hague, R.J., Rahman, R., Sanjuan-Alberte, P., Rawson, F.J., 2021. Toward hijacking bioelectricity in cancer to develop new Bioelectronic Medicine. Advanced Therapeutics 4, 2000248.

Roger, M., Fullard, N., Costello, L., Bradbury, S., Markiewicz, E., O'Reilly, S., Darling, N., Ritchie, P., Määttä, A., Karakesisoglou, I., Nelson, G., von Zglinicki, T., Dicolandrea, T., Isfort, R., Bascom, C., Przyborski, S., 2019.

Bioengineering the microanatomy of human skin. Journal of Anatomy 234, 438–455.

Rominiyi, O., Vanderlinden, A., Clenton, S.J., Bridgewater, C., Al-Tamimi, Y., Collis, S.J., 2020. Tumour treating fields therapy for glioblastoma: Current advances and Future Directions. British Journal of Cancer 124, pp.697–709.

Ronzier, E., Laurenson, A.J., Manickam, R., Liu, S., Saintilma, I.M., Schrock, D.C., Hammer, J.A., Rotty, J.D., 2022. The actin cytoskeleton responds to inflammatory cues and alters macrophage activation. Cells 11, 1806.

Rostam, H., Reynolds, P., Alexander, M., Gadegaard, N. and Ghaemmaghami, A., 2017. Image based Machine Learning for identification of macrophage subsets. Scientific Reports, 7(1).

Rouabhia, M., Park, H., Meng, S., Derbali, H. and Zhang, Z., 2013. Electrical Stimulation Promotes Wound Healing by Enhancing Dermal Fibroblast Activity and Promoting Myofibroblast Transdifferentiation. PLoS ONE, 8(8), p.e71660.

Rudnicki, M.S., Cirka, H.A., Aghvami, M., Sander, E.A., Wen, Q., Billiar, K.L., 2013. Nonlinear strain stiffening is not sufficient to explain how far cells can feel on fibrous protein gels. Biophysical Journal 105, 11–20.

Ruoff, R., Qian, D. and Liu, W., 2003. Mechanical properties of carbon nanotubes: theoretical predictions and experimental measurements. Comptes Rendus Physique, 4(9), pp.993-1008.

Russo, T.L., Peviani, S.M., Durigan, J.L., Salvini, T.F., 2008. Electrical stimulation increases matrix metalloproteinase-2 gene expression but does not change its activity in denervated rat muscle. Muscle & Nerve 37, pp.593–600.

Schwarzbauer, J.E., DeSimone, D.W., 2011. Fibronectins, their fibrillogenesis, and in vivo functions. Cold Spring Harbor Perspectives in Biology 3.

Sackett, S., Tremmel, D., Ma, F., Feeney, A., Maguire, R., Brown, M., Zhou, Y., Li, X., O'Brien, C., Li, L., Burlingham, W. and Odorico, J., 2018. Extracellular matrix scaffold and hydrogel derived from decellularized and delipidized human pancreas. Scientific Reports, 8(1).

Saldin, L., Cramer, M., Velankar, S., White, L. and Badylak, S., 2017. Extracellular matrix hydrogels from decellularized tissues: Structure and function. Acta Biomaterialia, 49, pp.1-15.

Saleh, N.B., Pfefferle, L.D., Elimelech, M., 2008. Aggregation kinetics of multiwalled carbon nanotubes in aquatic systems: Measurements and environmental implications. Environmental Science & Technology 42, 7963–7969.

Sallusto, F. and Baggiolini, M. (2008). Chemokines and leukocyte traffic. Nature Immunology, 9(9), pp.949-952.

Sanjuan-Alberte, P., Alexander, M., Hague, R. and Rawson, F., 2018. Electrochemically stimulating developments in bioelectronic medicine. Bioelectronic Medicine, 4(1).

Sanjuan-Alberte, P., Whitehead, C., Jones, J., Silva, J., Carter, N., Kellaway, S., Hague, R., Cabral, J., Ferreira, F., White, L. and Rawson, F., 2022. Printing biohybrid materials for bioelectronic cardio-3D-cellular constructs. iScience, 25(7), p.104552.

Sapudom, J., Karaman, S., Mohamed, W.K., Garcia-Sabaté, A., Quartey, B.C., Teo, J.C., 2021. 3D in vitro M2 macrophage model to mimic modulation of tissue repair. npj Regenerative Medicine 6.

Sarmin, A., El Moussaid, N., Suntornnond, R., Tyler, E., Kim, Y.-H., Di Cio, S., Megone, W., Pearce, O., Gautrot, J., Dawson, J., Connelly, J., 2022. Multi-scale analysis

of the composition, structure, and function of decellularized extracellular matrix for human skin and wound healing models. Biomolecules 12, 837.

Sarrazin, S., Lamanna, W. and Esko, J., 2011. Heparan Sulfate Proteoglycans. Cold Spring Harbor Perspectives in Biology, 3(7), pp.a004952-a004952.

Saulis, G., Lapė, R., Pranevičiūtė, R. and Mickevičius, D., 2005. Changes of the solution pH due to exposure by high-voltage electric pulses. Bioelectrochemistry, 67(1), pp.101-108.

Savitri, C., Ha, S.S., Liao, E., Du, P., Park, K., 2020. Extracellular matrices derived from different cell sources and their effect on macrophage behavior and wound healing. Journal of Materials Chemistry B 8, pp.9744–9755.

Sawkins, M.J., Bowen, W., Dhadda, P., Markides, H., Sidney, L.E., Taylor, A.J., Rose, F.R.A.J., Badylak, S.F., Shakesheff, K.M., White, L.J., 2013. Hydrogels derived from demineralized and decellularized bone extracellular matrix. Acta Biomaterialia 9, 7865–7873.

Sayyah, M., MalekiPooya, M., Khansooz, M., Pourabbasi, M., Irandoust, K., Taheri, M., H'mida, C., Halouani, J., Trabelsi, K., Chtourou, H., Bragazzi, N., Clark, C., 2022. Responses of some matrix metalloproteinases activities to an acute session of endurance exercise and electrical stimulation in induced myocardial infarction in Wistar rats 26, pp.4755–4761.

Schraufstatter, I., Zhao, M., Khaldoyanidi, S. and DiScipio, R., 2012. The chemokine CCL18 causes maturation of cultured monocytes to macrophages in the M2 spectrum. Immunology, 135(4), pp.287-298.

Scotton, M.F., Miot, H.A., Abbade, L.P., 2014. Factors that influence healing of chronic venous leg ulcers: A retrospective cohort. Anais Brasileiros de Dermatologia 89, 414–422.

Sen, C.K., Roy, S., 2008. Redox signals in wound healing. Biochimica et Biophysica Acta (BBA) - General Subjects 1780, 1348–1361.

Senftle, F., Grant, J. and Senftle, F. (2010). Low-voltage DC/AC electrolysis of water using porous graphite electrodes. Electrochimica Acta, 55(18), pp.5148-5153.

Serban, M.A., Liu, Y., Prestwich, G.D., 2008. Effects of extracellular matrix analogues on primary human fibroblast behavior. Acta Biomaterialia 4, 67–75.

Shahraki, S., Bideskan, A.E., Aslzare, M., Tavakkoli, M., Bahrami, A.R., Hosseinian, S., Matin, M.M., Rad, A.K., 2022. Decellularization with Triton X-100 provides a suitable model for human kidney bioengineering using human mesenchymal stem cells. Life Sciences 295, 120167.

Shannon, G.S., Novak, T., Mousoulis, C., Voytik-Harbin, S.L., Neu, C.P., 2015. Temperature and concentration dependent fibrillogenesis for improved magnetic alignment of collagen gels. RSC Advances 5, 2113–2121.

Shchukin, E.D., Pertsov, A.V., Amelina, E.A., Zelenev, A.S., 2001. 3. In: Colloid and Surface Chemistry. Elsevier Science.

Shi, C., Pamer, E.G., 2011. Monocyte recruitment during infection and inflammation. Nature Reviews Immunology 11, pp.762–774.

Shin, S., Bae, H., Cha, J., Mun, J., Chen, Y., Tekin, H., Shin, H., Zarabi, S., Dokmeci, M., Tang, S. and Khademhosseini, A., 2011. Carbon Nanotube Reinforced Hybrid Microgels as Scaffold Materials for Cell Encapsulation. ACS Nano, 6(1), pp.362-372.

Shipp, D., Sinjab, F. and Notingher, I., 2017. Raman spectroscopy: techniques and applications in the life sciences. Advances in Optics and Photonics, 9(2), p.315.

Shridhar, A., Amsden, B., Gillies, E. and Flynn, L., 2019. Investigating the Effects of Tissue-Specific Extracellular Matrix on the Adipogenic and Osteogenic Differentiation of Human Adipose-Derived Stromal Cells Within Composite Hydrogel Scaffolds. Frontiers in Bioengineering and Biotechnology, 7.

Shukla, N.M., Sato-Kaneko, F., Yao, S., Pu, M., Chan, M., Lao, F.S., Sako, Y., Saito, T., Messer, K., Hayashi, T., Cottam, H.B., Corr, M., Carson, D.A., 2022. A triple high throughput screening for extracellular vesicle inducing agents with immunostimulatory activity. Frontiers in Pharmacology 13.

Singer, A. and Clark, R. (1999). Cutaneous Wound Healing. New England Journal of Medicine, 341(10), pp.738-746.

Singh, S.P., Schwartz, M.P., Lee, J.Y., Fairbanks, B.D., Anseth, K.S., 2014. A peptide functionalized poly(ethylene glycol) (PEG) hydrogel for investigating the influence of biochemical and biophysical matrix properties on tumor cell migration. Biomaterials Science 2, 1024.

Slivka, P.F., Dearth, C.L., Keane, T.J., Meng, F.W., Medberry, C.J., Riggio, R.T., Reing, J.E., Badylak, S.F., 2014. Fractionation of an ECM hydrogel into structural and soluble components reveals distinctive roles in regulating macrophage behavior. Biomater. Sci. 2, 1521–1534.

Somaiah, C., Kumar, A., Mawrie, D., Sharma, A., Patil, S., Bhattacharyya, J., Swaminathan, R. and Jaganathan, B., 2015. Collagen Promotes Higher Adhesion, Survival and Proliferation of Mesenchymal Stem Cells. PLOS ONE, 10(12), p.e0145068.

Song, B., Zhao, M., Forrester, J. and McCaig, C. (2002). Electrical cues regulate the orientation and frequency of cell division and the rate of wound healing

in vivo. Proceedings of the National Academy of Sciences, 99(21), pp.13577-13582.

Soo, C., Shaw, W.W., Zhang, X., Longaker, M.T., Howard, E.W., Ting, K., 2000. Differential expression of matrix metalloproteinases and their tissue-derived inhibitors in cutaneous wound repair. Plastic & Reconstructive Surgery 105, pp.638–647.

Spiller, K.L., Anfang, R.R., Spiller, K.J., Ng, J., Nakazawa, K.R., Daulton, J.W., Vunjak-Novakovic, G., 2014. The role of macrophage phenotype in vascularization of tissue engineering scaffolds. Biomaterials 35, 4477–4488.

Stankovich, S., Dikin, D.A., Dommett, G.H., Kohlhaas, K.M., Zimney, E.J., Stach, E.A., Piner, R.D., Nguyen, S.B.T., Ruoff, R.S., 2006. Graphene-based composite materials. Nature 442, pp.282–286.

Stauffer, D., Aharony, A., 1994. Chapter 1 - Forest Fires Fractal Oil Fields and Diffusion. In: Introduction to Percolation Theory (1 Ed.). CRC Press, Florida, pp.1-14.

Stejskal, J., Trchová, M., Bober, P., Morávková, Z., Kopecký, D., Vrňata, M., Prokeš, J., Varga, M., Watzlová, E., 2016. Polypyrrole salts and bases: Superior conductivity of nanotubes and their stability towards the loss of conductivity by deprotonation. RSC Advances 6, pp.88382–88391.

Stejskalová, A., Fincke, V., Nowak, M., Schmidt, Y., Borrmann, K., von Wahlde, M., Schäfer, S., Kiesel, L., Greve, B. and Götte, M., 2021. Collagen I triggers directional migration, invasion and matrix remodeling of stroma cells in a 3D spheroid model of endometriosis. Scientific Reports, 11(1).

Steketee, M., van der Merwe, Y. and Faust, A., 2017. Matrix bound vesicles and miRNA cargoes are bioactive factors within extracellular matrix bioscaffolds. Neural Regeneration Research, 12(10), p.1597.

Stojkov, G., Niyazov, Z., Picchioni, F., Bose, R.K., 2021. Relationship between structure and rheology of hydrogels for various applications. Gels 7, 255.

Storm, C., Pastore, J.J., MacKintosh, F.C., Lubensky, T.C., Janmey, P.A., 2005. Nonlinear elasticity in biological gels. Nature 435, 191–194.

Stuart, K., Panitch, A., 2008. Influence of chondroitin sulfate on collagen gel structure and mechanical properties at physiologically relevant levels. Biopolymers 89, 841–851.

Sun, H., Zhou, J., Huang, Z., Qu, L., Lin, N., Liang, C., Dai, R., Tang, L. and Tian, F., 2017. Carbon nanotube-incorporated collagen hydrogels improve cell alignment and the performance of cardiac constructs. International Journal of Nanomedicine, Volume 12, pp.3109-3120.

Sun, T., Jackson, S., Haycock, J.W., MacNeil, S., 2006. Culture of skin cells in 3D rather than 2D improves their ability to survive exposure to cytotoxic agents. Journal of Biotechnology 122, pp.372–381.

Sun, Y., Reid, B., Ferreira, F., Luxardi, G., Ma, L., Lokken, K., Zhu, K., Xu, G., Sun, Y., Ryzhuk, V., Guo, B., Lebrilla, C., Maverakis, E., Mogilner, A. and Zhao, M., 2019. Infection-generated electric field in gut epithelium drives bidirectional migration of macrophages. PLOS Biology, 17(4), p.e3000044.

Sundaresan, M., Yu, Z.-X., Ferrans, V.J., Irani, K., Finkel, T., 1995. Requirement for generation of H2O2 for platelet-derived growth factor signal transduction. Science 270, 296–299.

Sweeney, E., Roberts, D., Corbo, T. and Jacenko, O., 2010. Congenic Mice Confirm That Collagen X Is Required for Proper Hematopoietic Development. PLoS ONE, 5(3), p.e9518.

Takakura, A., Beppu, K., Nishihara, T., Fukui, A., Kozeki, T., Namazu, T., Miyauchi, Y. and Itami, K., 2019. Strength of carbon nanotubes depends on their chemical structures. Nature Communications, 10(1).

Tang, V., 2020. Collagen, stiffness, and adhesion: the evolutionary basis of vertebrate mechanobiology. Molecular Biology of the Cell, 31(17), pp.1823-1834.

Tao, W., Zhu, X., Yu, X., Zeng, X., Xiao, Q., Zhang, X., Ji, X., Wang, X., Shi, J., Zhang, H., Mei, L., 2016. Black phosphorus nanosheets as a robust delivery platform for cancer theranostics. Advanced Materials 29, 1603276.

Tapias, L.F., Ott, H.C., 2014. Decellularized scaffolds as a platform for bioengineered organs. Current Opinion in Organ Transplantation 19, 145–152.

Tedesco, S., De Majo, F., Kim, J., Trenti, A., Trevisi, L., Fadini, G.P., Bolego, C., Zandstra, P.W., Cignarella, A., Vitiello, L., 2018. Convenience versus biological significance: Are PMA-differentiated THP-1 cells a reliable substitute for blood-derived macrophages when studying in vitro polarization? Frontiers in Pharmacology 9.

Temple, J., Velliou, E., Shehata, M., Lévy, R., Gupta, P., 2022. Current strategies with implementation of three-dimensional cell culture: The challenge of quantification. Interface Focus 12.

Thorne, J.T., Segal, T.R., Chang, S., Jorge, S., Segars, J.H., Leppert, P.C., 2015. Dynamic reciprocity between cells and their microenvironment in reproduction1. Biology of Reproduction 92.

Tian, D.M., Wan, H.H., Chen, J.R., Ye, Y.B., He, Y., Liu, Y., Tang, L.Y., He, Z.Y., Liu, K.Z., Gao, C.J., Li, S.L., Xu, Q., Yang, Z., Lai, C., Xu, X.J., Ruan, C.S., Xu, Y.S., Zhang, C., Luo, L., Yan, L.P., 2022. In-situ formed Elastin-based hydrogels enhance wound healing via promoting innate immune cells recruitment and angiogenesis. Materials Today Bio 15, 100300.

Tibbitt, M. and Anseth, K., 2009. Hydrogels as extracellular matrix mimics for 3D cell culture. Biotechnology and Bioengineering, 103(4), pp.655-663.

Tidwell, T.R., Røsland, G.V., Tronstad, K.J., Søreide, K., Hagland, H.R., 2022. Metabolic flux analysis of 3D spheroids reveals significant differences in glucose metabolism from matched 2D cultures of colorectal cancer and pancreatic ductal adenocarcinoma cell lines. Cancer & Metabolism 10.

Timraz, S., Rezgui, R., Boularaoui, S. and Teo, J. (2015). Stiffness of Extracellular Matrix Components Modulates the Phenotype of Human Smooth Muscle Cells in Vitro and Allows for the Control of Properties of Engineered Tissues. Procedia Engineering, 110, pp.29-36.

Tolg, C., Telmer, P., Turley, E., 2014. Specific sizes of hyaluronan oligosaccharides stimulate fibroblast migration and excisional wound repair. PLoS ONE 9.

Trębacz, H., Barzycka, A., 2023. Mechanical properties and functions of elastin: An overview. Biomolecules 13, 574.

Tsuchiya, S., Yamabe, M., Yamaguchi, Y., Kobayashi, Y., Konno, T. and Tada, K., 1980. Establishment and characterization of a human acute monocytic leukemia cell line (THP-1). International Journal of Cancer, 26(2), pp.171-176.

Tucker, R.P., Degen, M., 2019. The expression and possible functions of tenascin-W during development and disease. Frontiers in Cell and Developmental Biology 7.

Ud-Din, S. and Bayat, A., 2014. Electrical stimulation and cutaneous wound healing: a review of clinical evidence. Healthcare 2(4), 445-467.

Unuvar Purcu, D., Korkmaz, A., Gunalp, S., Helvaci, D.G., Erdal, Y., Dogan, Y., Suner, A., Wingender, G., Sag, D., 2022. Effect of stimulation time on the expression of human macrophage polarization markers. PLOS ONE 17.

Uribe-Querol, E. and Rosales, C., 2020. Phagocytosis: Our Current Understanding of a Universal Biological Process. Frontiers in Immunology, 11.

Ushiki, T., 1992. The three-dimensional ultrastructure of the collagen fibers, reticular fibers and elastic fibers: a review. Journal of Anatomy, 67(3), pp.186-199.

Uyama, T., Kitagawa, H. and Sugahara, K., 2007. Biosynthesis of Glycosaminoglycans and Proteoglycans. Comprehensive Glycoscience, pp.79-104.

Vaithilingam, J., Sanjuan-Alberte, P., Campora, S., Rance, G., Jiang, L., Thorpe, J., Burroughs, L., Tuck, C., Denning, C., Wildman, R., Hague, R., Alexander, M. and Rawson, F., 2019. Multifunctional Bioinstructive 3D Architectures to Modulate Cellular Behavior. Advanced Functional Materials, 29(38), p.1902016.

Valcourt, U., Alcaraz, L.B., Exposito, J.-Y., Lethias, C., Bartholin, L., 2015. Tenascin-X: Beyond the architectural function. Cell Adhesion & Migration 9, 154–165.

Valenick, L., Hsia, H. and Schwarzbauer, J., 2005. Fibronectin fragmentation promotes α4β1 integrin-mediated contraction of a fibrin–fibronectin provisional matrix. Experimental Cell Research, 309(1), pp.48-55.

van Helvert, S., Friedl, P., 2016. Strain stiffening of fibrillar collagen during individual and collective cell migration identified by AFM nanoindentation. ACS Applied Materials & Interfaces 8, 21946–21955.

Vardharajula, S., Tiwari, P., Erdal Eroğlu, Komal Vig, Dennis, V. and Singh, S., 2012. Functionalized carbon nanotubes: biomedical applications. International Journal of Nanomedicine, p.5361.

Vicente, R., Escalada, A., Coma, M., Fuster, G., Sánchez-Tilló, E., López-Iglesias, C., Soler, C., Solsona, C., Celada, A., Felipe, A., 2003. Differential voltage-dependent K+ channel responses during proliferation and activation in macrophages. Journal of Biological Chemistry 278, 46307–46320.

Vishwakarma, A., Sharpe, P., Shi, S., Ramalingam, M., 2015. Chapter 3 - Extracellular Matrix (ECM) Molecules. In: Stem Cell Biology and Tissue Engineering in Dental Sciences. Elsevier Acad. Press, Amsterdam.

Volk, S.W., Wang, Y., Mauldin, E.A., Liechty, K.W., Adams, S.L., 2011. Diminished type III collagen promotes myofibroblast differentiation and increases scar deposition in cutaneous wound healing. Cells Tissues Organs 194, pp.25–37.

Voytik-Harbin, S.L., Brightman, A.O., 1998. Small intestinal submucosa: A tissue derived extracellular matrix that promotes tissue-specific growth and differentiation of cells in vitro. Tissue Eng 4, 157–74.

Voytik-Harbin, S.L., Brightman, A.O., Kraine, M.R., Waisner, B., Badylak, S.F., 1997. Identification of extractable growth factors from small intestinal submucosa. Journal of Cellular Biochemistry 67, 478–491.

Výborný, K., Vallová, J., Kočí, Z., Kekulová, K., Jiráková, K., Jendelová, P., Hodan, J., Kubinová, Š., 2019. Genipin and EDC crosslinking of extracellular matrix

hydrogel derived from human umbilical cord for neural tissue repair. Scientific Reports 9.

Wallace, H., Basehore, B., Zito, P., 2023. Wound Healing Phases. StatPearls [Internet], Treasure Island, FL.

Wang, H., Yu, H., Zhou, X., Zhang, J., Zhou, H., Hao, H., Ding, L., Li, H., Gu, Y., Ma, J., Qiu, J., Ma, D., 2022. An overview of extracellular matrix-based Bioinks for 3D bioprinting. Frontiers in Bioengineering and Biotechnology 10.

Wang, J., Guo, J., Wu, S., Feng, H., Sun, S., Pan, J., Zhang, J. and Beebe, S., 2012. Synergistic Effects of Nanosecond Pulsed Electric Fields Combined with Low Concentration of Gemcitabine on Human Oral Squamous Cell Carcinoma In Vitro. PLoS ONE, 7(8), p.e43213.

Wang, L., Zhang, S., Wu, H., Rong, X., Guo, J., 2018. M2b macrophage polarization and its roles in diseases. Journal of Leukocyte Biology 106, 345–358.

Wang, X., Ansari, A., Pierre, V., Young, K., Kothapalli, C.R., von Recum, H.A., Senyo, S.E., 2022. Injectable extracellular matrix microparticles promote heart regeneration in mice with post-ischemic heart injury. Advanced Healthcare Materials 11, 2102265.

Wang, X., Xu, H., Huang, Y., Gu, S. and Jiang, J., 2016. Coupling Effect of Water and Proteoglycans on the In Situ Toughness of Bone. Journal of Bone and Mineral Research, 31(5), pp.1026-1029.

Wassenaar, J.W., Gaetani, R., Garcia, J.J., Braden, R.L., Luo, C.G., Huang, D., DeMaria, A.N., Omens, J.H., Christman, K.L., 2016. Evidence for mechanisms underlying functional benefits of a myocardial matrix hydrogel for Post-MI Treatment. Journal of the American College of Cardiology 67, pp.1074–1086.

Wathiong, B., Deville, S., Jacobs, A., Smisdom, N., Gervois, P., Lambrichts, I., Ameloot, M., Hooyberghs, J., Nelissen, I., 2019. Role of nanoparticle size and sialic acids in the distinct time-evolution profiles of nanoparticle uptake in hematopoietic progenitor cells and monocytes. Journal of Nanobiotechnology 17.

Watt, M.R., Gerhardt, R.A., 2020. Factors that affect network formation in carbon nanotube composites and their resultant electrical properties. Journal of Composites Science 4, 100.

Wells, R.G., 2008. The role of matrix stiffness in regulating cell behavior. Hepatology 47, 1394–1400.

Wenstrup, R.J., Florer, J.B., Cole, W.G., Willing, M.C., Birk, D.E., 2004. Reduced type I collagen utilization: A pathogenic mechanism in COL5A1 haplo-insufficient Ehlers-Danlos syndrome. Journal of Cellular Biochemistry 92, 113–124.

White, L.J., Keane, T.J., Smoulder, A., Zhang, L., Castleton, A.A., Reing, J.E., Turner, N.J., Dearth, C.L., Badylak, S.F., 2018. The impact of sterilization upon extracellular matrix hydrogel structure and function. Journal of Immunology and Regenerative Medicine 2, 11–20.

White, L.J., Taylor, A.J., Faulk, D.M., Keane, T.J., Saldin, L.T., Reing, J.E., Swinehart, I.T., Turner, N.J., Ratner, B.D., Badylak, S.F., 2017. The impact of detergents on the tissue decellularization process: A TOF-Sims Study. Acta Biomaterialia 50, 207–219.

Wilgus, T.A., Roy, S., McDaniel, J.C., 2013. Neutrophils and wound repair: Positive actions and negative reactions. Advances in Wound Care 2, pp.379–388.

Witte, M.B., Barbul, A., 1997. General principles of wound healing. Surgical Clinics of North America 77, pp.509–528.

Won, J.-Y., Lee, M.-H., Kim, M.-J., Min, K.-H., Ahn, G., Han, J.-S., Jin, S., Yun, W.-S., Shim, J.-H., 2019. A potential dermal substitute using decellularized dermis extracellular matrix derived bio-ink. Artificial Cells, Nanomedicine, and Biotechnology 47, 644–649.

Wu, S., Hui, K.S., Hui, K.N., 2018. 2D black phosphorus: From preparation to applications for Electrochemical Energy Storage. Advanced Science 5, 1700491.

Wynn, T., 2008. Cellular and molecular mechanisms of fibrosis. The Journal of Pathology, 214(2), pp.199-210.

Xu, R., Boudreau, A., Bissell, M.J., 2009. Tissue architecture and function: Dynamic reciprocity via extra- and intra-cellular matrices. Cancer and Metastasis Reviews 28, 167–176.

Xie, Y., Rizzi, S.C., Dawson, R., Lynam, E., Richards, S., Leavesley, D.I., Upton, Z., 2010. Development of a three-dimensional human skin equivalent wound model for investigating novel Wound healing therapies. Tissue Engineering Part C: Methods 16, pp.1111–1123.

Yanagishita, M., 1993. Function of proteoglycans in the extracellular matrix. Pathology International, 43(6), pp.283-293.

Yang, H., Song, L., Sun, B., Chu, D., Yang, L., Li, M., Li, H., Dai, Y., Yu, Z., Guo, J., 2021. Modulation of macrophages by a paeoniflorin-loaded hyaluronic acid-based hydrogel promotes diabetic wound healing. Materials Today Bio 12, 100139.

Yang, Q., Ma, L., Xiao, S., Zhang, D., Djoulde, A., Ye, M., Lin, Y., Geng, S., Li, X., Chen, T., Sun, L., 2021. Electrical conductivity of multiwall carbon nanotube

bundles contacting with metal electrodes by nano manipulators inside sem. Nanomaterials 11, 1290.

Yao, Y., Xu, X.-H., Jin, L., 2019. Macrophage polarization in physiological and pathological pregnancy. Frontiers in Immunology 10.

Yu, C., Shi, L., Yao, Z., Li, D., Majumdar, A., 2005. Thermal conductance and thermopower of an individual single-wall carbon nanotube. Nano Letters 5, 1842–1846.

Yu, H., Zhao, H., Huang, C. and Du, Y., 2017. Mechanically and Electrically Enhanced CNT–Collagen Hydrogels As Potential Scaffolds for Engineered Cardiac Constructs. ACS Biomaterials Science & Engineering, 3(11), pp.3017-3021.

Yuan, X., Arkonac, D., Chao, P. and Vunjak-Novakovic, G. (2014). Electrical stimulation enhances cell migration and integrative repair in the meniscus. Scientific Reports, 4(1).

Yussof, S.J., Omar, E., Pai, D.R., Sood, S., 2012. Cellular events and biomarkers of wound healing. Indian Journal of Plastic Surgery 45, pp.220–228.

Zagon, I., Sassani, J., Ruth, T. and McLaughlin, P. (2000). Cellular dynamics of corneal wound re-epithelialization in the rat. Brain Research, 882(1-2), pp.169-179.

Zhang, F., Zheng, L., Cheng, S., Peng, Y., Fu, L., Zhang, X. and Linhardt, R., 2019. Comparison of the Interactions of Different Growth Factors and Glycosaminoglycans. Molecules, 24(18), p.3360.

Zhang, Q., Raoof, M., Chen, Y., Sumi, Y., Sursal, T., Junger, W., Brohi, K., Itagaki, K., Hauser, C.J., 2010. Circulating mitochondrial damps cause inflammatory responses to injury. Nature 464, 104–107.

Zhang, T., Day, J.H., Su, X., Guadarrama, A.G., Sandbo, N.K., Esnault, S., Denlinger, L.C., Berthier, E., Theberge, A.B., 2019. Investigating fibroblast-induced collagen gel contraction using a dynamic Microscale platform. Frontiers in Bioengineering and Biotechnology 7.

Zhang, T., Tang, M., Yao, Y., Ma, Y. and Pu, Y., 2019. MWCNT interactions with protein: surface-induced changes in protein adsorption and the impact of protein corona on cellular uptake and cytotoxicity. International Journal of Nanomedicine, Volume 14, pp.993-1009.

Zhang, W., Du, A., Liu, S., Lv, M., Chen, S., 2021. Research progress in decellularized extracellular matrix-derived hydrogels. Regenerative Therapy 18, pp.88–96.

Zhang, X., Chen, X., Hong, H., Hu, R., Liu, J., Liu, C., 2022. Decellularized extracellular matrix scaffolds: Recent trends and emerging strategies in tissue engineering. Bioactive Materials 10, 15–31.

Zhang, X., Zhou, W., Chen, X., Liu, Y. and Chen, K., 2016. Significant decrease in thermal conductivity of multi-walled carbon nanotube induced by inter-wall van der Waals interactions. Physics Letters A, 380(21), pp.1861-1864.

Zhang, Z., Li, X.-J., Liu, Y., Zhang, X., Li, Y.-Y., Xu, W.-S., 2007. Recombinant human decorin inhibits cell proliferation and downregulates TGF-β1 production in hypertrophic scar fibroblasts. Burns 33, pp.634–641.

Zhao, M., Bai, H., Wang, E., Forrester, J. and McCaig, C. (2003). Electrical stimulation directly induces pre-angiogenic responses in vascular endothelial cells by signaling through VEGF receptors. Journal of Cell Science, 117(3), pp.397-405.

Zhao, M., Pu, J., Forrester, J. and McCaig, C. (2002). Membrane lipids, EGF receptors, and intracellular signals colocalize and are polarized in epithelial cells moving directionally in a physiological electric field. The FASEB Journal, 16(8), pp.857-859.

Zhao, M., Song, B., Pu, J., Wada, T., Reid, B., Tai, G., Wang, F., Guo, A., Walczysko, P., Gu, Y., Sasaki, T., Suzuki, A., Forrester, J., Bourne, H., Devreotes, P., McCaig, C. and Penninger, J., 2006. Electrical signals control wound healing through phosphatidylinositol-3-OH kinase-γ and PTEN. Nature, 442(7101), pp.457-460.

Zhao, R., Liang, H., Clarke, E., Jackson, C. and Xue, M., 2016. Inflammation in Chronic Wounds. International Journal of Molecular Sciences, 17(12), p.2085.

Zhao, Z., Raeber, T., Murdoch, B., Partridge, J., McCulloch, D. and McKenzie, D., 2020. Unifying the optical and electrical properties of amorphous carbon: application to hopping photoconductivity and memristance. Journal of Applied Physics, 128(21), p.215109.

Zhao, Z., Vizetto-Duarte, C., Moay, Z.K., Setyawati, M.I., Rakshit, M., Kathawala, M.H., Ng, K.W., 2020. Composite hydrogels in three-dimensional in vitro models. Frontiers in Bioengineering and Biotechnology 8.

Zheng, C. and Levenston, M., 2015. Fact versus artifact: Avoiding erroneous estimates of sulfated glycosaminoglycan content using the dimethylmethylene blue colorimetric assay for tissue-engineered constructs. European Cells and Materials, 29, pp.224-236.

Zheng, M., Chen, J., Kirilak, Y., Willers, C., Xu, J. and Wood, D., 2005. Porcine small intestine submucosa (SIS) is not an acellular collagenous matrix and contains porcine DNA: Possible implications in human

implantation. Journal of Biomedical Materials Research Part B: Applied Biomaterials, 73B(1), pp.61-67.

Zhou, J., Wu, P., Sun, H., Zhou, H., Zhang, Y., Xiao, Z., 2019. Lung tissue extracellular matrix-derived hydrogels protect against radiation-induced lung injury by suppressing epithelial–mesenchymal transition. Journal of Cellular Physiology 235, pp.2377–2388.

Zhou, Q., Meng, F., Liu, Z. and Shi, S., 2013. The Thermal Conductivity of Carbon Nanotubes with Defects and Intramolecular Junctions. Journal of Nanomaterials, pp.1-7.

Zhu, Y., Sköld, C.M., Liu, X., Wang, H., Kohyama, T., Wen, F.-Q., Ertl, R.F., Rennard, S.I., 2001. Collaborative interactions between neutrophil elastase and metalloproteinases in extracellular matrix degradation in three-dimensional collagen gels. Respiratory Research 2, 295.

Zizzo, G., Hilliard, B.A., Monestier, M., Cohen, P.L., 2012. Efficient clearance of early apoptotic cells by human macrophages requires M2C polarization and Mertk induction. The Journal of Immunology 189, 3508–3520.

“I think I’m quite ready for another adventure”

- Bilbo Baggins